3D-PTV of particle-laden turbulent pipe flows

Document Version:
Publisher's PDF, also known as Version of Record (includes final page, issue and volume numbers)

Please check the document version of this publication:

• A submitted manuscript is the version of the article upon submission and before peer-review. There can be important differences between the submitted version and the official published version of record. People interested in the research are advised to contact the author for the final version of the publication, or visit the DOI to the publisher's website.
• The final author version and the galley proof are versions of the publication after peer review.
• The final published version features the final layout of the paper including the volume, issue and page numbers.

Link to publication

3D-PTV of particle-laden turbulent pipe flows

PROEFSCHRIFT

ter verkrijging van de graad van doctor aan de
Technische Universiteit Eindhoven, op gezag van de
rector magnificus, prof.dr.ir. C.J. van Duijn, voor een
commissie aangewezen door het College voor
Promoties in het openbaar te verdedigen
op woensdag 26 september 2012 om 14.00 uur

door

Jorge Luiz Goes Oliveira

geboren te Aracaju, Brazilië

Dit proefschrift is goedgekeurd door de promotor:

prof.dr.ir. J.J.H. Brouwers

Copromotor:

dr. C.W.M. van der Geld

Table of Contents

Summary

3D-PTV of particle-laden turbulent pipe flows

Turbulent dispersed two-phase flows are ubiquitous in both industry and nature. Flows of this kind are characterized by particles, droplets or bubbles dispersed within a carrier phase. Predicting the behavior of this kind of flows is therefore of quite some interest in engineering applications. However, due to the complex nature of the problem, the available models are usually simplified and not able to fully predict fluid and particle behavior for the whole range of applications.

Experiments are indispensable tools to understand the underlying physics of dispersed two-phase flows. Experiments therefore serve to improve the efficiency and reliability of numerical or theoretical models. However, the lack of consistent experimental data makes validation of existent models difficult.

Among the numerous turbulent dispersed two-phase flows, a particular class possesses challengeable and interesting properties that need disclosure: flows where the dispersed phase is able to interact with turbulent eddies. This class of dispersed two-phase flows is even more interesting and of practical importance in an inhomogeneous turbulent velocity field such as found in pipes. This work aims at experimental clarification of the essential physics of turbulent particle-laden pipe flows with a characteristic ratio of turbulent carrier-phase RMS velocity and terminal velocity of inertia particles, u_{rms}/U_{TV}, of order one.

An experimental setup is arranged in such way that the liquid and particle three-dimensional velocities in upward and downward vertical flows can be measured. The optical technique three-dimensional particle tracking velocimetry (3D-PTV) is applied to gather Lagrangian and Eulerian statistics for both flow tracers and inertia particles. To the best of our knowledge, no Lagrangian results have been reported for particle-laden pipe flows.

The role of inertia, flow turbulence and flow orientation with respect to gravity on concentration profile and mean relative velocity of particle-laden pipe flows is presented. The effect of particle feedback on the fluid is presented with δ-forcing. The relevance of the

break-up mechanism in the transport of inertia particles in transient pipe flows is discussed. The main features of Lagrangian velocity and acceleration statistics of flow tracers and inertia particles are disclosed.

1

Introduction

Turbulent dispersed two-phase flows are ubiquitous in both industry and nature. For example, the dispersion of pollutants in an urban environment, sediment transport or the fluidized catalytic cracking of carbohydrates are often studied.[1] Flows of this kind are characterized by particles, droplets or bubbles dispersed within a carrier phase. The occurrence of such flows in pipes is large as well, with applications ranging from pneumatic conveying systems to chemical reactor design. Predicting the behavior of this kind of flows is therefore of quite some interest in engineering applications. However, due to the complex nature of the problem, the available models are usually simplified and not able to fully predict fluid and particle behavior for the whole range of applications.

Single-phase turbulent flows are intensively studied as well. In the range of low to moderate Reynolds numbers, Direct Numerical Simulation (DNS) of the Navier-Stokes equations enables the computation of complete turbulent flow fields without the need of any modeling assumptions. This method is well known to be limited by the requirement of quite some computational power, even at moderate Reynolds numbers. Single-phase turbulent flows at high Reynolds numbers or in complex flow geometries demand huge computational effort. In such conditions, predictions are only possible by modeling parts of governing equations, in particular the small scales, resulting in the so-called closure problem: the process of averaging leads to terms which require heuristic modeling.

The stochastic nature of the carrier-phase turbulence is further complicated by the dispersed phase. Its presence makes such type of flow far more complex than its single-phase counterpart. When particles are present in a fluid flow, the only way to exactly describe the system, including the interaction of the phases, is to fully resolve the particle surfaces, demanding severe mesh refinement at the surroundings of particles. The presence

of particles therefore significantly enhances the requirements with regard to computational memory and time. As a result, extra assumptions are needed to simplify the system, such as treating finite-size particles as point forces in the fluid domain.

In this context, experiments are indispensable tools to understand the underlying physics of dispersed two-phase flows. Experiments therefore serve to improve the efficiency and reliability of numerical or theoretical models. However, the lack of consistent experimental data makes validation of existent models difficult.

Among the numerous turbulent dispersed two-phase flows, a particular class possesses challengeable and interesting properties that need disclosure: flows where the dispersed phase is able to interact with turbulent eddies. The terminal velocity of the dispersed phase, U_{TV}, is attained when gravitational and drag forces on a single particle are in equilibrium in a quiescent fluid. When a characteristic root-mean-square velocity of the turbulent carrier phase, u_{rms}, and the terminal velocity are of same order of magnitude, $u_{rms}/U_{TV} \approx O(1)$, significant interaction between the dispersed phase and turbulent eddies is expected. For example, the entrapment of particles in vortical flow structures can modify the time-averaged settling velocity.

This class of dispersed two-phase flows is even more interesting and of practical importance in an inhomogeneous turbulent velocity field such as found in pipes. This thesis aims at clarifying some essential physics of turbulent dispersed two-phase pipe flows with $u_{rms}/U_{TV} \approx O(1)$ by means of experiments and analysis. Particle-laden flow is chosen because solid particles make the control of the inertial characteristics of the dispersed phase, such as the mass density and volume, easier. In addition, the shape is controlled and precisely known while the difference in mass densities of carrier and dispersed phases can be varied at will. Two categories of polystyrene inertia particles are employed to represent the dispersed phase, with particle diameters corresponding to 0.80 and 0.96 mm. Polystyrene particles with 0.2 mm are employed as flow tracers. The ratio of mass densities of applied particles and of the carrier fluid (water) is 1.05. Vertical flow directions are also chosen, since the alignment (or counter alignment) of the main flow and gravity facilitates the analysis due to symmetry in azimuthal direction.

Experimental approaches in fluid flows are often subdivided into Eulerian and Lagrangian. While the first approach employs a stationary observer to measure flow quantities, in the second particles are followed on their path through the flow and their changing behavior is monitored as a function of time. Therefore, an experimental technique

which allows statistical analysis in both Eulerian and Lagrangian reference frames is desirable.

Two main categories of techniques are often applied in the acquisition of Lagrangian statistics: sonar and optical. The first is in general employed for low particle number densities; one or few more particles in the measurement volume at a certain time and during short measurement periods.[2] This is certainly a drawback when a large amount of particles is required to obtain reliable statistics. An optical technique allows a considerable range of particle number densities and sizes[3] and has therefore been chosen for the present work.

The optical technique three-dimensional particle tracking velocimetry (3D-PTV) is applied to gather Lagrangian and Eulerian statistics of particle-laden turbulent pipe flows. This technique is chosen instead of PIV for the following reasons: the inhomogeneous nature of pipe flow where particle statistics are in general averaged on discrete radial positions and the sparse particle field, particularly for the dispersed phase.

3D-PTV particle-laden pipe flow experiments have been performed in a test rig always at the same bulk flow Reynolds number (Re_b), 10300, based on the pipe diameter and bulk velocity. Measurements at the specified Reynolds number favor direct comparison to literature results. Lagrangian measurements in flow geometries with non-zero mean velocity component are scarce. The work of Suzuki and Kasagi[4] represents one of the few exceptions. For the practical pipe flow, only the 3D-PTV results of Walpot et al.[5] at flow Reynolds number, 5300 and 10300, are available to our knowledge. At the same Re_b, Veenman[6] provided Eulerian and Lagrangian computations of single-phase pipe flow, with DNS. However, these reference Eulerian and Lagrangian results have only been obtained for single-phase pipe flows in fully developed flow conditions. To the best of our knowledge, no Lagrangian results have been reported for particle-laden pipe flows.

With the aim of evaluating the effect of flow orientation with respect to gravity on the concentration profiles of particles, the experimental setup is arranged in such way that the liquid and particle statistics in upward and downward vertical flows can be measured. To analyze the role of flow turbulence level on the time-averaged mean relative velocity, different stages of flow development are also tested at $Re_b = 10300$. In chapter 3, it is shown that turbulent features provide a convenient way to distinguish flow conditions from the fully developed case.

Two types of inertia particles with Stokes number, based on the relaxation time for particles in stationary flow and on viscous scales, equal to 2.3 and 3.3 are applied. The mean volumetric concentration in the range 0.5×10^{-6} to 1.7×10^{-4} is varied in order to investigate above which limit two-way coupling comes into play. The effect of particle feedback on the fluid is presented with δ-forcing. For the category of particles and velocimetry results, a limiting value for mean concentration which can affect the frictional pressure drop is provided.

The outline of the thesis is as follows. In Chapter 2, the 3D-PTV experimental setup is validated by comparing Eulerian and Lagrangian results of a single-phase pipe flow in fully developed conditions at Re_b = 10300 with literature results. New experimental methods are explored and presented, paving the way for measurement of Lagrangian particle statistics, be it tracers or be it inertial particles, at tube Reynolds numbers 20,000 and higher. Chapter 3 presents the role of inertia, flow turbulence and flow orientation with respect to gravity on concentration profile and mean relative velocity of particle-laden pipe flows. In Chapter 4, the relevance of the break-up mechanism in the transport of inertia particles in transient pipe flows is discussed. The main features of Lagrangian velocity and acceleration statistics of flow tracers and inertia particles are disclosed in Chapter 5. Finally, Chapter 6 presents main conclusions of this thesis and recommendations for future work. Each chapter in this thesis is written in the format of articles in order to submit them to publication. As a result, some parts of this thesis may be present in more than one chapter.

References

[1]   C. Poelma, J. Westerweel and G. Ooms: "Turbulence statistics from optical whole-field measurements in particle-laden turbulence". Experiments in Fluids 40(3): p/347-363, (2006).

[2]   N. Mordant, P. Metz, J.-F. Pinton, and O. Michel: "Acoustic technique for Lagrangian velocity measurement". Review of Scientific Instruments, 76, 025105, 2005.

[3]   A.M. Crawford, N. Mordant and E. Bodenschatz: "Joint statistics of the Lagrangian acceleration and velocity in fully developed turbulence". Physical review letters 94, 024501, 2005.

[4]   Y. Suzuki and N. Kasagi: "Turbulent air-flow measurement with the aid of 3-D particle tracking velocimetry in a curved square bend". Flow, turbulence and combustion 63, 415-442, 2000.

[5]   R. J. E. Walpot, J. G. M. Kuerten, and C. W. M. van der Geld, "Experimental determination of Lagrangian velocity statistics in turbulent pipe flow". Flow, Turbulence and Combustion 76(2), 163-175, 2006.

[6]   M. P. B. Veenman, "Statistical analysis of turbulent pipe flow: A numerical approach" Ph.D. thesis, Technische Universiteit Eindhoven (2004).

2

Lagrangian and Eulerian statistics of pipe flows measured with 3D-PTV at moderate and high Reynolds numbers

Three-dimensional particle tracking velocimetry (3D-PTV) measurements have provided accurate Eulerian and Lagrangian high-order statistics of velocity fluctuations and correlations at Reynolds number 10300, based on the bulk velocity and the pipe diameter. Spatial resolution required in the analysis method and number of correlation samples required for Lagrangian and Eulerian statistics have been quantified. Flaws in a previously published analyzing method have been overcome. Furthermore, new experimental solutions are presented to facilitate similar measurements at Reynolds numbers of 15000 and beyond.

6

2.1   Introduction

To experimentally determine statistical properties of a turbulent velocity field in a Lagrangian particle frame of reference is difficult. This determination is nevertheless essential for the development of stochastic models of turbulent transport in applications such as combustion, pollutant dispersion and industrial mixing; see Pope[1] and Yeung.[2] The difficulty is primarily caused by the presence of a wide range of dynamical time scales, a property inherent in turbulence. For a complete description of particle statistics it is necessary to follow particle paths with very fine spatial and temporal resolution, of the order of the Kolmogorov length and time scales, l_k and τ_k respectively. To capture the large scale behavior trajectories should be tracked for long times, *i.e.* multitudes of τ_k. This obviously necessitates access to an experimental measurement volume with a typical length scale of the order of the bulk velocity times a typical Lagrangian correlation time, as will be defined in section 2.2; see Biferale *et al.*[3]

As a means to testing experimental results, comparison with Direct Numerical Simulation (DNS) of the Navier-Stokes equations can be made in the range of low to moderate Reynolds numbers. The DNS enables computation of complete turbulent flow fields without the need of any modeling assumptions. This method is well known to be limited by the requirement of quite some computational power, even at moderate Reynolds numbers. Extension to higher Reynolds number is possible with the aid of Lagrangian stochastic models, see Brouwers[4] for example, but then experiments are required to furnish essential correlation parameters and validation data. Lagrangian statistics of turbulent flows play an essential role in Lagrangian stochastic models. In homogeneous turbulent shear flow, Pope[5] found good agreement between autocorrelation functions determined by DNS and the ones calculated by a linear Lagrangian stochastic model. In realistic inhomogeneous turbulent flows, much less information is available.

Lagrangian experimental techniques such as three-dimensional particle tracking velocimetry, 3D-PTV, are for the above reasons a necessity in turbulence research. Despite the higher practicality of inhomogeneous turbulence, experimental Lagrangian results in the literature are mostly restricted to homogeneous turbulence. Lagrangian measurements in flow geometries with non-zero mean velocity component are scarce. The work of Suzuki and Kasagi[6] represents one of the few exceptions. For the practical pipe flow, only the 3D-PTV results of Walpot *et al.*[7] are available to our knowledge. Veenman[8] provided

Eulerian and Lagrangian computations of pipe flow, with DNS, at Re_b = 5300 and 10300. Walpot et al.[7] presented description at Re_b = 5300 and some preliminary results at Re_b = 10300 and compared with the data of Veenman[8]. The present study is an extension of the work of Walpot et al.[7] using essential ingredients of their experimental set-up and utilizing the Veenman[8] code for comparison as well.

As compared to the work of Walpot et al.[7], the following changes and extensions are made in their measurement and analysis set-up:

• The test rig is equipped with 3 new cameras, each of the type Photron "HighSpeedStar" with 12-bit grayscale CMOS sensor and a resolution of 1024 x 1024 pixels. With the new cameras, the recording frequency of the experiments has been enhanced from 30 to 50 Hz. In addition, the higher sensitivity of the new cameras has shortened the exposure time from 40 to 20 µs; what allowed sharper measurement images;

• The homemade analyzing software used by Walpot et al.[7] has been replaced by a commercially available PTV code from La Vision GmbH, named Davis. In contrast to the new code, the old homemade software did not provide documentation nor a user-friendly interface. Moreover, it did not allow massive parallel imaging processing and the possibility of enhancing the image contrast between particles and background by the use of built-in image filters;

• The two analyzing methods of Lagrangian trajectory statistics are revisited. They were only tested by Walpot et al.[21] at Re_b = 5300 and compared with DNS data of Veenman[8] at this Reynolds number. In the present study, the methods are compared at Re_b = 10300 with the aid of new experimental data;

• The smoothening applied to particle trajectories by Walpot et al.[7] is also revisited. The cut-off frequency of the smoothing filter was determined by these authors with DNS computations which is an undesirable feature. An experimental method should function fully independent of numerical results. It will be proven that no smoothening is required if a suitable localization accuracy is attained. To be specific, a maximum triangulation error of the order of 40 µm will be required in the particle detection algorithm at Re_b = 10300.

The following experimental results will be reported:

• High-order Eulerian statistics of the velocity distribution, such as skewness and flatness, for Re_b = 10300. Skewness and flatness were measured by Walpot et al.[7] only for Re_b = 5300;

• A measure will be given for the number of correlation samples required to determine Lagrangian velocity statistics in the form of autocorrelations or cross-correlations at $Re_b = 10300$ with higher accuracy than 2 %;

• Lagrangian velocity autocorrelations and cross-correlations with time separations up to values of $\tau u_\tau R^{-1}$ of about 0.08; here, u_τ is the wall shear velocity and R the pipe radius. Similar Lagrangian statistics were obtained by Walpot et al.[7], but only for time separations up to $\tau u_\tau R^{-1}$=0.06.

In addition, new experimental methods will be explored and presented which pave the way for measurement of Lagrangian particle statistics, be it tracers or be it inertial particles, at tube Reynolds numbers 20,000 and higher.

The structure of the paper is as follows. In Section 2.2, the experimental setup is presented, including specifications of flow tracers, calibration unit, cameras support and illumination systems. Optical requirements for 3D-PTV are also explained. Sections 2.3 and 2.4 provide the 3D-PTV procedure for identification of individual particle trajectories and the analysis method, respectively. Section 2.5 presents Eulerian and Lagrangian results at $Re_b = 10300$. Although higher Reynolds numbers have not actually been measured, Section 2.6 presents a systematic discussion for overcoming typical 3D-PTV challenges at higher Re_b. Finally, conclusions are presented in Sections 2.7.

2.2   Experimental setup

The requisites for 3D-PTV in pipe flows are: an experimental setup capable of generating and reproducing particular process conditions; a mechanical construction to avoid relative motion between cameras and the measurement volume even if calibration plates are inserted; illumination equipment; image processing to identify the geometrical center of particles; an analysis method of particle trajectories. These are discussed below.

2.2.1   Test rig

Turbulent pipe flow has been created in a water loop driven by a centrifugal pump. The in-line 3 kW centrifugal pump of type DPV18-30, manufactured by "Duijvelaar pompen", allows Reynolds numbers, based on the bulk velocity, U_b, and pipe diameter, D, in the range 10^3 to 10^5. A frequency controller permits fine-tuning of the Reynolds number by

adjusting the mass flow rate of the upward vertical flow in the measurement section; see Fig. 2.1.
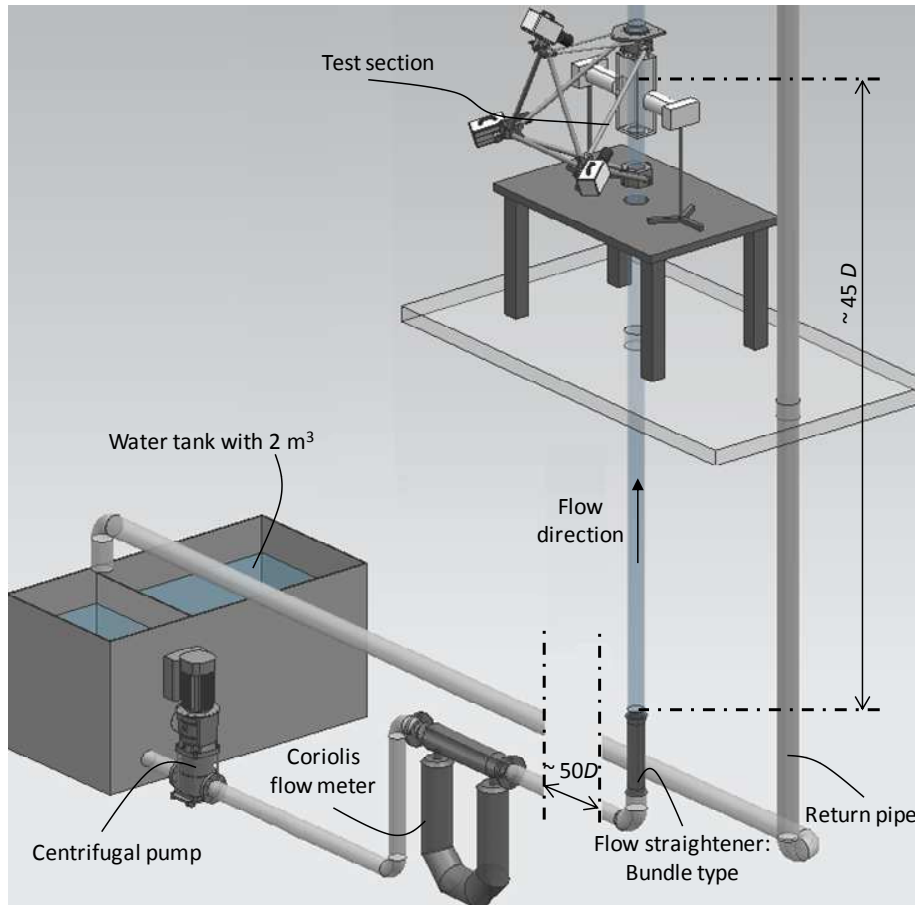
Figure 2.1 Schematic of the 3D-PTV experimental setup for pipe flow.

The mass flow rate is measured by means of a Micro Motion Elite CMF300 mass flow and mass density meter, whose inaccuracy is less than 0.5% of the registered flow rate. There is no requirement of fully developed flow measurements in Coriolis meters. A water reservoir, located at the bottom of the setup, contains about 2 m^3 of water. This value facilitates water temperature stabilization and Reynolds number control. Temperature during a test-run was essentially constant, varying typically 0.1°C only. A submerged pump has been placed inside the water reservoir in order to promote homogeneous dispersion of the flow tracers.

A flow straightener, tube bundle conditioner of ISO 5167-1:1991, see Miller[9], has been placed downstream of the 90º bend, see Fig. 2.1. The flow straightener removes secondary flows and shortens the required length to obtain a fully developed flow. At 45D further downstream, this flow condition has been achieved in the test section. At 25D downstream of the test section, the water enters a container which is connected to the main tank via a return pipe.

The measurement section consists of a glass pipe to ensure optical accessibility. A water-filled rectangular glass box around the pipe minimizes optical distortions. The pipe diameter is chosen relatively large, 100 mm inner diameter, because measurements at high Reynolds numbers are required. For a certain Reynolds number, bulk velocities are lower for higher tube diameters, which is advantageous for the acquisition of Lagrangian statistics.

2.2.2 Flow tracers

Polystyrene seeding particles with a diameter of 0.2 mm and a density of 1.05 g/cm^3 have been added to the water as flow tracers. In order to assure that these particles follow the flow, time and length scales of particles, τ_p and l_p, respectively, should be less than the fluid scales, τ_f and l_f. The subscripts p and f denote particle and fluid. The relaxation time for particles in stationary flow is shown by Albrecht et al.[10] to be:

$$\tau_p = (d^2\rho_p/18\mu)(1 + 0.5\rho_f/\rho_p) \tag{2.1}$$

where d is the particle diameter, ρ the mass density and μ the dynamic viscosity. A relaxation time of $\tau_p \approx 4$ ms is obtained for the tracers.

The fluid timescale τ_f is taken to be the Kolmogorov one, τ_k, for turbulent pipe flow at $Re_b = 10300$. In the inhomogeneous pipe flow at hand, assessment of a mean Kolmogorov timescale can be done with $\tau_k = (v/\varepsilon)^{1/2}$, where v is the kinematic viscosity and ε, the kinetic energy dissipation per unit mass. In approximation, $\varepsilon = 4u_\tau^2 U_b/D$, where u_τ is the wall shear velocity and D the pipe diameter; see Bakewell et al.[11] For $Re_b < 105$, the wall shear velocity can be estimated as $u_\tau = (U_b^2 f /8)^{1/2}$ with $f = aRe_b^{-m}$, $m = 0.25$ and $a = 0.316$; see Hinze.[12] For water flows at atmospheric conditions, $v \approx 10^{-6}$ m^{2}s^{-1}, and an 83 ms estimation of τ_k is obtained. The presented mean estimation of τ_k is inside the range of Kolmogorov timescales as computed by DNS at $Re_b = 10300$: 40 to 315 ms.

The Kolmogorov length is now compared to the diameter of the seeding particles in order to confirm that the tracers follow fluid fluctuations. Based on acceleration measurements, Volk *et al.*[13] observed that neutrally buoyant particles behaves as fluid ones if $d/l_k < 2$. Here $l_k = (v^3/\varepsilon)^{1/4}$ is the Kolmogorov length. In the DNS code of Veenman[8] for turbulent pipe flow at $Re_b = 10300$, the Kolmogorov length was about 0.6 mm in the pipe core and 0.2 mm at the wall region. As already mentioned, the diameter of the tracers is 0.2 mm.

Lastly, the terminal velocity of tracers, U_{TV}, is here evaluated in order to show that gravitational effects can be neglected. This term is often used to characterize suspensions and is a measure of the settling velocity a particle can achieve in a stationary fluid when gravitational and drag forcers are in equilibrium. The terminal velocity is represented by Eq. (2.2):

$$U_{TV} = \{(4\,(\rho_p - \rho_f)\,d_p\,g) / (3C_D\,\rho_f)\}^{1/2} \qquad (2.2)$$

where g is the gravity acceleration and C_D the drag coefficient. The latter is a function of the particle Reynolds number, $Re_p = d_p|(U_{rel}|/v$, which is based on the particle diameter and the terminal velocity. For $0.01 < Re_p < 20$, Clift *et al.*[14] defined a correlation for C_D as given by Eq. (2.3):

$$C_D = (24 / Re_p)\,(1 + 0.1315Re_p^{0.82-0.05\log Re_p}) \qquad (2.3)$$

A numerical value for U_{TV} can be obtained by an iterative computation concerning Eq. (2.2), Eq. (2.3) and Re_p. An estimation of 1 mm/s was obtained for U_{TV}, while the bulk flow velocity, U_b, is approximated 100 mm/s for the present case. Since $U_b \gg U_{TV}$, $\tau_p < \tau_k$ and $l_p < l_k$, the employed particles can work as flow tracers.

2.2.3 Mechanical construction for camera support and reproducible calibration

Descriptions of the camera support and calibration unit are now presented. The optical requirements for achieving high accuracy measurements are first provided. Lastly, requirements of the illumination apparatus are specified.

A. Optical requirements for 3D-PTV

To determine without ambiguities the center of a particle in the measurement space, a minimum of three cameras is required. When the center of a particle is determined for one

camera (2D), there is a line of possible crossing points for a second camera recording. The use of a third camera restricts the particle projection to a unique point. Therefore, three "HighSpeedStar" cameras with 12-bit grayscale CMOS sensor and a resolution of 1024 x 1024 pixels have been utilized to capture almost instantaneous 3D particle positions in an approximate measurement volume of 1x1x1 dm^3. The cameras can record at 1000 Hz at full resolution, but were operated at 50 Hz to maximize the flow measurement time. Recordings are performed until the internal memory of the cameras becomes full during approximately 2 minutes. The above estimate of τ_k shows that maximum physically relevant frequencies are about 12 Hz for Re_b = 10300, making a 50 Hz sampling rate sufficient according to the Nyquist Theorem.

Settings of cameras and lens arrangement must be properly chosen in order to obtain sharp images of moving particles. While a minimum depth of field must be guaranteed to obtain sharp recordings in the whole volume of the measurement section, a minimum field of view is needed to obtain trajectories long enough to measure all relevant flow scales. For the present experiment, the settings can be summarized as:

- Sensor resolution 1 pixel = 17 µm^2;
- Focal length of 105 mm;
- Exposure time of 20 µs;
- Distance from the lens to the object of roughly 800 mm.

The magnification (*M*) of the particle image by a single lens is given by Eq. (2.4):

$$M = f / (f - d_o) \qquad\qquad (2.4)$$

where f and d_o denote focal length and the distance from the lens to the object, respectively. Given the resolution of the cameras and the size of the tracers, f and d_o have been selected such that tracers occupy an area of 2 x 2 pixels of the camera sensor.

B.   *Cameras support system and calibration unit*

A statically determined approach has been applied to a mechanical design, where no relative movement between the cameras and measurement volume is allowed throughout the calibration and 3D-PTV measurements. Following Walpot *et al.*[16], three cameras are attached to the flow tube by a stiff and lightweight equilateral triangular frame constructed between them, see Fig. 2.2. A total of 24 degrees of freedom, which includes three translations and three rotations for the three cameras and the measurement section, have

been prescribed once, either as positions to be held or desired motions to be set by manipulation. Due to the statically determined design, there is no incorporation of unknown thermal stresses in the frame or flow tube.

To satisfy the optical requests previously described, the frame holds the cameras at an approximate distance of 800 mm to the measurement volume, assuring appropriate depth of field, magnification and field of view. The angles between their optical axes have been set over a reference value of 40° to minimize the error in 3D localization of a particle, see Kieft *et al.*[15] Appropriate positioning of the cameras can be achieved by inclined holders with incorporated elastic hinges.
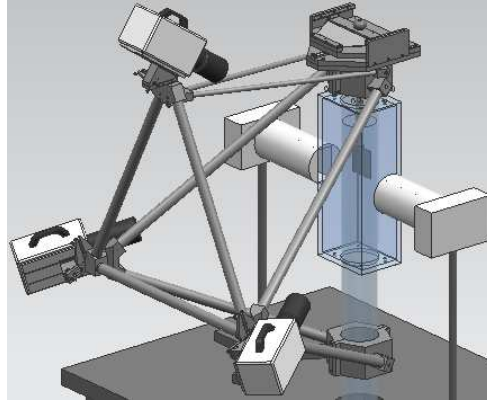
Figure 2.2 Schematic of the camera support system, stroboscopic light sources and the calibration unit inserted in the test section.

An in-situ calibration method has been utilized to transform the two-dimensional pixel information of each camera to world coordinates. A calibration unit precisely moves a grid with regular inter-spaced points throughout the measurement volume to certain positions, with high reproducibility. The bigger and well resolved the volume covered by the calibration plate, the smaller interpolation and extrapolation errors of the calibration functions are.

The grid points are essentially holes with a diameter of 0.3 mm, so that the projections of the dots on the camera sensor are at least several pixels in diameter. The grid is manufactured out of a 2.5 mm thick glass plate which is single-sidedly coated with a chromium coating of 150 nm thickness. The grid points are made up out of circular voids in the coating. The grid diameters are accurate within 0.5 µm. The relative position of two neighboring grid points is accurate within 0.1 µm.

Downstream of the measurement section, a pipe segment can be removed for calibration purposes. The centrifugal pump allows a stationary water-level just above the measurement volume, given that the energy provided by the centrifugal pump is in equilibrium with the potential energy of the static head. Once the water level is static, the calibration unit is inserted, making possible a reproducible positioning of the calibration grid throughout the measurement volume; see Fig. 2.2.

C. Lighting systems

During the calibration procedure, the calibration grid is homogeneously illuminated from behind by means of four floodlight halogen lamps. A semi-transparent plastic sheet is placed between the optical correction box and the floodlight sets to ensure uniform lighting of the measuring volume in order to improve the contrast between the circular void grid points and the continuous surface of the calibration plate. Examples will be given later.

For lighting the measurement volume during the 3D-PTV measurements, powerful light sources are necessary for recordings with short exposure times. While the use of a continuous light source would result in serious heat generation and the efficiency of an expensive laser would decrease as a result of illuminating a big volume of approximate 0.1 x 0.1 x 0.1 m^3, two strong stroboscopic light sources with an output of about 5 J per pulse each have successfully been applied. They are positioned at the sides of the optical correction box; see Fig. 2.2.

The strobes were custom-built in our laboratory to maximize the light output at a maximum of 60 Hz with light pulse duration of approximately 40 µs. A better image contrast was achieved by setting the exposure time of the cameras to 20 µs. In 20 µs, particles displace no more than 3 µm and, therefore, this time window was applied. Forced convection of air was necessary to cool down the electronic board that controls the stroboscope system.

The digital delay/pulse generator DG535 assured a perfect synchronization between the recordings of the three cameras and the lighting pulse generated by the stroboscope equipment.

2.3   Particle tracking algorithm

A commercial 3D-PVT imaging code from La Vision GmbH, named Davis, has been used to obtain tracers' trajectories. Algorithm details of the Davis PTV tracking code can be found in Maas[17] and Dracos.[18]

In Fig. 2.3, a flowchart describes the 3D-PTV procedure for identification of individual particle trajectories. Calibration and flow measurement images are processed in order to output files which contain time reference and spatial positions of individual particle trajectories to the analysis method.
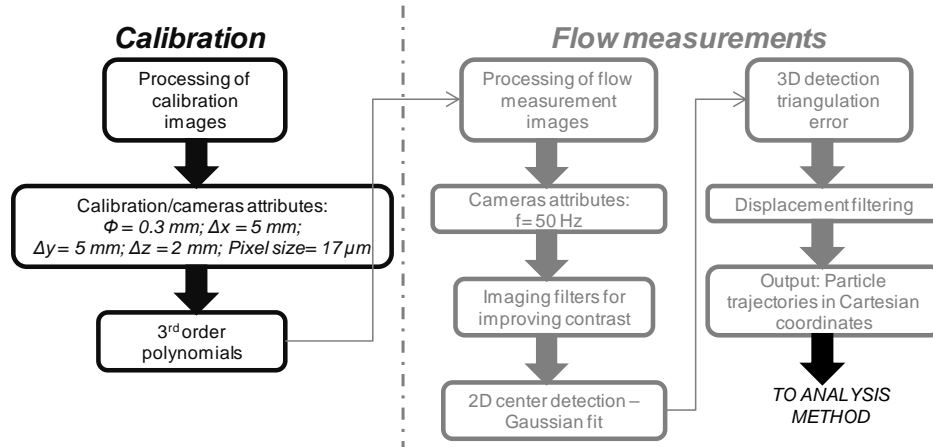
Figure 2.3 Flowchart for 3D-PTV procedure. Calibration and flow measurement images are processed until files with time reference and Cartesian positions of particle trajectories are exported to the analysis method.

To create the calibration functions which correlate the pixel information of each camera to the world coordinates, recordings of the calibration unit have been carried out with the same orientation: calibration plate plane is parallel to the pipe axis. No rotations are allowed, just translations in the coordinate direction perpendicular to the calibration plate plane. The recordings of the calibration plate are registered in 26 different positions, moved with constant increments, $\Delta z = 2$ mm, with an error of less than 1 µm.

The centers of the circular voids in the plate are equidistant in horizontal and vertical direction: Δx, Δy = 5 mm; see Fig.'s 2.4a, 2.4b, 2.4c, which provide the view of the calibration plate by each camera. With the information of the pixel size of the cameras, 17 µm^2, and the diameter of the circular voids, $\Phi = 0.3$ mm, 3rd order polynomials relate the pixel information to the physical dimensions of the calibration plate. As explained in section 2.2, linear interpolations and extrapolations of the generated polynomials are

16

extended to the whole volume of measurement. Root-mean-square (RMS) fit error of generated functions are smaller than 0.05 pixel; approximately 5 µm.

Once the calibration procedure is completed, the tube section is placed and flow measurements are recorded; see Fig.'s 2.4d, 2.4e, 2.4f. Built-in imaging filters improve the unsatisfactory contrast between particles and background caused by light reflections at the wall; see Fig.'s 2.3, 2.4g, 2.4h, 2.4i. The 2D determination of the center of a tracer in the cameras plane is done by a Gaussian fit and cataloged only if its intensity threshold is larger than a default value.

The 3D particle detection is then initiated, see Fig. 2.3. Since each detected particle on a camera plane is situated somewhere along a perspective line for each of the three cameras, the 3D position of a particle can be reconstructed at the position where the three perspective lines cross. The polynomials created during the calibration stage are used to determine the spatial Cartesian coordinates.

However, due to bias and random errors generated by undesired relative motion of cameras and setup, finite spatial and time resolution of cameras, blur effect from shutter speed etc., the projections of the perspective lines don't match perfectly. To find out the corresponding match of the perspective lines, a tolerance is necessary. The triangulation error is a 1D measure (e.g. in pixels) which allows such tolerance. Thus, it represents a direct measure of uncertainty on the 3D particle position determination for the whole 3D-PTV procedure.

At the present measurements, a maximum triangulation error equal to 0.2 pixel, roughly 20 µm, is enough to identify the 3D position of particles in the measurement space. However, a maximum triangulation error of 0.4 pixel is set to capture longer particle trajectories which are extended to regions in the space where the experimental uncertainties are higher. This was applied to achieve longer time spans in Lagrangian correlations. A further increase of the maximum triangulation error is risky, since higher levels of measurement noise and spurious vectors can lower the quality of Lagrangian trajectories.

Subsequent to the 3D particle position determination, the algorithm checks which particle in frame i+1 is most likely to match to a particle in frame i, see Fig. 2.3. During this last step, information of previous matches of the current particle and neighboring particles, up to frame i, is used to extrapolate the particle track to the most likely position in frame i+1. A range of allowed particle displacements, which are input at the imaging code, facilitates a proper matching.

17
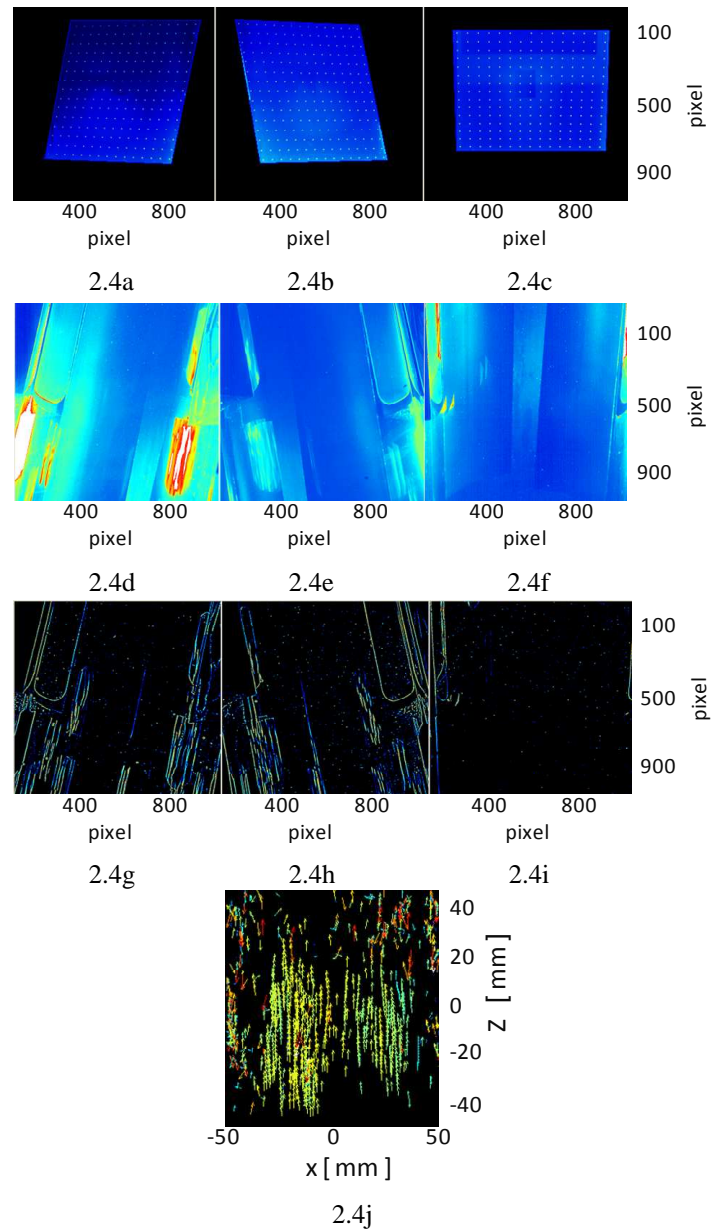
Figure 2.4. Photos of the 3D-PTV procedure for determining the center of tracers along each individual particle trajectory. Figures 2.4a, 2.4b, 2.4c show photos of the calibration unit; Fig.'s 2.4d, 2.4e, 2.4f illustrate raw images of pipe flow measurements; Fig.'s 2.4g, 2.4h, 2.4i present the action of imaging filters to improve contrast between tracers and background; and Fig. 2.4j shows the merging of individual tracer trajectories in a finite time window.

Finally, matrices with the spatial coordinates and the time reference of each particle trajectory successfully identified are exported to the analysis method, see Fig. 2.3. In Fig.'s 2.4a – 2.4i, photos of each camera show different stages of the 3D-PTV procedure. Figure 2.4j presents the merging of individual tracers' trajectories in a finite time window. The colorful vectors represent the orientation and magnitude of particle velocities. Most of the generated spurious vectors are located at the wall region and removed in a way to be described in the next section, 2.4.

2.4   Trajectory analysis

The particle tracking algorithm yields matrices which contain time reference and spatial positions of particle trajectories from the flow measurement images. Before the Lagrangian and Eulerian statistical analysis of turbulent pipe flow, the spatial positions are converted from Cartesian to cylindrical coordinates. Of course, the spurious trajectories generated during the 3D-PTV procedure are discarded. The flowchart of Fig. 2.5 summarizes the necessary steps in order to plot Lagrangian and Eulerian results.
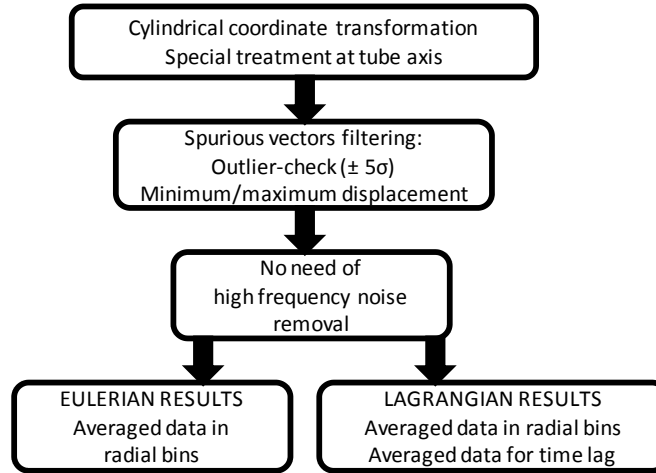
Figure 2.5 Flowchart for analysis method. Eulerian and Lagrangian results are the outputs.

Let σ represent the standard deviation for velocity components at a specific radial position. The subscripts r, θ and z denote radial, tangential and axial cylindrical coordinates, respectively. Since statistics in fully developed pipe flow are inhomogeneous in the radial direction, the transformation from Cartesian to cylindrical coordinates is made.

The removal of unrealistic trajectories has been accomplished by two filters: a length filter and a displacement outlier-check ($\pm 5\sigma_{r,\theta,z}$). The length filter consists of eliminating all trajectories of tracers outside a range of minimum and maximum positions of a particle track. Particle trajectories with just a few number of positions have higher probability of being false than trajectories with a large number of positions. A minimum number of positions is therefore required in order to account a particle trajectory. This procedure has proven to remove unrealistic particle trajectories. For example, elimination of particle trajectories comprising less than 10 spatial positions has been found to be efficient. On the other hand, a particle trajectory cannot exceed a maximum number of positions along the finite test section. No difference at final results was observed if the maximum limit varied from 80 to 300 positions per particle track.

The standard deviation applied in the outlier-check filter is derived from the present experiments. As an alternative, velocity standard deviations obtained from literature could be used as well. For example, standard deviations exceeding $Re_b = 10300$ can be found in Kunkel *et al.*[20]

At the proximity of the pipe centerline, $r/R = 0$, discontinuity in radial and tangential velocities for cylindrical coordinates can cause wrong differentiation of displacements in time. If a particle crosses $r = 0$, the radial velocity, u_r, may appear to be zero, and the tangential velocity, $u_\theta \approx \pi r/dt$; see Equations (2.5) and (2.6). The problem can be avoided by selecting a Cartesian frame of reference before a cylindrical one, and later converted.

$$u_r(t_j) = [\ r(t_{j+1}) - r(t_j)\ ]/dt \qquad\qquad (2.5)$$

$$u_\theta(t_j) = [\ \theta(t_{j+1}) - \theta(t_j)\ ]r(t_j)\ /dt \qquad\qquad (2.6)$$

Walpot *et al.*[7] identified high-frequency noise in their 3D-PTV experiments. The authors filtered their experimental data by applying the low-pass smoothing filter introduced by Savitzky and Golay[19] to the measured particle tracks. They repeated the filter 10 times using a 3rd order polynomial with right and left span of 8 points.

In the present 3D-PTV experiments, no need of filtering high frequency measurement noise has been observed. The results remain unchanged if the procedure as used by Walpot *et al.*[7] is adopted. Velocities derived by straightforward interpolations of consecutive 3D positions of a particle trajectory have been proved reliable to obtain pipe flow statistics. The application of Savitzy-Golay low-pass smoothing filter to correct the spatial position of

particles is unnecessary and also undesirable because of the necessity to know the cutoff frequency.

After the coordinate transformation and the removal of the spurious particle tracks, see Fig. 2.5, the differentiation in time of the validated trajectories generates the velocity vectors. For 3D-PTV Eulerian results, which are plotted at Section 2.5.1, the velocity vectors are gathered in discrete radial bins, the only inhomogeneous direction.

The velocity vectors are gathered in discrete radial positions in accordance to $r_i \pm \Delta r$, where the subscript i varies from 0 to 50; see Fig. 2.13. The length (L) of each discrete bin is 100 mm, while the radial band has a dimension of $2\Delta r$. Exceptions are the first and last grids which have a radial band dimension of Δr. At Re_b=10300, a radial discretization Δr equal to 0.5 mm has been proved reasonable to describe the Eulerian results. A small Δr is obviously required for a high resolution of velocity gradients such as $\partial U_z/\partial r$.

In the analysis of Lagrangian data, see Fig. 2.5, the same procedure as prescribed by Walpot et al.[21] will be applied. As these procedures are conveniently described with the aid of the present data, these explanations are given in Section 2.5.2.

2.5   Results

In this section, 3D-PTV results in fully developed pipe flow are compared to the Eulerian and Lagrangian outcomes at same Reynolds bulk number as provided by the validated direct numerical simulation (DNS) code developed by Veenman.[8] In this numerical method, simulations were executed in a finite part of a cylindrical pipe of length 5D by applying a Fourier-Galerkin spectral method in the streamwise and azimuthal periodic directions, and a Chebyshev-collocation method in the radial one. Eulerian and Lagrangian results are presented in subsections 2.5.1 and 2.52, respectively.

2.5.1   Eulerian results

3D-PTV particle trajectories have been registered in 21 individual measurement sets of 120 s each. The camera frame rate has been adjusted to 50 Hz for every experimental set. The differentiation of particle trajectories in time generates roughly 2.7 x 10^6 velocity vectors; see the square symbols in Fig. 2.6. The velocity vectors are ensemble-averaged in

distinct radial bands, which are delimited by a discrete width of $\pm\,\Delta r = 0.5$ mm around a chosen radius, see Fig. 2.13.

Velocity statistics are normalized by the centerline velocity, U_c, and plotted against the dimensionless distance to the pipe centerline, r/R, which represents the discrete radial bands. The centerline velocity is chosen as a normalization quantity instead of the wall shear velocity, u_τ, which is often used in the literature, because U_c can be determined more accurately in an experimental setup. Throughout this article, error bars, with size equal to $\pm 2\sigma_m$, indicate the magnitude of the error in the mean of a certain quantity, x, in Eq. (2.7), measured. Here, σ_m denotes:

$$\sigma_m = \{ \ [\Sigma x_i^2 - n^{-1}(\Sigma x_i)^2] \ / \ [n(n\text{-}1)] \ \}^{1/2} \tag{2.7}$$

with x_i the average value for a single measurement set and n the total number of measurement sets: 21.

In Fig. 2.6, the concentration, Φ_v, and the measured number of velocity vectors in the total period of 42 minutes are plotted. These quantities are represented by diamonds and squares, respectively. The registered number of velocity vectors rises from the pipe centerline to $r/R = 0.57$, where it is about 10^5 vectors, proportionally to the rise in volume of the experimental point. This is because the measured concentration of velocity vectors is homogeneous up to $r/R = 0.57$.
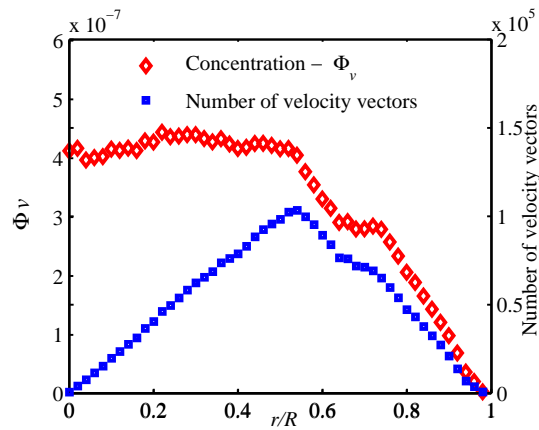
Figure 2.6 Concentration and total number of velocity vectors as function of the dimensionless radius, r/R. Square and diamond symbols denote the total number and concentration of velocity vectors, respectively.

There is a continuous drop in the number of measured particle trajectories from $r/R = 0.57$ to $r/R = 1$. The difficulties in measuring particle trajectories in this region are caused by light reflections, which stem from differences in the refractive indices of water, n ≈ 1.33, and glass, n ≈ 1.51, and the curvature of the glass pipe; see Fig.'s 2.4d, 2.4e and 2.4f. As a result, the contrast between tracers and background becomes poor. Difficulties in capturing tracer trajectories increase at the grid elements of the experimental mesh closer to the wall. From $r/R = 0.9$ to $r/R = 0.98$, there is an approximate reduction from 2×10^4 velocity vectors to 500.

A suitable description of pipe flow statistics has also been achieved in the wall region despite the fact that the uncertainties in the computation of averaged velocity statistics increase with the reduction in the number of velocity vectors there. This can be observed by the way that the 3D-PTV results match the DNS ones at the wall region in the Eulerian results to be presented along this section.

In Fig. 2.7, the mean axial velocity profiles as determined by the actual 3D-PTV experimental setup, denoted by diamonds, and DNS results of Veenman[8], denoted by a solid line, are shown. Mean streamwise velocity values are presented at the left axis of Fig. 2.7. Good agreement between experimental and DNS results has been obtained. Due to their negligible size, no error-bars can be discerned.
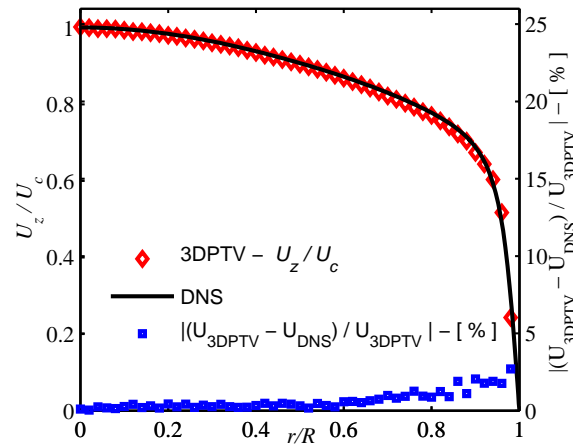
Figure 2.7 Mean streamwise velocity profiles for $Re_b = 10300$. The solid line represents DNS data of Veenman[8] and the diamonds, 3D-PTV results. Square symbols denote an assessment of the relative deviation between the presented results.

To quantify the degree of conformity between experimental and DNS results, Fig. 2.7 also provides the plot of the relative deviation between them, expressed here as a percentage value of $|(U_{3D\text{-}PTV} - U_{DNS})/U_{3D\text{-}PTV}|$ and represented by squares. The values of the relative deviation are shown at the right axis of Fig. 2.7.

The integration of the product of the mean axial velocity and the area of each point, $(U_z)_i \times (A_i)$, gives the mean volumetric flow rate, Q, which crosses the measurement volume. Temperature measurements are used to determine the water mass density, ρ. The product $\rho \times Q$ provides a measure of the mass flow rate for each measurement set. These values match the ones given by the Coriolis meter within statistical accuracy.

The relative deviation between DNS and 3D-PTV results is smaller than 1% until $r/R = 0.8$ and reaches 2.8% at $r/R = 0.98$. The rise in the relative deviation for $r/R > 0.8$ can be explained by a combination of three factors, as follows:

- The resolution of the discretization band at the wall. A smaller length of the radial band discretization, Δr, is required to reduce the deviation values in Fig. 2.7 due to the higher gradient of average axial velocity in the radial direction, $\partial U_z/\partial r$, there. While the mean axial velocity reduces 50% in the radial range from the pipe centerline to $r/R = 0.95$, it decreases to zero in the small region near the wall for the Reynolds number at hand;

- The reduced number of particle trajectories obtained there, see Fig. 2.6. The poor contrast between tracers and background due to the reflections at the wall just allowed a few particle trajectories to be acquired there, see Fig.'s 2.4d, 2.4e and 2.4f. Section 2.6 provides measures to overcome reflection problems at pipe walls;

- The relative error growth in the mean axial velocity calculation. The magnitude of the tracer displacement is smaller at the wall region. Therefore, the relative error in the computation of the mean axial velocity increases when velocity vectors are determined by differentiation of the particle trajectories in time.

The measurements of radial and tangential velocities are more challenging, since they present zero mean and standard deviations not bigger than 7 mm/s. With cameras frame rate at 50 Hz, displacements are smaller than 140 µm. However, the normalized probability density functions (PDFs) at $r/R=0.5$ demonstrate the capacities of the present 3D-PTV experimental measurements and analysis method, see Fig. 2.8.
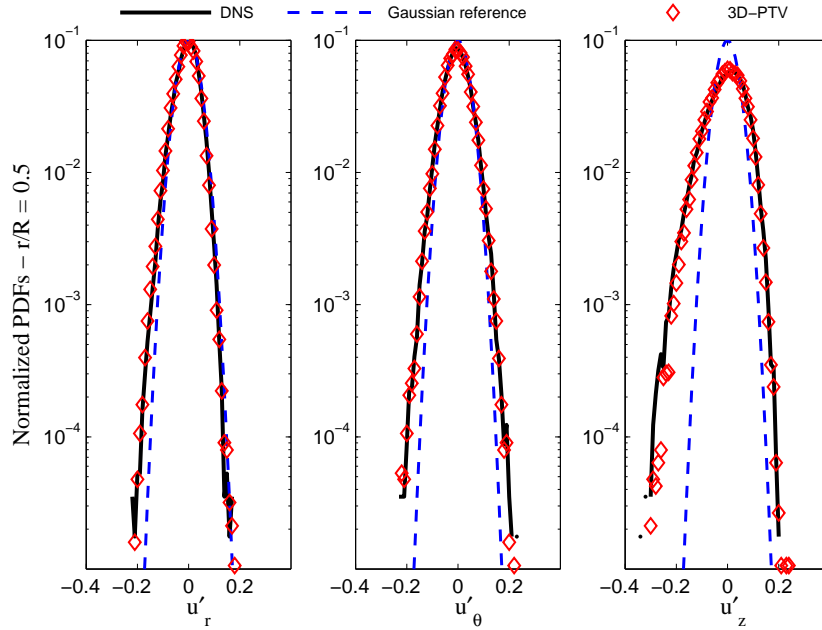
Figure 2.8 Normalized probability density functions for all cylindrical velocity components at *r/R*=0.5. The diamonds represent 3D-PTV results, while solid and dashed lines denote DNS data of Veenman[8] and a Gaussian reference, respectively.

In Fig. 2.8, 3D-PTV data closely match the ones obtained with DNS. The plot of the velocity fluctuation components in a logarithmic scale for y-axis shows also good agreement even at the tails far from the ensemble average. Similar results have been obtained at other radial positions. Gaussian reference distributions with the same mean and standard deviation, represented as dashed lines, are added as to show the well-known fact that, in inhomogeneous wall-bounded flows, the PDFs of the velocity components are bell-shaped but not Gaussian, see Moser *et al.*[22]

The main diagonal components of the Reynolds stress tensor $\sigma_{ij} = \langle u'_i u'_j \rangle$ are compared with DNS results of Veenman[8] in Fig. 2.9. For all mean-square-value (MSV) plots, the 3D-PTV data show good agreement with the DNS within measurement error, even close to the wall. Error-bars give an indication for the statistical error, $\pm 2\sigma_m$; see Eq. (2.7).
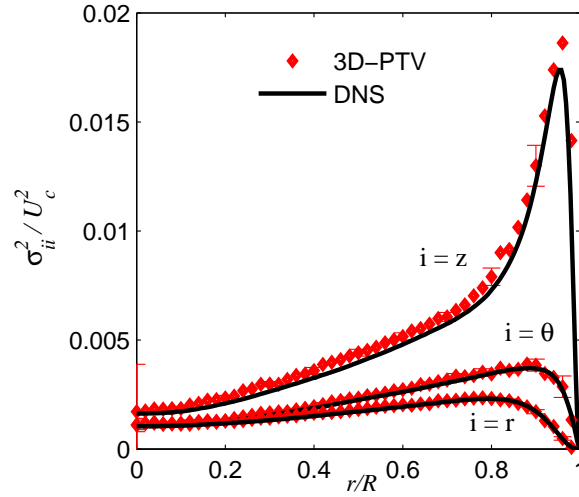
Figure 2.9 Velocity MSV profiles of turbulent pipe flow for all the cylindrical components at Re_b = 10300. The solid lines represent DNS data and the diamond symbols, 3D-PTV results.

MSV of the radial and tangential velocity components are smaller than the axial one. While at the center of the tube (r/R<0.2) turbulence is nearly homogeneous, an inhomogeneous behavior is seen closer to the wall area (0.8<r/R<1). The biggest standard deviation for tangential direction is around 6% of centerline velocity at $r/R \approx 0.9$, whereas, for the axial one, σ_z achieves $\approx$ 13% of U_c at $r/R \approx 0.95$.

For isotropic flows, the non-diagonal terms of σ_{ij} are zero. However, in the case of inhomogeneous turbulent pipe flow, the only decoupled direction is the tangential one, which means that correlations like, e.g., $u'_\theta u'_r$ and $u'_\theta u'_z$, are zero. The nonzero cross-component of σ_{ij} is $\langle u'_r u'_z \rangle$, which is presented in Fig. 2.10. Error-bars give an indication for the statistical error.
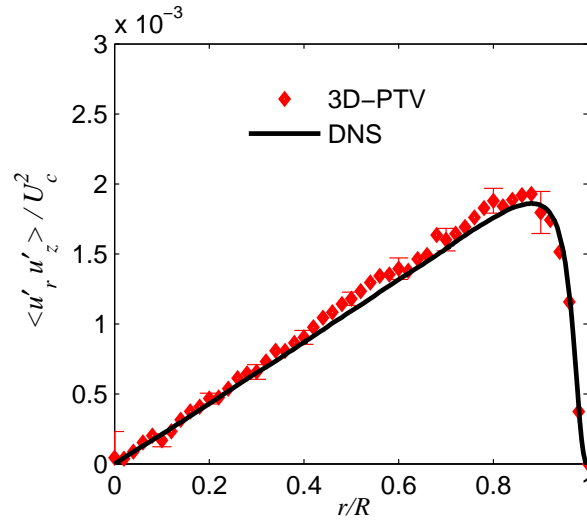
Figure 2.10 Reynolds stress component $\langle u'_r\, u'_z \rangle$ as function of the dimensionless radius at $Re_b = 10300$. The solid line represents DNS data and the diamonds, 3D-PTV results.

The mean equation of motion in the axial direction is represented in cylindrical coordinates by Eq. (2.8). Axial normal stress gradient is equal to the cross-stream shear-stress gradient:

$$\partial \langle p \rangle / \partial z = (1/r)\ \partial (r \langle T \rangle)/\partial r \tag{2.8}$$

where p is pressure and T is the total shear stress, which is a sum of the viscous stress, $\rho v\ d\langle U \rangle / dr$, and Reynolds stress, $\rho \langle u'_r u'_z \rangle$. Since at the wall, the Reynolds stress is zero, wall shear stress is due entirely to the viscous contribution. The viscous stress drops abruptly for a short distance; and, for $0 < r/R < 0.9$, the total shear stress is essentially due to the Reynolds stresses contribution. As the Reynolds number increases, the fraction of the pipe occupied by the viscous contribution decreases even more, see Pope[23], page 271.

The description of the skewness ($S = \langle u'^3 \rangle / \sigma^3$) and flatness ($F = \langle u'^4 \rangle / \sigma^4$) factors of the velocity components plotted along the radius for the fully developed turbulent pipe flow are shown in Fig. 2.11 and Fig. 2.12. As already mentioned, error-bars represent a 95% confidence interval of the mean of the calculated quantities.
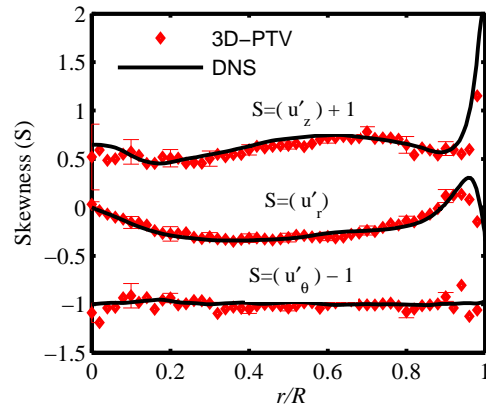
Figure 2.11 Velocity skewness of turbulent pipe flow for all cylindrical components at Re_b = 10300. The solid line represents DNS data and the diamonds, 3D-PTV results.
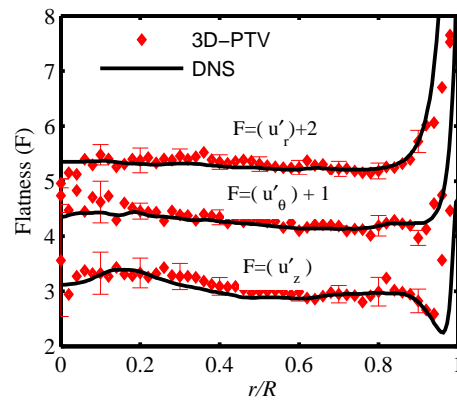
Figure 2.12 Velocity flatness of turbulent pipe flow for all cylindrical components at Re_b = 10300. The solid line represents DNS data and the diamonds, 3D-PTV results.

In inhomogeneous wall-bounded flows, the PDFs of the velocity components are bell-shaped but not exactly Gaussian; see Fig. 2.8. Gaussian distributions present skewness and flatness values equal to 0 and 3, respectively. The departure from Gaussian behavior increases as the wall is approached; see the skewness and flatness values for $r/R > 0.8$ in Fig. 2.11 and Fig. 2.12. In the near-wall region, the bursting processes of streaks that inject low-speed fluid into the core and sweep high-speed fluid towards the wall is responsible for increasing flatness values for all coordinate directions and skewness for the axial one.

In fully developed flow, rotational symmetry of the flow requires the tangential velocity PDF to be symmetric. As a consequence, tangential skewness should be zero $S(u'_\theta)$

= 0 and radial skewness should be zero at the centerline, $r = 0$; see Fig. 2.11. In addition, correlations involving u'_θ are zero as an outcome of the rotational symmetry.

The radial and streamwise fluctuations are interrelated. Particles moving towards the wall usually retain its original axial velocity for a while and will be most probably found in an external radius with a positive u'_z. The opposite conclusion holds for particles moving towards the core of the pipe. Skewness values of the radial and axial velocity components at the core pipe are negative until $r/R \approx 0.9$ for the present Reynolds number and become positive towards the wall. Only close to the wall, $r/R > 0.98$, radial skewness becomes negative again.

As a result, the transport in the radial direction of impulse in the axial direction, $\langle u'_r u'_z \rangle$, should be positive on average what shows a flux of energy of the mean flow towards the wall where deformation into turbulent kinetic energy, k, mainly occurs. The radial skewness is associated to the transport of k by velocity fluctuations. In the radial range where radial skewness is positive, turbulent kinetic energy, k, is removed and then transported to the wall where it is dissipated into heat and to the core pipe to feed the mean flow turbulence. More details can be found in Tennekes and Lumley[24].

2.5.2   Lagrangian results

In this section, Lagrangian results of pipe flow at $Re_b = 10300$ are presented. The analysis required for inhomogeneous turbulent pipe flow is not straightforward since particles move during the time of observation to areas with other statistical properties. Discretization in space and time is necessary in such a way that enough independent data are collected in each point. The analysis applied follows closely the one presented by Walpot et al.[21], but in the present study a minimum number of correlation samples required for the description of Lagrangian velocity statistics will be specified.

Walpot et al.[21] tested two analyzing methods for the assessment of Lagrangian statistics. These authors evaluated datasets provided by the DNS numerical code of Veenman[8] at $Re_b = 5300$. One of the methods (Method I in their numbering, also adopted here) checks whether particles cross a chosen radial position, r_i, satisfying Eq. (2.9):

$$(r(t_{j+1}) - r_i) (r(t_j) - r_i) < 0 \qquad\qquad (2.9)$$

When a particle fulfills this condition, meaning that a particle crosses r_i between two subsequent times, it starts to contribute to the Lagrangian correlations. For the situation

29

shown in Fig. 2.13, $t_{3/50}$ would be the starting time to give Lagrangian correlations at the radial position in the point labeled "i". It is obvious that within a finite time window it happens more often that a faster moving particle crosses the line at r_i than slowly moving particles. For this reason, Walpot et al.[21] applied weighing factors, inversely proportional to the magnitude of the initial velocity component. These weighing factors were introduced by McLaughlin and Tiederman[25] to correct velocity bias in LDA measurements.

Method II of Walpot et al.[21] gathers data in discrete radial bands: $r_i \pm \Delta r$, with Δr satisfying $2\Delta r > |u|\Delta t$. Here, u is a typical radial velocity value, f.e. the standard deviation of radial velocity fluctuations. In Method II, the particle trajectory sketched in Fig. 2.13 contributes to the Lagrangian correlations at grid "i" from $t_{1/50}$ to $t_{6/50}$. Each particle position from $t_{1/50}$ to $t_{6/50}$ serve as an initial position of a new trajectory. When such additional trajectories are taken into account, the number of data available for short time correlations is increased. For this reason, Walpot et al.[21] introduced these extra trajectories corresponding to what they named ghost particles.

The evaluation performed by Walpot et al.[21] with datasets based on the DNS of Veenman[8] at $Re_b = 5300$ pointed out that Method II yielded almost unbiased statistics, while Method I required the weighing factors to function properly. However, their comparison utilized DNS results and data for Reynolds number $Re_b = 5300$ only. Both methods have now been compared using data acquired by 3D-PTV at $Re_b = 10300$. Results are discussed below.

Lagrangian velocity autocorrelations and cross-correlations are defined by Eq. (2.10):

$$\rho_{ij}(\tau,r) \ = <u'_i(t_0)u'_j(t_0+\tau)> \tag{2.10}$$

where t_0 denotes an arbitrary initial time and τ the correlation time span. The calculation of the correlations $\rho_{ij}(\tau,r)$ is done by averaging all particles that are situated inside a discrete band centered at a radial position r in a certain time which is then marked t_0 for that particle. These correlation functions depend on the radial coordinate r but are independent of t_0. In addition, the correlations calculated by Methods I and II also need to meet the corresponding criteria above described.

Figure 2.13 Schematic of a particle trajectory which crosses the experimental grid "i". The circles represent particle positions tracked at a frequency of 50 Hz. With Method I, $t_{3/50}$ would be the starting time to give Lagrangian correlations at grid "i". With Method II, the particle trajectory contributes to Lagrangian correlations at each instant of time $t_{1/50}$ to $t_{6/50}$ in a way explained in the text.

Evaluation of velocity autocorrelations computed with the present experimental data at various radial positions showed deviations to DNS over 20% for Method I and up to 2% for Method II. In the evaluation of Method I, the same weighing factors were applied as in accordance to Walpot *et al.*[21] These authors tested only DNS data with Methods I and II, since experiments could introduce unknown side-effects. Later, Walpot *et al.*[7] successfully applied Method II to experimental data acquired by 3D-PTV.

Since Method II gives results one order of magnitude more accurate than Method I, Method II is applied in the remainder of this study. In addition, the use of a method that does not demand any type of biasing correction is desirable for the analysis of experimental data. A radial band width, Δr, of 0.5 mm and a camera frequency of 50 Hz sufficed to obtain negligible bias at $Re_b = 10300$.

With Method II, proper results have been achieved until time separations given by $\tau u_\tau R^{-1}$ about 0.08; where u_τ and R are the wall shear velocity and the pipe radius, respectively. To increase the band width Δr from 0.5 to 1.5 mm has not improved results

for longer time separations. It just increased the amount of data for correlation time spans in the range: $0 < \tau u_\tau R^{-1} < 0.06$, without significant changes in the results. A smaller band width resulted in the decrease of correlation samples for time separations shorter than 0.08. For sake of convenience the same Δr was applied in the analysis of Eulerian data.

The evaluation of Lagrangian velocity autocorrelations as obtained by Method II at different experimental grids with changeable Δr revealed that appropriate results were obtained if a number of correlation samples exceeding 2×10^4 were available for each discrete time lag; see Fig. 2.14b. Figure 2.14a shows the streamwise autocorrelation as a function of the time separation $\tau u_\tau R^{-1}$ at r/R=0.8.

14a   14b
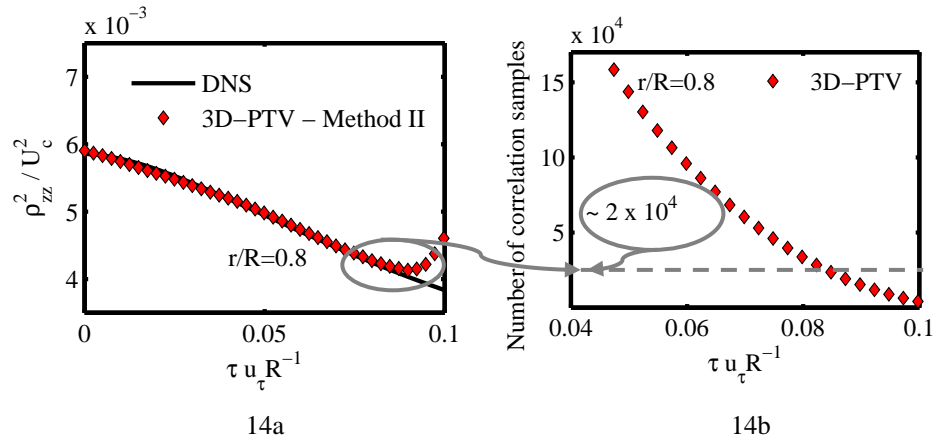
Figure 2.14 Evaluation of the analyzing Method II in the description of Lagrangian pipe flow statistics. Figure 2.14a shows the streamwise autocorrelation as a function of the time separation $\tau u_\tau R^{-1}$ at r/R=0.8. The solid line represents DNS data and the diamonds, 3D-PTV results. Figure 2.14b shows that a number of correlation samples exceeding 2×10^4 sufficed to obtain proper Lagrangian representation.

As already mentioned, additional trajectories corresponding to what was named ghost particles were taken into account on the computation of Lagrangian velocity autocorrelations and cross-correlations as defined by Eq. (2.10). This resulted in the increase of correlation samples for short time correlations as it is shown in Fig. 2.14b. For time correlations up to 0.08, the influence of ghost particles becomes reduced and the number of correlations samples decrease. Of course, this time separation corresponds to end positions of the longest trajectories obtained at the present measurements.

The computation of velocity autocorrelations and cross-correlations in a specific time separation provided good agreement to DNS if the number of correlation samples was over

an approximated value of 2×10^4. Deviations to DNS up to 2% were obtained with Method II if enough correlations samples were available.

When the amount of correlation samples is below 2×10^4, there is a sudden increase in the Lagrangian autocorrelation values. This is due to a lack of enough data in a discrete time separation to compute the proper mean of correlation samples; what increases the coherence of the velocity product in Eq. (2.10). Radial, tangential and streamwise Lagrangian autocorrelations at other radial positions showed similar results as in Fig. 2.14.

For the remaining of the Section, three dimensionless radial positions, *r/R*: 0.4, 0.6 and 0.8, are chosen to present results of Lagrangian velocity autocorrelations and cross-correlations, as defined by Eq. (2.10).

A. *Auto-correlations*

In Fig. 2.15, the number of correlation samples as a function of the time separation, $\tau u_\tau R^{-1}$, is plotted for *r/R* equal to 0.4, 0.6 and 0.8. Appropriate Lagrangian statistics have been achieved roughly for $0 < \tau u_\tau R^{-1} < 0.08$.
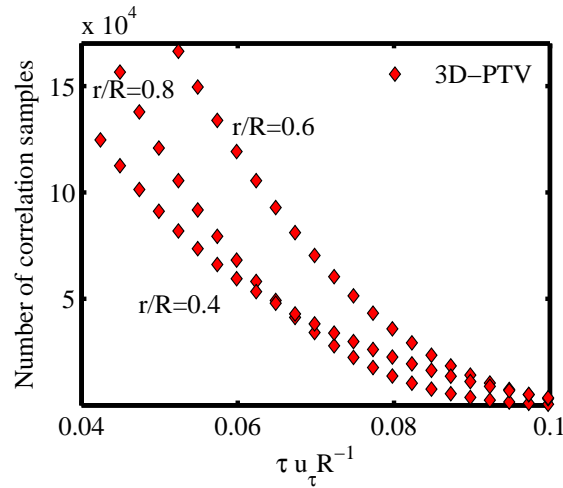
Figure 2.15 Number of correlation samples for Lagrangian statistics as a function of the time separation for the 3D-PTV results at *r/R*=0.4, *r/R*=0.6 and *r/R*=0.8.

Figures 2.16 – 2.18 show comparisons between 3D-PTV and DNS results for the Lagrangian radial, azimuthal and streamwise velocity autocorrelation functions, respectively. These outcomes are shown at three radial positions: *r/R*=0.4, *r/R*=0.6 and *r/R*=0.8.

33

Solid lines represent Lagrangian DNS data calculated by Eq. (2.10); diamonds denote 3D-PTV data. Error-bars, indicated by the dashed lines and with size equal to $\pm 2\sigma_m$, represent the statistical error in the 3D-PTV results. The error-bars are only plotted for r/R=0.4 and have similar magnitude for 3D-PTV data at r/R=0.6 and r/R=0.8. The starting point of the autocorrelation functions coincides with the MSV values presented in Fig. 2.9.
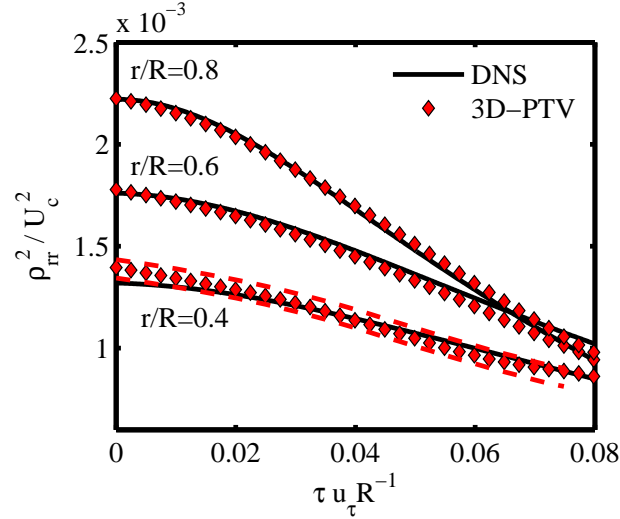
Figure 2.16 Lagrangian radial velocity autocorrelation functions at r/R=0.4, r/R=0.6 and r/R=0.8. Solid lines represent the DNS data and diamonds, 3D-PTV results. Dashed lines denote the error-bars at r/R=0.4.

Profiles of Lagrangian cylindrical autocorrelations for 3D-PTV and DNS agree within statistical accuracy until a separation time, $\tau u_\tau R^{-1}$, close to 0.08. When the autocorrelations exceed this time lag reference, the slope of the profiles changes; and the agreement between 3D-PTV and DNS Lagrangian results becomes poor.
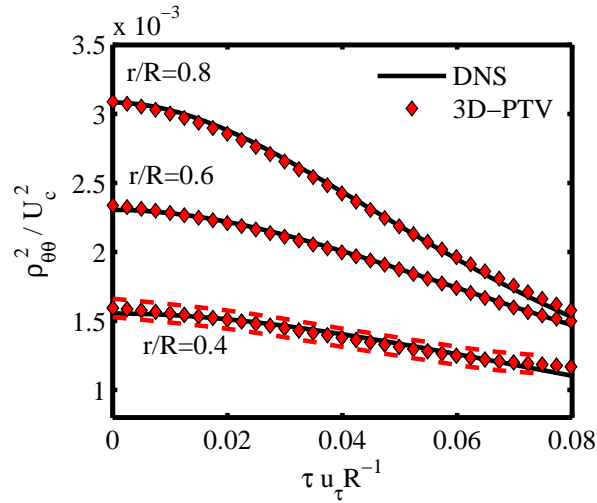
Figure 2.17 Lagrangian azimuthal velocity autocorrelation functions at *r/R*=0.4, *r/R*=0.6 and *r/R*=0.8. Solid lines represent the DNS data and diamonds, 3D-PTV results. Dashed lines denote the error-bars at *r/R*=0.4.
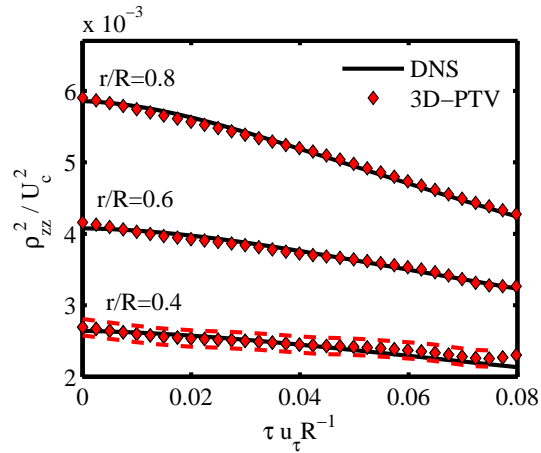
Figure 2.18 Lagrangian streamwise velocity autocorrelation functions at *r/R*=0.4, *r/R*=0.6 and *r/R*=0.8. Solid lines represent the DNS data and diamonds, 3D-PTV results. Dashed lines denote the error-bars at *r/R*=0.4.

In Fig.'s 2.16 – 2.18, it is possible to observe a slower decay of autocorrelation values at radial positions closer to the pipe center. The inhomogeneous behavior of the flow close to the wall causes the autocorrelations to decay faster nearby the wall than in the pipe core. This behavior is better illustrated in Fig. 2.19, which shows normalized tangential

35

autocorrelation functions for the same previous radial positions. The azimuthal functions have been normalized with the corresponding starting values to highlight the decay rate.
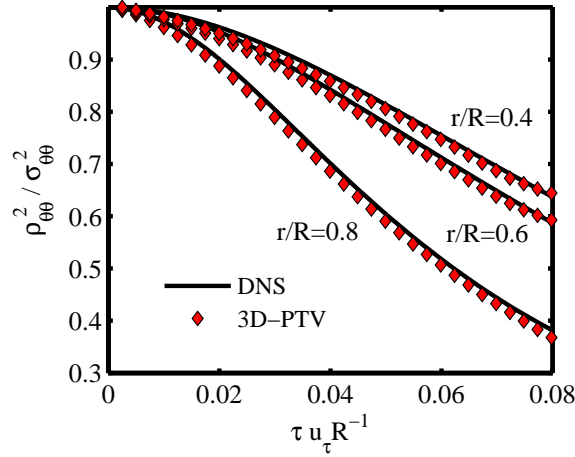
Figure 2.19 Normalized Lagrangian velocity autocorrelation functions for the tangential component at *r/R*=0.4, *r/R*=0.6 and *r/R*=0.8. The solid lines represent DNS data and the diamonds, 3D-PTV results.

B. Cross-correlations

3D-PTV and DNS results of the only non-zero cross-correlation functions, ρ_{rz} and ρ_{zr}, are shown at *r/R*=0.4, *r/R*=0.6 and *r/R*=0.8 in Fig. 2.20 and Fig. 2.21, respectively. The statistical error in the 3D-PTV results is indicated by the dashed lines with size equal to $\pm 2\sigma_m$; see Eq. (2.7). As already pointed out, cross-correlations involving the tangential component are equal to zero, since this component is uncoupled to the other two components. The starting point of the cross-correlations coincides with the Reynolds stress component $\langle u'_r u'_z \rangle$ values presented in Fig. 2.10.

A noteworthy difference between them is the considerably faster decay of ρ_{zr}. Particles which move towards the wall usually retain its original axial velocity for a while and will be most probably found in an external radius with a positive u'_z. The opposite conclusions can be driven to particles moving towards the core of the pipe where those particles with negative radial velocities most probably shall have a negative u'_z; and, as a consequence, the average product of u'_z and u'_r is positive. A particle moving in the radial direction tends to retain its original total axial velocity for a while, $u_z(t_0 +\tau) \approx u_z(t_0)$; resulting in an average increase of the absolute value of the velocity fluctuation; given that $\langle u_z \rangle$ varies along the

36

radius. Then, the average product $\langle u'_r(t_0)u'_z(t_0+\tau)\rangle$ is larger or as big as $\langle u'_r(t_0)u'_z(t_0)\rangle$. The same cannot be said about $\langle u'_z(t_0)u'_r(t_0+\tau)\rangle$, since $\langle u_r \rangle = 0$ everywhere.
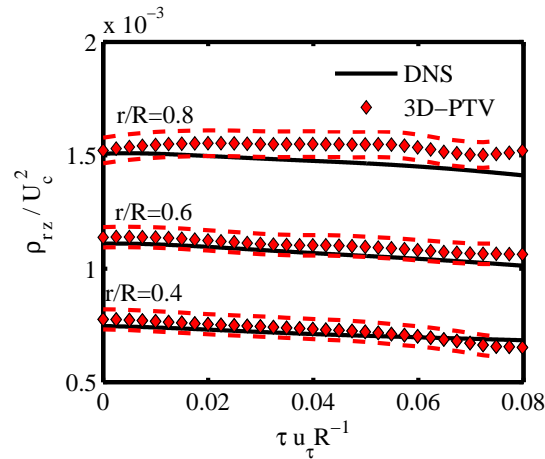
Figure 2.20 Lagrangian velocity cross-correlation functions, ρ_{rz}, at r/R=0.4, r/R=0.6 and r/R=0.8. The solid line represents DNS data and diamonds symbols, 3D-PTV results.
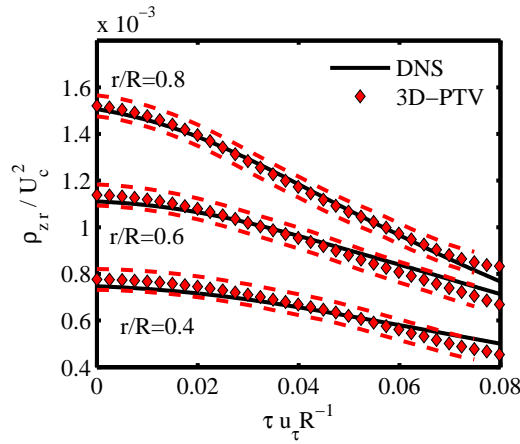
Figure 2.21 Lagrangian velocity cross-correlation functions, ρ_{zr}, at r/R=0.4, r/R=0.6 and r/R=0.8. The solid line represents DNS data and diamonds symbols, 3D-PTV results.

2.6   Measures to facilitate 3D-PTV at Reynolds numbers above 14000

The above determination of high-order Lagrangian and Eulerian statistics in turbulent pipe flow shows that high accuracy is attainable at $Re_b = 10300$. We explored measures to warrant high accuracy at higher Reynolds numbers and these are now discussed, along with an inventory of challenges to be met.

A discussion about precision of 3D-PTV measurements, resolution of the analysis method and pipe flow scales is addressed in subsection 2.6.1. The inventory of challenges in higher Reynolds numbers, e.g. over 20,000, include measurements in the near-wall zone, light reflection at pipe walls, acquisition of longer particle trajectories and illumination limitations. While subsection 2.6.2 presents measures in evaluation to overcome some of the mentioned problems, subsection 2.6.3 provides untested suggestions.

2.6.1 Discussion: 3D-PTV precision, analysis method resolution and pipe flow scales

Of primary importance is the necessary 3D-PTV precision, represented by the maximum triangulation error, $\Delta_{tri,}$ and the radial resolution of the analysis method, Δr. The discussion of the results in the previous section provides reference values. The mean streamwise velocity profiles for 3D-PTV of Fig. 2.7 in section 2.5, with width Δr equal to 0.5 mm, showed deviations to DNS less than 1% for 0< r/R< 0.8 and exceeding 2% for 0.95< r/R< 1. The rise in the relative deviation near the wall region makes clear that Δ_{tri} and Δr are critical in the region near the wall, *i.e.* for 0.95< r/R< 1. This is particularly important if higher, *i.e.* above 14000, Reynolds numbers are studied since the wall region becomes smaller and velocity gradients more steep.

It stands to reason that the width of a radial band, $2\Delta r$, is coupled to the decrease in the mean axial velocity component in width Δr. In the core, Δr is chosen such that ΔU_z in Δr is ½U_c/ 90 (45 radial bands, each with width $2\Delta r$). In order to retain this velocity decrease per radial band in the near wall zone, also there 45 radial bands are required. This implies $\Delta r \approx$ 55 µm in the near-wall-zone. This estimation of Δr is of the same order of magnitude as the present uncertainty in the particle's center determination, represented by Δ_{tri}. It is obvious that the real dimension of Δ_{tri}, so in µm not in pixels, is also coupled to the decrease in the mean axial velocity component accuracy. An analogous scaling as applied above would result in an approximate value of 4.5 µm for the precision necessary to Δ_{tri} in the near-wall-zone.

It is proposed to work with two zones in radial direction to solve the above mentioned problem concerning the distinct flow scales in the pipe core and in the near-wall-zone. One zone ranges from the pipe centerline to a radius where the axial velocity component drops to 50% of the axial centerline velocity, $r_{(Uz=0.5Uc)}$; the other domain ranges from this radius

to the wall. For Re_b = 10300, the 50% drop in the axial velocity component occurs roughly at r/R = 0.95. With increasing Reynolds number this value becomes closer to 1.

2.6.2   Measures in evaluation

A.   *Measurements in the near-wall zone*

Higher precision measurements in the near-wall-zone can be achieved by in-situ calibration. In the present calibration system, a precision plate is traversed in a limited rectangular volume in the test section, see Fig. 2.22. Positions of tracer particles can only be reconstructed in the near-wall region by extrapolation of the calibration functions.
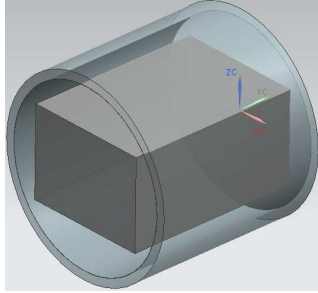
Figure 2.22 Schematic shows the volume which the calibration plate traverses. 3rd order calibration functions are created. Particle trajectories identified in the near-wall zone are converted from pixel to world coordinates by extrapolation of calibration polynomials.

A prototype was designed as a new concept of calibration system in order to promote in-situ calibration in the near-wall zone. The schematic of such prototype is shown in Fig. 2.23. Inter-spaced circular voids are created in a circular calibration plate which is moved by a step-motor in equidistant steps. Obviously, the near-wall-zone is covered by the calibration plate. A precision screw or an adaptation of the transverse system used for the above measurements can achieve accurate traversing.

The new calibration system was not applied to the present measurements. The camera frame holder at hand was designed to observe the calibration plate in a plane parallel to the pipe axis. The visualization of grid points of the circular calibration plate is distorted by the present cameras view. Modifications of the camera support system would therefore have been necessary to apply the new prototype. The concept of the new calibration system is saved to provide more accurate results in the near-wall region in future experiments.
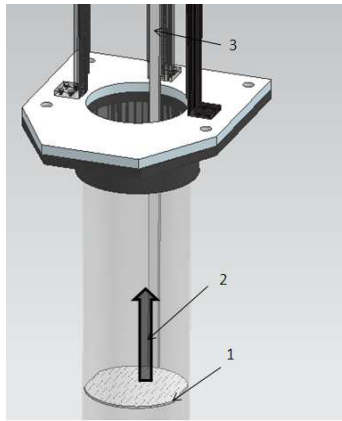
Figure 2.23 Schematic of a prototype with a circular calibration plate (1) to promote an in-situ calibration of the near-wall region. The circular plate is traversed along the axial pipe direction (2) by means of a precision screw. The precision screw is attached to a rod (3) which moves the circular plate.

B. Measurements in the near-wall zone

If conventional light sources are applied for the near-wall zone, the problem of light reflection at the pipe walls has to be overcome. Some tricks can improve the contrast between particles and background at regions close to the wall. For example, the use of a black paint or tape at the inner pipe walls can provide better contrast. The use of proper imaging processing filters can also help in identifying tracers at the wall region. The higher threshold caused by light reflections at the wall can be partially suppressed with dedicated algorithms.

However, these solutions do not completely solve the reflection problem. The only way to systematically avoid reflections in pipes is to eliminate the differences in refractive indices. A solution for eliminating reflections has been found in the use of matching refractive indices of pipe material and fluid. For water flows, the use of polymers like Fluorinated Ethylene Propylene (FEP) satisfies the criterion of matching refractive indices. This possibility has been examined by us, see Fig. 2.24.

This possible solution was not applied to the present mechanical construction due to the bad mechanical properties of this kind of polymer as compared to glass. In order to achieve no relative motion between cameras and a FEP pipe, the mechanical design concept must be revisited. In addition, lack of full transparency has been found for FEP

pipes, demanding light sources more powerful than the present stroboscopes and an increase of the exposure time of cameras. For these reasons, the mounting of a FEP test tube is saved as a possibility for future measurements of water flows bounded by transparent walls of a sort.
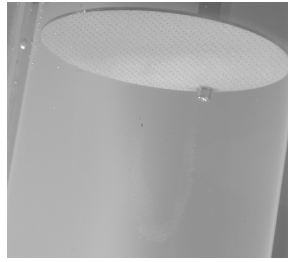
Figure 2.24 Photograph of a circular plate submerged in water inside a fluorinated ethylene propylene (FEP) pipe. This solution promotes an in-situ calibration of the wall region and eliminates the light reflections at the wall for water flows.

2.6.3   Untested measures

A.   *Measurements in the near-wall zone*

A possibility for improving the precision in the near-wall-zone with the same experimental set-up is the use of new lenses with adapted magnification. In order to achieve a precision value of 4.5 µm in the near-wall zone as discussed in section 2.6.1, the projection of real space in the camera pixel should be reduced approximately from 100 to 11 µm/pixel. The field of view would be reduced from 100 to 11 mm in the near-wall-zone. As the mean velocity near the wall is small, maximum Lagrangian correlation times measured will be sufficiently large in the near-wall zone for Reynolds numbers up to 20,000. In the center zone, the present lenses can be utilized.

An advantage of the higher spatial resolution is the possibility of reducing the diameter of a tracer particle. Near the wall time and length scales of the flow are smaller than in the pipe core and capturing these scales at higher Reynolds numbers requires smaller tracer particles. Other lenses are therefore a prerequisite for measurements at higher Reynolds numbers. A drawback is the need for longer measurement times since the measurement volume is reduced and less particles pass by (assuming the tracer particle concentration is kept constant) while the same statistical accuracy is needed.

B. *Acquisition of longer particle trajectories*

Regardless of the possibility of change in the field of view, the increase in Reynolds number will demand solutions for the acquisition of longer particle trajectories. Despite the flow scales in the pipe core or in the near-wall-zone, for Reynolds number over 20,000, the concept of our mechanical 3D-PTV construction will require modification for attaining high precision for Δ_{tri} and a higher spatial resolution for Δr. A possibility is the use of a moving frame system traversing along the axial direction of the flow.

C. *Light reflection at the pipe walls*

Accurate determination of particle trajectories in the near-wall region also requires a solution to the problem of light reflections; see Fig.'s 2.4d, 2.4e, 2.4f and 2.6. A polarization filter is efficient in filtering out the reflections but absorbs too much light reflected by the tracers. A laser illumination technique would make it possible to use fluorescent particles and wavelength filters for the cameras, to filter out the wavelengths associated with the reflected light. Powerful lasers can also operate in higher frequencies than conventional light sources, but they will result in inefficient lighting systems if the beam has to be split up to cover the whole measurement area. Again, the introduction of a separately measured wall zone might offer opportunities as this reduces the actual volume to be lighted by the laser. The core region can be illuminated in the way applied in the present work.

D. *Illumination of large volumes at high frequencies*

To determine Lagrangian statistics in a turbulent pipe flow from the Kolmogorov timescale, τ_k, to the Lagrangian correlation time, τ_c, the camera frame rate must be set few times higher than the Kolmogorov frequency, $1/\tau_k$. To achieve such frequencies with the present high-speed cameras is not a problem. But it is a problem for the home-made illumination system because of the generation of heat and the life-time of the light bulbs. The obvious solution is an increased number of light bulbs and an alternating feeding of the bulbs, but this solution is not low-cost. Recent progress with light-emitting diode (LED) bulbs may hopefully provide an alternative solution in the near future.

2.7 Conclusions

High order Lagrangian and Eulerian statistics, such as skewness and flatness, of turbulent pipe flow at $Re_b = 10300$ have been determined by 3D-PTV. To the knowledge of the authors, similar accuracy for high order Lagrangian statistics was only experimentally obtained at $Re_b = 5300$ by Walpot et al.[7] The newly measured data are essential for the quantification of parameters in, and validation of, Lagrangian stochastic models[4] to predict turbulent dispersion.

The minimum amount of data in a discrete time separation needed for the description of Lagrangian velocity statistics, autocorrelations or cross-correlations, has been determined for $Re_b = 10300$ by comparison with DNS-data of Veenman[8]. Good agreement is found if the number of correlation samples exceeds 2×10^4.

Velocities derived by straightforward interpolations of consecutive 3D positions of a particle trajectory have been found to yield accurate pipe flow statistics at $Re_b = 10300$, if a maximum triangulation error of the order of 40 µm is allowed in the particle detection algorithm. There is no need to correct the spatial position of particles with smoothing filters, as done by Walpot et al.[7] The application of a Savitz-Golay low-pass smoothing filter to correct the spatial position of particles with a third order polynomial and a filter span of 17 points is found to be unnecessary with the measurement accuracies specified in the above. Naturally, such low-pass filtering is undesirable because of the *a priori* unknown cut-off frequency.

References

[1]   S. B. Pope: "Lagrangian PDF methods for turbulent flows". Annu. Rev. Fluid Mech. 26, 23 (1994).

[2]   P. K. Yeung: "Lagrangian investigations of turbulence". Annu. Rev. Fluid Mech. 34, 115 (2002).

[3]   L. Biferale, E. Bodenschatz, M. Cencini, A. S. Lanotte, N. T. Ouellette, F. Toschi, and H. Xu: "Lagrangian structure functions in turbulence: A quantitative comparison between experiment and direct numerical simulation". Physics of Fluids 20, 065103 (2008).

[4]   J. J. H. Brouwers: "On diffusion theory in turbulence". Journal of Engineering Mathematics, 44: 277 – 295, 2002.

[5]   S. B. Pope: "Stochastic Lagrangian Models of Velocity in Homogeneous Turbulent Shear Flow". Physics of Fluids 14(5), 1696-1702, (2002).

[6]   Y. Suzuki and N. Kasagi: "Turbulent air-flow measurement with the aid of 3-D particle tracking velocimetry in a curved square bend". Flow, turbulence and combustion 63, 415-442, 2000.

[7]   R. J. E. Walpot, C. W. M. van der Geld, and J. G. M. Kuerten: "Determination of the coefficients of Langevin models for inhomogeneous turbulent flows by three-dimensional particle tracking velocimetry and direct numerical simulation", Physics of Fluids 19, 045102 (2007).

[8]   M. P. B. Veenman, "Statistical analysis of turbulent pipe flow: A numerical approach," Ph.D. thesis, Technische Universiteit Eindhoven (2004).

[9]   R. W. Miller: 1996, Flow Measurement Engineering Handbook. McGraw-Hill, 3rd edition.

[10]   H. -E. Albrecht, M. Borys, N. Damaschke, and C. Tropea: Laser Doppler and phase Doppler measurement techniques. Springer-Verlag 2003.

[11]   H. P. Bakewell and J. Lumley: 1967, "Viscous sublayer and adjacent wall region in turbulent pipe flow". Physics of Fluids 10(9), 1880-1889.

[12]   J. O. Hinze: 1975, Turbulence. McGraw-Hill.

[13]   R. Volk, E. Calzavarini, E. Lévêque, J.-F. Pinton: "Dynamics of inertial particles in a turbulent von Kármán flow", J. Fluid. Mech. 668, 223-235 (2011).

[14]   R. Clift, K. J. R. Grace and M. E. Weber: 1978, "Bubbles, drops and particles". New York: Academic Press.

[15]   R. N. Kieft, K. R. A. M. Schreel, G. A. J. van der Plas, and C. C. M. Rindt: 2002, "The application of a 3D-PTV algorithm to a mixed convection flow". Experiments in Fluids 33, 603-611.

[16]   R. J. E. Walpot, P. C. J. N. Rosielle, and C. W. M. van der Geld, "Design of a set-up for high-accuracy 3D-PTV measurements in turbulent pipe flow". Measurement, Science and Technology 17, 3015-3026, 2006.

[17]   H. -G. Maas, "Contributions of digital photogrammetry to 3D-PTV", in "Three-dimensional velocity and vorticity measuring an image analysis techniques", Ed. Th. Dracos, Kluwer Academic Publishers, 1996.

[18]   T. Dracos, "Particle tracking in three-dimensional space", in "Three-dimensional velocity and vorticity measuring an image analysis techniques", Ed. Th. Dracos, Kluwer Academic Publishers, 1996.

[19]   A. Savitzky, and M. Golay: "Smoothing and differentiation of data by simplified least squares procedures". Analytical chemistry 36(8), 1627-1639, (1964).

[20]   G. J. Kunkel, J. J. Allen and A. J. M. Smits: "Further support for Townsend's Reynolds number similarity hypothesis in high Reynolds number rough-wall pipe flow". Physics of Fluids 19, 055109 (2007).

[21]   R. J. E. Walpot, J. G. M. Kuerten, and C. W. M. van der Geld, "Experimental determination of Lagrangian velocity statistics in turbulent pipe flow". Flow, Turbulence and Combustion 76(2), 163-175, 2006.

[22]   R. D. Moser, J. Kim, and N. N. Mansour: "Direct numerical simulation of turbulent channel flow up to Reτ = 590". Physics of Fluids 11(4), 943-945, 1999.

[23]   S. B. Pope,: 2000, Turbulent Flows. Cambridge University Press.

[24]   H. Tennekes and J. L. Lumley, A First Course in Turbulence (MIT, Cambridge, 1972).

[25]   D. K. McLaughlin and W. G. Tiederman: "Bias correction for individual realization of laser anemometer measurements in turbulent flows". Physics of Fluids 16(12), 2082-2088, 1973.

3

The role of Inertia and Turbulence on Concentration Profile and Mean Relative Velocity in Particle-laden Pipe flow

3D-PTV is applied to particle-laden pipe flows in various stages of development, characterized by both normal and higher levels of turbulence than in fully developed flow. All flows are tested at Reynolds number 10300 based on the bulk velocity and the pipe diameter. The effects of particle Stokes numbers, flow direction (upward or downward) and mean concentration on radial particle distribution, mean relative velocity and fluctuating velocities of particles and of fluid are shown. Reduction of the mean relative velocity is related to the increase in flow turbulence. Explanations of the interaction of inertia particles with flow turbulence are provided in particular for the large impact of flow orientation on concentration profiles. Two-way coupling is relevant for flows with mean volumetric concentrations exceeding 7×10^{-5}. Turbulence augmentation is observed with increasing mean concentration of particles.

3.1 Introduction

Turbulent dispersed two-phase flows are abundant in both industry and nature. For example, the dispersion of pollutants in an urban environment, sediment transport or the fluidized catalytic cracking of carbohydrates are of major importance. The ability to predict the behavior of this type of flow - either using numerical or theoretical models – is beneficial to a wide range of disciplines. A better understanding of this kind of flow would be a great benefit to scale-up process equipment or to improve mixing efficiencies. However, a lack of consistent experimental data currently makes validation of both numerical and theoretical results difficult; see Poelma *et al.*[1]

Particle-laden flow in pipes has numerous engineering applications ranging from pneumatic conveying systems to chemical reactor design and is one of the most thoroughly investigated subjects in the area of multiphase flow; see Kartusinsky *et al.*[2] Turbulence modulation in two-phase flows has been described by a number of models; see Gore and Crowe[3], Hetsroni[4] and Elgobashi.[5] However, due to the complex nature of the problem, these simplified models are not able to fully predict fluid and particle behavior for the whole range of applications.

When particles are in the flow, the only way to exactly describe the system, including the interaction of the phases, is to fully resolve stresses at the mobile particle surfaces. In order to calculate the total force on a particle exerted by the fluid, the stress tensor needs to be integrated over the surface (and the body forces over the volume). Numerical computations require significant memory and processing speed and only very simple geometries with a limited numbers of particles can be studied, see Tryggvason *et al.*[6] Most numerical work therefore uses simplifications, e.g. assuming the particle to be a point-force and choosing a model for the particle equation of motion; see Poelma.[7]

The dispersion of inertial particles in turbulent flows is characterized by macroscopic phenomena such as non-homogeneous distribution, large-scale clustering, and preferential concentration due to the inertial bias between particles and surrounding fluid; see Wang and Maxey.[8] The distribution of particles may be crucial in determining collision frequency, breakage efficiency, agglomeration, reaction rates, deposition and entrainment; see Marchioli *et al.*[9]

From an engineering viewpoint, the transient states of particle-laden flows are also interesting. In a number of industrial applications, including separation techniques and

47

droplet-laden flows, particle distributions never reach equilibrium; see Soldati.[10] In industrial loops, turbulent particle-laden pipe flows often do not achieve a steady state due to the length limitations; see Laws *et al.*[11] The required length for fully developed conditions enhances with increasing bulk Reynolds number.

We would have preferred to study both upward and downward flow in fully-developed turbulent conditions. However, in our experimental setup the development length was too small to reach fully-developed turbulent downward flow. Therefore, in order to study the effect of different stages of development, we considered both upward and downward flow without flow straightener. In addition, criteria are sought and will be presented which quantify the state of development of the flow in terms of flow variables. It will be shown with the aid of these characterizations that the most well-developed downflow is nearly fully developed. The only part of a cross-section area where the flow is not yet fully developed is near the center of the channel while the concentration profiles will be found to be mainly affected by flow direction, Stokes number and other parameters in the remaining area of the flow.

In the present study, 3D-PTV is applied to particle-laden pipe flows in various stages of development in order to investigate the impact of varying turbulence levels on particle behavior, in particular on the mean relative velocity. All flows are tested at Reynolds number 10300, based on the bulk velocity and the pipe diameter. Due to inertial bias between inertia particles and the carrier phase, the impact of flow direction (upward and downward) on radial particle distributions is studied. The influence of mean concentration on the fluctuating velocities of particles and fluid is also evaluated. Particles with diameters equal to 0.8 and 0.96 mm are chosen. Mass density of inertia particles (1050 kg/m^3) slightly exceeds the mass density of the carrier fluid (~1000 kg/m^3).

Particle properties (volume and mass density) are selected with the aim of testing particle-laden flows for which the terminal velocity of the dispersed phase, U_{TV}, is of the same order of magnitude as the root-mean-square velocity of the carrier phase, u_{rms}. Interesting phenomena have been reported when $u_{rms}/U_{TV} \approx O(1)$: entrapment of bubbles or particles in vortical flow structures, transport of dispersed phase towards the flowing edges of eddies where static equilibrium of forces over an inertial body can modify its rise or settling velocity and the effects of crossing trajectories; see Sene *et al.*[12] and Spelt and Biesheuvel[13], for example.

The structure of the paper is as follows. In Section 3.2, the experimental setup is presented, including specifications of flow tracers and inertia particles, calibration unit, camera support and illumination systems. Optical requirements for 3D-PTV are also explained. Sections 3.3 and 3.4 provide the 3D-PTV procedure for identification of individual particle trajectories and the analysis method, respectively. A description of the experimental conditions is provided in Section 3.5.

Results are presented in Section 3.6. Reference turbulent single-phase pipe flows are characterized in sub-Section 3.6.1. Radial concentrations of inertia particles, mean axial velocity and Mean Square Value (MSV) of velocity for fluid and dispersed phases are shown in sub-Sections 3.6.2, 3.6.3 and 3.6.4, respectively. In sub-Section 3.6.5, results of the magnitude of the mean axial relative velocity as a function of flow turbulence level are presented.

Analyses of the experimental results are given in Section 3.7. The role of inertia on the wall-normal distributions and mean relative velocities is interpreted in Section 3.8. In this same section, fluid turbulence modulation by the presence of inertia particles is discussed. Conclusions are summarized in Section 3.9.

3.2   Experimental setup

3.2.1   Test rig

Turbulent particle-laden pipe flows have been created in a water loop driven by a centrifugal pump; see Fig. 3.1. The in-line 3 kW centrifugal pump of type DPV18-30, manufactured by "Duijvelaar pompen", allows Reynolds numbers, based on the bulk velocity, U_b, and pipe diameter, D, in the range 10^3 to 10^5.

A set of valves is arranged in such a way that downward and upward vertical flows are possible. In upward flows, a frequency controller permits fine-tuning of the Reynolds number by adjusting the mass flow rate in the measurement section. In downward flows, mass flow rate is adjusted by controlling pressure drop over a valve.

The mass flow rate is measured by means of a Micro Motion Elite CMF300 mass flow and mass density meter, whose inaccuracy is less than 0.5% of the registered flow rate. A water reservoir (tank I), located at the bottom of the setup, contains about 2 m^3 of water.

This value facilitates water temperature stabilization and Reynolds number control. Temperature during a test-run was essentially constant, varying typically 0.1ºC only.
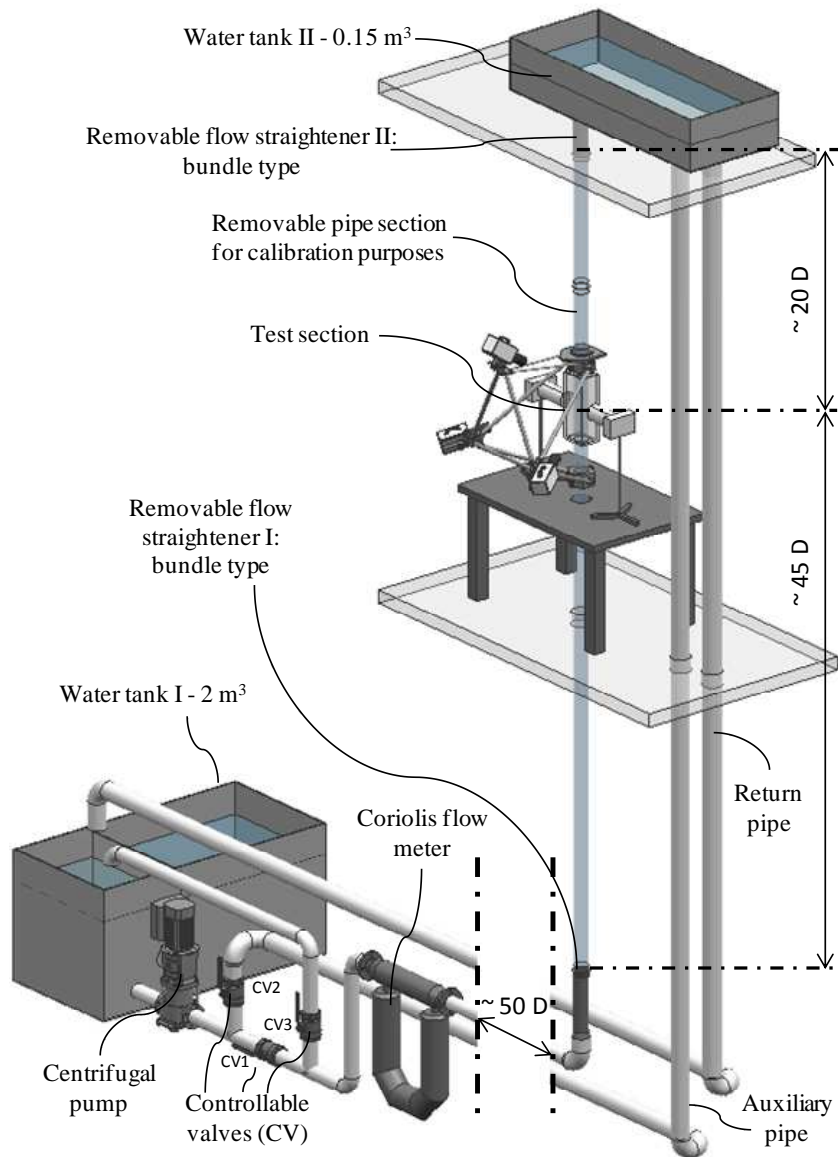

Figure 3.1 Schematic of the 3D-PTV experimental setup for downward or upward pipe flow.

Submerged pumps are placed in the reservoir tanks at the bottom and at the top of the setup in order to promote homogeneous dispersion of the added tracers and inertial

particles. The volume of the top tank is smaller, ≈ 0.15 m³, facilitating control of the concentration of particles.

The measurement section consists of a glass pipe to ensure optical accessibility. A water-filled rectangular glass box around the pipe minimizes optical distortions. The pipe diameter is chosen relatively large, 100 mm inner diameter, because measurements at high Reynolds numbers are required. For a certain Reynolds number, bulk velocities are lower for higher tube diameters, which is advantageous for the acquisition of Lagrangian statistics.

Flow straighteners, tube bundle conditioners of ISO 5167-1:1991, see Miller[14], are employed to remove strong secondary flow effects. For upward flows, the bundle conditioner I is placed downstream of a 90º bend; see Fig. 3.2a. Flow straightener I consists of a set of pipes with an internal diameter of 10 mm and an approximate length of 50 cm. It is constructed in such way that it can be replaced by a straight pipe section.
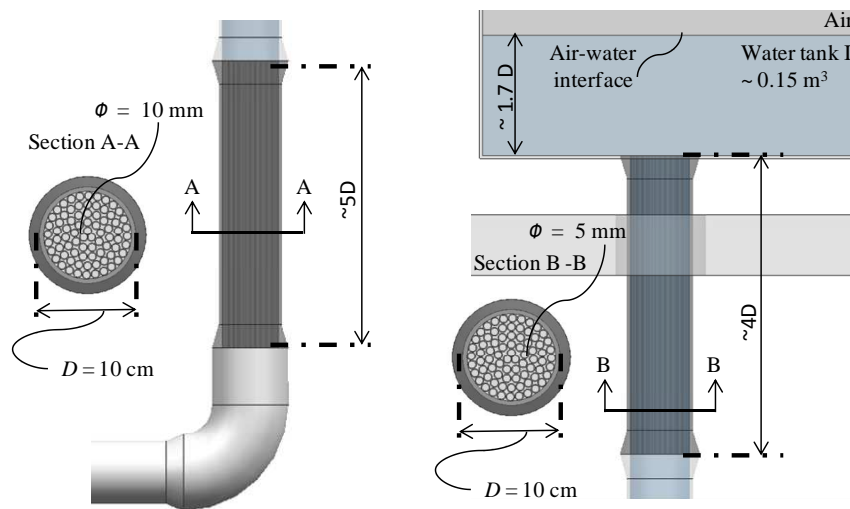
Figure 3.2 Schematics of the entrance regions. 3.2a: details of the bundle flow straightener I; 3.2b: details of the bundle flow conditioner II.

For downward flows, the bundle conditioner II is placed downstream of the bottom of tank II in the pipe that conducts the flow to the test section; see Fig. 3.2b. Flow straightener II consists of a set of pipes with an internal diameter of 5 mm and an approximate length of 40 cm. As bundle conditioner I, it can also be replaced by a straight pipe section.

3.2.2   Particle properties

Properties of polystyrene particles applied in the present particle-laden experiments are given in Table 3.1. The fluid time-scale τ_f in the Stokes number, St, is based on viscous scales; see info below Table 3.1. The fluid length-scale is the Kolmogorov scale for fully developed single-phase pipe flow at $Re_b = 10300$ as computed by Veenman.[15] The Kolmogorov length is about 0.6 mm in the pipe core and 0.2 mm in the wall region. For evaluation of the particle timescale, τ_p, the relaxation time for particles in stationary flow is used; see Albrecht et al.[16]:

$$\tau_p = (d^2\rho_p/18\mu)(1 + 0.5\rho_f/\rho_p) \tag{3.1}$$

where μ is the dynamic viscosity and ρ_p and ρ_f are the mass density of particles and of fluid, respectively. A relaxation time of $\tau_p \approx 4$ ms is obtained for the tracers. Note that the fluid inertia is accounted for by the added mass coefficient 0.5 which close to a wall is increased to about 0.7; see van der Geld.[17]

Table 3.1 Properties of particles applied in the present particle-laden experiments

Particles	Mass density [kg/m^3]	Diameter d_p [mm]	Terminal velocity, $/U_{TV}$/* [mm/s]	*Re_p	** $St = \tau_p/\tau_f$	*** Length-scale ratio: d_p/l_k
Tracers	1050	0.2	1.0	0.18	0.14	0.33 – 1
Type I (PI)	1050	0.8	10.2	7.76	2.31	1.33 – 4
Type II (PII)	1050	0.96	13.1	11.92	3.33	1.6 – 4.8

* Settling velocity of a particle in an infinite, stagnant pool of water.

** Fluid time-scale is based on viscous scales as given by: $\tau_f = v/u_\tau^2$. For $Re_b < 10^5$, the wall shear velocity can be estimated as $u_\tau = (U_b^2 f/8)^{1/2}$ with $f = a\, Re_b^{-m}$, $m= 0.25$ and $a = 0.316$; see Hinze.[18] τ_f is roughly 28 ms.

*** Kolmogorov length-scales for a fully developed single-phase pipe flow at $Re_b = 10300$ as computed from the DNS code developed by Veenman[15]: ≈ 0.6 mm at pipe centerline and ≈ 0.2 mm close to the wall.

The terminal velocity is attained in quiescent fluid when gravitational and drag forces are in equilibrium:

$$U_{TV} = \{(4\,(\rho_p - \rho_f)\,d_p\,g) / (3C_D\,\rho_f)\}^{1/2} \tag{3.2}$$

where g is the gravity acceleration and C_D the drag coefficient. The latter is a function of the particle Reynolds number, $Re_p = d_p|U_{TV}|/v$, which is based on the particle diameter and the terminal velocity. In the Stokes regime, C_D is given by Eq. (3.3). For $1< Re_p< 1000$, Schiller and Naumann[19] proposed a correlation for C_D given by Eq. (3.4):

$$C_D = (24 \,/\, Re_p); \text{ for } Re_p < 1 \qquad\qquad (3.3)$$

$$C_D = (24 \,/\, Re_p)\,(1 + 1/6\, Re_p^{2/3}); \text{ for } 1 < Re_p < 1000 \qquad\qquad (3.4)$$

A value for U_{TV} is obtained by an iterative computation concerning Eq. (3.2) and Eq.'s (3.3) or (3.4). Since the bulk flow velocity, U_b, is approximately 100 mm/s for the flows at hand, the ratio U_b/U_{TV} is of order 10^2 for seeding particles. Since $U_b \gg U_{TV}$, $\tau_p < \tau_f$ and $d_p < l_k$, the employed seeding particles work well as flow tracers. For particles of type I and II, the ratio U_b/U_{TV} is of order 10, $\tau_p > \tau_f$ and $d_p > l_k$. Therefore, particles type I and II have significant inertial characteristics to not behave as tracers.

3.2.3   Mechanical construction for camera support and reproducible calibration

Brief descriptions of the camera support and calibration unit are now presented. The applied optical settings and descriptions of the illumination and recording apparatus are also provided. More information is found in Oliveira *et al.*[20]

Three "HighSpeedStar" cameras with 12-bit grayscale CMOS sensor and a resolution of 1024 x 1024 pixels have been utilized to capture almost instantaneous 3D particle positions in an approximate measurement volume of 0.1x0.1x0.1 m³. The cameras can record at 1000 Hz at full resolution, but were operated at 50 Hz to maximize the flow measurement time. Recordings are performed until the internal memory of the cameras becomes full during approximately 2 minutes. Maximum physically relevant frequencies are about 12 Hz for $Re_b = 10300$, making a 50 Hz sampling rate sufficient according to the Nyquist Theorem.

Settings of cameras and lens arrangement have been chosen as: sensor resolution (1 pixel = 17 µm²), focal length (105 mm), exposure time (20 µs), distance from the lens to the object (~ 800 mm). These settings guarantee sharp images of moving particles in the whole volume of the measurement.

A statically determined approach has been applied to a mechanical design, where no relative movement between the cameras and measurement volume is allowed throughout the calibration and 3D-PTV measurements. Following Walpot *et al.*[21], three cameras are attached to the flow tube by a stiff and lightweight equilateral triangular frame constructed between them, see Fig. 3.1. A total of 24 degrees of freedom, which include three translations and three rotations for the three cameras and the measurement section, have

been prescribed once, either as positions to be held or desired motions to be set by manipulation. Due to the statically determined design, there is no incorporation of unknown thermal stresses in the frame or flow tube.

An in-situ calibration method has been utilized to transform the two-dimensional pixel information of each camera to world coordinates. A calibration unit precisely moves a grid with regular inter-spaced points throughout the measurement volume to certain positions, with high reproducibility. The bigger and well resolved the volume covered by the calibration plate, the smaller interpolation and extrapolation errors of the calibration functions are.

On the top of the measurement section, a pipe segment can be removed for calibration purposes. The centrifugal pump allows a stationary water-level just above the measurement volume, given that the energy provided by the centrifugal pump is in equilibrium with the potential energy of the static head. Once the water level is static, the calibration unit is inserted, making possible a reproducible positioning of the calibration grid throughout the measurement volume.

During the calibration procedure, the calibration grid is homogeneously illuminated from behind by means of four floodlight halogen lamps. For lighting the measurement volume during the 3D-PTV measurements, two strong stroboscopic light sources with an output of about 5 J per pulse each have successfully been applied. The digital delay/pulse generator DG535 assured a perfect synchronization between the recordings of the three cameras and the lighting pulse generated by the stroboscope equipment.

3.3   Particle tracking algorithm

A commercial 3D-PVT imaging code from La Vision GmbH, named Davis, has been used to obtain trajectories of tracers and inertia particles. Algorithm details of the Davis PTV tracking code can be found in Maas[22] and Dracos[23].

The 3D-PTV procedure for identification of individual particle trajectories is given by Oliveira *et al.*[20] Calibration and flow measurement images are processed in order to transfer files which contain time reference and spatial positions of individual particle trajectories to the analysis method. Here, the only difference from the 3D-PTV procedure as applied by Oliveira *et al.*[20] is the use of built-in imaging filters of Davis in order to obtain images with only inertial particles and images with only flow tracers. This task is

facilitated by the bigger imaging projection area of inertia particles on the camera sensor, exceeding the projection of tracers in 16 or 25 times.

Reduced levels of noise are obtained for the trajectories of inertia particles. For tracers, noise is significant and removed in the trajectory analysis method. After the imaging segmentation stage, the procedure to determine the 3D particle position and to identify particle trajectories is the same.

3.4   Trajectory analysis

The particle tracking algorithm yields matrices which contain time reference and spatial positions of particle trajectories from the flow measurement images. Transformation from Cartesian (x,y,z) to cylindrical (r,θ,z) coordinates facilitates pipe flow statistical analyses; see Oliveira *et al.*[20]

The removal of unrealistic trajectories has been accomplished by two filters: a length filter and a displacement outlier-check ($\pm 5\sigma_{r,\theta,z}$). The length filter consists of eliminating all trajectories of tracers outside a range of minimum and maximum positions of a particle track. The term σ represents the standard deviation for velocity components at a specific radial position. Here, the standard deviation applied in the outlier-check filter is derived from the present experiments.

In the present 3D-PTV experiments, no need of filtering high frequency measurement noise has been observed. Tracer and inertia particle velocities derived by straightforward interpolations of consecutive 3D positions of a particle trajectory have been proven reliable to obtain particle-laden pipe flow statistics.

After the coordinate transformation and the removal of the spurious particle tracks, differentiation in time of the validated trajectories generates the velocity vectors. For Eulerian results, the velocity vectors are gathered in discrete radial bins in accordance to $r_i \pm \Delta r$, where the subscript i varies from 1 to 50. The axial length (L) of each discrete bin is 100 mm, while the radial band has a dimension of $2\Delta r$. At Re_b=10300, a radial discretization Δr equal to 0.5 mm has been found appropriate to describe the Eulerian results; see Oliveira *et al.*[20]

Lagrangian results can also be gathered in discrete radial bands: $r_i \pm \Delta r$, with Δr satisfying $2\Delta r > |u|\Delta t$. Here, u is a typical radial velocity value, *e.g.* the standard deviation of radial velocity fluctuations. A radial band width, Δr, of 0.5 mm and a camera frequency

55

of 50 Hz sufficed to obtain negligible bias at $Re_b = 10300$. More information is found in Oliveira et al.[20]

3.5   Particle-laden experimental conditions

A category of particle-laden experiments (2P) is shown in a map proposed by Elgobashi[5], see Fig. 3.3. Downward and upward vertical flows have been measured in various stages of development at the same bulk Reynolds number, Re_b. The bulk velocity of each flow, U_b, was adapted to temperature changes to keep $Re_b \approx 10300$. Single-phase flows (1P) serve as a reference for two-phase flows.

Particle-laden flows with mean volumetric concentrations, $<\Phi_v>$, ranging from $5\text{x}10^{-6}$ to $1.7\text{x}10^{-4}$ have been tested. The presence or absence of flow conditioners I and II affects the stage of flow development in the test section. In upward flows, 3D-PTV measurements are performed at $45D$ downstream of the entrance section; in downward flows, at $20D$. In upflow with flow straightener I fully developed pipe flow is obtained.[20]
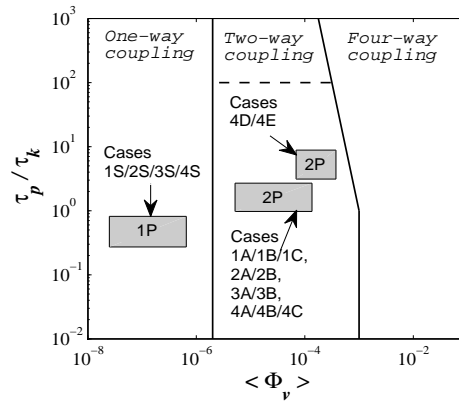
Figure 3.3 Experimental conditions represented in the map of regimes of interaction between particles and turbulence as proposed by Elgobashi.[5]

In Fig. 3.3, the rectangular areas represent mean concentration and time-scale ratios of particles in the present experiments. Single-phase flow measurements are represented by 1P in the region denoted as "one-way coupling"; only tracers are employed. Particle-laden measurements are represented by 2P in the region denoted as "two-way coupling"; tracers

and inertial particles type I or II are added to the water flow. Mean concentration of tracers less than 10^{-6} is also applied to the particle-laden experiments.

Properties of inertial particles type I or II (volume and mass density) are selected with the aim of testing particle-laden flows which have a characteristic root-mean-square velocity representative of the turbulent carrier phase, u_{rms}, and the terminal velocity of the dispersed phase, U_{TV}, of same order of magnitude: $u_{rms}/U_{TV} \approx O(1)$.

A particle-laden experimental case is represented here by a number (1, 2, 3 or 4) which indicates the flow direction and the presence or absence of a flow conditioner; and a letter (A, B, C, D or E), indicating the applied mean concentration of inertia particles. A summary of all tested particle-laden cases is shown in Table 3.2. The reference single-phase flows are specified by 1S, 2S, 3S or 4S. The letter S denotes single-phase flow and the numbers are as defined above.

Table 3.2 Summary of the single-phase and particle-laden flow experiments. All experimental runs have been performed at Reb = 10300

Case	Inertial particles	Flow Direction	Development Length	Flow Straightener	$<\Phi_v> \times 10^{-5}$
1A	Type I (PI)	Upward	45D	Bundle I	3.2
1B	Type I (PI)	Upward	45D	Bundle I	1.4
1C	Type I (PI)	Upward	45D	Bundle I	0.5
1S	--	Upward	45D	Bundle I	--
2A	Type I (PI)	Upward	45D	--	3.2
2B	Type I (PI)	Upward	45D	--	1.9
2S	--	Upward	45D	--	--
3A	Type I (PI)	Downward	20D	--	2.3
3B	Type I (PI)	Downward	20D	--	1.0
3S	--	Downward	20D	--	--
4A	Type I (PI)	Downward	20D	Bundle II	7.0
4B	Type I (PI)	Downward	20D	Bundle II	2.8
4C	Type I (PI)	Downward	20D	Bundle II	1.8
4D	Type II (PII)	Downward	20D	Bundle II	17.0
4E	Type II (PII)	Downward	20D	Bundle II	8.3
4S	--	Downward	20D	Bundle II	--

3.6   Results

3.6.1   Characterizing turbulent single-phase pipe flows at $Re_b = 10300$

Tracer trajectories have been registered for turbulent single-phase pipe flows in four distinct flow conditions by 3D-PTV; see Section 3.5. With a camera frame rate of 50 Hz, the differentiation of particle trajectories in time generates on average 2×10^6 velocity vectors in each flow case. The velocity vectors are gathered in discrete radial bins in accordance to $r_i \pm \Delta r$, with $\Delta r = 0.5$ mm; see Section 3.4.

Flow velocity statistics of case 1S, upward flow with the bundle flow straightener I, have already been investigated; see results in Oliveira *et al.*[20] This case represents the so-called fully developed flow. For case 1S, mean fluctuating velocity components achieve the lowest fluctuation levels among all single-phase experiments.

In order to establish a relationship among cases 1S/2S/3S/4S, the Mean Square Value (MSV) of the velocity fluctuations is determined for each flow condition. The MSV velocity is defined as the product of mean velocity fluctuations: $<u_h u_q>$. Subscripts h and q represent cylindrical coordinates (r, θ, z). Let the overbar character indicate cross-section average.

$$\overline{<u_h u_q>} = (_0\!\int^R <u_h u_q> 2\pi r \, dr)/(\pi R^2) \tag{3.5}$$

By considering the diagonal components $<u_h^2>$ and averaging them in accordance to (3.5), it is possible to compare MSV of fluctuating velocities averaged in the cross-section for each single-phase flow case; see Fig 3.4.
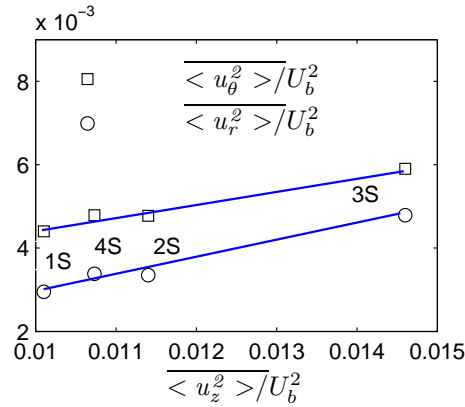
Figure 3.4 Diagonal components of the Reynolds stress tensor averaged in the cross-section for four distinct flow conditions. Computed values are normalized by the square of the bulk velocity of each flow, U_b^2. Lines are added to guide the eye.

The averaged diagonal components, $\overline{<u_h^2>}$, are normalized by the square of the bulk flow velocity, U_b^2, of the corresponding experiment. Here, U_b is chosen for normalization since it was set at each experiment to keep the same Re_b, 10300, irrespective of temperature changes. The bulk velocity is chosen as normalization quantity instead of the wall shear velocity, u_τ, which is often used in the literature, because U_b can be determined more accurately in our experimental setup.

Disturbances created at the entrance affect turbulent flow levels. With sufficient development length, cross-section average turbulence of cases 2S/3S/4S as quantified by Eq. (3.5) becomes equal to the one presented by case 1S. In the presence of flow straighteners, the turbulence intensity levels at the test section are smaller; compare case 2S to 1S for upward flows and 3S to 4S for downward flows in Fig. 3.4. At 20D downstream of the entrance section, flow velocity statistics of downward flow with the bundle flow straightener II (case 4S) are not yet fully developed. Figure 3.4 neatly groups and shows the trend of these measurement conditions.

Linear fits for the computed values of $\overline{<u_h^2>}$ yields:

$$\overline{<u_\theta^2>}/U_b^2 = 0.32\overline{<u_z^2>}/U_b^2 \tag{3.6}$$

$$\overline{<u_r^2>}/U_b^2 = 0.4\overline{<u_z^2>}/U_b^2 \tag{3.7}$$

The quality of the fits is expressed by the two parameters r_s^2 and F, defined as follows:

$$r_s^2 = \sum_{i=1}^{n}(\hat{O}_i - \overline{O})^2 \Big/ \sum_{i=1}^{n}(O_i - \overline{O})^2 \tag{3.8}$$

$$F = \left\{ \sum_{i=1}^{n}(\hat{O}_i - \overline{O})^2 \Big/ \sum_{i=1}^{n}(O_i - \hat{O}_i)^2 \right\}(n-K)/(K-1) \tag{3.9}$$

Here, n is the number of measurements with outcome O_i, $\hat{O}_i$ the predicted values and $\overline{O}$ the mean of the set (O_i); the number of parameters determined in the fit is K. In Eq. (3.6), r_s^2 and F are equal to 0.98 and 81, respectively. In Eq. (3.7), r_s^2 and F correspond to 0.98 and 84, respectively.

The transient states of pipe flow are of practical interest. In industrial loops, turbulent pipe flows often do not reach fully developed conditions due to the length limitations; see

Laws *et al.*[11] The required length enhances with increasing bulk Reynolds number. As observed in Fig. 3.4, the MSV velocities of cases 2S/3S/4S exceed those of case 1S. The fits, Eq. (3.6) and Eq. (3.7), distinguish flow conditions from the fully developed one in a convenient way.

For flow cases with flow straighteners, 1S and 4S, ratios of the diagonal components of the Reynolds stress tensor, $<u_z^2>/<u_r^2>$ and $<u_z^2>/<u_\theta^2>$, increase linearly from the pipe centerline to a radial position about $r/R = 0.8$ at $Re_b = 10300$; see Fig 3.5. The linear inhomogeneous behavior at the pipe core is characteristic for fully developed pipe flows. This feature is observed for case 4S even though this case is not yet fully developed. For $r/R > 0.8$, the increase in $<u_z^2>/<u_r^2>$ and $<u_z^2>/<u_\theta^2>$ exceeds the typical linear growth. The axial normal stress remains bigger than the tangential and radial components, and the ratios achieve values exceeding 10 close to the wall.
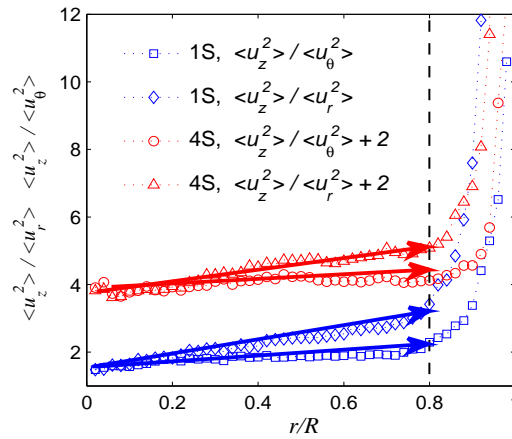
Figure 3.5 Ratios of the diagonal components of the Reynolds stress tensor, $<u_z^2>/<u_r^2>$ and $<u_z^2>/<u_\theta^2>$, for cases 1S and 4S. The presence of the Bundle flow straighteners I and II assures a characteristic linear behavior in the pipe core ($0 < r/R < 0.8$).

For single-phase experiments without flow conditioners, cases 2S and 3S, the linear inhomogeneous behavior for $0 < r/R < 0.8$ is not achieved. This linear feature at the pipe core is only observed for turbulent pipe flows which approach fully developed conditions.

A summary of the single-phase flows tested at $Re_b = 10300$ is shown in Table 3.3. Linear fits are applied for $<u_z^2>/<u_r^2>$ and $<u_z^2>/<u_\theta^2>$ in flows which achieve a linear behavior in the radial range $0 < r/R < 0.8$. Values for r_s^2 and F statistics are also included.

Table 3.3 Summary of the single-phase flow experiments at $Re_b = 10300$

Case	Flow Direction	Flow Conditioner	Development length	Linear behavior	$\langle u_z^2\rangle/\langle u_r^2\rangle =$ $a(r/R)+b$ in $0<r/R<0.8$	$\langle u_z^2\rangle/\langle u_\theta^2\rangle =$ $c(r/R)+d$ in $0<r/R<0.8$
1S	Upward	Bundle I	45D	Yes	a=0.55; b=1.5 r_s^2=0.83; F=176	c=1.9; d=1.5 r_s^2=0.98; F=1850
2S	Upward	--	45D	No	--	--
3S	Downward	--	20D	No	--	--
4S	Downward	Bundle II	20D	Yes	a=0.48; b=1.7 r_s^2=0.76; F=75	c=1.9; d=1.7 r_s^2=0.93; F=497

In this subsection, the present single-phase flow measurements have been categorized. This is achieved by evaluating turbulent flow features. In the remaining of section 3.6, particle-laden flow results are presented and compared to the above reference single-phase flows.

3.6.2 Concentration of inertial particles

The number of tracer trajectories measured in the range r/R = 0.6 to 1 decreases with increasing r/R - value. The difficulties in measuring tracer trajectories in this region were mainly due to light reflections stemming from differences in the refractive indices of water, n ≈ 1.33, and glass, n ≈ 1.51, and the curvature of the glass pipe. Light reflections deteriorate the contrast between tracers and background. However, the fluid flow could also be measured for r/R > 0.6 despite the lower number of usable tracers there. The measured concentration of tracers is roughly linear from r/R = 0 to 0.6 and decreases towards the wall for all particle-laden flows. In Oliveira et al.[20], Eulerian statistics of a single-phase turbulent pipe flow acquired by 3D-PTV have been found to be trustworthy in the near-wall zone if a number of velocity vectors per radial bin exceeding 1000 was acquired. The same criterion is also applied here.

In the detection of inertia particle trajectories, the contrast problem between particles and background did not occur. The bigger imaging projection area of inertia particles on the camera sensor, exceeding the projection of tracers 16 or 25 times, avoided problems on the identification of particles. While the projection of a tracer image occupies nearly an area of 2x2 pixels, the projection of inertia particles occupies 8x8 or 10x10 pixels. Roughly, every 3D inertia particle position identified in the tracking algorithm corresponds to a real particle. On average, an approximate amount of 3 x 10^5 particle positions was

identified in each particle-laden case. 3D particle positions were identified with a camera frame rate of 50 Hz in average periods of 50 minutes. In this period, a volume corresponding to ≈ 2.3 m^3 crosses the test section. Thus, accurate measurements of concentration profiles of inertia particles have been obtained.

Throughout this article, the errors of time-averaged values of a measured quantity x are estimated with the aid of the so-called standard error, σ_m. Confidence intervals of 95% are considered. For a quantity which is measured n times, with instantaneous results x_i and mean $<x>$, the standard error is given by:

$$\sigma_m = [\sum_{i=1}^{n} (x_i - <x>)^2 / (n\,(n-1))]^{1/2} \tag{3.10}$$

The effects of upward or downward flow direction, presence or absence of flow straightener and mean concentration, $<\Phi_v>$, in the range 0.5×10^{-6} to 1.7×10^{-4} on the concentration profiles of inertia particles, $\Phi_v\,(r/R)$, are presented in Fig.'s 3.6 – 3.10. Here, $\Phi_v\,(r/R)$ represents the time-averaged volume of particles within the volume of the corresponding bin element; see (3.11) and (3.12):

$$<N_{bin,i}> = (1/m) \sum_{j=1}^{m} N_{bin,i}\,(j) \tag{3.11}$$

$$\Phi_v\,(bin,i) = <N_{bin,i}> (V_{particle}/V_{bin,i}) \tag{3.12}$$

where j denotes a single photograph and m is the total number of photographs. The subscript bin,i denotes a discrete radial position, r/R. The term $<N_{bin,i}>$ represents the averaged number of particles which occur in a discrete radial bin. $V_{particle}$ denotes volume of a particle and $V_{bin,i}$, volume of a bin. The mean concentration of inertia particles, $<\Phi_v>$, refers to the mean of $\Phi_v\,(bin,i)$ in all bins, Eq. (3.13). The subscript k represents the total number of radial bins, here 50.
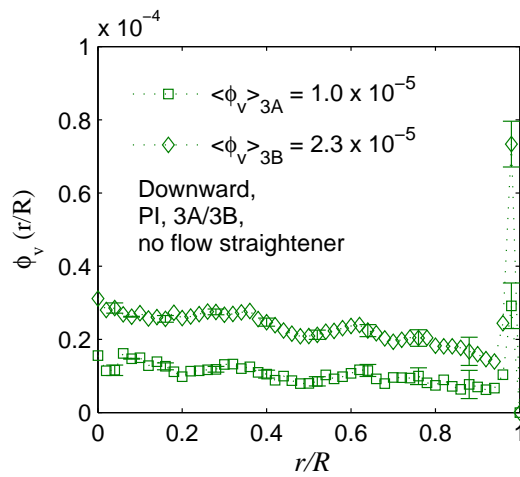
$$<\Phi_v> = (1/k) \sum_{bin,i=0}^{k-1} \Phi_v\,(bin,i) \tag{3.13}$$
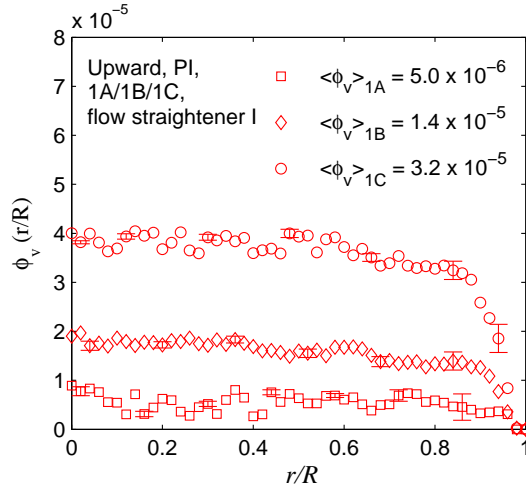
Figure 3.6 Effect of the mean concentration, $<\Phi_v>$, on the concentration profiles of inertial particles, Φ_v (r/R), in upward flow and in the presence of a flow straightener. Results are plotted for particle-laden cases 1A/1B/1C. Experiments are performed with particles type I in three distinct mean volumetric concentrations, $<\Phi_v>$: 5.0×10^{-6}, 1.4×10^{-5} and 3.2×10^{-5}.
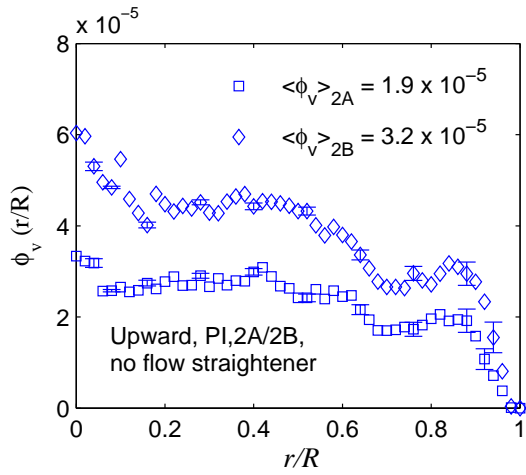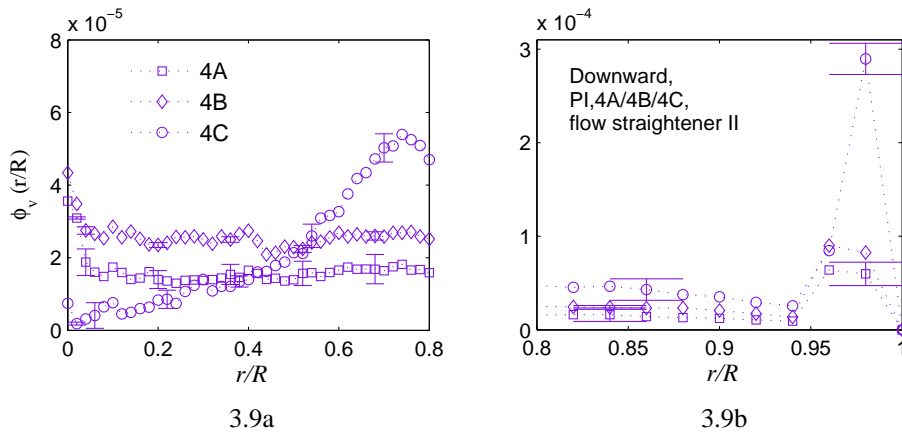

Figure 3.7 Effect of mean concentration, $<\Phi_v>$, on the concentration profiles of inertial particles, Φ_v (r/R), in upward flow and in the absence of a flow straightener. Results are plotted for particle-laden cases 2A/2B. Experimental runs are performed with particles type I in two distinct mean volumetric concentrations, $<\Phi_v>$: 1.9×10^{-5} and 3.2×10^{-5}.

Figure 3.8 Effect of mean concentration, $<\Phi_v>$, on the concentration profiles of inertial particles, $\Phi_v\,(r/R)$, in downward flow and in the absence of a flow straightener. Results are plotted for particle-laden cases 3A/3B. Experimental runs are performed with particles type I in two distinct mean volumetric concentrations, $<\Phi_v>$: 1.0×10^{-5} and 2.3×10^{-5}. Dotted lines are added to guide the eye.

3.9a   3.9b
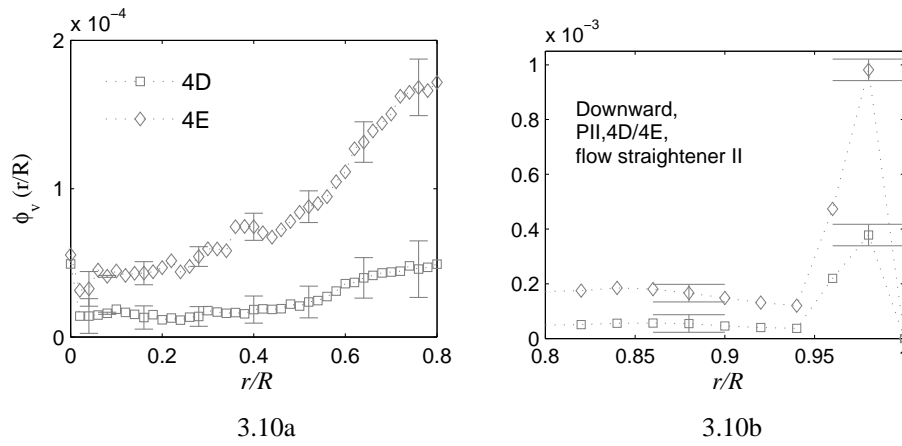
Figure 3.9 Effect of mean concentration, $<\Phi_v>$, on the concentration profiles of inertial particles, $\Phi_v\,(r/R)$, in downward flow and in the presence of a flow straightener. Results are plotted for particle-laden cases 4A/4B/4C. Experimental runs are performed with particles type I in three distinct mean volumetric concentrations, $<\Phi_v>$: 1.8×10^{-5}, 2.8×10^{-5} and 7.0×10^{-5}. Dotted lines are added to guide the eye. Figure 3.9a presents results in the range $0 <r/R< 0.8$ and Fig. 3.9b, in the range $0.8 <r/R< 1$. The number of line markers corresponds to the number of bins measured; notice the difference in scales.

3.10a

3.10b

Figure 3.10 Effect of mean concentration, $<\Phi_v>$, on the concentration profiles of inertial particles, $\Phi_v(r/R)$, in downward flow and in the presence of a flow straightener. Results are plotted for particle-laden cases 4D/4E. Experimental runs are performed with particles type II in two distinct mean volumetric concentrations, $<\Phi_v>$: 8.3×10^{-5} and 1.7×10^{-4}. Dotted lines are added to guide the eye. Figure 3.10a presents results in the range $0 <r/R< 0.8$ and Fig. 3.10b, in the range $0.8 <r/R< 1$. The number of line markers corresponds to the number of bins measured; notice the difference in scales.

Close to the pipe walls in upward flows, for $r/R > 0.85$ a reduction in Φ_v occurs; see cases 1A/1B/1C and 2A/2B in Fig.'s 3.6 and 3.7. For downward flows, there is a peak at $r/R \approx 0.98$; see cases 3A/3B, 4A/4B/4C and 4D/4E in Fig.'s 3.8, 3.9 and 3.10, respectively. Therefore, the direction of the vertical flow, upward or downward, is associated to changes in the concentration profiles, $\Phi_v(r/R)$, particularly in the near-wall zone.

For upward flows, the ratio of the mean concentration from $0 <r/R< 0.8$ to $0.8 <r/R< 1$, $R_\Phi = <\Phi_v>_{(0<r/R<0.8)}/<\Phi_v>_{(0.8<r/R<1)}$, is 1.72, 1.75 and 1.65 for upward flow cases 1A/1B/1C, respectively. Both terms $<\Phi_v>_{(0<r/R<0.8)}$ and $<\Phi_v>_{(0.8<r/R<1)}$ are computed similarly to the mean concentration, $<\Phi_v>$, Eq. (3.13), but in the indicated parts of the measurement section volume. Without the bundle flow straightener I, R_Φ increased to 1.97 and 1.92 for upward flows cases 2A/2B, respectively.

Without the bundle flow straightener II, the ratio R_Φ is 1.10 and 1.17 for downward flows cases 3A/3B, respectively. With the existence of a peak in concentration about $r/R \approx$ 0.98, R_Φ still exceeds 1. In the presence of the bundle flow straightener II, R_Φ reduced to 0.75 and 0.81 for downward flows cases 4A/4B, respectively. Increasing $<\Phi_v>$ to 7.0×10^{-5}, a further reduction to 0.47 was noticed for downward flow case 4C. By replacing particles

65

type I by particles type II and with a further increase of $<\Phi_v>$ to 8.3 x 10^{-5} and 1.7 x 10^{-4}, R_Φ became 0.33 and 0.41 for downward flows cases 4D/4E, respectively.

The ratio of the maximum concentration found in a discrete bin to the mean concentration, $\Phi_{v,\max}/<\Phi_v>$, is 2.92 and 3.17 for downward cases 3A/3B. For downward cases 4A/4B, this ratio became 3.55 and 3.21, respectively. By increasing $<\Phi_v>$ to 7.0×10^{-5}, the ratio increases to 4.15 for 4C. By replacing particles type I by particles type II and with a further increase of $<\Phi_v>$ to 8.3 x 10^{-5} and 1.7 x 10^{-4}, the ratio increases to 4.5 and 5.8 for cases 4D/4E, respectively.

A summary of the results for concentration profiles and the values of the proposed ratios to characterize the present experiments are shown in Table 3.4. Information about the bundle flow straighteners I and II and about particles P-I and P-II is found in Section 3.2 for case of reference.

Table 3.4 Results of the inertia particle concentrations for the present experiments

Case	Inertial particles	Flow Direction	Flow Straightener	d_p/R $\times10^{-3}$	$<\Phi_v>\times$ 10^{-5}	R_Φ*	$\dfrac{\Phi_{v,\max}}{<\Phi_v>}$	$r_{\max}/R$
1A	Type I	Upward	Bundle I	16.0	0.5	1.72	1.51	~ 0
1B	Type I	Upward	Bundle I	16.0	1.4	1.75	1.42	~ 0
1C	Type I	Upward	Bundle I	16.0	3.2	1.65	1.25	~ 0
2A	Type I	Upward	--	16.0	1.9	1.97	1.74	~ 0
2B	Type I	Upward	--	16.0	3.2	1.92	1.81	~ 0
3A	Type I	Downward	--	16.0	1.0	1.10	2.92	~ 0.98
3B	Type I	Downward	--	16.0	2.3	1.17	3.17	~ 0.98
4A	Type I	Downward	Bundle II	16.0	1.8	0.75	3.55	~ 0.98
4B	Type I	Downward	Bundle II	16.0	2.8	0.81	3.21	~ 0.98
4C	Type I	Downward	Bundle II	16.0	7.0	0.47	4.15	~ 0.98
4D	Type II	Downward	Bundle II	19.2	8.3	0.33	4.58	~ 0.98
4E	Type II	Downward	Bundle II	19.2	17.0	0.41	5.80	~ 0.98

* R_Φ is defined as: $<\Phi_v>_{(0<r/R<0.8)}/<\Phi_v>_{(0.8<r/R<1)}$

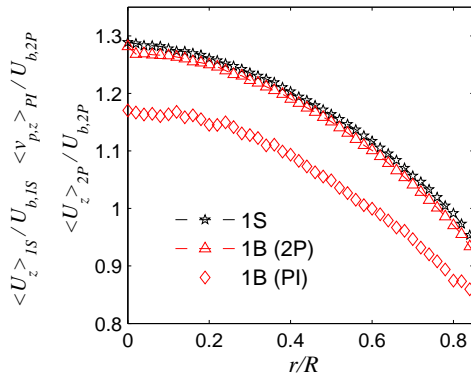### 3.6.3   Mean axial velocity profiles

Inertia particle and tracer trajectories have been registered by 3D-PTV in a camera frame rate of 50 Hz. The differentiation of particle trajectories in time generates on average 2 x 10^6 velocity vectors for tracers and 3 x 10^5 for inertia particles in each particle-laden case. The velocity vectors are ensemble-averaged in distinct radial bands, which are

delimited by a discrete width of $\pm \Delta r = 0.5$ mm around a chosen radius, see Oliveira *et al.*[20] and section 3.4 above.

The effects of upward or downward flow direction, presence or absence of flow straightener and mean concentration on the mean axial velocity profiles of fluid, $<U_z>$, and inertia particles, $<v_{p,z}>$, are presented in Fig.'s 3.11 – 3.16. The flow bulk velocity, U_b, was adjusted to keep the same Re_b for each experiment, 10300. Inertia particle and tracer velocity profiles are normalized in these figures by the corresponding U_b. In each plot, the reference single-phase velocity profile is also shown. Tests with a different set of inertia particles are performed in cases 4D/4E. Error-bars with sizes comparable to the dimensions of symbols shown in Fig.'s 3.11 – 3.16 are computed by the standard error, Eq. (3.10), in 95% confidence intervals. These errors could therefore not be indicated separately in these figures.

To check the fluid mean axial velocity profiles of particle-laden cases, the following procedure was followed. For each fluid flow profile, the product of the fluid mean axial velocity and the area of each discrete bin, $(<U_z>)_k \times A_k$, was integrated to obtain the mean volumetric flow rate, Q, which crossed the measurement volume. Temperature measurements yielded the water mass density, ρ. The product $\rho \times Q$ gave the mass flow rate for each experimental set, which corresponded to the ones given by the Coriolis meter within its inaccuracy range. The mass flow rate is measured by means of a Micro Motion Elite CMF300 Coriolis mass flow and mass density meter, whose inaccuracy is less than 0.5% of the registered flow rate.

In Fig. 3.11, the mean axial velocity profiles of inertia particles and tracers for case 1B are presented. Results for cases 1A/1C are similar. No significant changes in the axial velocity profiles are noticed when the mean volumetric concentration, $<\Phi_v>$, is varied from 0.5×10^{-5} to 3.2×10^{-5} in upward flows in the presence of flow straightener I. Similarity in particle-laden results is also found between cases 2A and 2B. No significant changes in the axial velocity profiles are noticed when the mean $<\Phi_v>$ is varied from 1.9×10^{-5} to 3.2×10^{-5} in upward flows in the absence of flow straightener.
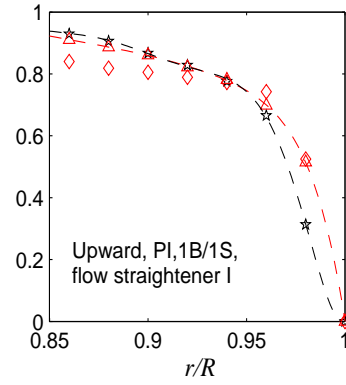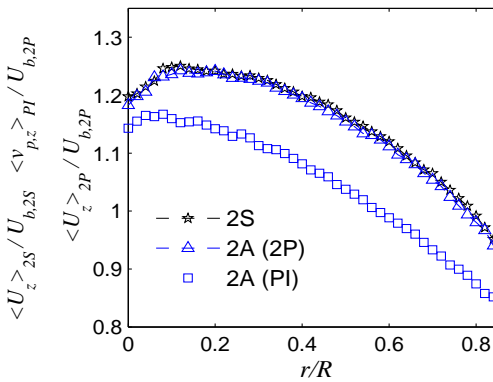
3.11a 3.11b

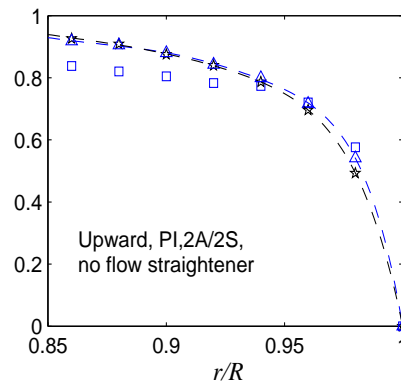**Figure 3.11** Mean axial velocity profiles, $<U_z>$ and $<v_{p,z}>$, for particle-laden case 1B. The velocities are normalized by the bulk velocity of each flow, U_b. The subscript 1S denotes single-phase flow, and 2P and PI, tracers and inertia particles type I in two-phase flow. In case 1B, $<\Phi_v>$ is 1.4×10^{-5}. Dashed lines are added to guide the eye. Error-bars have same sizes as symbols. Figure 3.11a presents velocity profiles in the range $0 <r/R< 0.85$ and Fig. 3.11b, in the range $0.85 <r/R< 1$. The number of line markers corresponds to the number of bins measured; notice the difference in scales.

3.12a 3.12b

Figure 3.12 Mean axial velocity profiles, $<U_z>$ and $<v_{p,z}>$, for particle-laden case 2A. The velocities are normalized by the bulk velocity of each flow, U_b. The subscript 2S denotes single-phase flow, and 2P and PI, tracers and inertia particles type I in two-phase flow. In case 2A, $<\Phi_v>$ is 1.9×10^{-5}. Dashed lines are added to guide the eye. Error-bars have same sizes as symbols. Figure 3.12a presents velocity profiles in the range $0 <r/R< 0.85$ and Fig. 3.12b, in the range $0.85 <r/R< 1$.The number of line markers corresponds to the number of bins measured; notice the difference in scales.

Comparison of mean axial fluid velocities for single-phase and two-phase flows, cases 1S and 1B, indicates a slight reduction in the mean flow velocity in the radial range: 0 <r/R< 0.93. This reduction is compensated by an increase in mean fluid velocity in the range 0.93 <r/R< 1. Upflow cases 2A and 2S also present similar changes in the mean flow velocity profiles as observed for upflow cases 1S and 1B.

For case 1B, the mean relative velocity between particles and fluid is observed to be about constant from 0 <r/R< 0.6, roughly 10 mm/s, and decreases for r/R > 0.6. For r/R > 0.90, the mean flow and particle velocities are roughly equal; see Fig. 3.11b. For case 2A, the mean relative velocity is observed to be about constant from 0.3 <r/R< 0.7, about 10 mm/s. The mean relative velocity difference is reduced for r/R< 0.3 and r/R>0.7. For r/R > 0.95, the mean flow and particle velocities are almost equal. By observing cases 1B and 2A, mean particle velocities in the absence of the flow straightener I approached the fluid mean ones in a bigger part of the flow section, i.e. for r/R< 0.3 and r/R > 0.7; see Fig.'s 3.12a and 3.12b. In contrast to case 2A, the mean relative velocity for case 1B is roughly 10 mm/s for r/R< 0.3.

We now proceed with the description of downflow velocity profiles with <Φ_v> less than 2.8x10^{-5}, cases 3A/3B and 4A/4B.
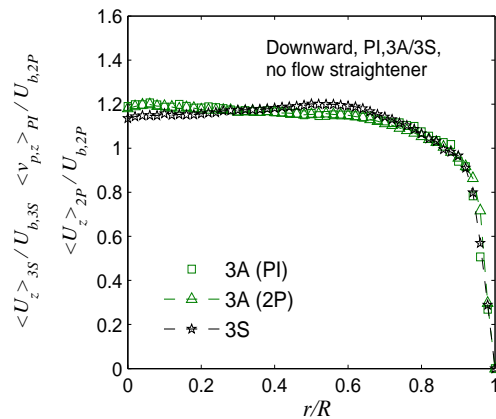
Figure 3.13 Mean axial velocity profiles, <U_z> and <$v_{p,z}$>, for particle-laden case 3A. The velocities are normalized by the bulk velocity of each flow, U_b. The subscript 3S denotes single-phase flow, and 2P and PI, tracers and inertia particles type I in two-phase flow. In case 3A, <Φ_v> is 1.0×10^{-5}. Dashed lines are added to guide the eye. Error-bars have same sizes as symbols.

3.14a   3.14b
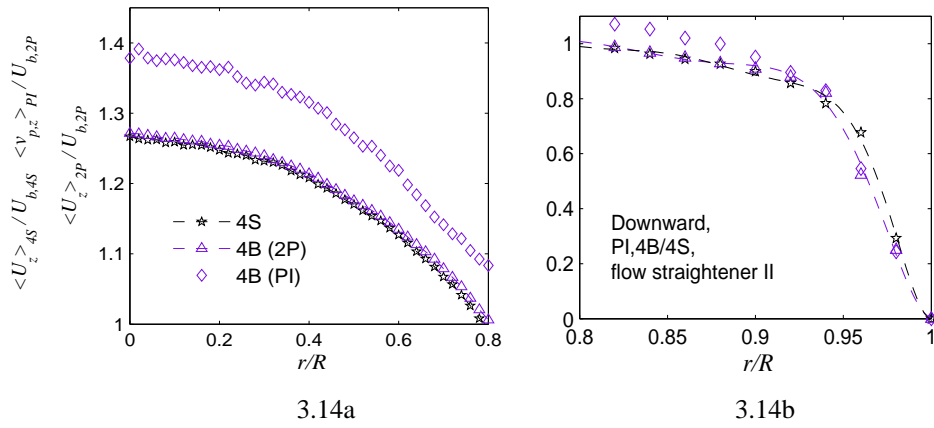
Figure 3.14 Mean axial velocity profiles, $<U_z>$ and $<v_{p,z}>$, for particle-laden case 4B. The velocities are normalized by the bulk velocity of each flow, U_b. The subscript 4S denotes single-phase flow, and 2P and PI, tracers and inertia particles type I in two-phase flow. In case 4B, $<\Phi_v>$ is 2.8×10^{-5}. Dashed lines are added to guide the eye. Error-bars have same sizes as symbols. Figure 3.14a presents velocity profiles in the range $0 < r/R < 0.80$ and Fig. 3.14b, in the range $0.80 < r/R < 1$. The number of line markers corresponds to the number of bins measured; notice the difference in scales.

In Fig. 3.13, the mean axial velocity profiles of inertia particles and tracers for case 3A are presented. Results for case 3B are similar. No significant changes in the axial velocity profiles are noticed when the mean volumetric concentration, $<\Phi_v>$, is varied from $1.0\mathrm{x}10^{-5}$ to $2.3\mathrm{x}10^{-5}$ in downward flows in the absence of flow straightener. Similarity in particle-laden results is also found between cases 4A and 4B. No significant changes in the axial velocity profiles are noticed when $<\Phi_v>$ is varied from $1.8\mathrm{x}10^{-5}$ to 2.8×10^{-5} in downward flows in the presence of the flow straightener II. However, changes take place for the mean axial velocity profiles of inertia particles and tracers for cases 4C/4D/4E. If the mean concentration of inertia particles, $<\Phi_v>$, exceeds $7.0\mathrm{x}10^{-5}$, the profiles of $<U_z>$ and $<v_{p,z}>$ for tracers and inertia particles are profoundly different from cases 4A/4B at lower $<\Phi_v>$.

For case 3A, there is a significant change in the mean fluid velocity profile compared to the single-phase reference flow, case 3S, in the radial range: $0 < r/R < 0.8$. For the same radial range, the profiles of $<U_z>$ and $<v_{p,z}>$ for tracers and inertia particles in case 3A are almost constant. For $r/R > 0.8$, there is good agreement between mean fluid velocities for 3A and 3S. The difference between particle and fluid mean velocities is almost zero along

70

the measurement section for particle-laden downward flows in the absence of the flow straightener II.

In contrast to cases 3A and 3S, good agreement between the fluid mean velocities of the single-phase and two-phase flows is observed for cases 4B and 4S in the presence of the flow straightener II. Comparison of mean axial fluid velocities for single-phase and two-phase flows, cases 4S and 4B, indicates a slight increase in flow velocity in the radial range: $0 < r/R < 0.93$. This increase is compensated by a reduction in fluid velocity in the range $0.93 < r/R < 1$, see Fig. 3.14b.

Mean particle velocities increased for cases 4A/4B in comparison to cases 3A/3B. The mean relative velocity between particles and fluid is observed to be about constant from $0 < r/R < 0.4$, roughly 10 mm/s, and decreases for $r/R > 0.4$. For $r/R > 0.9$, the mean flow and particle velocities are roughly equal.

We now proceed with the description of downflow velocity profiles with $<\Phi_v>$ exceeding 7.0×10^{-5}, cases 4C/4D/4E.
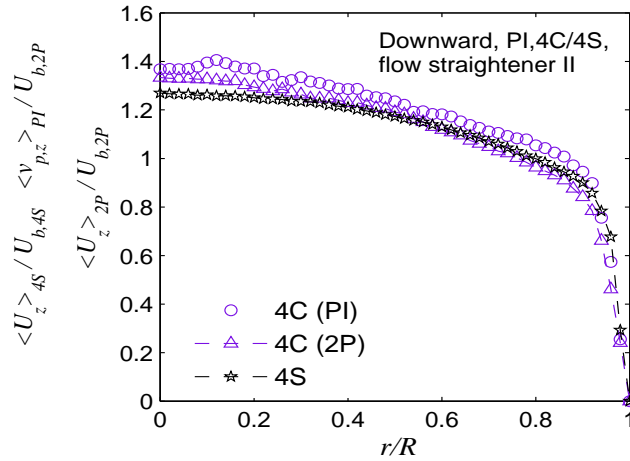
Figure 3.15 Mean axial velocity profiles, $<U_z>$ and $<v_{p,z}>$, for particle-laden case 4C. The velocities are normalized by the bulk velocity of each flow, U_b. The subscript 4S denotes single-phase flow, and 2P and PI, tracers and inertia particles type I in two-phase flow. In case 4C, the $<\Phi_v>$ is 7.0×10^{-5}. Dashed lines are added to guide the eye. Error-bars have same sizes as symbols.
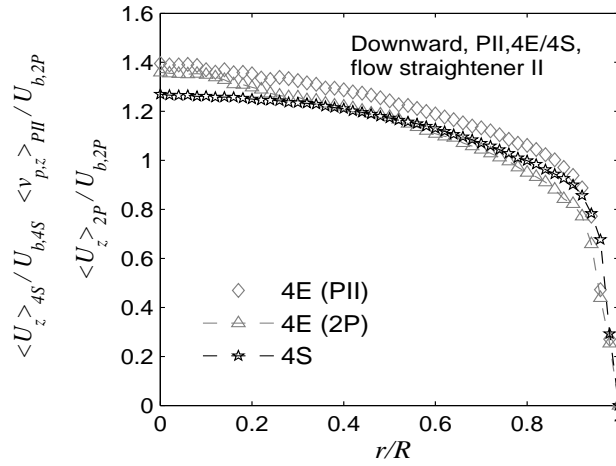
Figure 3.16 Mean axial velocity profiles, $<U_z>$ and $<v_{p,z}>$, for particle-laden case 4E. The velocities are normalized by the bulk velocity of each flow, U_b. The subscript 4S denotes single-phase flow, and 2P and PII, tracers and inertia particles type II in two-phase flow. In case 4E, $<\Phi_v>$ is 1.7×10^{-4}. Dashed lines are added to guide the eye. Error-bars have same sizes as symbols.

In Fig. 3.15, the mean axial velocity profiles of inertia particles and tracers for case 4C are presented. As mentioned, changes on the profiles of $<U_z>$ and $<v_{p,z}>$ are observed for fluid and particles when the mean concentration, $<\Phi_v>$, exceeds 7.0×10^{-5} in downward flows in the presence of the flow straightener II. For case 4C, there is significant change in fluid velocity profile in comparison to case 4S. The fluid velocity is reduced in the radial range: $0.6 <r/R< 1$. This reduction is compensated by an increase in fluid velocity in the range $0 <r/R< 0.6$. The mean fluid velocity in case 4C is roughly equal to the particle mean velocity for $r/R > 0.9$.

In Fig. 3.16, the mean axial velocity profiles of inertia particles and tracers for case 4E are presented. Results for case 4D are similar. No significant changes on the axial velocity profiles are noticed when the mean concentration, $<\Phi_v>$, is varied from 8.3×10^{-5} to 1.7×10^{-4} in downward flows in the presence of the flow straightener II. Results resemble the profiles of case 4C and are in contrast to cases 4A and 4B. In the presence of particles with bigger diameter ($St = 3.3$), the mean velocity difference between inertia particles and tracers was enhanced on average for cases 4D/4E in comparison to case 4C.

The difference between particle and fluid velocities is almost zero at the pipe centerline; see Fig. 3.16. It increases from 0 at $r/R = 0$ to 12 mm/s at $r/R = 0.85$. For $r/R > 0.85$, the difference in velocity is reduced. For $r/R > 0.95$, the mean flow and particle velocities are roughly equal.

Comparison of mean axial fluid velocities for single-phase and two-phase flows, cases 4S and 4E indicates a reduction in flow velocity in the radial range: $0.55 < r/R < 1$. This reduction is compensated by an increase in fluid velocity in the range $0 < r/R < 0.55$.

3.6.4 Mean square value of velocity fluctuations for fluid and dispersed phase

The Mean Square Value (MSV) velocity is defined as the product of mean velocity fluctuations. Here, the following notations are applied to the MSV of fluid, $<u_h u_q>$, and of inertia particles, $<v_{p'h} v_{p'q}>$. Subscripts h and q represent cylindrical coordinates (r, θ, z). The effects of upward or downward flow direction, presence or absence of flow straightener and mean concentration on the MSV of the fluctuating velocity for fluid and dispersed phase $(St = 2.3)$ are presented in Fig.'s 3.18 – 3.22. Tests with a second set of inertia particles $(St = 3.3)$ are shown in Fig. 3.23. A cylindrical coordinate system with origin at the pipe centerline and with the axial axis anti-parallel to the gravitational acceleration is assumed for down- and upward flows; see Fig. 3.17.
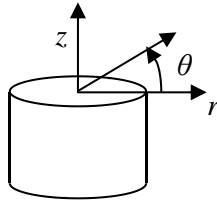
Figure 3.17 Cylindrical coordinate system for up- and downward flows. The origin is at the pipe centerline and the axial axis is anti-parallel to the gravitational acceleration.

Inertia particle and tracer MSV velocity profiles are normalized by the square of the bulk flow velocity, U_b^2, of the corresponding experiment. Here, U_b is chosen for normalization, since it was set at each experiment to keep the same Re_b, 10300. In each plot, the reference single-phase MSV velocity profiles are also shown. Error-bars are computed by the standard error, Eq. (3.10), in 95% confidence intervals.

In Fig.'s 3.18a and 3.18b, inertia particle and tracer MSV velocity profiles are presented for the case 1B. For isotropic flows, the MSV cross-components are zero. In

73

inhomogeneous fully developed pipe flows, the only decoupled direction is the tangential one, which means that correlations like, e.g., $<u_\theta \, u_r>$ and $<u_\theta u_z>$, are zero. The nonzero cross-components of $<u_h u_q>$ and $<v_p'_h \, v_p'_q>$ are $<u_r u_z>$ and $<v_p'_r \, v_p'_z>$ which are presented in Fig. 3.18b.

In Oliveira *et al.*[20], the MSV velocity profiles, $<u_r^2>$, $<u_z^2>$, $<u_\theta^2>$ and $<u_r u_z>$, of case 1S have been compared to the DNS results of Veenman.[15] For all MSV plots, the 3D-PTV data of case 1S presented good agreement with DNS within measurement error. MSV of radial and tangential velocity components are smaller than the axial one. While at the center of the tube (r/R<0.2) turbulence is nearly homogeneous, highly inhomogeneous behavior is seen closer to the wall area (0.8<r/R<1).

Good agreement is found for the fluid MSV velocity profiles for cases 1S/1B. Results for cases 1A/1C are similar. For fully developed particle-laden pipe flows in upward direction and in the presence of particles type I with $<\Phi_v>$ less than 3.2×10^{-5}, the turbulence is barely modified.

The dispersed phase MSV velocity profiles for radial and tangential components, $<v_p'_r^2>$ and $<v_p'_\theta^2>$, have similar behavior to the fluid profiles. For a given radial position, a fluid value of $<u_r^2>$ or $<u_\theta^2>$ is found inside the error range of a dispersed phase fluctuation value in a 95% confidence interval.
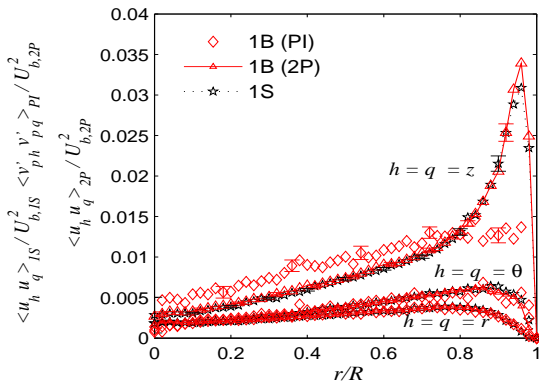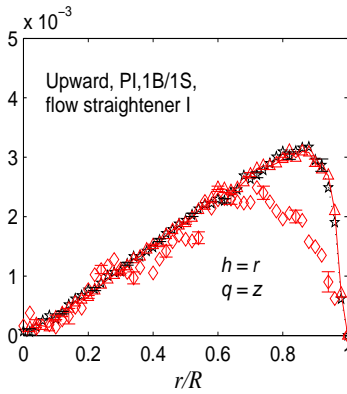
3.18a   3.18b

Figure 3.18 Normal (a) and cross-component (b) MSV velocity profiles, $<u_h u_q>$ and $<v_p'_h v_p'_q>$, for particle-laden case 1B. The MSV velocities are normalized by the square of the bulk velocity of each flow, U_b^2. The subscript 1S denotes single-phase flow, and 2P and PI, tracers and inertia particles type I in two-phase flow. In case 1B, $<\Phi_v>$, is 1.4×10^{-5}. Dotted and solid lines are added to guide the eye.

For comparing MSV experimental results, the fluctuation values are weighed with the area of the corresponding bin in order to get proper averages. This averaging procedure is adopted through this whole section. The dispersed phase MSV velocity profiles for the axial and cross-components, $<v_{p}'_{z}^{2}>$ and $<v_{p}'_{r}v_{p}'_{z}>$, differ from those of the fluid profiles. For the radial range $r/R< 0.8$, inertia particles values of $<v_{p}'_{z}^{2}>$ exceed on average 24 % the fluid ones. In the cross-component profiles, $<v_{p}'_{r}v_{p}'_{z}>$ and $<u_{r}u_{z}>$, particles and fluid have similar results only in the range $0 < r/R < 0.6$. For the radial range $0.6 < r/R < 1$, inertia particles values of $<v_{p}'_{r}v_{p}'_{z}>$ are smaller than the fluid ones.

In Fig. 3.19, the MSV velocity profiles of fluid and dispersed phase are presented for case 2A. The fluid MSV velocity profiles for case 1B are added to show the differences with the fully developed condition (the same procedure is adopted for the results of other developing particle-laden flows). Results for case 2B are similar. No significant changes in the MSV velocity profiles of fluid and inertia particles are noticed when the mean concentration, $<\Phi_{v}>$, is varied from 1.9×10^{-5} to 3.2×10^{-5} in upward flows in the absence of the flow straightener I. The fluid MSV velocity profiles of all components, $<u_{r}^{2}>$, $<u_{z}^{2}>$, $<u_{\theta}^{2}>$ and $<u_{r}u_{z}>$ for cases 2A/2B are similar to the single-phase flow, case 2S, in the presence of the inertial particles for the given concentrations.

In comparison to the fluid behavior in case 1B, the fluid profiles of $<u_{r}^{2}>$, $<u_{z}^{2}>$ and $<u_{\theta}^{2}>$ are increased for case 2B, particularly for $r/R < 0.4$. There, $<u_{r}^{2}>$, $<u_{z}^{2}>$ and $<u_{\theta}^{2}>$ are on average 23, 53 and 21 % bigger. Fluid profiles of the cross-component, $<u_{r}u_{z}>$, were similar in cases 2A/2S/1B; see Fig. 3.19c.

The dispersed phase MSV velocity profiles for radial and tangential components, $<v_{p}'_{r}^{2}>$ and $<v_{p}'_{\theta}^{2}>$, present similar behavior as the fluid profiles in cases 2A/2B. However, the dispersed phase axial and cross-components, $<v_{p}'_{z}^{2}>$ and $<v_{p}'_{r}v_{p}'_{z}>$, in cases 2A/2B, differ from those of the fluid profiles. Inertia particles values of $<v_{p}'_{z}^{2}>$, case 2A, are for the radial range $r/R< 0.4$ on average 22 % smaller than the fluid ones. In the cross-component profiles of $<v_{p}'_{r}v_{p}'_{z}>$ and $<u_{r}u_{z}>$, particles and fluid have similar values only in the range $0 < r/R < 0.55$. Inertia particles values of $<v_{p}'_{r}v_{p}'_{z}>$ are on average 23 % smaller there than the fluid ones.

For the whole category of particle-laden developing flows, values of cross-components including the tangential direction, $<u_{\theta} u_{r}>$, $<u_{\theta} u_{z}>$, $<v_{p}'_{\theta} v_{p}'_{r}>$ and $<v_{p}'_{\theta} v_{p}'_{z}>$, have been checked. They are close to zero and therefore are not shown.
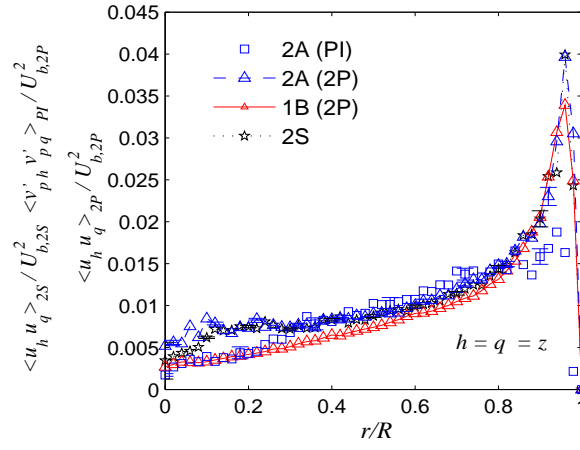
3.19a
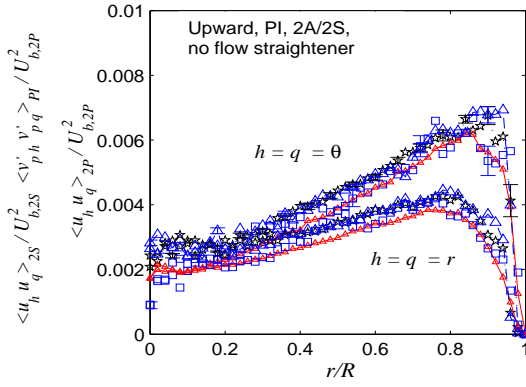
3.19b
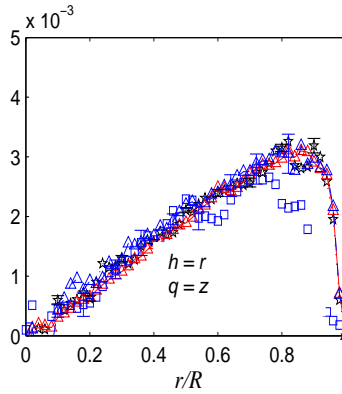
3.19c

Figure 3.19 Effect of different stages of development on the axial (a), radial and tangential (b), and cross-component (c) MSV velocity profiles, $<u_h u_q>$ and $<v_p'_h v_p'_q>$, for particle-laden case 2A. The MSV velocities are normalized by the square of the bulk velocity of each flow, U_b^2. The subscript 2S denotes single-phase flow, and 2P and PI, tracers and inertia particles type I in two-phase flow. In case 2A, $<\Phi_v>$ is 1.9×10^{-5}. Dotted, dashed and solid lines are added to guide the eye.

In Fig. 3.20, the MSV velocity profiles of fluid and dispersed phase are presented for case 3A. Results for case 3B are similar. No significant changes in the MSV velocity profiles of fluid and inertia particles are noticed when the mean concentration, $<\Phi_v>$, is varied from 1.0×10^{-5} to 2.3×10^{-5} in downward flows in the absence of the flow straightener II.

The fluid MSV velocity profiles of all components, $<u_r^2>$, $<u_z^2>$, $<u_\theta^2>$ and $<u_r u_z>$, for cases 3A/3B are modified in comparison with the single-phase flow, case 3S, in the presence of inertial particles for the given concentrations. Particularly at the pipe core ($0 < r/R < 0.6$), values of the fluid MSV, $<u_r^2>$, $<u_z^2>$, $<u_\theta^2>$ and $|<u_r u_z>|$, are increased by 23, 37, 24 and 20 %, respectively, for case 3A. The discrepancies with the fluctuation levels of a fully developed flow are increased in the presence of inertia particles; see the fluid MSV profiles of cases 1B/3A/3S in Fig. 3.20.

The dispersed phase MSV velocity profiles for radial and tangential components, $<v_p{'}_r^2>$ and $<v_p{'}_\theta^2>$, are similar to the fluid ones in case 3A. However, the dispersed phase axial and cross-components, $<v_p{'}_z^2>$ and $<v_p{'}_r v_p{'}_z>$, in case 3A, differ from those of the fluid profiles. For the radial range $0.4 < r/R < 1$, inertia particle values of $<v_p{'}_z^2>$, case 3A, exceed on average 14 % the fluid ones. In the cross-component profiles, inertia particle values of $|<v_p{'}_r v_p{'}_z>|$ are on average 24 % bigger in the range $0.2 < r/R < 0.8$.

3.20a

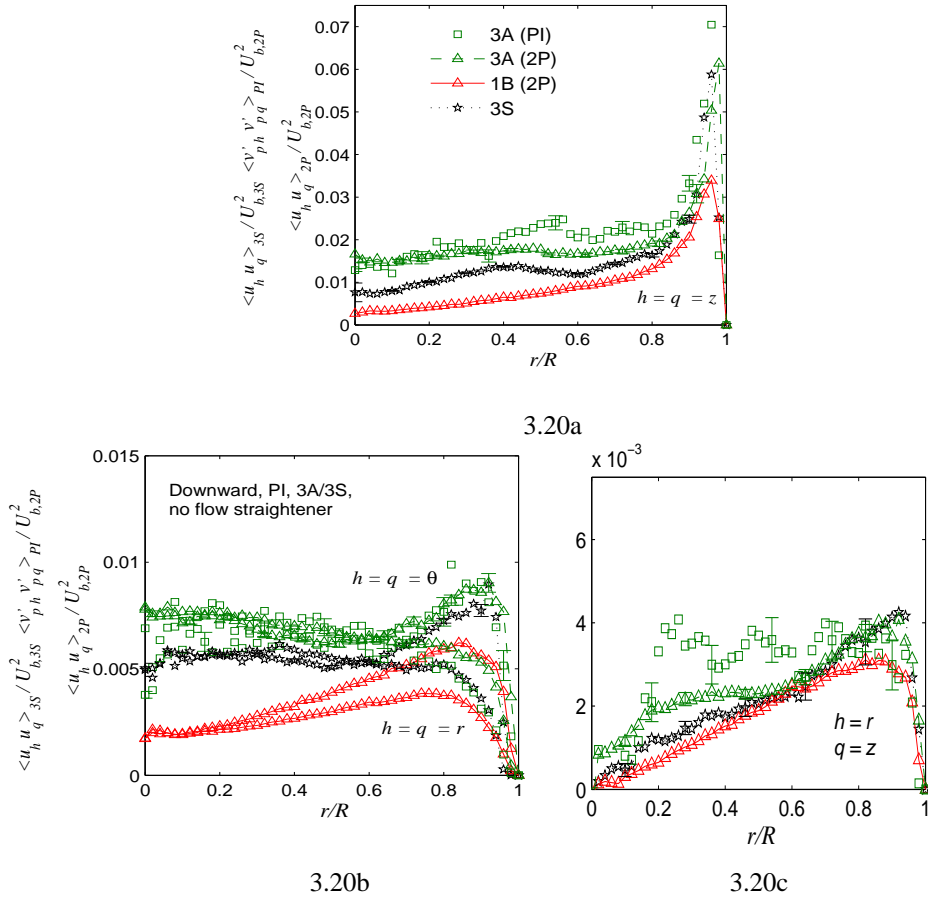3.20b   3.20c

Figure 3.20 Effect of different stages of development on the axial (a), radial and tangential (b), and cross-component (c) MSV velocity profiles, $\langle u_h u_q \rangle$ and $\langle v'_{p'h} v'_{p'q} \rangle$, for particle-laden case 3A. The MSV velocities are normalized by the square of the bulk velocity of each flow, U_b^2. The subscript 3S denotes single-phase flow, and 2P and PI, tracers and inertia particles type I in two-phase flow. In case 3A, the mean volumetric concentration, $\langle \Phi_v \rangle$, is 1.0×10^{-5}. Dotted, dashed and solid lines are added to guide the eye.

In Fig. 3.21, the MSV velocity profiles of fluid and dispersed phase are presented for case 4B. Results for case 4A are similar. No significant changes in the MSV velocity profiles of fluid and inertia particles are noticed when the mean concentration, $\langle \Phi_v \rangle$, is varied from 1.8×10^{-5} to 2.8×10^{-5} in downward flows in the presence of flow straightener II.

The fluid MSV velocity profiles of all components, $\langle u_r^2 \rangle$, $\langle u_z^2 \rangle$, $\langle u_\theta^2 \rangle$ and $\langle u_r u_z \rangle$, for cases 4A/4B are similar to the single-phase flow, case 4S, in the presence of inertial

particles for the given concentrations. The discrepancies with the fluctuation levels of a fully developed flow is particularly pronounced for the radial range 0.5 <*r/R*< 0.9; compare fluid MSV profiles of cases 4B/4S to the ones of case 1B in Fig. 3.21.

3.21a

3.21b

3.21c

Figure 3.21 Effect of different stages of development on the axial (a), radial and tangential (b), and cross-component (c) MSV velocity profiles, $<u_h u_q>$ and $<v_{p'h} v_{p'q}>$, for particle-laden case 4B. The MSV velocities are normalized by the square of the bulk velocity of each flow, U_b^2. The subscript 4S denotes single-phase flow, and 2P and PI, tracers and inertia particles type I in two-phase flow. In case 4B, the mean volumetric concentration, $<\Phi_v>$, is 2.8×10^{-5}. Dotted, dashed and solid lines are added to guide the eye.

The dispersed phase MSV velocity profiles for radial and tangential components, $<v_{p'r}^2>$ and $<v_{p'\theta}^2>$, are similar to the fluid ones in cases 4A/4B. However, the dispersed

phase axial and cross-components, $<v_{p'z}^2>$ and $<v_{p'r}v_{p'z}>$, in cases 4A/4B, differ from those of the fluid profiles. For the radial range $0.4 < r/R < 0.8$, inertia particle values of $<v_{p'z}^2>$, case 4B, exceed on average 17 % the fluid ones. In the cross-component profiles, inertia particle values of $|<v_{p'r}v_{p'z}>|$ are on average 23 % bigger in the range $0.2 < r/R < 0.8$.

In Fig. 3.22, the MSV velocity profiles of fluid and dispersed phase are presented for case 4C.

3.22a

3.22b

3.22c

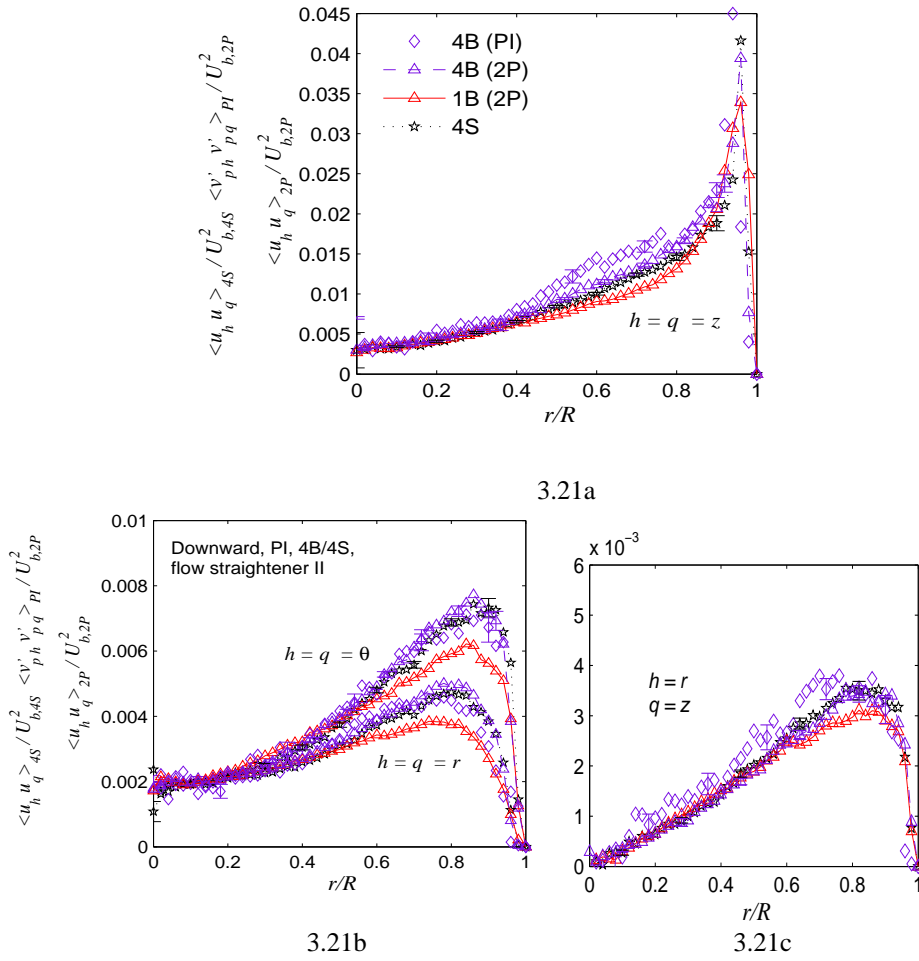**Figure 3.22** Effects of the mean volumetric concentration, $<\Phi_v>$, and different stages of development on the axial (a), radial and tangential (b), and cross-component (c) MSV velocity profiles, $<u_h u_q>$ and $<v_{p'h}v_{p'q}>$, for particle-laden case 4C. The MSV velocities are normalized by the square of the bulk velocity of each flow, U_b^2. The subscript 4S denotes single-phase flow, and 2P and PI, tracers and inertia particles type I in two-phase flow. In case 4C, $<\Phi_v>$ is 7.0×10^{-5}. Dotted, dashed and solid lines are added to guide the eye.

Results differ from cases 4A/4B. Significant changes are observed to the MSV velocity profiles of fluid and inertia particles when the mean concentration, $<\Phi_v>$, exceeds $7.0\mathrm{x}10^{-5}$ in downward flows in the presence of the flow straightener II; compare results of case 4B in Fig. 3.21 to results of case 4C in Fig. 3.22.

The fluid MSV velocity profiles of components, $<u_z^2>$, $<u_\theta^2>$ and $<u_r u_z>$, for case 4C differ from the single-phase flow, case 4S. For the axial component, $<u_z^2>$, an average increase of 30% is observed for all cross-section. For $<u_\theta^2>$ and $|<u_r u_z>|$, a cross-section averaged increase of 8% and 13% are observed. The radial component $<u_r^2>$ is in better agreement to the fluid MSV profile of case 4S. As a consequence, the discrepancies with the fluctuation levels of a fully developed flow is increased; compare fluid MSV profiles of cases 4C to the ones of case 1B in Fig. 3.22.

When $<\Phi_v>$ exceeds 7.0×10^{-5}, changes also take place to the dispersed phase MSV velocity profiles of all components, $<v_{p}'^2_r>$, $<v_{p}'^2_\theta>$, $<v_{p}'^2_z>$ and $<v_p' r v_p' z>$. Differences between inertia particle and fluid MSV profiles of case 4C are increased in comparison with those of case 4B; compare Fig. 3.21 to Fig. 3.22.

In Fig. 3.23, the MSV velocity profiles of fluid and dispersed phase are presented for case 4E. Results are similar to case 4D. No significant changes on the MSV velocity profiles are noticed when the mean concentration, $<\Phi_v>$, is varied from 8.3×10^{-5} to 1.7×10^{-4} in downward flows in the presence of the flow straightener II.

Values for the fluid MSV velocity components of case 4E are increased in comparison to the components of case 4C; compare Fig. 3.22 to Fig. 3.23. In the presence of particles type II and for $<\Phi_v>$ exceeding 8.3×10^{-5}, fluid MSV components are increased in downward flows in the presence of the flow straightener II.

In comparison to single-phase flow case 4S, the increase in the fluid MSV velocity components of case 4E, $<u_r^2>$, $<u_z^2>$, $<u_\theta^2>$ and $|<u_r u_z>|$, is on average 11, 45, 14 and 20 %, respectively, in the entire cross-section. As a consequence, the discrepancies with the fluctuation levels of a fully developed flow is increased; compare fluid MSV profiles of cases 4E to the ones of case 1B in Fig. 3.23.

3.23a

3.23b

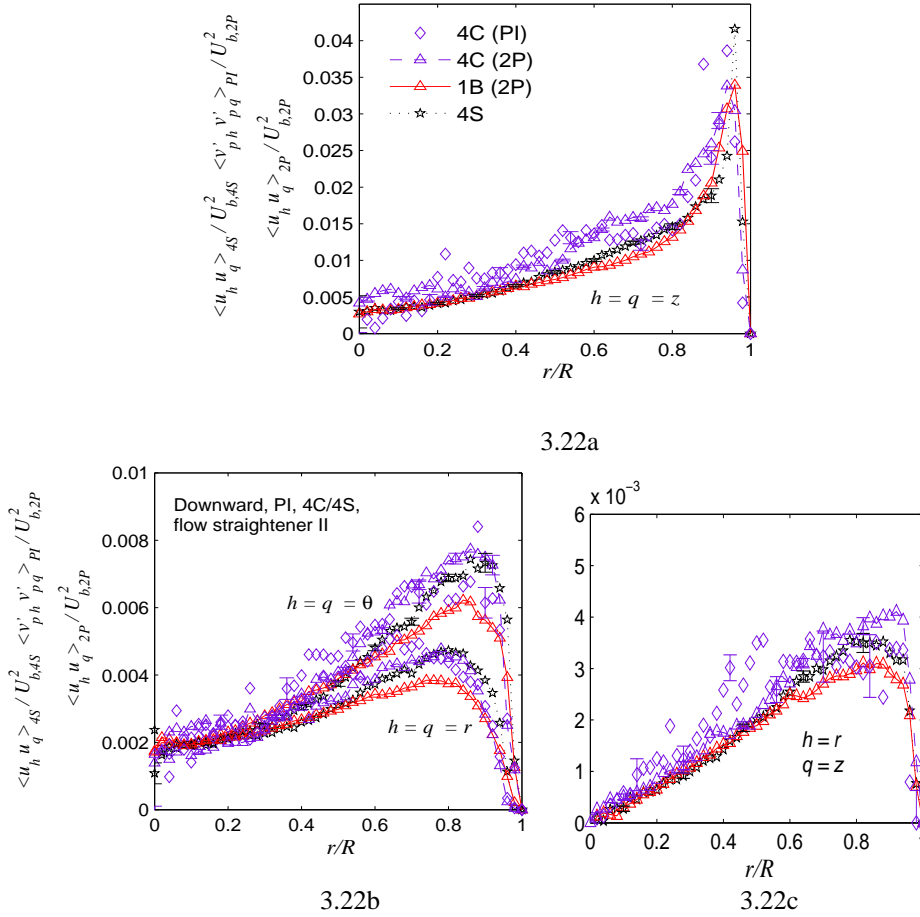
3.23c
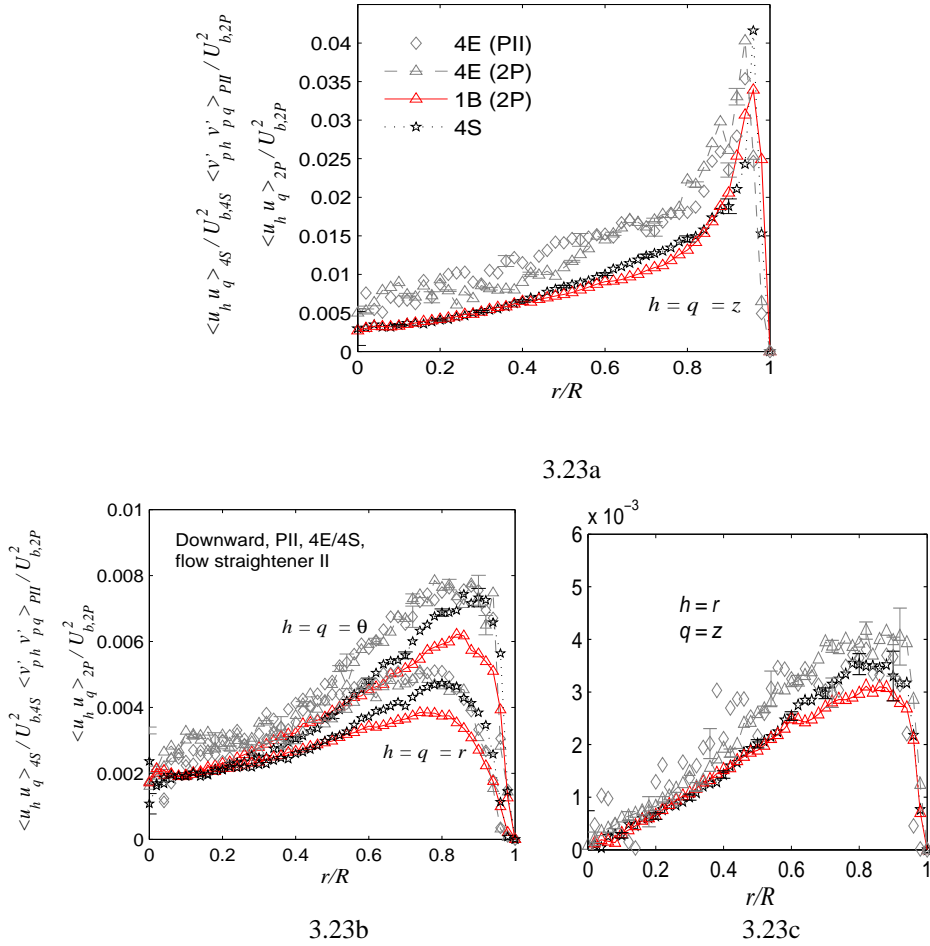
Figure 3.23 Effects of the mean volumetric concentration, $<\Phi_v>$, and different stages of development on the axial (a), radial and tangential (b), and cross-component (c) MSV velocity profiles, $<u_h u_q>$ and $<v'_{ph} v'_{pq}>$, for particle-laden case 4E. The MSV velocities are normalized by the square of the bulk velocity of each flow, U_b^2. The subscript 4S denotes single-phase flow, and 2P and PII, tracers and inertia particles type II in two-phase flow. In case 4E, $<\Phi_v>$ is 1.7×10^{-4}. Dotted, dashed and solid lines are added to guide the eye.

A summary of the MSV velocity results presented in Fig.'s 3.18 – 3.23 is found in Tables 3.5 – 3.7. In Table 3.5, cross-section averaged fluid turbulence ratios of present particle-laden flows to the corresponding single-phase references (cases 1S, 2S, 3S, 4S) are shown. The ratios are computed for all significant MSV velocity components, $<u_r^2>$, $<u_z^2>$, $<u_\theta^2>$ and $<u_r u_z>$, and for the sum of components: $<u^2> = <u_r^2> + <u_z^2> + <u_\theta^2>$. The MSV

velocities are normalized by the square of the bulk velocity of each flow, U_b^2. The cross-section averaging computation for the axial MSV component is performed according to Eq. (3.14); the overbar indicates cross-section average:

$$\overline{<u_z^2>} = (_0\!\!\int^R <u_z^2>2\pi r\, dr)/(\pi R^2) \tag{3.14}$$

Table 3.5 Cross-section averaged fluid turbulence ratios of present particle-laden flows to the corresponding single-phase references (cases 1S, 2S, 3S, 4S)

Case	1A	1B	1C	2A	2B	3A	3B	4A	4B	4C	4D	4E
$\dfrac{\overline{(<u_z^2>/U_b^2)}_{2P}}{\overline{(<u_z^2>/U_b^2)}_{1P}}$	1.04	1.02	1.05	1.02	1.03	1.17	1.20	1.08	1.09	1.30	1.43	1.45
$\dfrac{\overline{(<u_r^2>/U_b^2)}_{2P}}{\overline{(<u_r^2>/U_b^2)}_{1P}}$	0.99	1.01	1.01	1.03	1.01	1.25	1.24	1.05	1.05	1.01	1.10	1.11
$\dfrac{\overline{(<u_\theta^2>/U_b^2)}_{2P}}{\overline{(<u_\theta^2>/U_b^2)}_{1P}}$	1.01	0.99	1.01	1.02	1.01	1.16	1.15	1.04	1.03	1.08	1.13	1.14
$\dfrac{\overline{(<u^2>/U_b^2)}_{2P}}{\overline{(<u^2>/U_b^2)}_{1P}}$	1.03	1.01	1.04	1.02	1.02	1.18	1.20	1.07	1.08	1.19	1.29	1.31
$\dfrac{\overline{(<u_r u_z>/U_b^2)}_{2P}}{\overline{(<u_r u_z>/U_b^2)}_{1P}}$	1.01	1.01	1.02	1.01	1.02	1.08	1.09	1.01	1.00	1.13	1.19	1.20

Table 3.5 clearly shows how the flow turbulence is modified by the presence of inertia particles at the given concentrations and flow conditions. At 45D far from the entrance region, upward particle-laden flows with and without the Bundle flow straightener I experience a minor increase in the MSV velocities. The increase in flow turbulence levels of cases 1A/1B/1C and 2A/2B is about 2 % of the single-phase cross-section averaged values. In these cases, mean concentrations, $<\Phi_v>$, are less than 3.2×10^{-5}.

At 20D from the entrance region and with $<\Phi_v>$ less than 2.3×10^{-5}, downward particle-laden flows without the Bundle flow straightener II experience a significant increase in the MSV velocity components, about 20 %. At 20D far from the entrance region and with $<\Phi_v>$ less than 2.8×10^{-5}, downward particle-laden flows with the Bundle flow straightener II experience a clear increase in the MSV velocity axial component, about 8 %. Remaining components of cases 4A/4B are less affected by the presence of inertia particles.

At 20D from the entrance region and with $<\Phi_v>$ exceeding 7.0×10^{-5}, downward particle-laden flows with the Bundle flow straightener II have significant increase in the

MSV velocity axial component, about 30 % for case 4C and 44 % for cases 4D/4E. The remaining components of cases 4C/4D/4E are also affected, but less. In cases 4D/4E, inertia particles type II have been applied.

In Table 3.6 the cross-section averaged fluid turbulence ratios of particle-laden flows to the reference flow (case 1B) are presented. This last case 1B represents the fluid turbulence of a fully developed particle-laden flow in a weak two-way coupling. Results for cases 1A/1C are similar to case 1B. The cross-section averaging computation for the MSV components is performed according to Eq. (3.14). The MSV velocities are normalized by the square of the bulk velocity of each flow, U_b^2.

Table 3.6 Cross-section averaged fluid turbulence ratios of present particle-laden flows to the fully developed particle-laden reference (case 1B)

Case	1A	1B	1C	2A	2B	3A	3B	4A	4B	4C	4D	4E
$\dfrac{(\overline{<u_z^2>}/U_b^2)_{2P}}{(<u_z^2>/U_b^2)_{1B}}$	1.02	1	1.03	1.11	1.12	1.67	1.71	1.15	1.16	1.36	1.51	1.53
$\dfrac{(\overline{<u_r^2>}/U_b^2)_{2P}}{(<u_r^2>/U_b^2)_{1B}}$	0.98	1	1.00	1.16	1.14	2.02	2.00	1.21	1.21	1.16	1.26	1.27
$\dfrac{(\overline{<u_\theta^2>}/U_b^2)_{2P}}{(<u_\theta^2>/U_b^2)_{1B}}$	1.02	1	1.02	1.11	1.10	1.57	1.56	1.15	1.14	1.19	1.24	1.25
$\dfrac{(\overline{<u^2>}/U_b^2)_{2P}}{(<u^2>/U_b^2)_{1B}}$	1.02	1	1.03	1.12	1.13	1.70	1.74	1.15	1.16	1.28	1.40	1.42
$\dfrac{(\overline{<u_r u_z>}/U_b^2)_{2P}}{(<u_r u_z>/U_b^2)_{1B}}$	1.00	1	1.01	1.03	1.04	1.28	1.29	1.07	1.06	1.25	1.34	1.35

At 45D from the entrance region, upward particle-laden flows without the Bundle flow straightener I have the fluid MSV velocities about 10 % higher than case 1B. The mean concentrations of cases 2A/2B are of same order of cases 1B/1C. With sufficient development length, fluctuation levels of cases 2A/2B become similar to those of case 1B.

At 20D from the entrance region, downward particle-laden flows without the Bundle flow straightener II have the fluid MSV velocities about 70 % higher than case 1B. At 20D far from the entrance region, downward particle-laden flows with the Bundle flow straightener II have the fluid MSV velocities about 15 % higher than case 1B. The mean concentrations of cases 3A/3B/4A/4B are of same order of cases 1B/1C. With sufficient

development length, fluctuation levels of cases 3A/3B/4A/4B become similar to those of case 1B.

At 20D from the entrance region and with $<\Phi_v>$ exceeding 7.0×10^{-5}, downward particle-laden flows with the Bundle flow straightener II have significant increase in the MSV velocity components. Particularly, the fluid MSV axial component has 30 - 50 % higher levels in comparison to case 1B. For cases 4C/4D/4E, it is possible that the fluid fluctuation levels will differ from case 1B after enough development length to achieve a fully developed condition. It seems that the coupling effect between particles and fluid is increased for $<\Phi_v>$ exceeding 7.0×10^{-5}.

Table 3.7 shows the cross-section averaged deviations of inertia particles and fluid MSV velocity components for the present particle-laden flows. The averaged deviations are computed for all significant components. The cross-section averaging computation of the deviation for the axial MSV component is performed according to Eq. (3.15); the overbar indicates cross-section average:

$$\overline{|<v_p{'}_z^2>-<u_{z,2P}^2>|} = \frac{\int_0^R |<v_p{'}_z^2>-<u_{z,2P}^2>|2\pi r dr}{\pi R^2} \tag{3.15}$$

Table 3.7 Cross-section averaged deviations of inertia particle and fluid MSV velocity components for the present particle-laden flows

Case	1A	1B	1C	2A	2B	3A	3B	4A	4B	4C	4D	4E
$\dfrac{\overline{\|<v_p{'}_z^2>-<u_{z,2P}^2>\|}}{\overline{<u_{z,2P}^2>}}$	0.23	0.24	0.22	0.12	0.11	0.12	0.11	0.13	0.12	0.17	0.12	0.13
$\dfrac{\overline{\|<v_p{'}_r^2>-<u_{r,2P}^2>\|}}{\overline{<u_{r,2P}^2>}}$	0.05	0.04	0.03	0.09	0.08	0.11	0.12	0.07	0.08	0.10	0.07	0.07
$\dfrac{\overline{\|<v_p{'}_\theta^2>-<u_{\theta,2P}^2>\|}}{\overline{<u_{\theta,2P}^2>}}$	0.05	0.06	0.04	0.07	0.08	0.07	0.08	0.06	0.05	0.11	0.07	0.06
$\dfrac{\overline{\|<v_p{'}_r v_p{'}_z>-<u_r u_{z,2P}>\|}}{\overline{\|<u_r u_{z,2P}>\|}}$	0.25	0.26	0.24	0.19	0.18	0.21	0.19	0.20	0.18	0.19	0.17	0.16

With the results of Table 3.7, it is noticed that inertia particle MSV differs from the fluid MSV particularly for the components involving the axial coordinate, $<v_p{'}_z^2>$ and $<v_p{'}_r v_p{'}_z>$. While the deviations in the MSV components, $<v_p{'}_r^2>$ and $<v_p{'}_\theta^2>$, are in general

less than 10 % of the fluid MSV, deviations for $<v_{p}'^2_z>$ and $|<v_p',_r v_p',_z>|$ can be higher than 20 %.

Cases 1A/1B/1C presented the biggest deviations for MSV components, $<v_p'^2_z>$ and $<v_p',_r v_p',_z>$, among all particle-laden experiments. With increasing flow turbulence levels, the cases 2A/2B, 3A/3B and 4A/4C/4B/4E had the mean deviations reduced for MSV components involving the axial direction: $\overline{|<v_p'^2_z>-<u^2_{z,2P}>|}$ and $\overline{|<v_p',_r v_p',_z>-<u_r u_{z,2P}>|}$.

3.6.5   Mean axial relative velocity and flow turbulence

Inspection of Fig.'s 3.11 – 3.16 revealed distinct trends of the mean axial velocity profiles of fluid and particles. As will be shown in this section, the difference between particle and fluid mean velocities in the axial coordinate, $<v_{rel,z}> = <v_{p,z}> - <U_z>$, varies from the terminal velocity, U_{TV}, to roughly zero. Values of U_{TV} for particles type I and II, -10.2 and -13.1 mm/s, respectively, were computed in Section 3.2.2. Assuming a cylindrical coordinate system with origin at the pipe centerline and with the axial axis anti-parallel to the gravitational acceleration, the signs of $<v_{rel,z}>$ and U_{TV} are negative for both upward and downward particle-laden flows.

The relative velocity $<v_{rel,z}>$ is close to U_{TV} in the range $r/R < 0.8$ for particle-laden cases 1A/1B/1C. These two-phase flows were measured in a situation where the corresponding single-phase flow is fully developed, case 1S. In Fig. 3.24, the difference between $<v_{rel,z}>$ and U_{TV} is plotted versus the radial coordinate for the cases mentioned. Error-bars with sizes comparable to the dimensions of symbols shown are computed by the standard error, Eq. (3.10), in 95% confidence intervals.
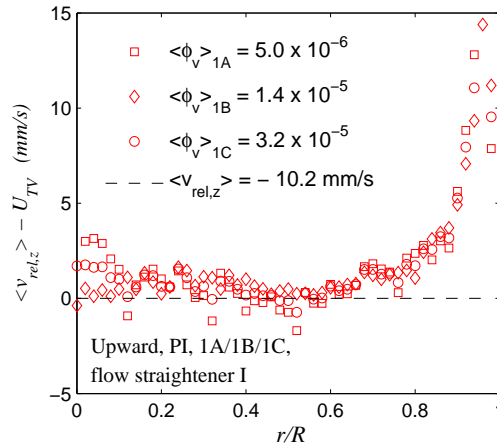
Figure 3.24 Difference between particle and fluid mean velocities in the axial coordinate, $<v_{rel,z}>$, for particle-laden cases 1A/1B/1C. The dashed line represents $U_{TV} = <v_{rel,z}>$. Error-bars have same sizes as symbols. Squares, diamonds and circles represent results of cases 1A, 1B and 1C, respectively.

For $r/R > 0.8$, the approximation $U_{TV} \approx <v_{rel,z}>$ is incorrect. The particle mean axial velocity approaches the fluid mean one with increasing radial distance.

A similar finding as in Fig. 3.24 for the radial range $r/R < 0.8$, namely $U_{TV} \approx <v_{rel,z}>$, was also observed by Suzuki *et al.*[24] who performed particle-laden experiments in a turbulent downward channel flow. In their research, particle-laden results were obtained for fully developed flows. They observed that the velocity difference between the carrier phase and the inertia particles is approximately the terminal velocity. They also observed a reduction of the magnitude of the mean relative axial velocity in the near-wall zone, by about 10 % of U_{TV}.

In the particle-laden cases 2A/2B, 3A/3B and 4A/4B/4C/4D/4E, the equality of the terminal velocity and the mean axial relative velocity, $U_{TV} \approx <v_{rel,z}>$, in the radial range $r/R < 0.8$ is not observed. As seen in Fig.'s 3.25 – 3.28, mean axial velocities of inertia particles approach the fluid ones at some radial positions.

Figure 3.25 Difference between particle and fluid mean velocities in the axial coordinate, $\langle v_{rel,z} \rangle$, for particle-laden cases 2A/2B. The dashed line represents $U_{TV} = \langle v_{rel,z} \rangle$. Error-bars have same sizes of symbols. Squares and diamonds represent results of cases 2A and 2B, respectively.
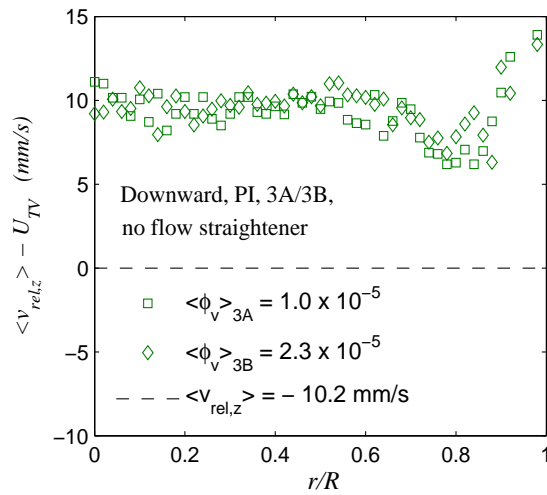
Figure 3.26 Difference between particle and fluid mean velocities in the axial coordinate, $\langle v_{rel,z} \rangle$, for particle-laden cases 3A/3B. The dashed line represents $U_{TV} = \langle v_{rel,z} \rangle$. Error-bars have same sizes of symbols. Squares and diamonds represent results of cases 3A and 3B, respectively.

88
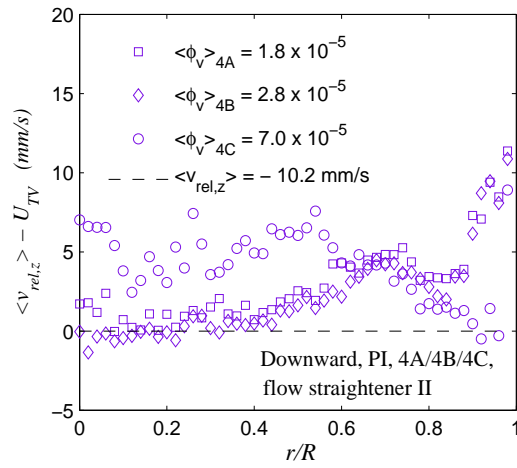
Figure 3.27 Difference between particle and fluid mean velocities in the axial coordinate, $<v_{rel,z}>$, for particle-laden cases 4A/4B/4C. The dashed line represents $U_{TV} = <v_{rel,z}>$. Error-bars have same sizes of symbols. Squares, diamonds and circles represent results of cases 4A, 4B and 4C, respectively.
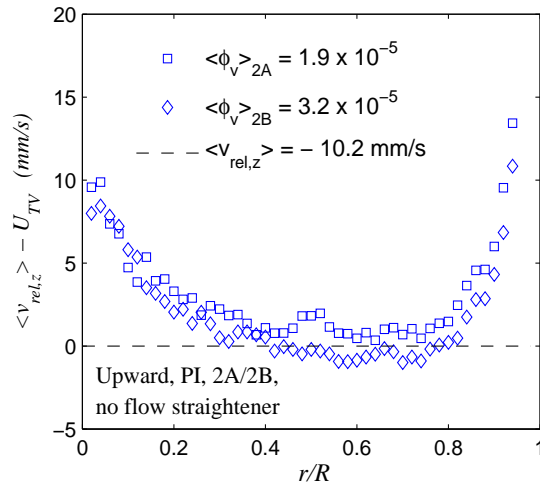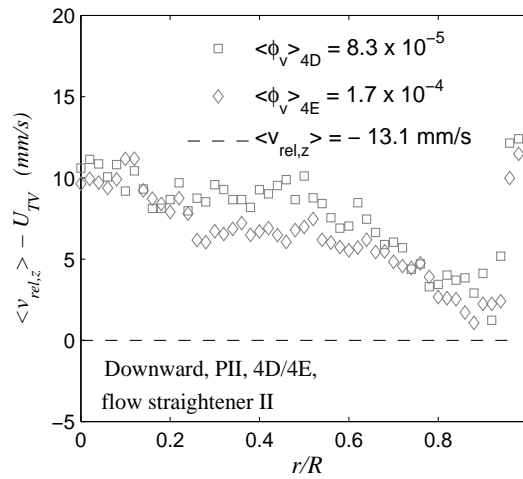

Figure 3.28 Difference between particle and fluid mean velocities in the axial coordinate, $<v_{rel,z}>$, for particle-laden cases 4D/4E. The dashed line represents $U_{TV} = <v_{rel,z}>$. Error-bars have same sizes of symbols. Squares and diamonds represent results of cases 4D and 4E, respectively.

For upward flows without flow straightener, cases 2A and 2B, the mean axial relative velocity approaches the terminal velocity, $U_{TV} \approx \langle v_{rel,z} \rangle$, only in the range $0.4 < r/R < 0.8$. For the radial range $0 < r/R < 0.4$, $|\langle v_{rel,z} \rangle|$ reduces gradually until the mean axial velocity of inertia particles approaches the fluid one in the pipe centerline. For $r/R > 0.8$, the mean particle velocity approaches the mean fluid one with increasing radial distance similar to cases 1A/1B/1C.

The equality of U_{TV} and $\langle v_{rel,z} \rangle$ is not observed in the radial range $0 < r/R < 0.8$ for downward flows, cases 3A/3B and 4A/4B/4C/4D/4E. For the downward flows in absence of a flow straightener, cases 3A/3B, the particle mean axial velocity almost matches the fluid axial one, $\langle v_{p,z} \rangle \approx \langle U_z \rangle$, in nearly the entire range $0 < r/R < 0.8$. For $0.6 < r/R < 0.8$, there is a slight increase in $|\langle v_{rel,z} \rangle|$.

For downward flows with flow straightener II, cases 4A and 4B, the equality of U_{TV} and $\langle v_{rel,z} \rangle$ is only observed for $0 < r/R < 0.4$. From $r/R = 0.4$ to 0.8, the magnitude of the mean axial relative velocity, $|\langle v_{rel,z} \rangle|$, becomes smaller until reaching half of the terminal velocity value for inertia particles type I, roughly -5 mm/s.

For case 4C, the profile of $\langle v_{rel,z} \rangle$ is quite different from the ones shown for cases 4A and 4B. Values of $|\langle v_{rel,z} \rangle|$ are approximate 40% of $|U_{TV}|$ for inertia particles type I in the range $0 < r/R < 0.6$ and increase to 85% of $|U_{TV}|$ at $r/R \approx 0.8$. Significant differences in the results of $\langle v_{rel,z} \rangle$ were found when the mean volumetric concentration of particles exceeds 7.0×10^{-5}.

For downward flows with flow straightener II, cases 4D and 4E, the mean axial relative velocity profiles show similar behavior as in case 4C. In these cases, inertia particles type II were applied. Values of $|\langle v_{rel,z} \rangle|$ are close to 25% of $|U_{TV}|$ for particles type II at the pipe centerline and raise gradually to 80% at $r/R \approx 0.8$.

In all downward flows, $\langle v_{p,z} \rangle$ approaches $\langle U_z \rangle$ for $r/R > 0.8$ in a similar fashion to upward flows. Careful inspection of Fig.'s 3.18 – 3.23 and 3.24 – 3.28 shows that the reduction in $|\langle v_{rel,z} \rangle|$ in the radial range $0 < r/R < 0.8$ coincides with the occurrence of increased levels of turbulence. The diagonal components of the Reynolds stress tensor, $\langle u_r^2 \rangle$, $\langle u_z^2 \rangle$ and $\langle u_\theta^2 \rangle$ are enhanced for developing flows. At the same radial position, the higher the discrepancies with the fully developed result, the bigger the reduction in $|\langle v_{rel,z} \rangle|$.

In order to further investigate the relation between relative velocity and turbulence level, a convenient measure of the latter is now defined. It is the ratio of the local

turbulence intensity for developing flows to the one obtained in the fully developed cases (1A/1B/1C) in the radial range $0 < r/R < 0.8$. The local turbulence intensity is given by: $I_{r/R} = [(<u_z^2> + <u_r^2> + <u_\theta^2>)^{1/2}]_{r/R}$. Next, the turbulence intensity $I_{r/R}$ is scaled with the bulk velocity of the corresponding flow, $I_{r/R}/U_b$. Case 1B is chosen as reference for the fully developed case. Cases 1A and 1C gave similar results. In Fig.'s 3.29 – 3.32, a plot of $(U_{TV} - <v_{rel,z}>)/U_{TV}$ and of the ratios of local turbulence intensity for developing particle-laden flows to the fully developed one, $(I_{r/R}/U_b)_{developing}/(I_{r/R}/U_b)_{1B}$ are shown. The standard error, Eq. (3.10), produced error-bars with sizes comparable to the size of markers shown in Fig.'s 3.29 – 3.32.
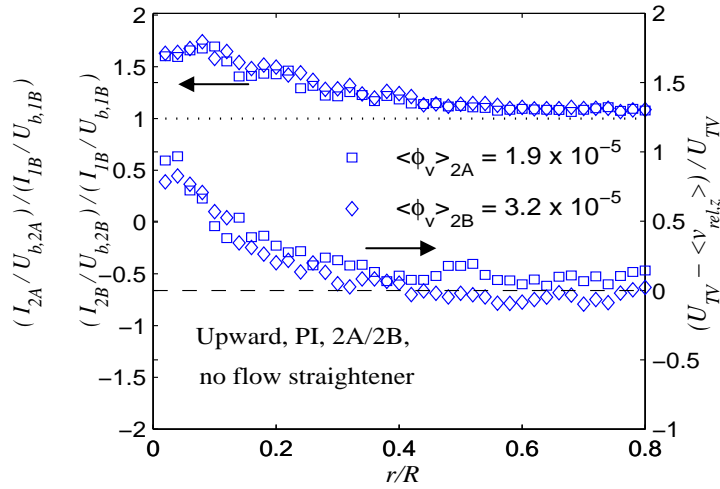
Figure 3.29 Effect of the local turbulence intensity ratio, $(I_{r/R}/U_b)_{developing}/(I_{r/R}/U_b)_{1B}$, on the mean axial relative velocity for particle-laden cases 2A and 2B. Results are scaled with the bulk velocity of the corresponding flow, U_b. The dashed line represents $U_{TV} = <v_{rel,z}>$. Dotted line corresponds to $I_{1B}/U_{b,1B} = I_{2A}/U_{b,2A} = I_{2B}/U_{b,2B}$. Squares and diamonds represent results of cases 2A and 2B, respectively.
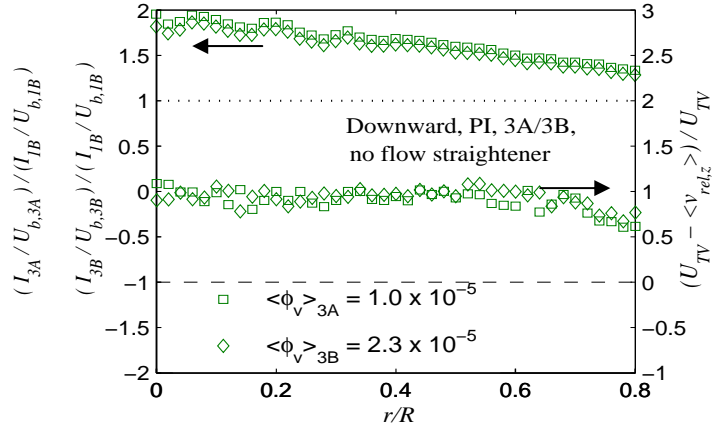
Figure 3.30 Effect of the local turbulence intensity ratio, $(I_{r/R}/U_b)_{developing}/(I_{r/R}/U_b)_{1B}$, on the mean axial relative velocity for particle-laden cases 3A and 3B. Results are scaled with the bulk velocity of the corresponding flow, U_b. The dashed line represents $U_{TV} = <v_{rel,z}>$. Dotted line corresponds to $I_{1B}/U_{b,1B} = I_{3A}/U_{b,3A} = I_{3B}/U_{b,3B}$. Squares and diamonds represent results of cases 3A and 3B, respectively.
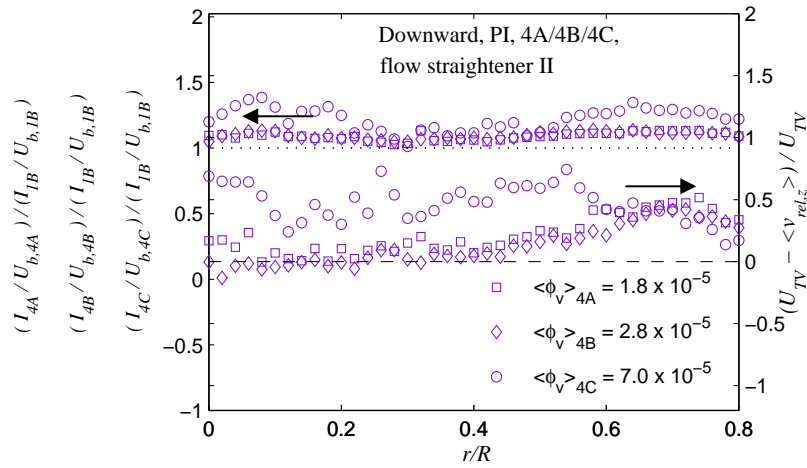
Figure 3.31 Effect of the local turbulence intensity ratio, $(I_{r/R}/U_b)_{developing}/(I_{r/R}/U_b)_{1B}$, on the mean axial relative velocity for particle-laden cases 4A, 4B and 4C. Results are scaled with the bulk velocity of the corresponding flow, U_b. The dashed line represents $U_{TV} = <v_{rel,z}>$. Dotted line corresponds to $I_{1B}/U_{b,1B} = I_{4A}/U_{b,4A} = I_{4B}/U_{b,4B} = I_{4C}/U_{b,4C}$. Squares, diamonds and circles represent results of cases 4A, 4B and 4C, respectively.

92
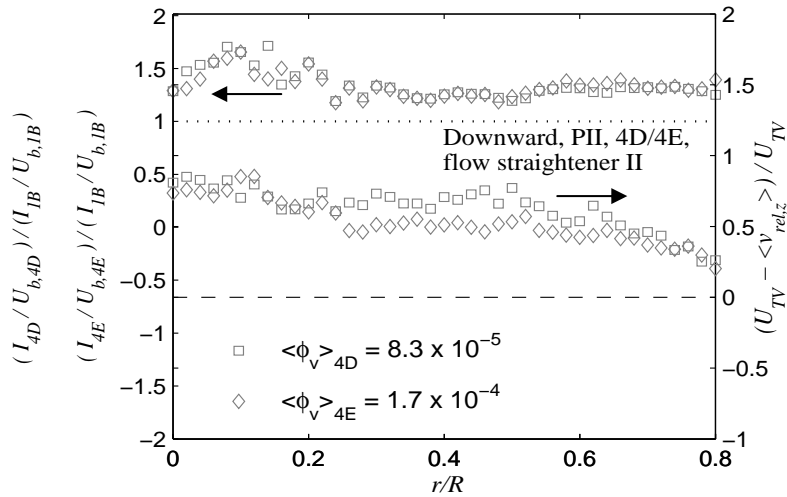
Figure 3.32 Effect of the local turbulence intensity ratio, $(I_{r/R}/U_b)_{developing}/(I_{r/R}/U_b)_{1B}$, on the mean axial relative velocity for particle-laden cases 4D and 4E. Results are scaled with the bulk velocity of the corresponding flow, U_b. The dashed line represents $U_{TV} = <v_{rel,z}>$. Dotted line corresponds to $I_{1B}/U_{b,1B} = I_{4D}/U_{b,4D} = I_{4E}/U_{b,4E}$. Squares and diamonds represent results of cases 4D and 4E, respectively.

By comparing the trends in $(U_{TV} - <v_{rel,z}>)/U_{TV}$ to the ratios of local turbulence intensity for developing particle-laden flows to the fully developed one, $(I_{r/R}/U_b)_{developing}/(I_{r/R}/U_b)_{1B}$, it is observed that a rise in the values of $(U_{TV} - <v_{rel,z}>)/U_{TV}$ coincides with an increase in $(I_{r/R}/U_b)_{developing}/(I_{r/R}/U_b)_{1B}$. In Fig. 3.29, for example, it is noticed that U_{TV} is close to $<v_{rel,z}>$ for $0.4 < r/R < 0.8$. In this radial range, the ratios $I_{2A}/U_{b,2A}$ and $I_{2B}/U_{b,2B}$ approach $I_{1B}/U_{b,1B}$. From $r/R \sim 0.4$ to the pipe centerline, $|<v_{rel,z}>|$ reduces gradually until the mean axial velocity of inertia particles approaches the fluid one at $r/R = 0$. The reduction on $|<v_{rel,z}>|$ coincides with the increase of the ratios $(I_{2A}/U_{b,2A}/I_{1B}/U_{b,1B})$ and $(I_{2B}/U_{b,2B}/I_{1B}/U_{b,1B})$ from 1.1 at $r/R = 0.4$ to 1.6 at $r/R = 0$. The relation between the rise in values of $(U_{TV} - <v_{rel,z}>)/U_{TV}$ and the increase in $(I_{r/R}/U_b)_{developing}/(I_{r/R}/U_b)_{1B}$ is also noted in the remaining results.

To get a better overview of the relation between the reduction of the magnitude of the mean axial relative velocity, $|<v_{rel,z}>|$, and the increase on local turbulence intensity, values of $(U_{TV} - <v_{rel,z}>)/U_{TV}$ x $(I_{r/R}/U_b)_{developing}/(I_{r/R}/U_b)_{1B}$ are plotted for all experimental data in

Fig. 3.33. Data of the fully developed cases 1A/1C are also included. Only data in the radial range $0 < r/R < 0.8$ is considered.
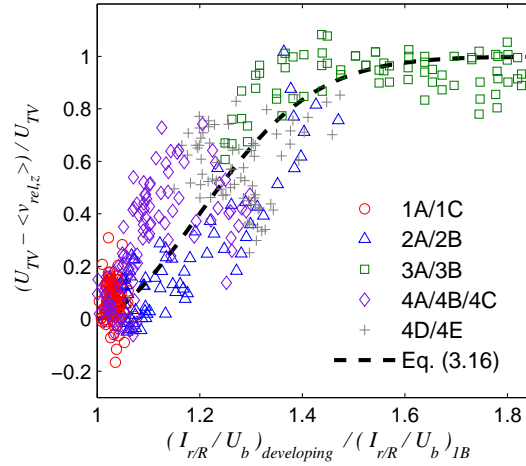
Figure 3.33 Relation between the reduction on the magnitude of the mean axial relative velocity, $|<v_{rel,z}>|$, and the increase on local turbulence intensity as given by $(I_{r/R}/U_b)_{developing} /(I_{r/R}/U_b)_{1B}$. All particle-laden experiments are taken into account. Only data in the radial range $0 < r/R < 0.8$ is considered. The dashed line represents a data fit as given by Eq. (3.16).

For $(I_{r/R}/U_b)_{developing} /(I_{r/R}/U_b)_{1B} > 1.6$, values of $(U_{TV} - <v_{rel,z}>)/U_{TV}$ approach 1 in an asymptotic way. In these situations, the inertia particles have almost the same mean velocity as the flow tracers. A fit of all experimental data presented in Fig. 3.33 is given by Eq. (3.16):

$$(U_{TV} - <v_{rel,z}>)/U_{TV} = \tanh \{a \, | \frac{(I_{r/R}/U_b)_{developing}}{(I_{r/R}/U_b)_{1B}} - 1 |^b \} \qquad (3.16)$$

where the fit parameters a and b are equal to 4.75 and 1.5, respectively. The quality of the fit is expressed by the two parameters r_s^2 and F, defined in Eq. (3.8) and (3.9). In Eq. (3.16), r_s^2 and F are equal to 0.82 and 2136, respectively. Relation (3.16) has the proper asymptotic limits for $(I_{r/R}/U_b)_{developing}/(I_{r/R}/U_b)_{1B}$ going to zero and going to infinity.

3.7 Analysis

3.7.1   Interaction between particles and turbulent fluid flow

The effects of flow developing stage, of flow direction and of mean concentration on the mean axial and mean fluctuating velocity profiles of particles and fluid have been presented in Sections 3. 6.3 and 3.6.4, respectively. In Section 3.6.5, results concerning the mean axial relative velocity, $\langle v_{rel,z} \rangle$, have been presented. A decrease of the magnitude of $\langle v_{rel,z} \rangle$ was observed to coincide with increasing flow turbulence, as quantified by $(I_{r/R}/U_b)_{developing}/(I_{r/R}/U_b)_{1B}$.

The RMS velocity, u_{rms}, is the square root of the MSV velocity, $\langle u^2 \rangle$: $u_{rms} = \langle u^2 \rangle^{0.5}$. The ratio of the RMS fluid velocities to the particle terminal velocity, $|u_{rms}/U_{TV}|$, indicates the degree of interaction between particles and turbulent flow structures. Many in depth analytical and numerical studies revealed that the rise velocity of bubbles is reduced by turbulence due to the increased residence time of bubbles in the downward side of large vortices, where a theoretical static equilibrium point occurs; see Aliseda and Lasheras[25], for example. Particle entrapment in flow structures was investigated by Sene et al.[12] They showed that the characteristic ratio u_{rms}/U_{TV} indicates if vortical structures can trap a bubble or a particle. For $u_{rms}/U_{TV} \gg 1$, trapping occurs in all flow structures, whereas if $u_{rms}/U_{TV} \ll 1$ little interaction with vortices is to be expected. Spelt and Biesheuvel[13] found reduction in the mean rise velocity of bubbles, even 50 % of U_{TV}, for isotropic turbulence with $u_{rms}/U_{TV} > 0.2$. They suggested that for higher values of u_{rms}/U_{TV} the slowing down of the bubbles is associated with the eddy zones; although the mechanism is presumably not that of trapping them in vortex cores, but rather transporting them towards the downward flowing edges of the eddies, where the reduction of the velocity is predominantly caused by inertia forces and not by viscous forces.

In turbulent pipe flows, turbulent properties are inhomogeneous in the radial direction. The ratio $|u_{rms}/U_{TV}|$ for a direction-dependent RMS velocity, $|\langle u_h^2 \rangle^{0.5}/U_{TV}|$, is of interest in the present particle-laden pipe flows. Figure 3.34 shows the ratio of the normal components of the smallest RMS fluid values, which correspond to cases 1A/1B/1C (see Fig. 3.18a), to the terminal velocity of inertia particles type I.
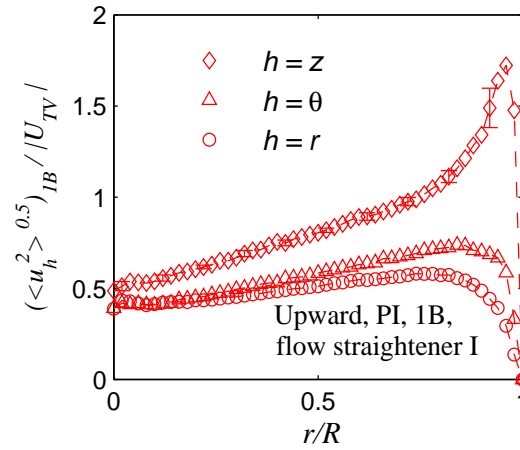
Figure 3.34 Ratios of RMS fluid velocity fluctuations of normal components to the terminal velocity of particles type I, $|<u_h^2>^{0.5}/U_{TV}|$, for case 1B. A mean volumetric concentration, $<\Phi_v>$, equal to 1.4×10^{-5} has been applied to case 1B. Dashed lines are added to guide the eye. Error-bars are indicated for $h=z$.

The values in Fig. 3.34 suggest significant interaction between the particle motion and the turbulent flow field, since $|<u_h^2>^{0.5}/U_{TV}|$ is of order 1. The ratio of the axial component for case 1B to the terminal velocity of particles I exceeds 1 for the radial range $0.7 < r/R < 0.99$. In this region, a decrease of the magnitude of $<v_{rel,z}>$ with decreasing distance to the wall has been found for all particle-laden cases.

Aliseda and Lasheras[25] presented a cartoon to explain the theoretical static equilibrium point of forces on bubbles to elucidate the interaction with large vortices in a homogeneous and isotropic turbulent flow. Adapting their approach to the present vertical particle-laden pipe flows, a similar picture of the interaction of inertia particles (with $\rho_p/\rho_f \approx 1.05$) with the turbulent flow structures is presented in Fig. 3.35.
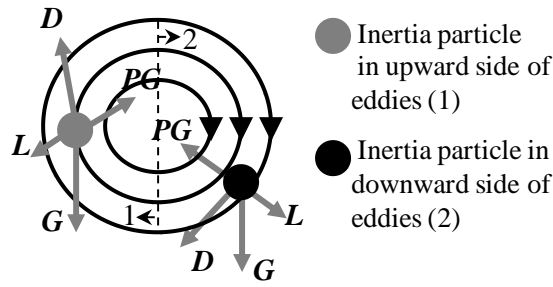
Figure 3.35 Schematics of the interaction of particles and turbulent flow eddies in particle-laden flows for $|u_{rms}/U_{TV}| \approx O(1)$. Particles interact with vortex structures carried by the mean flow. The cylindrical coordinate system used is shown in the left side. Region 1 represents the upward side of eddies and region 2 the downward side. The terms D, L, G and PG represent drag, lift, gravitational and pressure-gradient forces, respectively.

Bubbles in turbulent flows with $|u_{rms}/U_{TV}| \approx O(1)$ experience a reduction in the mean rise velocity due to the increased residence time in the downward side of turbulent eddies.[25] This means that bubbles spend longer periods in the region denoted as "2" in Fig. 3.35. Obviously, the gravitational force direction is upward in that case. Particles heavier than fluid and with $u_{rms}/U_{TV} \approx O(1)$ (corresponding to the present experiments) are expected to have longer residence times in the upward side of eddies; region 1 in Fig. 3.35.

Cartoons like Fig. 3.35 show the complexity of particle-flow interaction and may explain the reduction in relative velocity to some extent. However, they fail to explain the differences in concentration profiles found in upward and downward flows. These differences will be explained in the next section.

3.7.2   Governing equations for fluid and particles

In the particle-laden pipe flows tested here, upward and downward flows had different concentration profiles. The higher particle concentrations in the pipe core for upward flows and in the near wall-zone for downward flows revealed that orientation with respect to gravity matters. Also Fig.'s 3.11 – 3.16 and 3.24 – 3.28 revealed different mean relative velocity profiles of fluid and particles for up- and downflow. In order to better comprehend these results, the equations of motion for fluid and particles are now investigated.

An Eulerian-Lagrangian formulation is adopted for the equations of motion, distinguishing a continuous fluid phase, and a discrete particle phase in which each particle

is described by a set of equations for its position and velocity. The governing equations for the fluid consist of the continuity and the Navier-Stokes equations, Eq.'s (3.17) and (3.18). The particle action on the fluid is represented by δ-forcing, made possible by assuming that flow gradients are constant in the particle volume, see Mazzitelli *et al.*[29] The fluid flow in the volume of the particle is ignored and the local flow around the particle is not resolved in an attempt to elucidate the trends found.

$$\nabla . \boldsymbol{U} = 0 \tag{3.17}$$

$$\partial \boldsymbol{U}/\partial t + \boldsymbol{U}.\nabla \boldsymbol{U} = -\nabla P/\rho_f + v\,\nabla^2 \boldsymbol{U} + \boldsymbol{g} + \Sigma_i\,\boldsymbol{a}_{p,i}\,\delta(\boldsymbol{x} - \boldsymbol{x}_{p,i})V_p \tag{3.18}$$

In Equations (3.17) and (3.18), ρ_f and $\boldsymbol{U}$ denote the fluid mass density and velocity, P pressure, t time, v fluid kinematic viscosity, V_p particle volume and $\boldsymbol{g}$ gravity acceleration. The expression $\Sigma_i\,\boldsymbol{a}_{p,i}\,\delta(\boldsymbol{x} - \boldsymbol{x}_{p,i})V_p$ describe the feedback by all particles on the fluid. The terms $\boldsymbol{x}_p$ and $\boldsymbol{a}_p$ denote particle position and fluid acceleration induced by a particle. Terms in bold indicate vectors.

Because of axisymmetry, a cylindrical polar coordinate system (r, θ, z) rather than a Cartesian one is chosen to represent the governing equations in the remainder of this section. The origin of the cylindrical coordinate system is located at the pipe centerline and the gravity acceleration, $\boldsymbol{g}$, is anti-parallel to the z-axis; see Fig. 3.17. The velocity components in radial, axial and tangential directions are denoted by: $\boldsymbol{U}_r = <U_r> + u_r$, $\boldsymbol{U}_z = <U_z> + u_z$ and $\boldsymbol{U}_\theta = <U_\theta> + u_\theta$, respectively. The notation $<U>$ indicates mean value of $\boldsymbol{U}$ and the lowercase letters the fluctuating components. The Reynolds stresses for the turbulent flows are represented by $<u_r^2>$, $<u_z^2>$, $<u_\theta^2>$ and $<u_r u_z>$. Cross-components involving u_θ can be neglected, e.g. $<u_\theta u_r>$ and $<u_\theta u_z>$. Results of present experiments indicate that azimuthal gradients, $\partial/\partial\theta$, and the mean tangential velocity, $<U_\theta>$, can be neglected, also for developing flows. By averaging Eq.'s (3.17) and (3.18), continuity and Navier-Stokes equations for radial and axial components, Eq.'s (3.19), (3.20) and (3.21), are found. The azimuthal momentum equation only describes the relation of the tangential velocity correlations $<u_\theta u_r>$ and $<u_\theta u_z>$ and is therefore not presented.

$$(1/r)\,\partial(r<U_r>)/\partial r + \partial(<U_z>)/\partial z = 0 \tag{3.19}$$

$<U_r>\partial(<U_r>)/\partial r + <U_z>\partial(<U_r>)/\partial z + \partial(<u_r u_z>)/\partial z + (1/r)\partial(r<u_r^2>)/\partial r - (<u_\theta^2>)/r = -$

$(\partial P/\partial r)/\rho_f + v\partial^2(<U_r>)/\partial z^2 + (v/r)\partial(r\{\partial(<U_r>)/\partial r\})/\partial r - (v/r^2)(<U_r>) + <a_{p,r}>_L\,n(r)V_p \tag{3.20}$

$<U_r>\,\partial(<U_z>)/\partial r + <U_z>\,\partial(<U_z>)/\partial z + \partial(<u_z^2>)/\partial z + (1/r)\,\partial(r<u_r u_z>)/\partial r = -\,(\partial P/\partial z)/\rho_f +$

$v\partial^2(<U_z>)/\partial z^2 + (v/r)\partial(r\{\partial(<U_z>)/\partial r\})/\partial r + g + <a_{p,z}>_L\,n(r)V_p$ $\qquad$ (3.21)

The last terms in Eq.'s (3.20) and (3.21), $<a_{p,r}>_L\,n(r)V_p$ and $<a_{p,z}>_L\,n(r)V_p$, describe the feedback by all particles on the radial and axial momentum equations, respectively. Their definitions will be shown at this section. The term $n(r)$ denotes the local particle number density. The Lagrangian notation $<\;>_L$ is used to indicate an ensemble average over particles in a certain radial bin.

For fully developed pipe flows, the mean fluid radial velocity and velocity axial gradients are negligible apart from $\partial P/\partial z$; $<U_r> = 0$ and $\partial/\partial z = 0$. Radial and axial components of the Reynolds-averaged Navier-Stokes equations take the form of Eq.'s (3.22) and (3.23).

$$\partial<u_r^2>/\partial r + (<u_r^2> - <u_\theta^2>)/r = -\,(\partial P/\partial r)/\rho_f + <a_{p,r}>_L\,n(r)V_p \qquad (3.22)$$

$\partial<u_r u_z>/\partial r + <u_r u_z>/r = -\,(\partial P/\partial z)/\rho_f + (v/r)\partial(r\{\partial(<U_z>)/\partial r\})/\partial r + g + <a_{p,z}>_L\,n(r)V_p$ $\quad$ (3.23)

In order to quantify the terms $<a_{p,r}>_L$ and $<a_{p,z}>_L$, the particle equation of motion is introduced in the form of Eq. (3.24):

$\rho_p V_p\,(dv_p/dt) = V_p\,(\rho_p - \rho_f)\,\boldsymbol{g} + \rho_f V_p\,(DU/Dt) + \rho_f V_p\,C_{AM}\,[(DU/Dt) - (dv_p/dt)] - (1/8)\rho_f C_D\,\pi$

$d_p^2|\boldsymbol{v_p} - \boldsymbol{U}|(\boldsymbol{v_p} - \boldsymbol{U}) - \rho_f V_p\,C_L\,(\boldsymbol{v_p} - \boldsymbol{U})\times\boldsymbol{\omega} + \boldsymbol{F_{rest}}$ $\qquad$ (3.24)

where the terms ρ, d_p, V and dv_p/dt represent mass density, particle diameter, volume and particle acceleration, respectively. The subscripts f and p denote fluid and particle. The terms C_{AM}, C_D and C_L denote added mass, drag and lift coefficients, respectively. The expression $\boldsymbol{F_{rest}}$ comprises history terms and other forces. The velocity of the particle relative to the fluid and the vorticity of the flow field, $\nabla\times\boldsymbol{U}$, are given by $\boldsymbol{v_{rel}} = (\boldsymbol{v_p} - \boldsymbol{U})$ and $\boldsymbol{\omega}$, respectively. For the pipe flows at hand, only the gradient of axial velocity in the radial direction, $\partial U_z/\partial r$, is significant. The lift force accounts for every possible form of lift on a particle. History effects are neglected; $\boldsymbol{F_{rest}} \approx 0$. The fluid acceleration is represented by DU/Dt, see Eq. (3.25); and is the unperturbed fluid acceleration that would be measured in the absence of a particle at its center.

$$DU/Dt = \partial\boldsymbol{U}/\partial t + \boldsymbol{U}.\nabla\boldsymbol{U} \qquad (3.25)$$

The particle acceleration in Eq. (3.24), dv_p/dt, is now averaged and split into the radial and axial components as given by $<dv_{p,r}/dt>_L$ and $<dv_{p,z}/dt>_L$:

$$<dv_{p,r}/dt>_L = [\rho_f(1+C_{AM}) <DU_r/Dt>_L - (3\rho_f C_D/4d_p)|v_{rel}|<v_{rel,r}>_L - \rho_f C_L <v_{rel,z} \partial U_z/\partial r>_L] /$$

$$(\rho_p + \rho_f C_{AM}) \tag{3.26}$$

$$<dv_{p,z}/dt>_L = [(\rho_p - \rho_f)g + \rho_f (1+C_{AM}) <DU_z/Dt>_L - (3\rho_f C_D/4d_p)|v_{rel}|<v_{rel,z}>_L +$$

$$\rho_f C_L <v_{rel,r} \partial U_z/\partial r>_L] / (\rho_p + \rho_f C_{AM}) \tag{3.27}$$

For particles with a small diameter, the drag term in Eq.'s (3.26) and (3.27) is more significant than the remaining ones. With increasing d_p, a particle acquires enough inertia, $(\rho_p + C_{AM} \rho_f) V_p$, not to behave as a fluid particle. In our analysis, all acceleration terms are relevant.

In Eq.'s (3.22) and (3.23), $<a_{p,r}>_L$ and $<a_{p,z}>_L$ originate from the action of pressure and viscous terms on the particle surface. By inspection of Eq. (3.24), these contributions stem from the fluid acceleration, added mass, drag, lift and history forces averaged over particles for a given radial position. The gravitational force is not included in the term $<a_{p,z}>_L$. The terms $<a_{p,r}>_L$ and $<a_{p,z}>_L$ are given by Eq.'s (3.28) and (3.29):

$$<a_{p,r}>_L = -C_{AM} <DU_r/Dt - dv_{p,r}/dt>_L + (3C_D/4d_p)|v_{rel}|<v_{rel,r}>_L + C_L <v_{rel,z} \partial U_z/\partial r>_L \tag{3.28}$$

$$<a_{p,z}>_L = -C_{AM} <DU_z/Dt - dv_{p,z}/dt>_L + (3C_D/4d_p)|v_{rel}|<v_{rel,z}>_L - C_L <v_{rel,r} \partial U_z/\partial r>_L \tag{3.29}$$

In order to predict the changes in the fluid flow due to the presence of particles, the Reynolds-averaged Navier-Stokes equations must be solved with inclusion of the terms $<a_{p,r}>_L$ and $<a_{p,z}>_L$. By replacing $<dv_{p,r}/dt>_L$ and $<dv_{p,z}/dt>_L$ in Eq.'s (3.28) and (3.29) with Eq.'s (3.26) and (3.27), it is possible to rewrite $<a_{p,r}>_L$ and $<a_{p,z}>_L$ as:

$$<a_{p,r}>_L = [C_{AM} (\rho_f - \rho_p) <DU_r/Dt>_L + (3\rho_p C_D/4d_p)|v_{rel}|<v_{rel,r}>_L + \rho_p C_L <v_{rel,z} \partial U_z/\partial r>_L] /$$

$$(\rho_p + \rho_f C_{AM}) \tag{3.30}$$

$$<a_{p,z}>_L = [C_{AM} (\rho_f - \rho_p) <DU_z/Dt>_L + (3\rho_p C_D/4d_p)| v_{rel} |<v_{rel,z}>_L + C_{AM} (\rho_p - \rho_f) g -$$

$$\rho_p C_L <v_{rel,r} \partial U_z/\partial r>_L] / (\rho_p + \rho_f C_{AM}) \tag{3.31}$$

The gravity term in Eq. (3.31) only affects $<a_{p,z}>_L$ via an added mass term. The lift terms on Eq.'s (3.30) and (3.31) are now rearranged. By rewriting v_{rel} and $\partial U/\partial r$ as a sum of mean and fluctuating parts: $v_{rel} = <v_{rel}> + v_{rel}'$ and $\partial U/\partial r = \partial<U>/\partial r + \partial u/\partial r$, and expanding the Lagrangian-averaged product term: $<v_{rel} \partial U/\partial r>_L$, the following expressions are obtained:

$$<v_{rel,r}\ \partial U_z\ /\partial r >_L\ =\ <(<v_{rel,r}>)\ \partial <U_z>/\partial r>_L\ +\ <v_{rel}'_r\ \partial u_z\ /\partial r >_L\ +\ <v_{rel}'_r>_L\ \partial <U_z>_L/\partial r\ +$$

$$<v_{rel,r}>_L<\partial u_z/\partial r>_L \tag{3.32}$$

$$<v_{rel,z}\ \partial U_z\ /\partial r >_L\ =<(<v_{rel,z}>)\ \partial <U_z>/\partial r>_L\ +\ <v_{rel}'_z\ \partial u_z\ /\partial r >_L\ +\ <v_{rel}'_z>_L\ \partial <U_z>_L/\partial r\ +$$

$$<v_{rel,z}>_L<\partial u_z/\partial r>_L \tag{3.33}$$

The third and fourth terms on the RHS of Eq.'s (3.32) and (3.33) are zero, since $<v_{rel}'_r>_L$, $<v_{rel}'_z>_L$ and $<\partial u_z/\partial r>_L = 0$. By replacing $<v_{rel,z}\ \partial U_z\ /\partial r >_L$ and $<v_{rel,r}\ \partial U_z\ /\partial r >_L$ in Eq.'s (3.30) and (3.31) with Eq.'s (3.32) and (3.33), the terms $<a_{p,r}>_L$ and $<a_{p,z}>_L$ are rewritten into Eq.'s (3.34) and (3.35):

$$<a_{p,r}>_L = [\ C_{AM}\ (\rho_f - \rho_p)\ <DU_r/Dt >_L + (3\rho_p\ C_D /\ 4d_p)\ |v_{rel}|\ <v_{rel,r}>_L + \rho_p\ C_L <v_{rel}'_z\ \partial u_z/\partial r >_L +$$

$$\rho_p\ C_L <(<v_{rel,z}>)\ \partial <U_z>/\partial r>_L]\ /\ (\rho_p + \rho_f\ C_{AM}) \tag{3.34}$$

$$<a_{p,z}>_L\ =\ [C_{AM}\ (\rho_f\ -\ \rho_p)\ <DU_z/Dt >_L\ +\ (3\rho_p\ C_D\ /4d_p)|\ v_{rel}\ |<v_{rel,z}>_L +\ C_{AM}\ (\rho_p\ -\ \rho_f)g\ -$$

$$\rho_p\ C_L <(<v_{rel,r}>)\ \partial <U_z>/\partial r>_L - \rho_p\ C_L <v_{rel}'_r\ \partial u_z/\partial r >_L]\ /\ (\rho_p + \rho_f\ C_{AM}) \tag{3.35}$$

A. Concentration profiles

In order to explain the differences in the measured concentration profiles for up- and downward flows, the local averaged feedback by particles on fluid in the radial direction, $<a_{p,r}>_L$, is now evaluated. Evaluation of Eq. (3.34) is performed with experimental data of one upward case (1B) and one downward case (4B). The analysis performed with the mentioned data can be extended to the remaining up- and downflow cases.

The term $<DU_r/Dt >_L$ in Eq. (3.34) is computed via the LHS of Eq. (3.22): $\partial <u_r^2>/\partial r$ $+(<u_r^2>)/r - (<u_\theta^2>)/r$. For case 1B, experimental data of $<u_r^2>$ and $<u_\theta^2>$ as a radial function is found in Fig. 3.18a; and for case 4B, in Fig. 3.21b. For the computation of mean lift force term, $<(<v_{rel,z}>)\partial <U_z>/\partial r>_L$, experimental data is given in Fig.'s 3.11 and 3.14 for cases 1B and 4B, respectively. For the computation of the fluctuating lift force term, $<v_{rel}'_z\ \partial u_z\ /\partial r >_L$, experimental data is not available in a Lagrangian reference frame. Therefore, the following approximation is carried out: $<v_{rel}'_z\ \partial u_z/\partial r >_L* \approx <(v_p'_{rms,z} - u_{rms,z})\ \partial <U_z>/\partial r>_L$; where $v_p'_{rms,z} = <v_p'_z^2>^{0.5}$; $u_{rms,z} = <u_z^2>^{0.5}$. It is obvious that the fluctuating component in axial direction of the relative velocity cannot be evaluated at the center of the particle from experimental data. Bagchi and Balachandar[26] introduced special measures to assess this velocity in a DNS with two-way coupling, but there is no way a similar procedure can be

applied to experimental data. The above approximation utilizes rms-values as typical measures for the fluctuating velocity components in order to at least have two values at the same position in the flow. This is believed to be important in pipe flow with typically large gradients in radial direction. Because of the large gradients, $<\partial u_z /\partial r >_L^*$ is replaced by $\partial <U_z>_L/\partial r$. The resulting estimate may be off by ±40%, but this will not affect the result of the reasoning below. The only way to investigate the accuracy of the above estimate is by means of a dedicated DNS analysis which is currently being performed in our group but which is beyond the scope of the present investigation. Moreover, we believe that a proper analysis of experimental data should be fully based on experimental data and not on additional information which can only be obtained by DNS or other methods. We believe that expressions for the drag force and the lift force based on potential flow considerations are unpractical from the point of view of the experimentalist. For this approximation, experimental data are available in Fig.'s 3.11, 3.14, 3.18a and 3.21a. In a fully developed flow, the drag term of the radial component is zero since $<v_{rel,r}>_L = 0$.

For cases 1B and 4B, all force terms in the RHS of Eq. (3.34) are plotted as a function of radial coordinate in Fig. 3.36. Radial force terms of Eq. (3.34) are plotted in Fig.'s 3.36a and 3.36b for case 1B and in Fig.'s 3.36c and 3.36d for case 4B. A hypothetical mean lift force for the radial component is also plotted for sake of evaluating a common approximation applied to the motion of inertia particles, namely $<v_{rel,z}>_L \approx U_{TV}$. The terms $F_{ADM,r}$, $F_{D,r}$, $<F_{L,r}>$, $F_L'_r$ and $<F_{L,UTV,r}>$ correspond to:

- $F_{ADM,r} = C_{AM} (\rho_f - \rho_p) <DU_r/Dt>_L /(\rho_p + \rho_f C_{AM})$;
- $F_{D,r} = (3\rho_p C_D /4d_p)|v_{rel}|<v_{rel,r}>_L /(\rho_p + \rho_f C_{AM})$;
- $<F_{L,r}> = \rho_p C_L <(<v_{rel,z}>) \partial <U_z>/\partial r>_L /(\rho_p + \rho_f C_{AM})$;
- $F_L'_r = \rho_p C_L <v_{rel}'_z \partial u_z/\partial r>_L^*/(\rho_p + \rho_f C_{AM})$;
- $<F_{L,UTV,r}> = \rho_p C_L <U_{TV} \partial (<U_z>)/\partial r>_L /(\rho_p + \rho_f C_{AM})$.

The sum of all force terms, except the hypothetical $<F_{L,UTV,r}>$, results in $<a_{p,r}>_L$. Each force term stands for force per mass unit [N/kg or m/s^2].
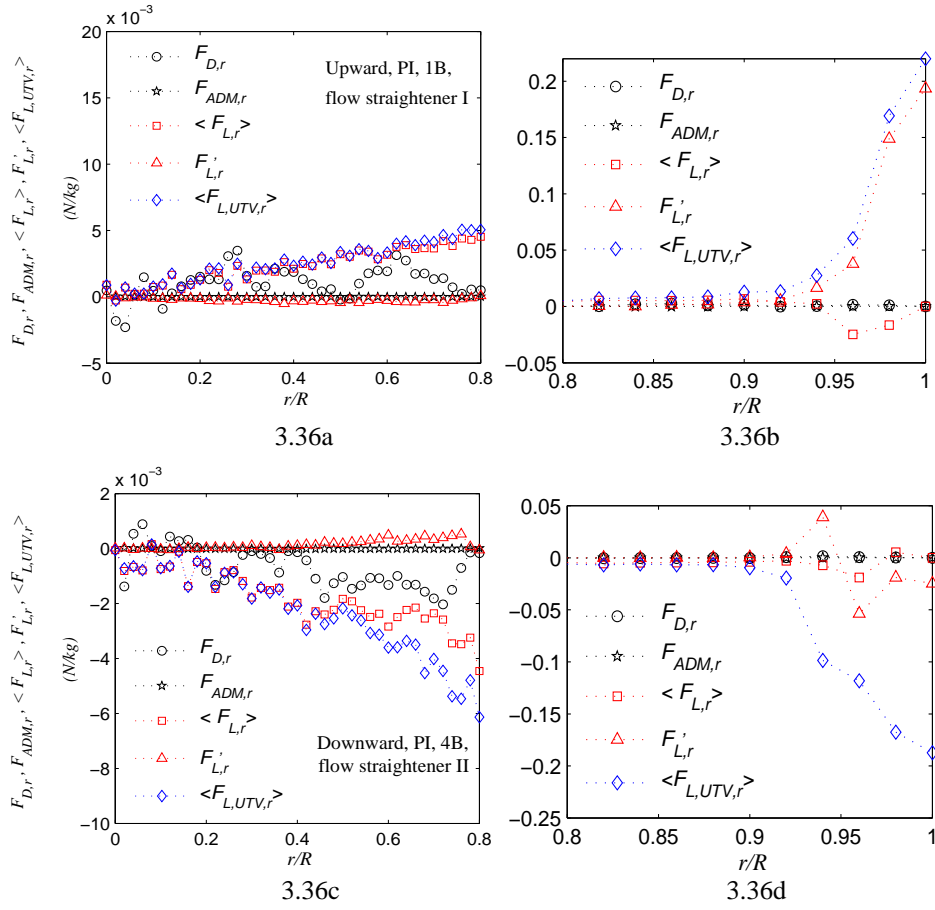
Figure 3.36 Local averaged radial force per unit of mass exerted on fluid by particles for particle-laden cases 1B (a, b) and 4B (c, d). Results for the radial range $0 < r/R < 0.8$ are shown in Fig.'s 3.36a and 3.36c, and for the range $0.8 < r/R < 1$ in Fig.'s 3.36b and 3.36d; notice the difference in scales. The expressions $F_{ADM,r}$, $F_{D,r}$, $<F_{L,r}>$ and $F_{L}'_r$ denote modified added mass, drag, mean lift and fluctuating lift forces, respectively, for the radial component. The expression $<F_{L,UTV,r}>$ denotes the mean lift for the approximation: $<v_{rel,z}>_L \approx U_{TV}$. Dotted lines are added to guide the eye.

The magnitudes of the radial forces in the wall region exceed the magnitudes in the pipe core. The lift force terms are dominant. The contribution of the modified added mass force term, $F_{ADM,r}$, is negligible everywhere. Note that Fig. 3.36 presents the local mean radial acceleration imposed to the fluid by a particle. The force exerted on the particle by the fluid is in opposite direction.

For $0 < r/R < 0.8$, the mean lift force, $<F_{L,r}>$, is dominant. The proposed approximation for the fluctuating lift force, $F_L'{}_r$, is negligible in this range and dominant for $0.8 < r/R < 1$, particularly for case 1B. The difference $v_{p}'{}_{rms,z} - u_{rms,z}$ is significant in the range $0.8 < r/R < 1$ for upward particle-laden cases; see Fig.'s 3.18a, 3.19a and 3.36b. For case 4B, the approximation for the fluctuating lift is not as meaningful as in case 1B, since the difference $v_{p}'{}_{rms,z} - u_{rms,z}$ is reduced in the range $0.8 < r/R < 1$ for downward particle-laden cases; see Fig.'s 3.20a, 3.21a, 3.22a, 3.23a and 3.36d.

For $0 < r/R < 0.8$, the hypothetical mean lift force, $<F_{L,UTV,r}>$, is comparable to the measured mean lift force, $<F_{L,r}>$. For $0.8 < r/R < 1$, the agreement between $<F_{L,r}>$ and $<F_{L,UTV,r}>$ is not observed. If $<v_{rel,z}>_L$ would be taken as U_{TV}, the mean lift force would be the dominant term for the range $0.8 < r/R < 1$.

For the present particle-laden flows, with $|u_{rms}/U_{TV}| \approx O(1)$, mean lift force is not dominant in the near-wall zone. In order to justify the different trends in $\Phi_v(r/R)$ profiles, it is hypothesized that the fluctuating form of the lift force, $<v_{rel}'{}_z \, \partial u_z/\partial r>_L$, is responsible for moving particles towards the core in upward experiments and towards the wall in downward flows. For dispersed flows with $|u_{rms}/U_{TV}| << 1$, the mean lift force is the most significant radial force for the whole cross-section, determining the trends of concentration profiles.

B. Feedback by particles on fluid in the axial direction

The local averaged feedback by particles on fluid in the axial direction, $<a_{p,z}>_L$, is now investigated. Evaluation of Eq. (3.35) is also performed with experimental data of upward case 1B and downward case 4B. This analysis can also be performed for the remaining up- and downflow cases.

The term $<DU_z/Dt>_L$ is computed via the LHS of Eq. (3.23): $\partial<u_r u_z>/\partial r + <u_r u_z>/r$. For case 1B, experimental data of $<u_r u_z>$ as a radial function is found in Fig. 3.18b; and for case 4B, in Fig. 3.21c. The mean lift force term, $<(<v_{rel,r}>)\partial<U_z>/\partial r>_L$, is zero since $<v_{rel,r}>_L = 0$. For the computation of the fluctuating lift force term, $<v_{rel}'{}_r \, \partial u_z/\partial r>_L$, experimental data is not available in a Lagrangian reference frame. Therefore, the following approximation is carried out: $<v_{rel}'{}_r \, \partial u_z/\partial r>_L{}^* \approx <(v_{p}'{}_{rms,r} - u_{rms,r}) \, \partial<U_z>/\partial r>_L$; where $v_{p}'{}_{rms,r} = <v_{p}'{}_r{}^2>^{0.5}$; $u_{rms,z} = <u_r{}^2>^{0.5}$. For such approximation, experimental data is available in Fig.'s 3.11, 3.14, 3.18a and 3.21b.

For cases 1B and 4B, all force terms in the RHS of Eq. (3.35) are plotted as a function of radial coordinate in Fig. 3.37. Axial force terms of Eq. (3.35) are plotted in Fig. 3.37a for case 1B and in Fig. 3.37b for case 4B. A hypothetical drag force for the axial component is also plotted for sake of evaluating a common approximation applied on the motion of inertia particles, namely $<v_{rel,z}>_L \approx U_{TV}$. The expressions $F_{ADM,z}$, $F_{D,z}$, F_g, $<F_{L,z}>$, $F_L'_z$ and $F_{D,UTV,z}$ correspond to:

- $F_{ADM,z} = C_{AM} (\rho_f - \rho_p) <DU_z/Dt>_L /(\rho_p + \rho_f C_{AM})$;
- $F_{D,z} = (3\rho_p C_D /4d_p)| v_{rel} |<v_{rel,z}>_L /(\rho_p + \rho_f C_{AM})$;
- $F_g = C_{AM} (\rho_p - \rho_f)g /(\rho_p + \rho_f C_{AM})$;
- $<F_{L,z}> = - \rho_p C_L <(<v_{rel,r}>) \partial<U_z>/\partial r>_L /(\rho_p + \rho_f C_{AM})$;
- $F_L'_z = - \rho_p C_L <v_{rel}'_r \partial u_z/\partial r>_L^* /(\rho_p + \rho_f C_{AM})$;
- $F_{D,UTV,z} = (3\rho_p C_D /4d_p)| v_{rel} |U_{TV} /(\rho_p + \rho_f C_{AM})$;

The sum of all force terms, except the hypothetical $F_{D,UTV,z}$, results in $<a_{p,z}>_L$. Each force term stands for force per unit of mass [N/kg or m/s^2].

3.37a   3.37b
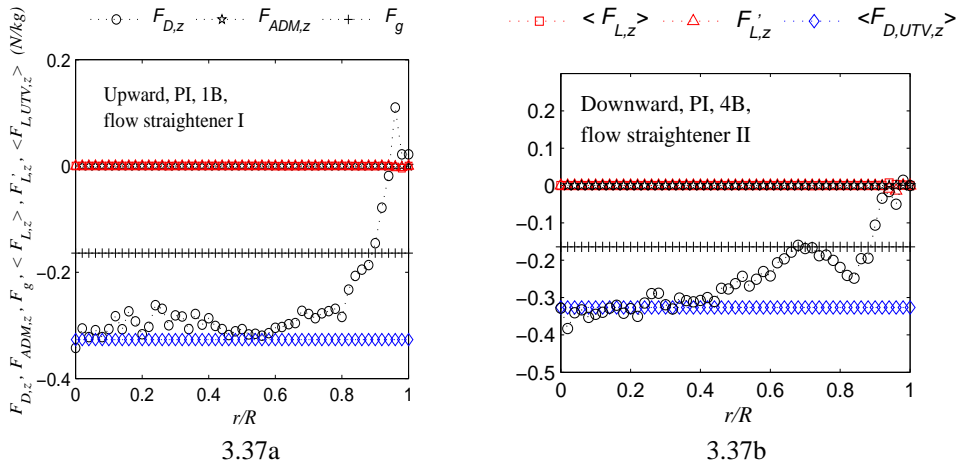
Figure 3.37 Local averaged axial force per unit of mass exerted on fluid by particles for particle-laden cases 1B (a) and 4B (b). The expressions $F_{ADM,z}$, $F_{D,z}$, F_g, $<F_{L,z}>$ and $F_L'_z$ denote modified added mass, drag, gravitational, mean lift and fluctuating lift forces, respectively, for the axial component. The expression $F_{D,UTV,z}$ denotes the drag for the approximation: $<v_{rel,z}>_L \approx U_{TV}$. Dotted lines are added to guide the eye.

Opposite to the radial forces, the magnitude of local averaged axial forces is bigger in the pipe core ($0 < r/R < 0.8$). The drag and gravitational terms, $F_{D,z}$ and F_g, are dominant. As mentioned, the gravity term in Eq. (3.35) only affects $<a_{p,z}>_L$ via an added mass term. The contributions of the modified added mass, mean lift and fluctuating lift force terms, $F_{ADM,z}$, $<F_{L,z}>$ and $F_{L',z}$, respectively, are negligible everywhere. For $0 < r/R < 0.8$, the drag force term, $F_{D,z}$, exceeds the gravitational term, F_g. For $0.8 < r/R < 1$, F_g is dominant. At this radial range, $F_{D,z}$ is reduced with decreasing distance to the wall. Notice that the term F_g differs from $F_{D,UTV,z}$ due to the added mass coefficient, C_{AM}.

The agreement between $F_{D,z}$ and the hypothetical $F_{D,UTV,z}$ is observed at the radial range $0 < r/R < 0.8$ for case 1B, and at $0 < r/R < 0.4$ for case 4B. If $<v_{rel,z}>_L$ would be taken as U_{TV}, the drag force would be also the dominant term close to the wall; $r/R > 0.8$. However, for the present particle-laden flows, with $|u_{rms}/U_{TV}| \approx O(1)$, this approximation is incorrect. For dispersed flows with $|u_{rms}/U_{TV}| << 1$, the drag force is the most significant axial force for the whole cross-section, including the near-wall zone.

C. The effect of particles feedback on the pressure drop

With the local averaged feedback by particles on fluid, $<a_{p,r}>_L$ and $<a_{p,z}>_L$, specified by Eq.'s (3.34) and (3.35), the radial and axial components of the Reynolds-averaged Navier-Stokes equations are now evaluated by averaging over the pipe cross-section:

$$(_0\int^R <a_{p,r}>_L \Phi_v(r) \, rdr) / (R^2/2) = \{_0\int^R \{ \, [(\partial P/\partial r)/\rho_f] - [<u_\theta^2>_L/r] \, \}rdr\}/(R^2/2) \qquad (3.36)$$

$$(_0\int^R r'dr' {}_0\int^{r'} <a_{p,z}>_L \Phi_v(r) \, rdr) / (R^4/4) = [(1/8)R^4(\partial P/\partial z)/\rho_f + \nu Q_{L,z}/\pi + {}_0\int^R <u_r u_z>_L \, r^2dr -$$

$$(1/8)R^4 g \,] / (R^4/4) \qquad (3.37)$$

The physical interpretation of the expressions (3.36) and (3.37) is based on the RHS's and will be made clear in the following. The terms $(\partial <u_r^2>/\partial r) + (<u_r^2>/r)$ in Eq. (3.22) disappear after integration. The term $Q_{L,z}$ in Eq. (3.37) is the volumetric flow rate crossing the test section. The particle density number is related to volume load by: $\Phi_v(r) = n(r)V_p$. Experimental data of upward case 1B and downward case 4B are employed in the analysis of Eq.'s (3.36) and (3.37). The conclusions of this analysis can also be extended to the remaining up- and downflow cases.

Radial profiles of $<a_{p,r}>_L \Phi_v(r)$ and $<a_{p,z}>_L \Phi_v(r)$ for up- and downflow, cases 1B and 4B, are observed in Fig. 3.38. Mean concentration profiles, $\Phi_v(r)$, for cases 1B and 4B are provided in Fig.'s 3.6 and 3.9, respectively.
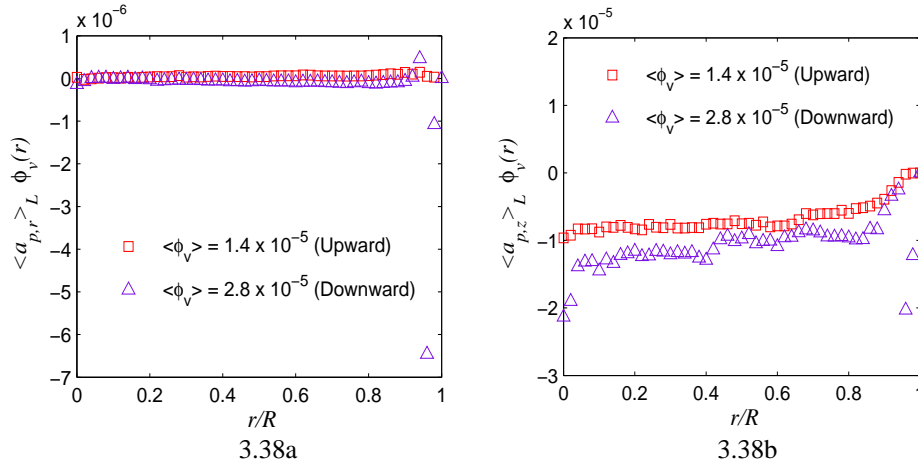
Figure 3.38 Force exerted by all particles in the radial (a) and axial (b) fluid motion. The terms $<a_{p,r}>_L \Phi_v$ and $<a_{p,z}>_L \Phi_v$ denote force per unit of mass N/kg. In upward case 1B and downward case 4B, mean volumetric concentrations, $<\Phi_v>$, equal to 1.4×10^{-5} and 2.8×10^{-5} have been applied, respectively.

For the downward particle-laden flow, case 4B, there is a maximum on the concentration profile of inertial particles, $\Phi_v(r/R)$, for $r/R \approx 0.97$. Due to this maximum of the volume load profile, the overall force contribution of particles to the fluid is bigger at the radial range $r/R > 0.8$ for case 4B than 1B. In Fig. 3.38b, the maximum at $r/R \approx 0.96$ in the profile of $<a_{p,z}>_L \Phi_v(r)$ for case 4B is due the overall gravitational force contribution, $F_g \Phi_v$; see Fig.'s 3.9, 3.37b and 3.38b.

The LHS of Eq. (3.37), $(_0\int^R r'dr'_0\int^{r'} <a_{p,z}>_L \Phi_v(r)\ rdr) / (R^4/4)$, yields in upflow (case 1B) a small number, -4.9×10^{-6} N/kg or m/s^2, as expected. The RHS of Eq. (3.37) is namely the total pressure gradient, $[(1/8)R^4(\partial P/\partial z)/\rho_f]/(R^4/4)$, minus the hydrostatic pressure gradient, $[(1/8)R^4 g]/(R^4/4)$, minus the viscous contribution, $(\nu Q_{L,z}/\pi)/(R^4/4)$, (about 1.5×10^{-4} N/kg in upflow) and minus the turbulent contribution, $(_0\int^R <u_r\ u_z>_L\ r^2 dr)/(R^4/4)$ (about 6.2×10^{-4} N/kg in upflow). The total pressure gradient minus the hydrostatic pressure gradient can also be computed from the well-known Darcy–Weisbach equation for single-phase turbulent pipe flows: $(dP/dz)_{Darcy} = f\ \rho_f\ U_b^2/2D$; where f is the friction factor, which can be taken from Moody's Diagram. For a smooth pipe at $Re_b \approx 10^4$, f is roughly 0.03.

107

With the pipe radius and the mass fluid density, $[(1/8)R^4(dP/dz)_{Darcy}/\rho_f]/(R^4/4)$ yields 7.5×10^{-4} N/kg, which is roughly the sum of viscous, $(\nu Q_{L,z}/\pi)/(R^4/4)$, and turbulent contributions, $({}_0\int^R \langle u_r u_z \rangle_L r^2 dr)/(R^4/4)$. This comparison makes obvious that in this case the particle concentration is low enough to hardly affect the frictional pressure drop (which is the total one minus the hydrostatic one). In downflow, case 4B, the numbers are the following: -5.0×10^{-6}, 1.5×10^{-4} and 6.3×10^{-4} N/kg for the LHS of Eq. (3.37), viscous and turbulent contributions, respectively. In cases 1B and 4B, mean volume concentrations equal to 1.4×10^{-5} and 2.8×10^{-5} have been applied.

Figure 3.38b makes clear why the contribution of the integral of $\langle a_{p,z} \rangle \Phi_v(r)$ to the pressure gradient is minor: at large radial distances $\langle a_{p,z} \rangle \Phi_v(r)$ is reduced due to the decrease on $\langle v_{rel,z} \rangle$ for $r/R > 0.8$. If the relative velocity component in z-direction would be U_{TV} everywhere, the integral of $\langle a_{p,z} \rangle \Phi_v(r)$ would yield -5.3×10^{-6} and -6.4×10^{-5} N/kg for cases 1B and 4B, respectively. Drag mainly determines the trend of $\langle a_{p,z} \rangle$.

The values of $({}_0\int^R \langle a_{p,r} \rangle_L \Phi_v(r) \ rdr)/(R^2/2)$, LHS of Eq. (3.36), are similarly small because of the low concentration of inertia particles: 6.4×10^{-8} for upflow case 1B and -3.7×10^{-7} N/kg for downflow case 4B. The pressure gradient in radial direction, $\{{}_0\int^R[(\partial P/\partial r)/\rho_f]rdr\}/(R^2/2)$, compensates the mean azimuthal fluctuating term: $\{- {}_0\int^R[\langle u_\theta^2 \rangle_L/r]rdr\}/(R^2/2)$. The last term equals -1.0×10^{-3} and -1.1×10^{-3} N/kg in up- and downflow cases 1B and 4B, respectively. The pressure gradient can be estimated from literature values; see Laws $et\ al.$[11], for example. The last one provided radial profiles of pressure as a function of mass fluid density and the bulk flow velocity. Integration of $\{{}_0\int^R[(\partial P/\partial r)/\rho_f]rdr\}/(R^2/2)$ with present experimental settings yields roughly 0.95×10^{-3} m^3/s^2. The physical significance of the integrated $\langle a_{p,r} \rangle_L$-equation is therefore the variation of pressure in radial direction due to centrifugal forces. Whether this pressure distribution is affected by the presence of particles is the subject of the present analysis. The results of the analysis remain practically the same if a lesser developed (in axial direction) flow is taken, showing that axial terms can be discarded for the present purposes.

However, if the relative velocity component in z-direction would be U_{TV} everywhere, the integral $({}_0\int^R \langle a_{p,r} \rangle_L \Phi_v(r) \ rdr)/(R^2/2)$ would yield 1.0×10^{-7} instead of 6.4×10^{-8} N/kg in upflow (case 1B) and -1.9×10^{-6} instead of -3.7×10^{-7} N/kg downflow (case 4B). The mean lift force component, $\langle F_{L,r} \rangle$, would have more influence on the computation of $\langle a_{p,r} \rangle_L$. This shows that small values of the mean relative velocity near the wall are essential in

keeping the integrated values of $<a_{p,r}>\Phi_v(r)$ small. If the relative velocity component in z-direction is taken to be U_{TV} everywhere, the mean lift force term, $<(<v_{rel,z}>)\ \partial<U_z>/\partial r>_L$, in $<dv_{p,r}/dt>$ is enhanced near the wall. Apparently, the lift force acts to reduce the mean relative velocity in the near-wall zone.

It is probably no coincidence that the Lagrangian averaged lift force is small in the near-wall zone because of the small averaged relative velocity there. A speculative explanation is then provided: the relative velocity is kept minimal at the wall region to reduce the dissipated power by the fluid, and then the entropy production. The dissipated power is a function of $v_{rel,z}{}^3$ and the radial range $0.8 < r/R < 1$ corresponds to 36 % of the cross-section area.

3.7.3   Wake interaction

For the particle-laden pipe flows at hand, experiments with mean volumetric concentrations less than 7.0×10^{-5} had minor changes on final results once $<\Phi_v>$ was varied. This was noticed on the aspect of the radial particle distributions, Fig.'s 3.6 – 3.10, and on the similarity of velocimetry results, Fig.'s 3.11 – 3.33, for cases 1A/1B/1C, 2A/2B, 3A/3B and 4A/4B.

For downward particle-laden flows with mean volumetric concentrations exceeding 7.0×10^{-5}, changes on particle distribution and velocities were observed. This was noticed for the different results for cases 4A/4B in comparison to cases 4C/4D/4E. The measurement conditions of the downward particle-laden flows of case 4 are similar: they cross the bundle flow straightener II at the entrance and samples are collected at 20D from the straightener outlet. Particles type II were applied in cases 4D/4E, while particles type I in cases 4A/4B/4C.

For example, cases 4A/4B showed similar $<v_{rel,z}>$ results, but different from cases 4C/4D/4E; see Fig.'s 3.27 and 3.28. The fluid and particle mean velocity profiles of cases 4C/4D/4E became peaky. Modifications were also observed on the aspect of concentration profiles, Φ_v (r/R), for cases 4C/4D/4E. The rise in the average concentration of inertia particles seems to be related to changes in distribution and velocimetry results from cases 4A/4B to cases 4C/4D/4E. These changes suggest a stronger effect on the two-way coupling between particles and fluid for cases 4C/4D/4E.

The collective effect of a large number of particles can modify the effective drag force on a particle due to screening effect and thereby influence the mean settling and dispersion characteristics; see Bagchi and Balachandar.[26] In order to evaluate if the wake interaction of the particle distributions had significant effect on the velocimetry results, it is proposed to evaluate the extension of the wake downstream of a single particle and the average inter-particle distance, D_p, for each specific particle-laden case. The computation of D_p is performed by considering the radial bin where the maximum time-averaged concentration of particles, $\Phi_{v,\max}$, was found; see Fig.'s 3.6 – 3.10 and Table 3.4. As a reference for the wake length behind a particle in an inhomogeneous flow, data of Suzuki *et al.*[24] can be of use. They found a wake extension of roughly 13 particle diameters, d_p, at the channel centerline. This length is reduced to nearly 10 d_p once the channel wall is approached.

The distance between the surfaces of finite-sized particles in a regular distribution is given by Eq. (3.38):

$$D_p/d_p = [\pi/(6\Phi_v)]^{1/3} - 1 \qquad\qquad (3.38)$$

The plot of the averaged inter-particle distance normalized by the particle diameter, D_p/d_p, for each specific particle-laden case is shown in Fig. 3.39. Values of D_p/d_p are presented only in the radial bin ($r_{\max}$) where the maximum time-averaged concentration of particles, $\Phi_{v,\max}$, was found. That happened in $r_{\max}/R \sim 0$ for upward flows, and in $r_{\max}/R \sim 0.98$ for downward flows. Triangle symbols represent the maximum concentration found for particle-laden cases 1A/1B/1C, 2A/2B, 3A/3B and 4A/4B. Circle, square and diamond represent results for cases 4C, 4D and 4E, respectively.
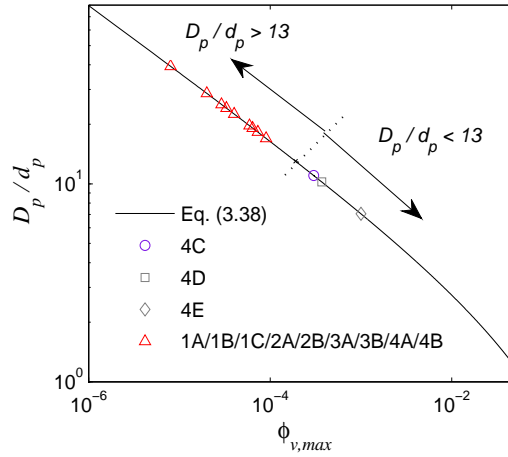
Figure 3.39 Ratio of inter-particle distance to particle diameter, D_p/d_p, in the radial bin (r_{max}) where the maximum time-averaged concentration of particles, $\Phi_{v,max}$, was found. The solid line represents Eq. (3.38). Circle, square and diamond represent cases 4C, 4D and 4E, respectively. Triangles represent the remaining particle-laden cases. The dashed line crosses the solid line in $D_p/d_p \sim 13$.

For cases 4C, 4D and 4E, $\Phi_{v,max}$ is about 3×10^{-4}, 4×10^{-4} and 10^{-3}, respectively. The aim of this approach is to identify if a strong interaction of the set of individual wakes in the pipe flow happened. That would be possible if the reference wake extension behind a particle exceeds the average inter-particle distance. If this situation took place, a strong interference of the set of wakes in the velocimetry values is expected. Considering that the reference provided by Suzuki *et al.*[24] is appropriate, a significant wake interaction should be expected for cases 4C/4D/4E in the near-wall region. This can explain differences from cases 4A/4B to cases 4C/4D/4E, and why the changes in the mean volume load, $<\Phi_v>$, did not affect cases 1A/1B/1C, 2A/2B and 3A/3B.

Even though $D_p/d_p < 13$ only in the near-wall zone for cases 4C/4D/4E, changes in results happened for the whole cross-section. Values of the fluid mean axial velocity for cases 4C/4D/4E became smaller than values of case 4S for $0.8 < r/R < 1$ and bigger for $0 < r/R < 0.6$. The stronger wake interaction as seen by cases 4C/4D/4E causes a reduction in velocities near the wall. By mass conservation, the fluid axial velocities increase in the core region.

3.8   Discussion

3.8.1   Inertia, wall-normal distributions and relative velocity

In the particle-laden flows measured, ratios of RMS fluid velocity to the terminal velocity of inertia particles are of order 1; $|u_{rms}/U_{TV}| \approx O(1)$. The magnitude of $<v_{rel,z}>$ reduced with increasing flow turbulence. Upward and downward flows had different concentration profiles. The high particle concentrations in the pipe core for upward flows and in the near wall-zone for downward flows revealed that orientation with respect to gravity affects radial distribution of particles.

With the observed trends being opposed to those in turbulent bubbly flows, it is conjectured that particles heavier than fluid and with $u_{rms}/U_{TV} \approx O(1)$ possess longer residence times in the upward side of eddies. That would explain the reduction of $|<v_{rel,z}>|$ with increasing flow turbulence. In order to explain the different trends in $\Phi_v (r/R)$ profiles, it is hypothesized that a fluctuating component of the lift force on particles, $<v_{rel\,z}' \, \partial u_z/\partial r >_L$, is responsible for moving particles towards the core in upward flows and towards the wall in downward flows.

The ratio of RMS fluid velocity to terminal velocity of particles with high inertia tends to go to zero: $|u_{rms}/U_{TV}| \rightarrow 0$. High inertia particles cross turbulent eddies with hardly any interaction. The relative velocity approaches the terminal velocity and in the presence of enough shear, a mean lift force in the form $<(<v_{rel,z}>) \, \partial(<U_z>)/\partial r >_L$ will be of importance in determining the wall-normal concentration profiles. For $|u_{rms}/U_{TV}| \rightarrow 0$, the magnitude of the mean lift component will overcome the fluctuating lift term, which was approximated in this work by: $<v_{rel\,z}' \, \partial u_z/\partial r >_L \approx <(v_{p\,'rms,z}' - u_{rms,z}) \, \partial<U_z>/\partial r >_L$; see previous section.

In the particle-laden experiments of Suzuki *et al.*[24], mean concentration profiles of flow tracers, $\Phi_v (r/R)$, were not far from a homogeneous distribution. For flow tracers, ratios of u_{rms}/U_{TV} considerably exceed 1; $u_{rms}/U_{TV} >> 1$. The terminal velocity of flow tracers is not significant and $|<v_{rel,z}>|$ is also small. In this situation, the turbulent motion of particles with low inertia is governed by the interaction with flow eddies and lift does not play a role.

In these experiments of Suzuki *et al.*[24], ceramic beads with mass density exceeding the carrier-phase (water) 3.85 times have been applied in downflow, resulting in a maximum concentration of inertia particles at the channel walls (exceeding 7 to 8 times the

concentrations at the channel core) and in a decrease of $|\langle v_{rel,z}\rangle|$ with decreasing distance to the wall. Ratios of RMS fluid velocity to the terminal velocity of inertia particles in their experiments are of order 0.2: $|u_{rms}/U_{TV}| \approx 0.2$. The mean lift, $\langle \langle v_{rel,z}\rangle \ \partial (\langle U_z\rangle)/\partial r \rangle_L$, can explain the maximum in $\Phi_v\ (r/R)$ profiles in the following way: in the the channel core, $\langle v_{rel,z}\rangle$ approaches the terminal velocity. In the near-wall zone, $|u_{rms}/U_{TV}|$ is about 0.25 and a small reduction of $|\langle v_{rel,z}\rangle|$ is observed: about 90 – 95% of U_{TV}. Due to the high velocity gradients, $\partial (\langle U_z\rangle)/\partial r$, and relative velocity, $\langle v_{rel,z}\rangle$, at the wall, the mean lift force is dominant and explains the maximum in the wall-normal concentration profiles. In their experiments, the magnitude of the fluctuating lift term, approximated in this work by: $\langle v'_{rel\ z}\ \partial u_z/\partial r \rangle_L \approx \langle (v'_{p\ rms,z} - u_{rms,z})\ \partial \langle U_z\rangle/\partial r \rangle_L$; is not relevant.

3.8.2   Relation between shear rate and drag coefficient

The influence of the shear on drag coefficients has been investigated numerically by Legendre and Magnaudet.[27] They analyzed the three-dimensional flow around a spherical bubble moving steadily in a viscous linear shear flow. The shear rate, Sr, is defined as the ratio of the velocity difference across the bubble (or particle) to the relative velocity; see Eq. (3.39):

$$Sr = (d_p\ \partial U_z/\partial r)/v_{rel} \tag{3.39}$$

For a particle Reynolds number in the range $0.1 < Re_p < 500$, the effect of shear on the drag coefficients was found[27] to be small for shear rates less than 0.2. The drag coefficient increases by less than 1% for $Sr = 0.02$ and by less than 5% for $Sr = 0.2$. The distributions of pressure and viscous effects at the bubble surface were close to the one corresponding to a uniform flow ($Sr = 0$). For shear rates between 0.2 and 1 and for Re_p equal to 300 or 500, the increase in drag coefficient was about 50%. The modification of the pressure distribution induced by inertia effects in the liquid is essentially responsible for the drag increase. To account for the shear rate influence on the computation of drag coefficients, a modified equation for C_D was made[27] by fitting data for $Re_p = 300$ and 500 and for $0.01 < Sr < 1$:

$$C_D = C_D^{\ *}\ (1 + 0.55\ Sr^2) \tag{3.40}$$

where $C_D^{\ *}$ is the value of the drag coefficient for uniform flow at the velocity of the center of the particle. For the data of $\partial U_z/\partial r$ given in Fig.'s 3.11 – 3.16, for $v_{rel} = U_{TV}$ and for particles I or II, Eq. (3.39) shows that Sr can exceed 1 for $r/R > 0.95$. This result indicates a

strong increase in the drag coefficient of particles flowing close to the wall ($r/R > 0.95$). For $r/R < 0.95$, the shear influence drops to values under 0.2, and the increase in drag due to shear is of minor importance.

If the terminal velocity is taken to predict the relative velocity for $r/R > 0.95$, it is possible to quantify the expected reduction of the mean relative velocity due to the shear rate effect. With $Sr = 1$, the drag coefficient is increased by 55 %. Since v_{rel} is a function of $C_D^{-1/2}$, a reduction in the mean relative velocity of order 20% is expected. In this region, reductions over 90% of U_{TV} were measured. Therefore, the main mechanisms to reduce $|<v_{rel,z}>|$ for $r/R > 0.95$ are not originating from an increase in drag coefficients due to shear rates. Note that Eq. (3.40) strictly holds for high Reynolds number ($Re_p = 300$ or 500), while $Re_p \leq 12$ in the present particle-laden flow cases.

3.8.3   Turbulence modulation

In Section 3.6.4, MSV velocity components of fluid and inertia particles have been presented. Cross-section averaged fluid turbulence ratios of particle-laden flows to the corresponding single-phase references showed an enhancement in the order of 5% for flows with $<\Phi_v>$ less than 3.2×10^{-5} and not far from fully developed conditions. In developing flows with $<\Phi_v>$ less than 2.3×10^{-5} and with high levels of turbulence, the presence of inertia particles caused turbulence enhancements in the order of 20 %. For flows with $<\Phi_v>$ exceeding 7.0×10^{-5} and not far from fully developed conditions, turbulence enhancements are about 20 - 30%. Apparently, for particle-laden flows with $|u_{rms}/U_{TV}| \approx O(1)$, inertia particles enhance turbulence and even the more so if their concentration is higher or if the level of turbulence is higher.

Here, turbulence enhancement has been achieved in particle-laden flows with $Re_p \leq 12$. Similar results have been obtained by Sato and Hishida[28] and by Suzuki et al.[24] The formers observed an increase in the streamwise turbulence intensity profiles of water by 500 μm glass particles with $Re_p \approx 40$. Suzuki et al.[24] observed higher levels of turbulence in channel flow with ceramic beads at $Re_p \approx 33$. The ceramic beads had Stokes number equal to 3.6, based on the ratio of the relaxation time for particles to viscous scales, and were applied at a mean volumetric load about 3.2×10^{-4}.

The present results are in disagreement to those of Hetsroni[4] and Elgobashi.[5] The former stated that turbulence is enhanced for $Re_p > 400$ due to the vortex shedding

phenomena and suppressed for low Re_p. Elgobashi[5] suggests a map based on the ratio of particle to Komogorov time-scales as a function of volume load. In that map, the present data fall in the range of turbulence reduction. Apparently, one or more parameters of influence are missing. We suppose that the ratio $|u_{rms}/U_{TV}|$ is also relevant to predict turbulence modulation.

Gore and Crowe[3] proposed the ratio of particle diameter to the integral length scale, d_p/l_e, to explain either increase or decrease of turbulent intensity of the carrier fluid with the addition of particles to the flow. A demarcation between increase or decrease was stated for $d_p/l_e \approx 0.1$. In a fully developed turbulent pipe flow, the integral length scale is of order $l_e/R \approx 0.2$; see Hetsroni.[4] In the present experiments, particles are of order 1 mm and $l_e \approx 10$ mm, resulting in $d_p/l_e \approx 0.1$. Therefore, their proposal cannot be examined by the present experiments.

3.9   Conclusions

3D-PTV has been applied to particle-laden pipe flows in up- and downflow for various development stages. The effect of the level of turbulence on the mean relative velocity and the effect of flow direction on concentration profiles have been investigated. All flows have been measured at Re_b =10300. The radial distribution, mean relative velocity and fluctuating velocities of particles and fluid have been measured. Inertia particles with Stokes number equal to 2.3 and 3.3 (based on the ratio of particle relaxation time to viscous scales) and at mean concentrations in the range 0.5×10^{-6} to 1.7×10^{-4} have been applied. The following conclusions and results are derived:

- Transient states of single-phase pipe flows at $Re_b = 10300$ have been characterized by turbulent features. By quantifying the cross-section averaged diagonal components of the Reynolds stress tensor, linear fits distinguish flow conditions from the fully developed one in a convenient way.

- Turbulent pipe flows close to fully developed conditions present linear inhomogeneous behavior in the pipe core. At $Re_b = 10300$, ratios of the diagonal components of the Reynolds stress tensor increase linearly from $r/R = 0$ to $r/R \approx 0.8$.

- When the terminal velocity of particles and a representative RMS turbulent flow velocity are of same order, i.e. $|u_{rms}/U_{TV}| \approx O(1)$, the mean relative velocity decreases with increasing level of flow turbulence.

115

- A correlation between the decrease of the magnitude of the mean axial relative velocity and the increase on local turbulence intensity is provided for the pipe core $(0 < r/R < 0.8$ at $Re_b = 10300)$.

- Flow orientation with respect to gravity has a strong effect on the concentration profile if $|u_{rms}/U_{TV}| \approx O(1)$, with wall peaking in downflow and core peaking in upflow. It is hypothesized that a fluctuating component of the lift force on particles, $<v'_{rel\ z}\ \partial u_z/\partial r>_L$, is responsible for these trends.

- Particle and fluid flow statistics experience significant changes when the concentration for a given radial position exceeds about 3×10^{-4}. Two-way coupling seems to come into play.

- Turbulence augmentation is observed with increasing mean concentration of particles with $Re_p < 12$, $St = 2.3$ or 3.3, $\rho_p/\rho_f \approx 1.05$ and $|u_{rms}/U_{TV}| \approx O(1)$. Criteria based only on Re_p, ratio of turbulence and particle length and time scales, and volume load do not suffice to predict the turbulent modulation found.

- The effect of particle feedback on the fluid is presented with δ-forcing. It is shown that the applied concentrations are too low to affect the frictional pressure drop. Only mean concentrations over 10^{-3} will affect the axial pressure drop for similar conditions (same category of particles and velocimetry results).

References

[1]   C. Poelma, J. Westerweel and G. Ooms: "Turbulence statistics from optical whole-field measurements in particle-laden turbulence". Experiments in Fluids 40(3): p/347-363, (2006).

[2]   A. I. Kartusinsky, E. E. Michaelides, M. T. Hussainov and Y. Rudi: "Effects of the variation of mass loading and particle density in gas–solid particle flow in pipes". Powder Technology, 193, 176-181, (2009).

[3]   R. A. Gore and C. T. Crowe, ''Effect of particle size on modulating turbulent intensity'' Int. J. Multiphase Flow, Vol. 15, No. 2, pp. 279-285, (1989).

[4]   G. Hetsroni: "Particles-Turbulence Interaction", Int. J. Multiphase Flow, Vol. 15, No. 5, pp. 735-746, (1989).

[5]   S. Elgobashi: "On Predicting Particle-Laden Turbulent Flows", Applied Scientific Research 52: 309-329, (1994).

[6]   G. Tryggvason, B. Bunner, A. Esmaeeli, D. Juric, N. Al-Rawahi, W. Tauber, J. Han, S. Nas and Y.-J. Jan: "A Front-Tracking Method for the Computations of Multiphase Flow", Journal of Computational Physics 169, 708–759, 2001.

[7]   C. Poelma, "Experiments in particle-laden turbulence - simultaneous particle/fluid measurements in grid-generated turbulence using particle image velocimetry" Ph.D. thesis, Delft University of Technology (2004).

[8]   L.-P. Wang and M. R. Maxey, ''Settling velocity and concentration distribution of heavy particles in homogeneous isotropic turbulence'', J. Fluid Mech. 256, 27 (1993).

[9]   C. Marchioli, M. V. Salvetti and A. Soldati: ''Some issues concerning large-eddy simulation of inertia particle dispersion in turbulent bounded flows'', Physics of Fluids 20, 040603 (2008).

[10]   A. Soldati, "On the influence of electrohydrodynamics and turbulence on particle transport and collection efficiency in wire-plate electrostatic precipitators", J. Aerosol Sci. 31, 293, (2000).

[11]   E. M. Laws, E. -H. Lim and J. L. Livesey: "Momentum balance in highly distorted turbulent pipe flows", Experiments in Fluids 5, 36 – 42, 1987.

[12]   K. J. Sene, J. C. R. Hunt and N. H. Thomas: "The role of coherent structures in bubble transport by turbulent shear flows". J. Fluid Mech. 259, 219–240, (1994).[13] P. D. M. Spelt and A. Biesheuvel: "On the motion of gas bubbles in homogeneous isotropic turbulence", J. Fluid. Mech., 336, 221-244, (1997).

[14]   R. W. Miller: 1996, Flow Measurement Engineering Handbook. McGraw-Hill, 3rd edition.

[15]   M. P. B. Veenman, "Statistical analysis of turbulent pipe flow: A numerical approach" Ph.D. thesis, Technische Universiteit Eindhoven (2004).

[16]   H. -E. Albrecht, M. Borys, N. Damaschke, and C. Tropea: Laser Doppler and phase Doppler measurement techniques. Springer-Verlag 2003.

[17]   C.W.M. van der Geld: "On the motion of a spherical bubble deforming near a plane wall", Journal of Engineering Mathematics, 2002, Volume 42, Number 2, Pages 91-118.

[18]   J. O. Hinze: 1975, Turbulence. McGraw-Hill.

[19]   L. Schiller and Z. Naumann: "A drag coefficient correlation". Z. Ver. Deutsch. Ing., 77 -318, (1935).

[20]   J. L. G. Oliveira, C. W. M. van der Geld and J. G. M. Kuerten: "Lagrangian and Eulerian statistics of pipe flows measured with 3D-PTV at moderate and high Reynolds numbers", submitted to Flow, Turbulence and Combustion.

[21]   R. J. E. Walpot, P. C. J. N. Rosielle, and C. W. M. van der Geld, "Design of a set-up for high-accuracy 3D-PTV measurements in turbulent pipe flow". Measurement, Science and Technology 17, 3015-3026, 2006.

[22]   H. -G. Maas, "Contributions of digital photogrammetry to 3D-PTV", in "Three-dimensional velocity and vorticity measuring an image analysis techniques", Ed. Th. Dracos, Kluwer Academic Publishers, 1996.

[23]   T. Dracos, "Particle tracking in three-dimensional space", in "Three-dimensional velocity and vorticity measuring an image analysis techniques", Ed. Th. Dracos, Kluwer Academic Publishers, 1996.

[24]   Suzuki, Y., Ikenoya, M. and Kasagi, N., "Simultaneous measurements of fluid and dispersed phases in a particle-laden turbulent channel flow with the aid of 3-D PTV", Experiments in Fluids, 185-193 (2000).

[25]   A. Aliseda and J. C. Lasheras: "Preferential concentration and rise velocity reduction of bubbles immersed in a homogeneous and isotropic turbulent flow", Physics of Fluids, volume 23, 093301, 2011.

[26]   P. Bagchi and S. Balachandar: "Effect of turbulence on the drag and lift of a particle", Physics of Fluids, volume 15, 11, (2003).

[27]   Legendre, D. and Magnaudet, J., ''The lift force on a spherical bubble in a viscous linear shear flow'', J. Fluid Mech. 368, pp. 81-126 (1998).

[28]   Y. Sato and K. Hishida: "Transport process of turbulence energy in particle-laden turbulent flow", Int. J. Heat and Fluid Flow, 17: 202-210, (1996).

[29]   I. M. Mazzitelli, D. Lohse and F. Toschi: "On the relevance of the lift force in bubbly turbulence", J. Fluid Mech. 488, 283 – 313, (2003).

4

Considerations about the concentration profiles of inertia particles and the break-up mechanism in transient particle-laden pipe flows

3D-PTV is applied to particle-laden pipe flows in various stages of development, characterized by both normal and higher levels of turbulence than in fully developed flow. All flows are tested at Reynolds number 10300, based on the bulk velocity and the pipe diameter. The effects of particle Stokes numbers, flow direction (upward or downward) and mean concentration (in the range $0.5\times10-6$ to $1.7\times10-4$) on the turbulence production are shown. The effect of the inhomogeneity of the turbulence on break-up criteria for particles is assessed. Measurements of the turbulence production and the direction-dependent Kolmogorov "constant" allow the evaluation of Hinze's[1] break-up criterion as a function of the radial coordinate. Maximum particle sizes at the pipe centerline can exceed those in the near-wall zone by more than a factor of 10. The effects of transient states and mean volumetric concentration on the particle break-up mechanism are evaluated. A correlation for particle break-up criterion is provided as a function of the radial coordinate.

4.1   Introduction

The dispersion of inertial particles in turbulent flows is characterized by macroscopic phenomena such as a non-homogeneous distribution, large-scale clustering, and preferential concentration due to the inertial bias between particles and surrounding fluid; see Wang and Maxey.[2] The distribution of the dispersed phase may be crucial in determining collision frequency, breakage efficiency, agglomeration, reaction rates, deposition and entrainment; see Marchioli *et al*.[3]

The occurrence of dispersed turbulent flows in pipes is large, with applications ranging from pneumatic conveying systems to chemical reactor design; see Kartusinsky *et al*.[4] Be it in oil pipelines or reactors, the accurate determination of inertia particle distributions is therefore of considerable interest in engineering applications, particularly for controlling the break-up mechanism.

The control of the break-up mechanism plays an essential role in industrial processes, i.e. to enhance transfers, to predict the particle size for determining the two-phase mixture behavior or simply to prevent it, see Risso.[5] Since Hinze (1956), the break-up mechanism has been related to turbulent stresses and turbulent dissipation in particular. However, turbulent pipe flow is inhomogeneous and, consequently, to define break-up criteria in pipes is not simple.

Accurate break-up criteria for pipe flows should take into account information about the concentration profile of the dispersed phase and the inhomogeneity of the turbulence. Other complications also arise. In applications such as separation techniques and droplet-laden flows, particle distributions never reach equilibrium; see Soldati.[6] In industrial loops, turbulent pipe flows often do not achieve a steady state due to the length limitations; see Laws *et al*.[7] The required length for fully developed conditions increases with increasing bulk Reynolds number. Consistent information about the transient state of dispersed turbulent flows is scarce, if non-existent.

In the present study, 3D-PTV is applied to particle-laden pipe flows in various stages of development in order to investigate the impact of varying flow turbulence levels on the break-up mechanism. With the aim of evaluating the effect of flow orientation with respect to gravity on the concentration profiles of particles, an experimental setup is arranged in such way that particle and fluid statistics in upward and downward vertical flows can be measured. The influence of mean volumetric concentration of particles (in the range

0.5×10^{-6} to 1.7×10^{-4}) on turbulence production is also evaluated. All flows are tested at Reynolds number 10300, based on the bulk velocity and the pipe diameter. Particles with diameters equal to 0.8 and 0.96 mm are chosen. Mass density of inertia particles (1050 kg/m^3) slightly exceeds the mass density of the carrier fluid ($\sim$1000 kg/m^3).

The terminal velocity of the dispersed phase, U_{TV}, is attained when gravitational and drag forces on a single particle are in equilibrium in a quiescent fluid. Particle properties (volume and mass density) are selected with the aim of testing particle-laden flows which have the characteristic root-mean-square velocity representative of the turbulent carrier phase, u_{rms}, and the terminal velocity of same order of magnitude: $u_{rms}/U_{TV} \approx O(1)$. Interesting phenomena have been reported when the ratio $u_{rms}/U_{TV} \approx O(1)$ is attained: entrapment of bubbles or particles in vortical flow structures; see Sene *et al.*[8] and Spelt and Biesheuvel[9], for example.

In order to quantify the break-up criterion of Hinze, the turbulent dissipation rate and the Kolmogorov constant have to be known. The former can be estimated from the turbulence production, while the latter can be determined from the Lagrangian velocity correlation function. The turbulent production depends on the cross component of the Reynolds stress tensor and the mean axial velocity. Therefore, the focus in this article is on the dependence of mean axial velocity, cross-component of the Reynolds stress tensor and Lagrangian velocity correlation function on flow orientation, stage of development and particle concentration.

The structure of the paper is as follows. In section 4.2, the experimental setup is presented. Description of the particle-laden experimental conditions is provided in section 4.3. It is shown that turbulent features provide a convenient way to distinguish flow conditions from the fully developed case.

Results are presented in section 4.4. Sub-section 4.4.1 presents results for the concentration profile of inertia particles. The mean axial velocity profiles for carrier and dispersed phases are shown in sub-section 4.4.2. Results of the cross-component of the Reynolds stress tensor are presented in sub-section 4.4.3. In sub-section 4.4.4, turbulence production results are shown. The determination of a direction-dependent Kolmogorov "constant" is provided in sub-section 4.4.5. Sub-section 4.4.6 presents the effect of inhomogeneous turbulence on break-up criteria for pipe flow at $Re_b = 10300$. Discussions about the experimental results and conclusions are given in section 4.5.

4.2 Experimental setup and particle properties

Information about the 3D-PTV experimental setup, particle tracking algorithm and analysis method of particle trajectories has been provided in Chapter 3. For sake of brevity, the reader is referred to Sections 3.2, 3.3 and 3.4. The experimental conditions are rigorously the same ones as applied in Chapter 3; however, the present analysis is given in the perspective of particle break-up. For sake of completeness, a brief description of the experimental conditions is given in Section 4.3. A summary of particle properties is found below in Table 4.1. More information about the applied particles is found in Section 3.2.2.

Table 4.1 Properties of particles applied in the present particle-laden experiments

Particles	*Mass density* [kg/m^3]	*Diameter* d_p [mm]	*Terminal velocity,* /U_{TV}/* [mm/s]	*Re_p	** $St = \tau_p/\tau_f$	*** *Length-scale ratio:* d_p/l_k
Tracers	1050	0.2	1.0	0.18	0.14	0.33 – 1
Type I (PI)	1050	0.8	10.2	7.76	2.31	1.33 – 4
Type II (PII)	1050	0.96	13.1	11.92	3.33	1.6 – 4.8

* Settling velocity of a particle in an infinite, stagnant pool of water.

** Fluid time-scale is based on viscous scales as given by: $\tau_f = v/u_\tau^2$. For $Re_b < 10^5$, the wall shear velocity can be estimated as $u_\tau = (U_b^2 f/8)^{1/2}$ with $f = a\,Re_b^{-m}$, $m = 0.25$ and $a = 0.316$; see Hinze.[10] τ_f is roughly 28 ms.

*** Kolmogorov length-scales for a fully developed single-phase pipe flow at $Re_b = 10300$ as computed from the DNS code developed by Veenman[11]: ≈ 0.6 mm at pipe centerline and ≈ 0.2 mm close to the wall.

4.3 Particle-laden experimental conditions

A division of particle-laden experiments (2P) is shown in a map proposed by Elgobashi[12], see Fig. 4.1. Downward and upward vertical flows have been measured in various stages of development at the same bulk Reynolds number, Re_b. The bulk velocity of each flow, U_b, was adapted to temperature changes to keep $Re_b ≈ 10300$. Single-phase flows (1P) serve as a reference for two-phase flows.
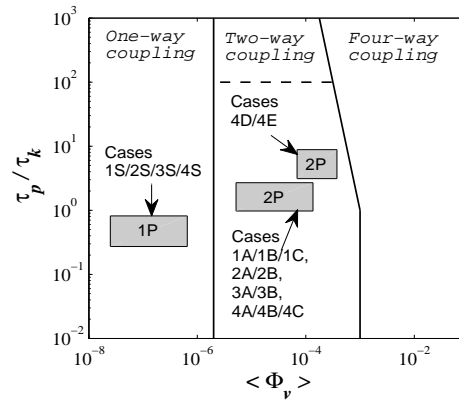
Figure 4.1 Experimental conditions represented in the map of regimes of interaction between particles and turbulence as proposed by Elgobashi.[12]

Particle-laden flows with mean concentrations, $<\Phi_v>$, ranging from 5 x 10^{-6} to 1.7 x 10^{-4} have been tested. The presence or absence of flow conditioners I and II, see Fig. 3.2, affects the stage of flow development in the test section. In upward flows, 3D-PTV measurements are performed at $45D$ downstream of the entrance section; in downward flows, at $20D$. In upflow with flow straightener I a fully developed pipe flow is obtained.[13]

In Fig. 4.1, the rectangular areas represent mean concentration and time-scale ratios of particles in the present experiments. Single-phase flow measurements are represented by 1P in the region denoted as "one-way coupling"; only tracers are employed. Particle-laden measurements are represented by 2P in the region denoted as "two-way coupling"; tracers and inertial particles type I or II, see Table 4.1, are added to the water flow. A mean concentration of tracers less than 10^{-6} is also applied to the particle-laden experiments.

Properties of inertial particles type I or II (volume and mass density) are selected with the aim of testing particle-laden flows which have a characteristic root-mean-square velocity representative of the turbulent carrier phase, u_{rms}, and the terminal velocity of the dispersed phase, U_{TV}, of same order of magnitude: $u_{rms}/U_{TV} \approx O(1)$.

A particle-laden experimental case is represented here by a number (1, 2, 3 or 4) which indicates the flow direction and the presence or absence of a flow conditioner; and a letter (A, B, C, D or E), indicating the applied mean concentration of inertia particles. A summary of all tested particle-laden cases is shown in Table 4.2. The reference single-phase flows are specified by 1S, 2S, 3S or 4S. The letter S denotes single-phase flow and the numbers, as defined above.

123

Table 4.2 Summary of the single-phase and particle-laden flow experiments. All experimental runs have been performed at Reb = 10300

Case	Inertial particles	Flow Direction	Development Length	Flow Straightener	$<\Phi_v>\times 10^{-5}$
1A	Type I (PI)	Upward	45*D*	Bundle I	3.2
1B	Type I (PI)	Upward	45*D*	Bundle I	1.4
1C	Type I (PI)	Upward	45*D*	Bundle I	0.5
1S	--	Upward	45*D*	Bundle I	--
2A	Type I (PI)	Upward	45*D*	--	3.2
2B	Type I (PI)	Upward	45*D*	--	1.9
2S	--	Upward	45*D*	--	--
3A	Type I (PI)	Downward	20*D*	--	2.3
3B	Type I (PI)	Downward	20*D*	--	1.0
3S	--	Downward	20*D*	--	--
4A	Type I (PI)	Downward	20*D*	Bundle II	7.0
4B	Type I (PI)	Downward	20*D*	Bundle II	2.8
4C	Type I (PI)	Downward	20*D*	Bundle II	1.8
4D	Type II (PII)	Downward	20*D*	Bundle II	17.0
4E	Type II (PII)	Downward	20*D*	Bundle II	8.3
4S	--	Downward	20*D*	Bundle II	--

4.3.1 Characterizing turbulent single-phase pipe flows at $Re_b = 10300$

Tracer trajectories have been registered for turbulent single-phase pipe flows in four distinct flow conditions by 3D-PTV. On average 2 x 10^6 velocity vectors have been obtained for each flow case. The velocity vectors are gathered in discrete radial bins in accordance to $r_i \pm \Delta r$, with $\Delta r = 0.5$ mm; see Section 3.4.

Flow velocity statistics of case 1S, upward flow with the bundle flow straightener I, have already been investigated.[13] This case represents the so-called fully developed flow. For case 1S, mean fluctuating velocity components achieve the lowest fluctuation levels among all single-phase experiments.

In order to establish a relationship among cases 1S/2S/3S/4S, the Mean Square Value (MSV) of the velocity fluctuations is determined for each flow condition. The MSV velocity is defined as the product of mean velocity fluctuations: $<u_h u_q>$. Subscripts h and q represent cylindrical coordinates (r, θ, z). Let the overbar character indicate cross-section average.

$$\overline{<u_h u_q>} = (_0\!\int^R <u_h u_q>2\pi r\, dr)/(\pi R^2) \tag{4.1}$$

By considering the diagonal components $<u_h^2>$ and averaging them in accordance to (4.1), it is possible to compare MSV of fluctuating velocities averaged in the cross-section for each single-phase flow case; see Fig 4.2.
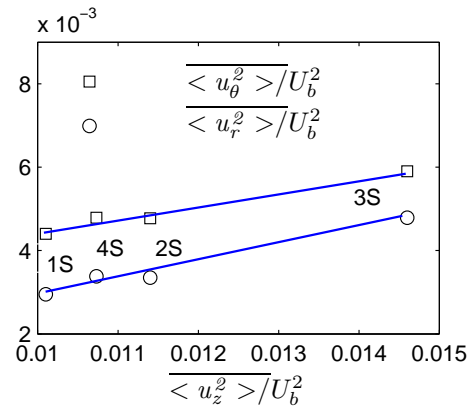
Figure 4.2 Diagonal components of the Reynolds stress tensor averaged in the cross-section for four distinct flow conditions. Computed values are normalized by the square of the bulk velocity of each flow, U_b^2. Lines are added to guide the eye.

The averaged diagonal components, $\overline{<u_h^2>}$, are normalized by the square of the bulk flow velocity, U_b^2, of the corresponding experiment. Here, U_b is chosen for normalization since it was set at each experiment to keep the same Re_b, 10300, irrespective of temperature changes. The bulk velocity is chosen as normalization quantity instead of the wall shear velocity, u_τ, which is often used in the literature, because U_b can be determined more accurately in our experimental setup.

Disturbances created at the entrance affect turbulent flow levels. With sufficient development length, cross-section average turbulence of cases 2S/3S/4S as quantified by Eq. (4.1) becomes equal to the one presented by case 1S. In the presence of flow straighteners, the turbulence intensity levels at the test section are smaller; compare case 2S to 1S for upward flows and 3S to 4S for downward flows in Fig. 4.2. At 20D downstream of the entrance section, flow velocity statistics of downward flow with the bundle flow straightener II (case 4S) are not yet fully developed. Figure 4.2 neatly groups and shows the trend of these measurement conditions.

Linear fits for the computed values of $\overline{<u_h^2>}$ yields:

$$\overline{<u_\theta^2>}/U_b^2 = 0.32\overline{<u_z^2>}/U_b^2 \qquad (4.2)$$

$$\overline{<u_r^2>}/U_b^2 = 0.4\overline{<u_z^2>}/U_b^2 \qquad (4.3)$$

The quality of the fits is expressed by the two parameters r_s^2 and F, defined as follows:

$$r_s^2 = \sum_{i=1}^{n}(\hat{O}_i - \overline{O})^2 / \sum_{i=1}^{n}(O_i - \overline{O})^2 \qquad (4.4)$$

$$F = \{ \sum_{i=1}^{n}(\hat{O}_i - \overline{O})^2 / \sum_{i=1}^{n}(O_i - \hat{O}_i)^2 \}(n-K)/(K-1) \qquad (4.5)$$

Here, n is the number of measurements with outcome O_i, $\hat{O}_i$ the predicted values and $\overline{O}$ the mean of the set (O_i); the number of parameters determined in the fit is K. In Eq. (4.2), r_s^2 and F are equal to 0.98 and 81, respectively. In Eq. (4.3), r_s^2 and F correspond to 0.98 and 84, respectively.

The transient states of pipe flow are of practical interest. In industrial loops, turbulent pipe flows often do not reach fully developed conditions due to the length limitations; see Laws *et al.*[7] The required length enhances with increasing bulk Reynolds number. As observed in Fig. 4.2, the MSV velocities of cases 2S/3S/4S exceed those of case 1S. The fits, Eq. (4.2) and Eq. (4.3), distinguish flow conditions from the fully developed one in a convenient way.

In this section, the present single-phase flow measurements have been categorized. This is achieved by evaluating turbulent flow features. In the next section, particle-laden flow results are presented and compared to the above reference single-phase flows.

4.4   Results

4.4.1   Concentration profiles of inertia particles

The number of tracer trajectories measured in the range $r/R = 0.6$ to 1 decreases with increasing r/R - value. The difficulties in measuring tracer trajectories in this region were mainly due to light reflections stemming from difference between the refractive indices of

water, n ≈ 1.33, and glass, n ≈ 1.51, and the curvature of the glass pipe. Light reflections deteriorate the contrast between tracers and background. However, the fluid flow could also be measured for $r/R > 0.6$ despite the lower number of usable tracers there. The measured concentration of tracers is roughly linear from $r/R = 0$ to 0.6 and decreases towards the wall for all particle-laden flows. In Oliveira *et al.*[13], Eulerian statistics of a single-phase turbulent pipe flow acquired by 3D-PTV have been found to be trustworthy in the near-wall zone if a number of velocity vectors per radial bin exceeding 1000 was acquired. The same criterion is also applied here.

In the detection of inertia particle trajectories, the contrast problem between particles and background did not occur. The bigger imaging projection area of inertia particles on the camera sensor, exceeding the projection of tracers by a factor of 16 or 25, avoided problems on the identification of particles. While the projection of a tracer image occupies nearly an area of 2x2 pixels, the projection of inertia particles occupies 8x8 or 10x10 pixels. Roughly, every 3D inertia particle position identified in the tracking algorithm corresponds to a real particle. On average, an approximate number of 3×10^5 particle positions was identified in each particle-laden case. 3D particle positions were identified with a camera frame rate of 50 Hz in average periods of 50 minutes. In this period, a volume corresponding to ≈ 2.3 m³ crosses the test section. Thus, accurate measurements of concentration profiles of inertia particles have been obtained.

Throughout this article, the errors of time-averaged values of a measured quantity x are estimated with the aid of the so-called standard error, σ_m. Confidence intervals of 95% are considered. For a quantity which is measured n times, with instantaneous results x_i and mean $<x>$, the standard error is given by:

$$\sigma_m = [\sum_{i=1}^{n} (x_i - <x>)^2 / (n\,(n-1))]^{1/2} \tag{4.6}$$

The effect of the flow orientation with respect to gravity on the concentration profiles of inertia particles, $\Phi_v\,(r/R)$, is presented in Fig. 4.3. Here, $\Phi_v\,(r/R)$ represents the time-averaged volume of particles within the volume of the corresponding bin element; see (4.7) and (4.8):

$$<N_{bin,i}> = (1/m) \sum_{j=1}^{m} N_{bin,i}\,(j) \tag{4.7}$$

$$\Phi_v\,(bin,i) = <N_{bin,i}> (V_{particle}/V_{bin,i}) \tag{4.8}$$

127

where j denotes a single photograph and m is the total number of photographs. The subscript *bin,i* denotes a discrete radial position, r/R. The term $<N_{bin,i}>$ represents the average number of particles in a discrete radial bin. $V_{particle}$ denotes the volume of a particle and $V_{bin,i}$ the volume of a bin. The mean concentration of inertia particles, $<\Phi_v>$, refers to the mean of Φ_v (*bin,i*) in all bins, Eq. (4.9). Symbol k represents the total number of radial bins, here 50.

$$<\Phi_v> = (1/k) \sum_{bin,i=0}^{k-1} \Phi_v (bin,i) \qquad (4.9)$$
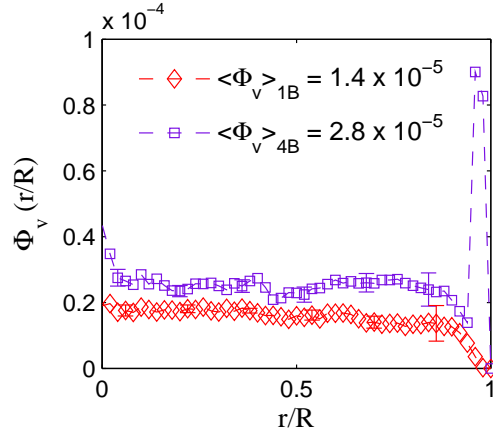
Figure 4.3 Effect of the flow orientation with respect to gravity on the concentration profiles of inertia particles, Φ_v (r/R), in upflow case 1B and in downflow case 4B. Experiments are performed with particles type I. For case 1B, the mean volumetric concentration, $<\Phi_v>$, is 1.4×10^{-5} and for case 4B, 2.8×10^{-5}. Dashed lines are added to guide the eye.

Close to the pipe walls in upflow ($r/R > 0.85$), Φ_v reduces with decreasing distance to the wall. Same trends for the concentration profile of case 1B are found for upflow cases with and without bundle flow straightener I, cases 1A/1C and 2A/2B, respectively. For downflows, there is a peak at about $r/R \approx 0.98$. This trend is also found for other downflow cases with and without bundle flow straightener II, cases 4A/4C/4D/4E and 3A/3B, respectively. Therefore, the direction of the vertical flow, upward or downward, is associated to changes in the concentration profiles, Φ_v (r/R), particularly in the near-wall zone ($0.8 < r/R < 1$). In downflow cases 4D and 4E, inertia particles type I ($St = 2.3$) were replaced by particles type II ($St = 3.3$). In cases 4D/4E, the maximum in Φ_v is also found at

$r/R \approx 0.98$. For sake of brevity, only the concentration of two cases, upflow 1B and downflow 4B, are shown. The plot in Fig. 4.3 is sufficient to depict the main features of the effect of the flow orientation with respect to gravity for the selected particle-laden pipe flows. More information about the concentration profiles of inertia particles, including all the plots, is given in section 3.6.2.

A summary of the results for concentration profiles is shown in Table 4.3. Some ratios were created to characterize the concentration profiles in the present experiments. For example, the ratio of the maximum concentration found in a discrete bin to the mean concentration, $\Phi_{v,max}/<\Phi_v>$, and the ratio of the mean concentration from $0 <r/R< 0.8$ to $0.8 <r/R< 1$, R_Φ. The ratio R_Φ is defined as $<\Phi_v>_{(0<r/R<0.8)}/<\Phi_v>_{(0.8<r/R<1)}$. Both terms $<\Phi_v>_{(0<r/R<0.8)}$ and $<\Phi_v>_{(0.8<r/R<1)}$ are computed similarly to the mean concentration, $<\Phi_v>$, Eq. (4.9), but in the indicated parts of the measurement section volume.

Table 4.3 Results of the inertia particle concentrations for the present experiments

Case	Inertial particles	Flow Direction	Flow Straightener	d_p/R $\times 10^{-3}$	$<\Phi_v>\times$ 10^{-5}	R_Φ*	$\dfrac{\Phi_{v,max}}{<\Phi_v>}$	r_{max}/R
1A	Type I	Upward	Bundle I	16.0	0.5	1.72	1.51	~ 0
1B	Type I	Upward	Bundle I	16.0	1.4	1.75	1.42	~ 0
1C	Type I	Upward	Bundle I	16.0	3.2	1.65	1.25	~ 0
2A	Type I	Upward	--	16.0	1.9	1.97	1.74	~ 0
2B	Type I	Upward	--	16.0	3.2	1.92	1.81	~ 0
3A	Type I	Downward	--	16.0	1.0	1.10	2.92	~ 0.98
3B	Type I	Downward	--	16.0	2.3	1.17	3.17	~ 0.98
4A	Type I	Downward	Bundle II	16.0	1.8	0.75	3.55	~ 0.98
4B	Type I	Downward	Bundle II	16.0	2.8	0.81	3.21	~ 0.98
4C	Type I	Downward	Bundle II	16.0	7.0	0.47	4.15	~ 0.98
4D	Type II	Downward	Bundle II	19.2	8.3	0.33	4.58	~ 0.98
4E	Type II	Downward	Bundle II	19.2	17.0	0.41	5.80	~ 0.98

* R_Φ is defined as: $<\Phi_v>_{(0<r/R<0.8)}/<\Phi_v>_{(0.8<r/R<1)}$

4.4.2 Mean axial velocity profiles

Inertia particle and tracer trajectories have been registered by 3D-PTV at a camera frame rate of 50 Hz. On average, 2×10^6 velocity vectors for tracers and 3×10^5 for inertia particles have been obtained for each particle-laden case. The velocity vectors are

ensemble-averaged in distinct radial bands, which are delimited by a discrete width of $\pm \Delta r$ = 0.5 mm around a chosen radius, see Oliveira *et al*.[13]

The effects of upward or downward flow direction on the mean axial velocity profiles of fluid, $<U_z>$, and inertia particles, $<v_{p,z}>$, are presented in Fig.'s 4.4 and 4.5. The flow bulk velocity, U_b, was adjusted to keep the same Re_b for each experiment, 10300. Inertia particle and tracer velocity profiles are normalized in these figures by the corresponding U_b. In each plot, the reference single-phase velocity profile is also shown. Error-bars in Fig.'s 4.4 and 4.5 have same sizes as symbols.

To check the fluid mean axial velocity profiles of particle-laden cases seen in Fig.'s 4.4 and 4.5, the following procedure was followed. For each fluid flow profile, the product of the fluid mean axial velocity and the area of each discrete bin, $(<U_z>)_k \times A_k$, was integrated to obtain the mean volumetric flow rate, Q, which crossed the measurement volume. Temperature measurements yielded the water mass density, ρ. The product $\rho \times Q$ gave the mass flow rate for each experimental set, which corresponded to the ones given by the Coriolis meter within its inaccuracy range. The mass flow rate is measured by means of a Micro Motion Elite CMF300 Coriolis mass flow and mass density meter, whose inaccuracy is less than 0.5% of the registered flow rate.

4.4a   4.4b

Figure 4.4 Effect of upward flow direction on the mean axial velocity profiles, $<U_z>$ and $<v_{p,z}>$, of particle-laden case 1B. The velocities are normalized by the bulk velocity of each flow, U_b. The subscript 1S denotes single-phase flow, and 2P and PI, tracers and inertia particles type I in two-phase flow. In case 1B, the mean volumetric concentration, $<\Phi_v>$, is 1.4×10^{-5}. Dashed lines are added to guide the eye. Error-bars have same sizes of symbols. Figure 4.4a presents velocity profiles in the range $0 <r/R< 0.85$ and Fig. 4.4b, in the range $0.85 <r/R< 1$. The number of line markers corresponds to the number of bins measured; notice the difference in scales.

In Fig. 4.4, the mean axial velocity profiles of inertia particles and tracers for case 1B are presented. Comparison of mean axial fluid velocities for single-phase and two-phase flows, cases 1S and 1B, indicates a slight reduction in the mean flow velocity in the radial range: $0 <r/R< 0.93$. This reduction is compensated by an increase in mean fluid velocity in the range $0.93 <r/R< 1$. Similar modifications to the mean axial fluid velocity of particle-laden case 1B are found for upward cases with and without the bundle flow straightener I, cases 1A/1C and 2A/2B, respectively.

4.5a   4.5b
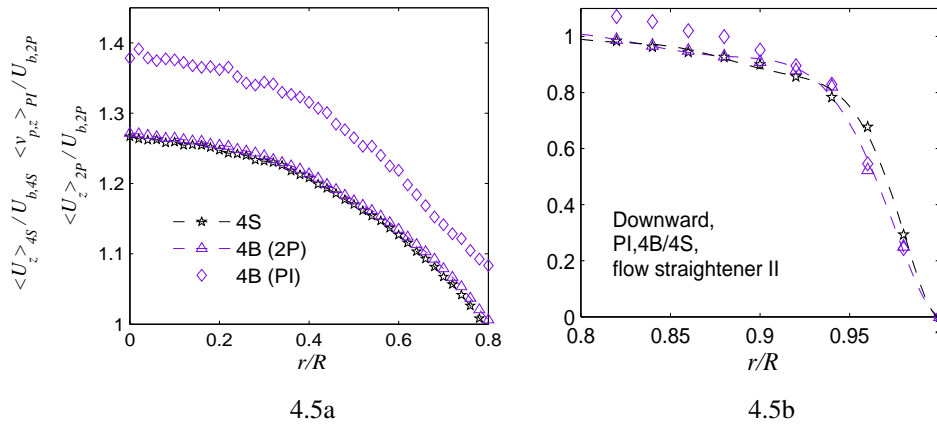
Figure 4.5 Effect of downward flow direction on the mean axial velocity profiles, $<U_z>$ and $<v_{p,z}>$, of particle-laden case 4B. The velocities are normalized by the bulk velocity of each flow, U_b. The subscript 4S denotes single-phase flow, and 2P and PI, tracers and inertia particles type I in two-phase flow. In case 4B, the mean volumetric concentration, $<\Phi_v>$, is 2.8×10^{-5}. Dashed lines are added to guide the eye. Error-bars have same sizes of symbols. Figure 4.5a presents velocity profiles in the range $0 <r/R< 0.80$ and Fig. 4.5b, in the range $0.80 <r/R< 1$. The number of line markers corresponds to the number of bins measured; notice the difference in scales.

In Fig. 4.5, the mean axial velocity profiles of inertia particles and tracers for downflow case 4B are presented. Comparison of mean axial fluid velocities for single-phase and two-phase flows, cases 4S and 4B, indicates a slight increase in flow velocity in the radial range: $0 <r/R< 0.93$. This increase is compensated by a reduction in fluid velocity in the range $0.93 <r/R< 1$. Similar changes to the mean axial fluid velocity of particle-laden case 4B are also found for other downward cases with and without the bundle flow straightener II, cases 4A/4C/4D/4E and 3A/3B, respectively. Therefore, the direction of the vertical flow, upward or downward, is associated to the changes in the mean axial velocity profiles.

Results are only shown for two cases, upflow 1B and downflow 4B. The plots in Fig.'s 4.4 and 4.5 are sufficient to depict the changes on the fluid profiles of selected particle-laden flows. These changes are related to modifications on the turbulence production of particle-laden flows, which are shown later in this section. More information about the mean axial velocity profiles of fluid and inertia particles is given in Section 3.6.3.

4.4.3 Cross-component of the Reynolds stress tensor

The effects of flow orientation with respect to gravity (upflow or downflow), different stages of development and mean volumetric concentration on the cross-component of the Reynolds stress tensor, $<u_r u_z>$, are presented in Fig. 4.7. The lowercase u indicates the fluctuating fluid velocity. Results are normalized by the square of the bulk flow velocity, U_b^2, of the corresponding experiment. Results for the reference single-phase cross-component are also shown. A cylindrical coordinate system with origin at the pipe centerline and with the axial axis anti-parallel to the gravitational acceleration is assumed for down- and upward flows; see Fig. 4.6.
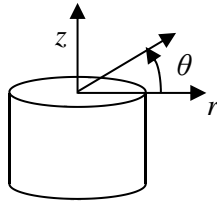
Figure 4.6 Cylindrical coordinate system for up- and downward flows. The origin is at the pipe centerline and the axial axis is anti-parallel to the gravitational acceleration.

In inhomogeneous fully developed pipe flows, the only decoupled direction is the tangential, which means that correlations $<u_\theta u_r>$ and $<u_\theta u_z>$ are zero. For all measured particle-laden developing flows, values of cross-components including the tangential direction have been checked. They are close to zero and therefore not shown.

In Oliveira *et al.*[13], results of the single-phase fully developed flow, case 1S, have been compared to the DNS results of Veenman.[11] The 3D-PTV data of case 1S presented good agreement with DNS within measurement error. Good agreement is found for the fluid cross-components of cases 1S and 1B (Fig. 4.7a). Results for cases 1A/1C are similar to the ones of 1B. For fully developed particle-laden pipe flows in upward direction and in the presence of particles type I with $<\Phi_v>$ less than 3.2×10^{-5}, the flow turbulence is barely modified. In fact, all particle-laden flows within the same development stage and with $<\Phi_v>$ less than 3.2×10^{-5} present similar results for $<u_r u_z>$. This also holds for upward flows without flow straightener, cases 2A/2B, for downward flows without flow straightener,

3A/3B, and for downward flows with the flow straightener II, cases 4A/4B. Therefore, only one of them is sufficient to present the main features of $<u_r u_z>$.

For all results presented in Fig.'s 4.7b – 4.7f, the cross-component profile of case 1B is added to show the differences with the fully developed condition. Upward flows at 45D from the entrance region and without the presence of the bundle flow straightener I, cases 2A/2B/2S, yields similar results to case 1B.

For comparing the experimental results, the fluctuation values are weighed with the area of the corresponding bin in order to get proper averages. This averaging procedure is adopted through this whole section. Results for particle-laden downflows at 20D from the entrance region and without the presence of the flow straightener, cases 3A/3B, are modified in comparison with the single-phase flow, case 3S. For those cases, cross-component values are increased for flows with mean concentrations about 1.0×10^{-5} and 2.3×10^{-5}. In the pipe core ($0 < r/R < 0.6$), values of $|<u_r u_z>|$ are increased by 20 % for case 3A. The discrepancies with the fluctuation levels of a fully developed flow are increased in the presence of inertia particles.

Results of downflows at 20D from the entrance region, with the presence of the bundle flow straightener II and with mean concentration less than 2.8×10^{-5}, cases 4A/4B, are similar to the reference single-phase flow, case 4S. The discrepancies with the fluctuation levels of a fully developed flow are particularly pronounced for the radial range $0.6 <r/R< 0.9$ (Fig. 4.7d). The cross-component results for downflow with a mean concentration about 7.0×10^{-5}, case 4C, differ from cases 4A/4B/4S. Significant changes are observed to $<u_r u_z>$ when the mean concentration, $<\Phi_v>$, exceeds 7.0×10^{-5} in downward flows in the presence of the flow straightener II. A cross-section averaged increase of 13% is observed for case 4C in comparison to case 4S. As a consequence, the discrepancies with the fluctuation levels of a fully developed flow are also increased.

Results of downflow at 20D from the entrance region, with the presence of the bundle flow straightener II and with mean concentration about 1.7×10^{-4}, case 4E, is presented in Fig. 4.7f. Results of case 4D are similar and therefore not shown. In cases 4D/4E, inertia particles type II have been applied. Values of the cross-component of case 4E are increased in comparison to the components of case 4C. In comparison to single-phase flow case 4S, the increase in $|<u_r u_z>|$ of case 4E is on average 20 % in the entire cross-section. As a consequence, the discrepancies with the fluctuation levels of a fully developed flow are increased.

134

4.7a

4.7b

4.7c

4.7d

4.7e

4.7f
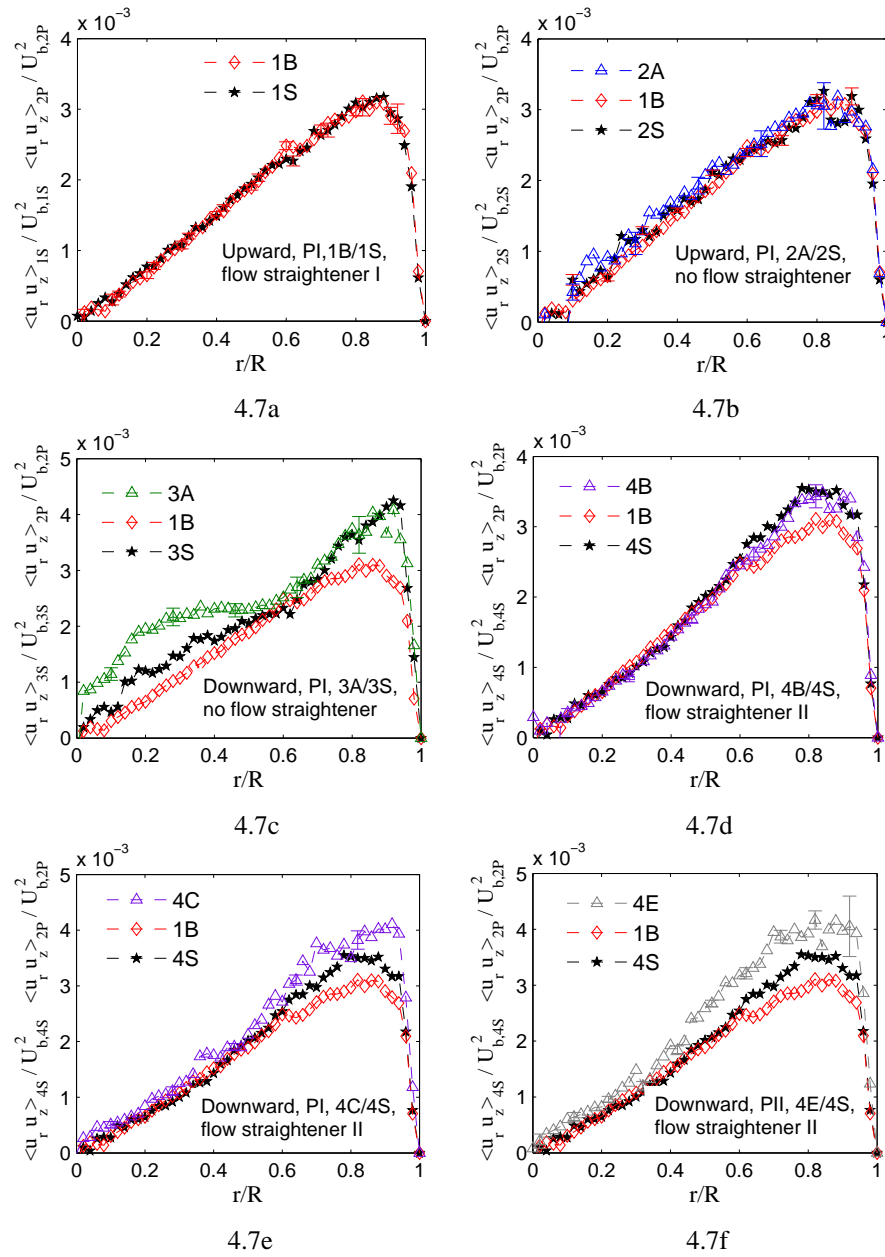
Figure 4.7 Effects of the mean concentration, $<\Phi_v>$, different stages of development and flow orientation with respect to gravity (upflow or downflow) on the cross-component of the Reynolds stress tensor, $<u_r u_z>$, for particle-laden flows 1B/2A/3A/4B/4C/4E. Results are normalized by U_b^2. The subscripts 1S/2S/3S/4S denote single-phase reference flows and 2P, tracers in two-phase flow. The terms PI and PII stand for inertia particles type I and II, respectively. Dashed lines are added to guide the eye.

135

A summary of the results presented in Fig. 4.7 is found in Table 4.4. Cross-section averaged ratios of present particle-laden flows to the corresponding single-phase references (cases 1S, 2S, 3S, 4S) are shown for $<u_r u_z>$. Results are normalized by U_b^2. The cross-section averaging is performed according to Eq. (4.10):

$$\overline{<u_r u_z>} = ({}_0\!\int^R <u_r u_z>2\pi r\,dr)/(\pi R^2) \tag{4.10}$$

Table 4.4 clearly shows how the cross-component of the Reynolds stress tensor is modified by the presence of inertia particles at the given concentrations and flow conditions. Only particle-laden flows with high levels of turbulence, cases 3A/3B, or flows with the highest volume loads, cases 4D/4E, present significant increase in the averaged cross-component in relation to the single-phase counterpart. About 9% for case 3B and 20 % for case 4E.

Table 4.4 Cross-section averaged ratios of the cross-components of the Reynolds stress tensor

Case	1A	1B	1C	2A	2B	3A	3B	4A	4B	4C	4D	4E
$\dfrac{\overline{(<u_r u_z>/U_b^2)}_{2P}}{\overline{(<u_r u_z>/U_b^2)}_{1P}}$	1.01	1.01	1.02	1.01	1.02	1.08	1.09	1.01	1.00	1.13	1.19	1.20
$\dfrac{\overline{(<u_r u_z>/U_b^2)}_{2P}}{\overline{(<u_r u_z>/U_b^2)}_{1B}}$	1.00	1	1.01	1.03	1.04	1.28	1.29	1.07	1.06	1.25	1.34	1.35

In Table 4.4 the cross-section averaged ratios of particle-laden flows to the reference flow (case 1B) are also presented. Case 1B represents the fluid turbulence of a fully developed particle-laden flow in weak two-way coupling. The averaged cross-components for cases 3B and 4E are, respectively, 29 and 35 % larger than for case 1B.

4.4.4 Turbulent production of energy

As will be seen in sub-section 4.4.6, the production of turbulent kinetic energy is important for the appraisal of particle break-up. The production of kinetic energy in the macro scales is given by:

$$P_k = \Sigma_i\, \Sigma_j <u_i u_j> (\partial<U_i>/\partial x_j) \tag{4.11}$$

in a Cartesian coordinate system $\{x_j\}$. For pipe flows not far from a fully developed condition, the only meaningful component is: $<u_r u_z> \partial<U_z>/\partial r$.

The effects of the flow orientation with respect to gravity (upflow or downflow) and different stages of development on the turbulence production, P_k, for particle-laden flows 1B/3A are presented in Fig. 4.8. Results are normalized by the cube of the bulk velocity of each flow divided by the pipe radius, U_b^3/R. Results for the reference single-phase flows cases 1S/3S are also shown. Figures 4.8a and 4.8c present profiles in the range $0 <r/R< 0.7$ and Fig.'s 4.8b and 4.8d, in the range $0.7 <r/R< 1$.

Good agreement is found for the results of cases 1S and 1B. Results for case 1B resemble the ones of other particle-laden upflows, cases 1A/1C/2A/2B, and are not shown here. For particle-laden upflows and in the presence of particles type I with $<\Phi_v>$ less than 3.2×10^{-5}, the turbulence production is barely modified. An exception is made for the radial location of the maximum in P_k , which is shifted from $r/R \approx 0.96$ to 0.98 in upflows (Fig. 4.8b).

For particle-laden downflows at $20D$ from the entrance region and without the presence of a flow straightener, cases 3A/3B, results are modified in comparison with the single-phase flow, case 3S. Results for case 3A are similar to the ones of case 3B. For these cases, turbulence production values are enhanced for flows with mean concentrations about 1.0×10^{-5} and 2.3×10^{-5}. Considering the entire cross-section, the averaged value of P_k is increased by 14 % for case 3A. The discrepancies with the turbulent production levels of a fully developed particle-laden flow are also increased, exceeding about 80% of the cross-section averaged value of P_k for case 1B.

4.8a

4.8b

4.8c

4.8d
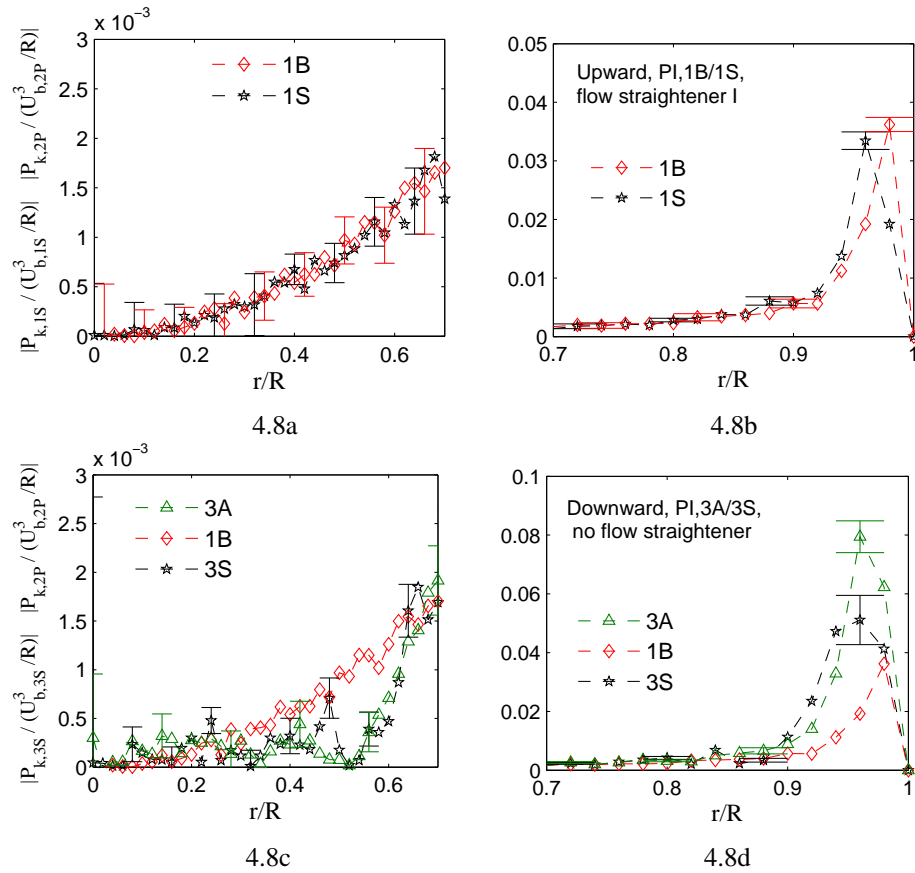
Figure 4.8 Effect of the flow orientation with respect to gravity (upflow or downflow) and different stages of development on the turbulence production, P_k, for particle-laden flows 1B/3A. Results are normalized by U_b^3/R. The subscripts 1S/3S denote single-phase reference flow and 2P, tracers in two-phase flow. Dashed lines are added to guide the eye. The number of line markers corresponds to the number of bins measured; notice the difference in scales.

The effect of the mean concentration, $<\Phi_v>$, on the turbulence production, P_k, for particle-laden downflows 4B/4C/4E is presented in Fig. 4.9. Results are also normalized by U_b^3/R. Results for the reference single-phase flow, case 4S, are also shown. Figures 4.9a, 4.9c and 4.9e present profiles in the range $0 <r/R< 0.7$ and Fig.'s 4.9b, 4.9d and 4.9f, in the range $0.7 <r/R< 1$. For the results presented in Fig. 4.9, the turbulence production profile of case 1B is added to show the differences with the fully developed condition.

4.9a

4.9b

4.9c

4.9d

4.9e

4.9f
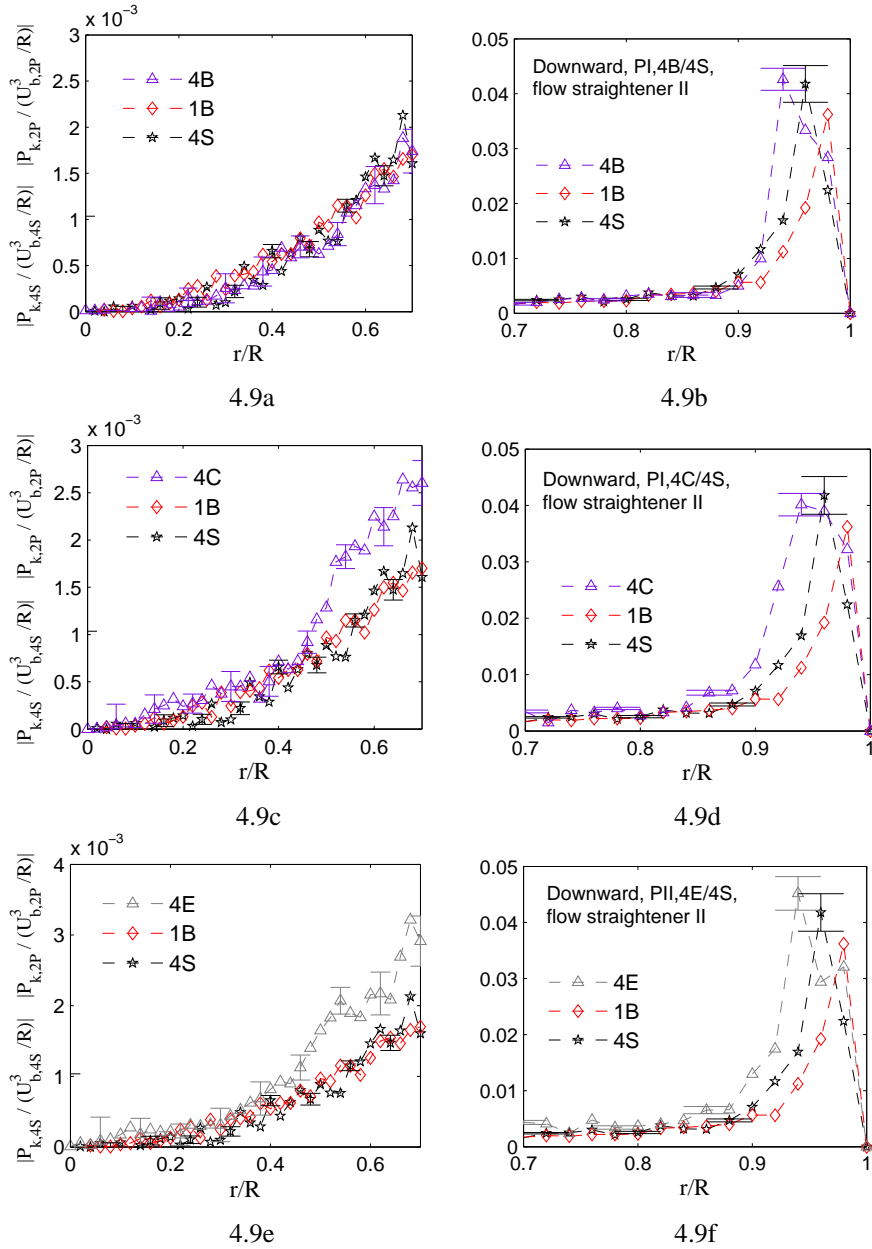
Figure 4.9 Effect of the mean concentration, $<\Phi_v>$ on the turbulence production, P_k, for particle-laden flows 4B/4C/4E. Results are normalized by U_b^3/R. The subscript 4S denotes single-phase flow and 2P, tracers in two-phase flow. Dashed lines are added to guide the eye. The number of line markers corresponds to the number of bins measured; notice the difference in scales. The terms PI and PII stand for inertia particles type I and II, respectively.

Results for cases 4A and 4D resemble the ones for cases 4B and 4E, respectively, and are not presented. For downflows at $20D$ from the entrance region, in the presence of bundle flow straightener II and with mean concentration less than 2.8×10^{-5}, cases 4A/4B, production is enhanced with respect to the reference single-phase flow, case 4S. The radial location of the maximum in P_k is shifted from $r/R \approx 0.96$ to 0.94 in downflows (Fig. 4.9b). Considering the entire cross-section, the averaged value of P_k is increased by 9 % for case 4B in comparison to case 4S and by 19% in comparison to the fully developed case 1B.

By increasing the mean volumetric concentration of particles in downflows from 2.8×10^{-5} to 7.0×10^{-5}, cases 4B and 4C, respectively, the discrepancies with the fluctuation levels of a fully developed flow, 1B, and the single phase reference flow, 4S, also increase. For case 4C, cross-section averaged values of P_k are increased by 33 and 51% in relation to cases 4S and 1B, respectively. With a further increase in the mean concentration to 1.7×10^{-4}, case 4E, cross-section averaged values of P_k are increased by 37 and 59% in relation to cases 4S and 1B, in the order mentioned.

The change from $r/R \approx 0.96$ to 0.94 in the position of the maximum in P_k is also observed for downflows 4C and 4E (Fig.'s 4.9d and 4.9f) and it is contrast to the shift in upflows from $r/R \approx 0.96$ to 0.98. For the selected particle-laden flows, flow orientation with respect to gravity affects the location of the maximum in P_k. With the changes in the fluid mean velocity profiles as observed in section 4.4.2, the mean strain rate is also modified. Figure 4.10 shows the effect of up- or downflow and different stages of development on the mean strain rate, $\partial<U_z>/\partial r$, for particle-laden flows 1B/3A/4B. Error-bars have same sizes as symbols. Figure 4.10a presents results in the range $0 <r/R< 0.80$ and Fig. 4.10b, in the range $0.80 <r/R< 1$.

4.10a   4.10b
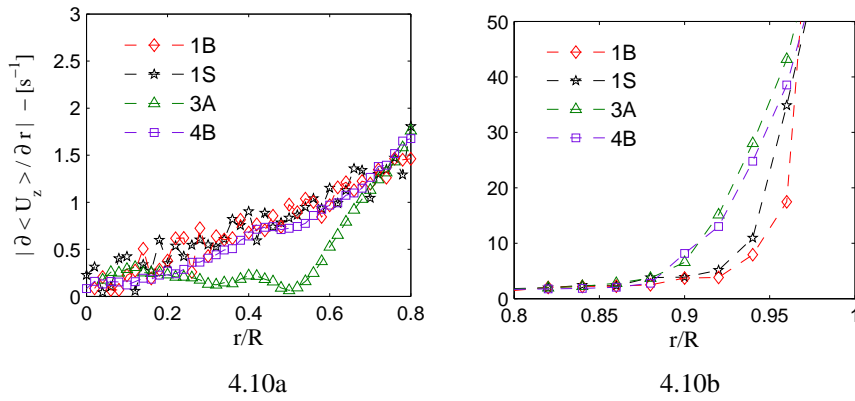
Figure 4.10 Effect of the flow orientation with respect to gravity (upflow or downflow) and different stages of development on the mean strain rate, $\partial<U_z>/\partial r$, for particle-laden flows 1B/3A/4B. The subscript 1S denotes single-phase fully developed flow. Dashed lines are added to guide the eye. The number of line markers corresponds to the number of bins measured; notice the difference in scales.

The gradient of the mean strain rate in radial direction is strongly modified at about $r/R \approx 0.88$ for particle-laden downflows and at about 0.92 for particle-laden upflows. For single-phase flows, this happens in radial positions about 0.90. The position shift in the maximum of P_k is apparently related to the changes in the mean strain rate profile, which can be understood in terms of local decrease in relative velocity. In upflows, the drag imposed to the fluid by particles results in a reduction of the fluid velocity in the pipe core. This reduction is compensated by mass conservation with an increase in the fluid velocity in the near wall-zone. The opposite trend is found in downflows. For case 3A, the flat profile of the mean strain rate in the range $0 < r/R < 0.5$ explains the small values of P_k there (Fig.'s 4.8c and 4.10a).

A summary of the results presented in Fig.'s 4.8 and 4.9 is found in Table 4.5. Cross-section averaged ratios of present particle-laden flows to the corresponding single-phase references (cases 1S, 2S, 3S, 4S) are shown for P_k. Comparisons to the fully developed reference flow (case 1B) are also presented. Results are normalized by U_b^3/R. The cross-section averaging is performed according to Eq. (4.12):

$$\overline{P_k} = (_0\!\int^R <u_r u_z> (\partial<U_z>/\partial r)2\pi r\,dr)/(\pi R^2) \qquad (4.12)$$

Table 4.5 Cross-section averaged ratios of the turbulence production

Case	1A	1B	1C	2A	2B	3A	3B	4A	4B	4C	4D	4E
$\dfrac{[\overline{P_k}/(U_b^3/R)]_{2P}}{[\overline{P_k}/(U_b^3/R)]_{1P}}$	1.01	1.02	1.02	1.03	1.03	1.14	1.15	1.08	1.09	1.33	1.35	1.37
$\dfrac{[\overline{P_k}/(U_b^3/R)]_{2P}}{[\overline{P_k}/(U_b^3/R)]_{1B}}$	0.99	1	1	1.03	1.03	1.81	1.79	1.18	1.19	1.51	1.58	1.59

In the measured development stages, turbulence production is larger than in fully developed flows. Turbulence production is enhanced for particle-laden flows with $|u_{rms}/U_{TV}|$ of order 1 and particles with $St = 2.3$ or 3.3, and even more so if the volumetric concentration is higher or if the level of turbulence is higher.

4.4.5 Direction-dependent Kolmogorov constant

The second order Lagrangian velocity structure function, $D_{kk}(\tau)$, is defined by Eq. (4.13):

$$D_{kk}(\tau) = <[u_k(\tau) - u_k(0)]^2> \qquad (4.13)$$

where τ is the correlation time span and u the fluctuating fluid velocity. The subscript k indicates cylindrical coordinate components (r, z, θ). The quantity $D_{kk}(\tau)$ determines the Kolmogorov constant C_0, which is necessary in the evaluation of particle break-up, see van Wissen *et al.*[14] Kolmogorov theory of local isotropy gives a scaling rule connecting the fluid structure functions with the universal Kolmogorov constant, C_0; see Pope.[15] The scaling rule is given by Eq. (4.14):

$$D_{kk}(\tau) = C_0 <\varepsilon>\tau \qquad (4.14)$$

where ε is the dissipation rate given by $\varepsilon = 2vS_{km}^2$. v is the kinematic viscosity and S_{km} the rate-of-strain tensor. The last one is given by: $S_{km} = (1/2)(\partial U_k/\partial x_m + \partial U_m/\partial x_k)$, with U the instantaneous fluid velocity and x the space coordinate. Eq. (4.14) is valid in the inertial sub-range for time τ in the interval: $\tau_k << \tau << \tau_c$. The Kolmogorov time-scale, τ_k, is representative of dissipative scales, while the Lagrangian correlation time, τ_c, is representative of large energy-containing scales. In turbulent flows, τ_k is related to τ_c by the Reynolds number: $\tau_k = \tau_c Re^{-1/2}$. Since turbulent pipe flows are inhomogeneous in radial direction, τ_k and τ_c are function of the radial coordinate. In section 3.2.2, an average

estimation for τ_k was computed, roughly 28 ms. For $Re_b = 10300$, that would result in the following average estimation of τ_c: 2.8 s.

Due to the hypothesis of local isotropy, turbulence statistics are invariant to rotations and reflections of the coordinate system. The local isotropy assumption implies that the structure functions in the three principal directions are equal and therefore C_0 is a constant. At the level of second order statistics, the local isotropy assumption for very large Reynolds numbers has been very successful, see Mydlarski and Warhaft.[16] However, the present Reynolds number is far from this limit. This makes it necessary to introduce a direction-dependent C_0^k. This was proposed by Pope[17] in a linear stochastic model for homogeneous shear flow. Later, Walpot et al.[18] followed the same proposal for the definition of C_0 for inhomogeneous pipe flow. According to Kolmogorov similarity, one should observe a plateau of C_0 in the inertial subrange. However, for the limited Reynolds numbers studied here, the inertial subrange has finite width. For finite Reynolds numbers, the plateaus of C_0 may be short or exist only as bumps, see Lien and D'asaro.[19] Therefore, the value of C_0 will be determined from the maximum in the function of $D_{kk}(\tau)/<\varepsilon>\tau$.

Lagrangian structure function for the radial velocity component scaled with $<\varepsilon>\tau$ is presented at r/R=0.7 in Fig. 4.11. The calculation of $D_{kk}(\tau,r)$ is done by averaging over flow tracers that are situated inside a discrete band centered at a radial position r. The solid line represents DNS data.[11] Diamonds represent flow tracers in particle-laden pipe flow for case 1B at $Re_b = 10300$. Dashed lines indicate error-bars. Information about the applied Lagrangian method of analyzing particle trajectories in pipes is provided in Oliveira et al.[13]
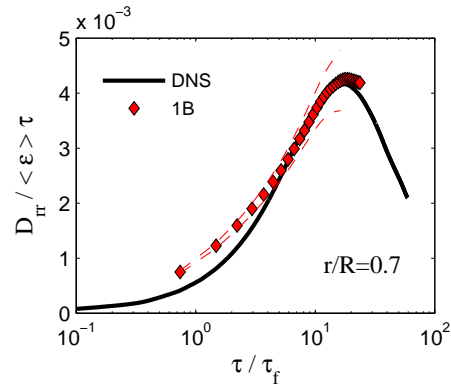
Figure 4.11 Lagrangian structure function for the radial velocity component scaled with $<\varepsilon>\tau$ at r/R=0.7 for case 1B. The solid line represents DNS at $Re_b = 10300$. Dashed lines indicate error-bars.

Trajectories of tracers have been registered long enough to achieve the time interval where the maximum occurs; see Fig. 4.11. The value of C_0^k is the value of $D_{rr}/\langle\varepsilon\rangle\tau$ at the maximum. Similar results are found at other radial positions and for tangential structure functions. For axial structure functions, the Lagrangian correlation times are bigger and the time interval where the maxima occur cannot be achieved due to the limited axial length of the measurement volume. For this case, the axial structure functions are fitted with a linear function in a time interval that is assumed to be in the inertial range; see Section 5.3.2. This approach was also done by Walpot et al.[18] Results for the direction-dependent C_0^k thus obtained are provided in Fig. 4.12. Values of C_0^k are roughly 3 in the pipe core ($r/R < 0.8$) and decrease with decreasing distance to the wall. The decrease of C_0^k with decreasing distance to the wall is for tracers also found by Choi et al.[20] for turbulent channel flow. This result is in good agreement to single-phase experimental results of Walpot et al.[18] and to the DNS computations of Veenman.[11]
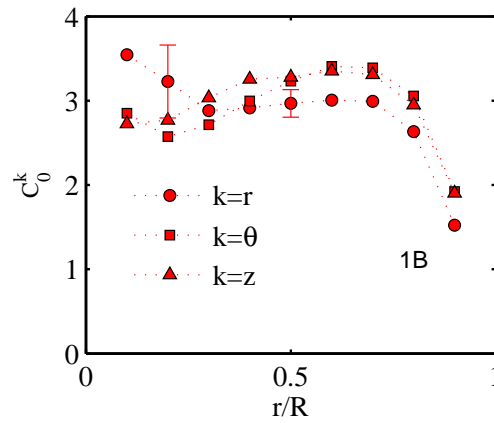
Figure 4.12 Direction-dependent Kolmogorov, C_0^k, constant computed for case 1B. k represents cylindrical coordinates (r, z, θ). Dotted lines are added to guide the eye.

As mentioned above, C_0 is a quantity necessary to determine break-up criteria. Since turbulent pipe flows are inhomogeneous in radial direction, the determination of a direction-dependent C_0^k is necessary. With the above determination of the Kolmogorov constant and turbulence production, all the ingredients to evaluate break-up criteria in pipe flows are available. The computation of a direction-dependent C_0^k for particle-laden flows is further investigated in Section 5.3.2.

144

4.4.6   Particle break-up in turbulent pipe flows

In many mixtures in process industry small particles occur that have a chance of being torn apart if exposed to too high fluid stresses; see van Wissen *et al.*[21] This section presents the effect of inhomogeneous turbulence in pipe flow at Re_b=10300 on the particle break-up mechanism. In principle, the break-up process is isotropic; however it is strongly dependent on the distance to the pipe wall. The prediction of the maximum particle diameter, $d_{p,max}$, in turbulent flows is usually based on the pioneering article by Hinze (1956). If particle sizes are in the inertial subrange, this approach states that a critical value of the following Weber number, We_{crit}, exists:

$$(\rho_f/\sigma\, We_{crit})^{3/5}\, d_{p,max} = C_0^{*-3/5}\, \varepsilon^{-2/5} \qquad (4.15)$$

where ρ_f is the mass density of the continuous phase, σ surface tension coefficient, ε turbulent dissipation and C_0^{*} the Kolmogorov constant.

Several authors, i.e Walter and Blanch[21] and Hesketh *et al.*[22], employed the approach given by Eq. (4.15) and proposed different expressions for We_{crit}. No universal correlation is available or takes into account all the possible effects for the prediction of break-up in pipe flows such as large mean-velocity gradients near the pipe wall.[5] Critical Weber numbers are usually a function of particle and fluid properties[21,22]. In other proposals for We_{crit}, the bulk flow velocity is also taken into, see Karabelas[23] for example. The terms on the LHS of Eq. (4.15) depend on the specific properties of the continuous and dispersed phase and on the proposal for We_{crit}. However, the terms on the RHS can be evaluated from the measured data discussed in this section and show how the maximum particle diameter depends on the radial coordinate, the particle concentration and the state of development of the turbulence. This will be investigated next.

In turbulent pipe flows, turbulent dissipation is largest near the wall. Apart from the viscous region near the wall and from a small area at the central region (where dissipation balances turbulent transport), turbulent dissipation is of the same order of magnitude as turbulence production[11], $\varepsilon \approx P_k$. Measurements of the latter in particle-laden up- and downward flows have been shown above together with the direction-dependent Kolmogorov constant, C_0^{k}, as given in Fig. 4.12. With these measurements, the RHS of Eq. (4.15) can be determined as a function of the radial coordinate. Here, values of a modified

145

constant, C_0^*, are computed by averaging C_0^z, C_0^r and C_0^θ at each radial bin. With the above determination of C_0^* and P_k, all the ingredients to evaluate existent break-up criteria for pipe flows which takes into account the inhomogeneity of the turbulence are available for the given Reynolds number.

The computation of the RHS of Eq. (4.15) is now carried out with the present experimental data. In Fig. 4.13, results are shown for particle-laden cases 1B/2A/3A/4B/4C/4E. The effects of different stages of development and mean volumetric concentration of particles (in the range 0.5×10^{-6} to 1.7×10^{-4}) on particle break-up are presented.

4.13a   4.13b
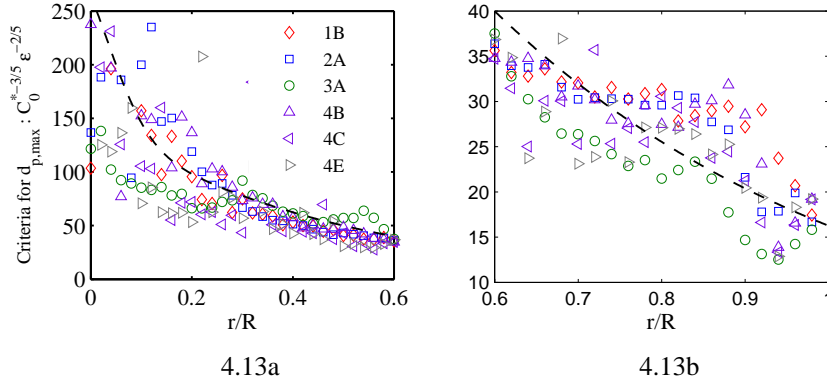
Figure 4.13 Effect of pipe inhomogeneous turbulence at $Re_b=10300$ on the particle break-up criterion. Turbulence dissipation is estimated from the turbulence production; $\varepsilon \approx P_k$. Particle-laden up- and downward flows have been measured in different stages of development with mean volumetric concentration of particles in the range 0.5×10^{-6} to 1.7×10^{-4}. Figure 4.13a presents results in the range $0 < r/R < 0.6$ and Fig. 4.13b, in the range $0.6 < r/R < 1$; notice the difference in scales.

As expected, small values of the quantity $C_0^{*-3/5} \varepsilon^{-2/5}$ are obtained close to the wall, meaning that smaller values of $d_{p,max}$ are found there. For given fluid and particle properties, values of $d_{p,max}$ at the pipe centerline exceed the ones in the near-wall zone by a factor of more than 10. The effects of transient states and mean volumetric concentrations are particularly observed in the critical region: the near-wall zone. In the measured development stages, $d_{p,max}$ is slightly reduced for $r/R > 0.6$. It was shown in Table 4.5 that cross-section turbulence production values were increased by factors of 1.8 for cases 3A/3B and of 1.6 for cases 4D/4E. These cases correspond to transient particle-laden flows

with high level of turbulence and high mean volumetric concentrations (order 10^{-4}), respectively. Since the effect of production in $d_{p,max}$ scales with the power -2/5, an increase in P_k of 80 % corresponds to a reduction in $d_{p,max}$ about 20%. As a consequence, results for cases 3A and 4E in Fig. 4.13b are only subtly decreased in comparison to the results of case 1B.

A fit of all experimental data presented in Fig. 4.13 is given by a sum of Gaussian functions:

$$(\rho_f / \sigma\ We_{crit})^{3/5}\ d_{p,max}\ =\ a_1\ exp\{-[(r/R - a_2)/\ a_3]^2\} + a_4\ exp\{-[(r/R - a_5)/\ a_6]^2\} \qquad (4.16)$$

The quality of the fit is expressed by the two parameters r_s^2 and F, defined in Eq. (4.4) and (4.5). In Eq. (4.16), r_s^2 and F are equal to 0.88 and 3391, respectively. The coefficients are given by: $a_1 = 133.3$, $a_2 = -0.04492$, $a_3 = 0.112$, $a_4 = 2.573 \times 10^{15}$, $a_5 = -27.87$ and $a_6 = 5.049$.

4.5   Discussion and conclusions

The determination of a break-up criterion with regards to a specific type of dispersed phase is beyond the scope of the present experimental study. Measurements of turbulence production and the direction-dependent Kolmogorov constant allow the evaluation of Hinze's[1] break-up criterion as a function of the radial coordinate. At $Re_b = 10300$ and for given fluid and particle properties, maximum particle sizes at the pipe centerline can exceed the ones in the near-wall zone by more than a factor of 10. Therefore, the concentration profiles of particles are fundamental for a proper break-up evaluation.

Flow orientation with respect to gravity affects the concentration profiles of inertia particles in particle-laden flows with $|u_{rms}/U_{TV}| \approx O(1)$, inertia particles with $St = 2.3$ or 3.3 and $\rho_p/\rho_f \approx 1.05$. The effect of up- and downflows on concentration profiles is different: with wall peaking in downflow and core peaking in upflow. Accurate predictions of the radial distribution of particles in a pipe are also essential for modeling phenomena such as collision frequency, reaction rates, deposition and entrainment. In the last section, the break-up criterion based on Hinze's[1] approach contemplated the influence of inhomogeneous turbulent pipe flow as a function of radial coordinate. In chapter 3, it was shown that flow orientation with respect to gravity, the ratio $|u_{rms}/U_{TV}|$ and the presence of shear affect the concentration profile of the dispersed phase. For the present class of

particle-laden flows with $|u_{rms}/U_{TV}| \approx O(1)$, $St = 2.3$ or 3.3 and $\rho_p/\rho_f \approx 1.05$, they hypothesized that a fluctuating component of the lift force on particles is responsible for moving particles towards the core in upward and towards the wall in downward flows.

For particles with high inertia, the ratio of RMS fluid velocity to terminal velocity tends to zero: $|u_{rms}/U_{TV}| \rightarrow 0$. High inertia particles cross turbulent eddies with hardly any interaction. The relative velocity approaches the terminal velocity and in the presence of enough shear, a mean lift force will be of importance in determining the wall-normal concentration profiles. For $|u_{rms}/U_{TV}| \rightarrow 0$, the magnitude of the mean lift component will dominate the fluctuating lift term. Particles with low inertia possess $u_{rms}/U_{TV} >> 1$. For this class of particles, the terminal velocity is not significant and the mean relative velocity is also small. In this situation, the turbulent motion of particles with low inertia is governed by the interaction with flow eddies and lift does not play a role.

In industrial loops, turbulent pipe flows often do not achieve a steady state due to the length limitations; see Laws *et al.*[7] The required length for fully developed conditions increases with increasing bulk Reynolds number. Therefore, the effect of transient states of dispersed turbulent flows on particle break-up must also be considered. For the present class of particle-laden flows with $|u_{rms}/U_{TV}| \approx O(1)$, $St = 2.3$ or 3.3 and $\rho_p/\rho_f \approx 1.05$, turbulence production is enhanced particularly in the critical region: the near-wall zone. The maximum particle size is reduced and even more so for high volumetric concentrations or for high level of turbulence.

References

[1]   J.O. Hinze. Fundamentals of the hydrodynamic mechanism of splitting in dispersion processes. A.I.Ch.E. Journal 1 (3), 289–295, 1956.

[2]   L.-P. Wang and M. R. Maxey, ''Settling velocity and concentration distribution of heavy particles in homogeneous isotropic turbulence'', J. Fluid Mech. 256, 27 (1993).

[3]   C. Marchioli, M. V. Salvetti and A. Soldati: ''Some issues concerning large-eddy simulation of inertia particle dispersion in turbulent bounded flows'', Physics of Fluids 20, 040603 (2008).

[4]   A. I. Kartusinsky, E. E. Michaelides, M. T. Hussainov and Y. Rudi: "Effects of the variation of mass loading and particle density in gas–solid particle flow in pipes". Powder Technology, 193, 176-181, (2009).

[5]   F. Risso: "The mechanisms of deformation and breakup of drops and bubbles", Multiphase Science and Technology, 12, pp. 1-50, 2000.

[6]   A. Soldati, "On the influence of electrohydrodynamics and turbulence on particle transport and collection efficiency in wire-plate electrostatic precipitators", J. Aerosol Sci. 31, 293, (2000).

[7]   E. M. Laws, E. -H. Lim and J. L. Livesey: "Momentum balance in highly distorted turbulent pipe flows", Experiments in Fluids 5, 36 – 42, 1987.

[8]   K. J. Sene, J. C. R. Hunt and N. H. Thomas: "The role of coherent structures in bubble transport by turbulent shear flows". J. Fluid Mech. 259, 219–240, (1994).

[9]   P. D. M. Spelt and A. Biesheuvel: "On the motion of gas bubbles in homogeneous isotropic turbulence", J. Fluid. Mech., 336, 221-244, (1997).

[10]   J. O. Hinze: 1975, Turbulence. McGraw-Hill.

[11]   M. P. B. Veenman, "Statistical analysis of turbulent pipe flow: A numerical approach" Ph.D. thesis, Technische Universiteit Eindhoven (2004).

[12]   S. Elgobashi: "On Predicting Particle-Laden Turbulent Flows", Applied Scientific Research 52: 309-329, (1994).

[13]   J. L. G. Oliveira, C. W. M. van der Geld and J. G. M. Kuerten: "Lagrangian and Eulerian statistics of pipe flows measured with 3D-PTV at moderate and high Reynolds numbers", submitted to Flow, Turbulence and Combustion.

[14]   R.J.E.van Wissen, K.R.A.M. Schreel and C.W.M. van der Geld: "Turbulence production by a steam-driven jet in a water vessel", Int. J. Heat Fluid Flow, Vol. 25 (2), pp. 173-179, 2004.

[15]   S. B. Pope, "Turbulent Flows ", Cambridge University Press, Cambridge, 2000.

[16]   L. Mydlarski and Z. Warhaftz: "Three-point statistics and the anisotropy of a turbulent passive scalar", Physics of Fluids vol. 10, number 11, 1998.

[17]   S. B. Pope, "Stochastic Lagrangian models of velocity in homogeneous turbulent shear flow," Phys. Fluids 14, 1696, 2002.

[18]   R. J. E. Walpot, C. W. M. van der Geld, and J. G. M. Kuerten: "Determination of the coefficients of Langevin models for inhomogeneous turbulent flows by three-dimensional particle tracking velocimetry and direct numerical simulation", Physics of Fluids 19, 045102 (2007).

[19]   R.-C. Lien and E. A. D'asaro: "The Kolmogorov constant for the Lagrangian velocity spectrum and structure function", Physics of Fluids vol. 14, number 12, 2002.

[20]   J. I. Choi, Y. Kyongmin, and L. Changhoon: "Lagrangian statistics in turbulent channel flow", Phys. Fluids 16, 779, 2004.

[21]   J. F. Walter and H. W. Blanch: "Bubble break-up in gas-liquid bioreactors: break-up in turbulent flows", Chem. Eng. J. 32, B7 – B17, 1986.

[22]   R. P. Hesketh, T. W. F. Russel and A. W. Etchells: "Bubble size in horizontal pipelines", A.I.Ch.E. Journal 33, 663–667, 1987.

[23]   A. J. Karabelas: Droplets size spectra generated in turbulent pipe flow of dilute liquid/liquid dispersions, A.I.Ch.E. Journal 24, 170–180, 1978.

Lagrangian velocity and acceleration statistics of fluid and inertia particles in a particle-laden pipe flow measured with 3D-PTV

Three-dimensional particle tracking velocimetry (3D-PTV) has been applied to particle-laden pipe flow with mean volumetric concentration of inertia particles equal to 1.4×10^{-5} at Reynolds number 10300, based on the bulk velocity and the pipe diameter. Velocity and acceleration Lagrangian as well as Eulerian statistics have been determined for flow tracers and for inertia particles with Stokes number equal to 2.3, based on the particle relaxation time and viscous scales. The decay of fluctuating velocity and acceleration Lagrangian correlations has been measured for fluid and dispersed phase at different radial positions for the given inhomogeneous flow. Ratios of Eulerian acceleration variance of inertia particles to the acceleration variance of flow tracers have been quantified for all cylindrical coordinate components. These ratios do not obey the power law found in von Kármán and wind-tunnel turbulent flows. The minimum number of correlation samples required for reliable Lagrangian statistics of inertia particles has been quantified.

5.1 Introduction

Turbulent dispersed two-phase flows are ubiquitous in both industry and nature. For example, the dispersion of pollutants in an urban environment, sediment transport or the fluidized catalytic cracking of carbohydrates are often studied; see Poelma *et al.*[1] Flows of this kind are characterized by particles, droplets or bubbles dispersed within a carrier phase. The occurrence of such flows in pipes is wide as well, with applications ranging from pneumatic conveying systems to chemical reactor design; see Kartusinsky *et al.*[2] The ability to predict the behavior of this kind of flow is therefore of quite some interest in engineering applications. However, due to the complex nature of the problem, available models are usually simplified and not able to fully predict fluid and particle behavior for the whole range of applications.

The experimental determination of statistical properties of particles in a Lagrangian frame of reference is essential for the development of stochastic models of turbulent transport in applications such as combustion, pollutant dispersion and industrial mixing; see Pope[3] and Yeung.[4] For a complete description of particle statistics it is necessary to follow particle paths with very fine spatial and temporal resolution, of the order of the Kolmogorov length and time scales, η and τ_k, respectively. To capture the large scale behavior in a turbulent pipe flow, trajectories should be tracked for long times, *i.e.* multitudes of τ_k. This obviously necessitates access to an experimental measurement volume with a typical length scale of the order of the bulk velocity times a typical Lagrangian correlation time; see Biferale *et al.*[5]

The determination of Lagrangian velocity correlations and structure functions allows the determination of Lagrangian stochastic models as the Langevin model for example; see Brouwers.[6] For the above reasons Lagrangian experimental techniques such as three-dimensional particle tracking velocimetry, 3D-PTV, are a necessity in turbulence research. Despite the higher practical impact of inhomogeneous turbulent flows, experimental Lagrangian results in the literature are mostly restricted to homogeneous turbulence. Lagrangian measurements in flow geometries with non-zero mean velocity component are scarce. The work of Suzuki and Kasagi[7] represents one of the few exceptions. For the industrially relevant pipe flow, only the 3D-PTV results of Walpot *et al.*[8] and Oliveira *et al.*[9] are available to our knowledge. Veenman[10] provided Eulerian and Lagrangian DNS computations of pipe flow at $Re_b = 5300$ and 10300. Walpot *et al.*[8] presented data for $Re_b =$

5300 and some preliminary results at $Re_b = 10300$. Recently, Oliveira *et al.*[9] presented new experimental Lagrangian results for pipe flow at $Re_b = 10300$ and compared these with DNS-data of Veenman.[10]

The present work aims at providing Lagrangian velocity and acceleration statistics of flow tracers and one class of *inertia particles* (with Stokes number 2.3 and diameter 0.8 mm) simultaneously. To our knowledge, consistent experimental data for the formulation of stochastic models for heavy particles in a turbulent particle-laden pipe flow has never been provided. In the present study, similarities in the results of Lagrangian velocity structure functions of tracers and *inertia particles* will be sought in order to validate a modified Langevin approach for heavy particle dispersion. 3D-PTV is applied to particle-laden pipe flow in upward vertical direction at bulk Reynolds number, $Re_b=10300$. Here, Re_b is based on the bulk velocity and the pipe diameter. Mean volumetric concentration of *inertia particles* is equal to 1.4×10^{-5}. The mass density of the *inertia particles* ($\rho_p \approx 1050$ kg/m^3) is bigger than the mass density of the carrier fluid ($\rho_f \approx 1000$ kg/m^3).

The structure of the paper is as follows. In Section 5.2, the experimental setup is presented, including specifications of flow tracers and inertial particles. Section 5.3 provides the 3D-PTV results for the particle-laden flow. Results concerning velocity and acceleration fluctuations of fluid and dispersed phase are provided. A discussion of these experimental results is given in Section 5.4. Finally, conclusions are presented in Section 5.5.

5.2 Experimental setup

5.2.1 Test rig

Turbulent particle-laden pipe flow has been created in a water loop driven by a centrifugal pump; see Fig. 5.1. The in-line 3 kW centrifugal pump of type DPV18-30, manufactured by "Duijvelaar pompen", allows Reynolds numbers based on the bulk velocity, U_b, and pipe diameter, D, in the range 10^3 to 10^5. A frequency controller permits fine-tuning of the Reynolds number by adjusting the mass flow rate of the upward vertical flow in the measurement section; see Fig. 5.1.

The mass flow rate is measured by means of a Micro Motion Elite CMF300 mass flow and mass density meter, whose inaccuracy is less than 0.5% of the registered flow rate. A

water reservoir contains about 2 m^3 of water. This value facilitates water temperature stabilization and Reynolds number control. Temperature during a test-run was essentially constant, varying typically 0.1°C only.

Submerged pumps are placed in the reservoir tank in order to promote homogeneous dispersion of the added tracers and *inertial particles*. The measurement section consists of a glass pipe to ensure optical accessibility. A water-filled rectangular glass box around the pipe minimizes optical distortions. The pipe diameter is chosen relatively large, 100 mm inner diameter, because measurements at high Reynolds numbers are required. For a certain Reynolds number, bulk velocities are lower for higher tube diameters, which is advantageous for the acquisition of Lagrangian statistics.

A flow straightener, tube bundle conditioner of ISO 5167-1:1991, see Miller[11], has been placed downstream of the 90º bend, see Fig. 5.1. The flow straightener removes secondary flows and shortens the required length to obtain a fully developed flow. At 45D further downstream, the location of the test section, a fully developed flow has been achieved.
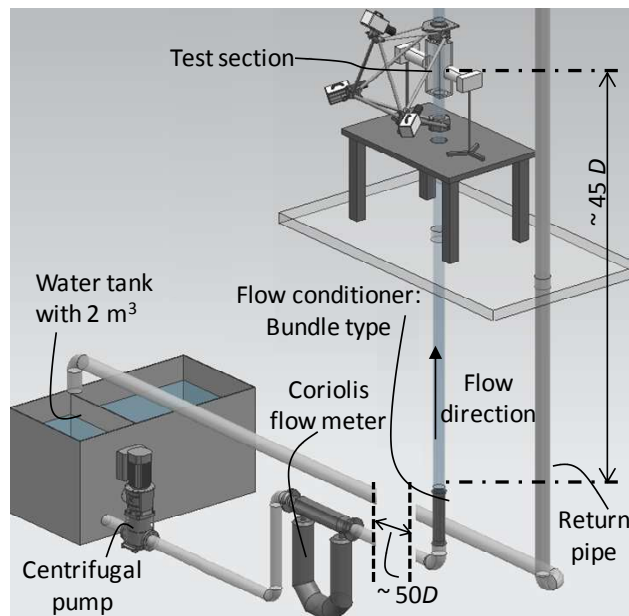
Figure 5.1 Schematic of the 3D-PTV experimental setup for particle-laden pipe flow.

5.2.2   Properties of applied particles

153

Properties of polystyrene particles applied in the present particle-laden experiment are given in Table 5.1. The fluid time-scale τ_f in the Stokes number, St, is based on viscous scales; see info below Table 5.1. The fluid length-scale is the Kolmogorov scale for fully developed single-phase pipe flow at $Re_b = 10300$ as computed by Veenman.[10] The Kolmogorov length is about 0.60 mm in the pipe core and 0.23 mm close to the wall. For evaluation of the particle timescale, τ_p, the relaxation time for particles in stationary flow is used; see Albrecht et al.[12]:

$$\tau_p = (d_p^2 \rho_p/18\mu)(1 + 0.5\rho_f/\rho_p) \tag{5.1}$$

where μ is the dynamic viscosity, d_p is the particle diameter and ρ_p and ρ_f are the mass densities of particles and of fluid, respectively. A relaxation time of $\tau_p \approx 4$ ms is obtained for the tracers. Note that the fluid inertia is accounted for by the added mass coefficient 0.5 which close to a wall is increased to about 0.7; see van der Geld.[13]

Table 5.1 Properties of particles applied in the present particle-laden experiment

Particles	Mass density [kg/m³]	Diameter d_p [mm]	Terminal velocity, U_{TV}* [mm/s]	*Re_p	** $St = \tau_p/\tau_f$	*** Length-scale ratio: d_p/η
Flow tracers	1050	0.2	1.0	0.18	0.14	0.33 − 1
Inertia particles	1050	0.8	10.2	7.76	2.31	1.33 − 3.5

* Settling velocity of a particle in an infinite, stagnant pool of water.

** Fluid time-scale is based on viscous scales as given by: $\tau_f = \nu/u_\tau^2$. For $Re_b < 10^5$, the wall shear velocity can be estimated as $u_\tau = (U_b^2 f/8)^{1/2}$ with $f = a\, Re_b^{-m}$, $m = 0.25$ and $a = 0.316$; see Hinze.[14] τ_f is roughly 28 ms.

*** Kolmogorov length-scales for a fully developed single-phase pipe flow at $Re_b = 10300$ as computed from the DNS code developed by Veenman[10]: ≈ 0.60 mm at pipe centerline and ≈ 0.23 mm close to the wall.

The terminal velocity specified in Table 5.1 is attained in quiescent fluid when gravitational and drag forces are in equilibrium:

$$U_{TV} = \{(4\,(\rho_p - \rho_f)\, d_p\, g) / (3C_D\, \rho_f)\}^{1/2} \tag{5.2}$$

where g is the gravity acceleration and C_D the drag coefficient. The latter is a function of the particle Reynolds number, $Re_p = d_p|U_{TV}|/\nu$, which is based on the particle diameter and

the terminal velocity. In the Stokes regime, C_D is given by Eq. (5.3). For $1 < Re_p < 1000$, Schiller and Naumann[15] proposed a correlation for C_D given by Eq. (5.4):

$$C_D = (24 \, / \, Re_p); \text{ for } Re_p < 1 \tag{5.3}$$

$$C_D = (24 \, / \, Re_p) \, (1 + 1/6 \, Re_p^{2/3}); \text{ for } 1 < Re_p < 1000 \tag{5.4}$$

A value for U_{TV} is obtained by an iterative computation using Eq. (5.2) and Eq.'s (5.3) or (5.4). Since the bulk flow velocity, U_b, is approximately 100 mm/s, the ratio U_b/U_{TV} is on the order of 10^2 for seeding particles, see Table 5.1. Since $U_b \gg U_{TV}$, $\tau_p < \tau_f$ and $d_p < l_k$, the employed seeding particles work well as flow tracers. For *inertia particles*, the ratio U_b/U_{TV} is on the order of 10, $\tau_p > \tau_f$ and $d_p > l_k$. Therefore, *inertia particles* have significant inertial characteristics to not behave as tracers.

5.3   Results

In this section, Lagrangian velocity and acceleration results of particle-laden pipe flow at $Re_b = 10300$ and with a mean volume load equal to 1.4×10^{-5} are presented. Similarities in the Lagrangian results of tracers and *inertia particles* are required in order to validate a modified Langevin approach for heavy particle dispersion. The experimental analysis required for inhomogeneous turbulent pipe flow is not straightforward since particles move during the time of observation to areas with other statistical properties. Discretization in space and time is necessary in such a way that enough independent data are collected in each point. The computation of Lagrangian statistics is done separately for each class of particles; see Table 5.1. The experimental analysis applied follows closely the ones presented by Oliveira *et al.*[9,16] and Walpot *et al.*[17] To determine Lagrangian statistics of particles trajectories, the analysis method gathers data in discrete radial bands: $r_i \pm \Delta r$, with Δr satisfying $2\Delta r > |u|\Delta t$. Here, u is a typical radial velocity value, e.g. the standard deviation of radial velocity fluctuations. The particle trajectory sketched in Fig. 5.2 contributes to the Lagrangian correlations in band "i" from $t_{1/50}$ to $t_{6/50}$. Each particle position from $t_{1/50}$ to $t_{6/50}$ serves as an initial position of a new trajectory. When these additional trajectories are taken into account, the number of data available for short time correlations is increased.
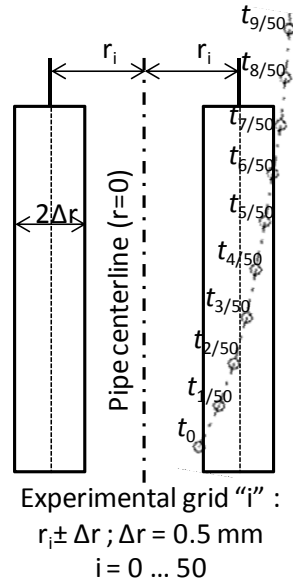
Figure 5.2 Schematic of a particle trajectory which crosses the experimental band of grid point "*i*". The circles represent particle positions tracked at a frequency of 50 Hz. The particle trajectory contributes to Lagrangian correlations at grid points "*i*" in a way explained in the text.

Lagrangian velocity auto- and cross-correlations are defined by Eq. (5.5), while Eq. (5.6) defines Lagrangian acceleration correlations:

$$\rho_{km}(\tau,r) \ = <u_k(t_0)u_m(t_{0+}\tau)> \tag{5.5}$$

$$\beta_{km}(\tau,r) \ = <a_k(t_0)a_m(t_{0+}\tau)> \tag{5.6}$$

The term t_0 denotes an arbitrary initial time and τ the correlation time span. The terms ρ and β denote Lagrangian velocity and acceleration correlations, respectively. The variables u and a represent the fluctuating velocity and acceleration, respectively. The subscripts k and m indicate cylindrical coordinate components (r, z, θ). The calculation of the correlations $\rho_{km}(\tau,r)$ and $\beta_{km}(\tau,r)$ is done by averaging over all particles that are situated inside a discrete band centered at a radial position r in a certain time which is then marked t_0 for that particle. These correlation functions depend on the radial coordinate r but are independent of t_0. Lagrangian velocity correlations are sought to determine the damping tensor in Langevin stochastic models.[6,810]

Presently, DNS computations are performed in which solid particles (with diameter 0.8 mm and mass density 1050 kg/m³) in water flow are represented by point particles. These computational results will be compared with the present experimental findings in another paper.

5.3.1 Velocity correlations

Two dimensionless radial positions are chosen to present results of Lagrangian velocity auto- and cross-correlations, as defined by Eq. (5.5), for both classes of particles: one close to the pipe core, r/R=0.5, and another not far from the wall, r/R=0.7. These radial points are sufficient to depict the main inhomogeneous turbulent features of the given particle-laden pipe flow. Errors of time-averaged values of a measured quantity x are estimated with the aid of the so-called standard error, σ_m. Confidence intervals of 95% are considered. For a quantity which is measured n times, with instantaneous results x_i and mean $<x>$, the standard error is given by:

$$\sigma_m = [\sum_{i=1}^{n} (x_i - <x>)^2 / (n\,(n-1))]^{1/2} \qquad (5.7)$$

Figure 5.3a shows normalized velocity autocorrelation functions for the axial component. Normalization is done with the starting point of the correlations; $\tau = 0$. Solid lines represent DNS data of Veenman[10] at the same Re_b. Diamonds and circles represent 3D-PTV data of flow tracers (FT) and *inertia particles* (IP), respectively. Error-bars are indicated only for tracers at r/R=0.5 and have similar sizes for other experimental results. Figure 5.3b shows the corresponding total number of correlation samples measured.
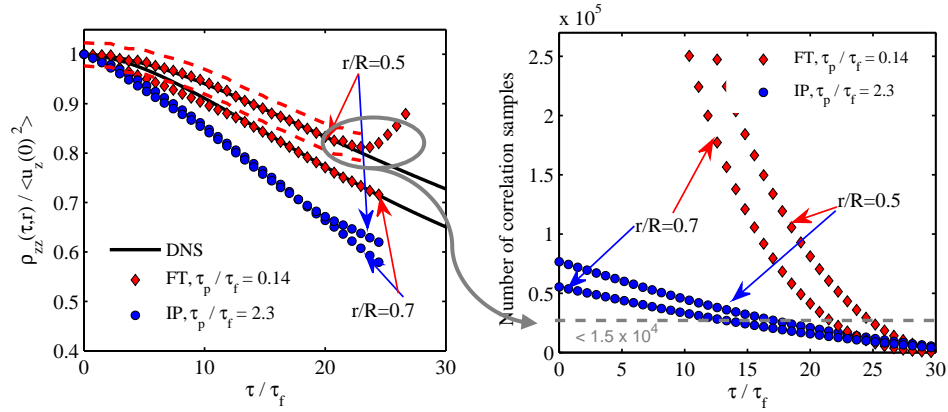
Figure 5.3 Comparison of measured autocorrelation functions for the axial component at *r/R*=0.5 and *r/R*=0.7 with DNS data of Veenman.[10] Diamonds and circles represent 3D-PTV data of flow tracers (FT) and *inertia particles* (IP), respectively. Dashed lines indicate error-bars. At *r/R*=0.5, values of $<u_{FT,z}(0)>$ and $<u_{IP,z}(0)>$ are 8.1 and 9.3 mm/s, respectively. At *r/R*=0.7, values of $<u_{FT,z}(0)>$ and $<u_{IP,z}(0)>$ are 9.6 and 10.1 mm/s, respectively.

Lagrangian axial velocity statistics of flow tracers are similar to the ones of a single-phase fully developed pipe flow represented by DNS until a time lag, τ/τ_f, of about 24. Here, τ_f is the fluid time-scale given by v/u_τ^2. It represents an average estimation for the Kolmogorov time-scale, which is a function of the radial coordinate in inhomogeneous turbulent pipe flows. At other radial positions, velocity correlations of flow tracers are also similar to the ones computed by DNS. Flow tracer results are in agreement with the single-phase flow measurements performed by Oliveira *et al.*[9] at the same Re_b. In a particle-laden flow with a mean volumetric concentration of *inertia particles* of $1.4×10^{-5}$ and with St = 2.3, Lagrangian statistics of flow tracers are hardly different from those in single-phase flow.

For $\tau/\tau_f >24$, there is a sudden increase in the velocity correlation function. This increase happens for both classes of particles and is related to a reduction in the number of correlation samples, which is shown in Fig. 5.3b. Increasing the band width Δr from 0.5 to 1.5 mm does not improve the results for longer time lags. It just increases the amount of data for correlation time spans in the range $0 < \tau/\tau_f < 18$ without significantly changing the Lagrangian velocity results for $\tau/\tau_f >24$. A further increase in Δr can induce significant changes on final results due to the differences in flow statistical properties along the radial

158

coordinate. A smaller band width results in a decrease of correlation samples for time lags in the range $0 < \tau/\tau_f < 18$. The bandwidth selected is therefore considered to be optimal. The evaluation of Lagrangian velocity autocorrelations at different radial positions with various bandwidths Δr reveals that reliable results are obtained for both flow tracers and *inertia particles*, if a number of correlation samples exceeding about 1.5×10^4 is available. A radial band width, Δr, of 0.5 mm and a camera frequency of 50 Hz suffice to obtain negligible bias for velocity Lagrangian statistics of both classes of particles at $Re_b = 10300$. A similar requirement for the minimum number of correlation samples was observed by Oliveira *et al.*[9]

Axial velocity correlations of flow tracers decay more slowly than the correlations of *inertia particles*. For *inertia particles* in $\tau = 24\,\tau_f$, the normalized autocorrelations are roughly: $\rho_{zz}/<u_z(0)^2> \approx 0.62$ at *r/R*=0.5 and 0.58 at *r/R*=0.7. For flow tracers in the same time lag, these values are 0.8 at *r/R*=0.5 and 0.7 at *r/R*=0.7. The slower decay for correlations of flow tracers is also observed for radial, azimuthal and cross-components as will be shown below. The faster decay in the correlations of *inertia particles* also holds at other radial positions. A discussion about the differences in the velocity de-correlation process of both classes of particles is provided in section 5.4.

Figures 5.4 and 5.5 show 3D-PTV results for normalized radial and azimuthal velocity autocorrelations, respectively, at *r/R*=0.5 and *r/R*=0.7. Normalization is done with the starting point of the correlations at $\tau = 0$. Solid lines represent DNS data of Veenman[10] at the same Re_b. Diamonds and circles represent 3D-PTV data of flow tracers (FT) and *inertia particles* (IP), respectively. Error-bars, indicated by the dashed lines and with size equal to $\pm 2\sigma_m$, are only plotted for one dataset and have similar magnitude for the remaining 3D-PTV results.
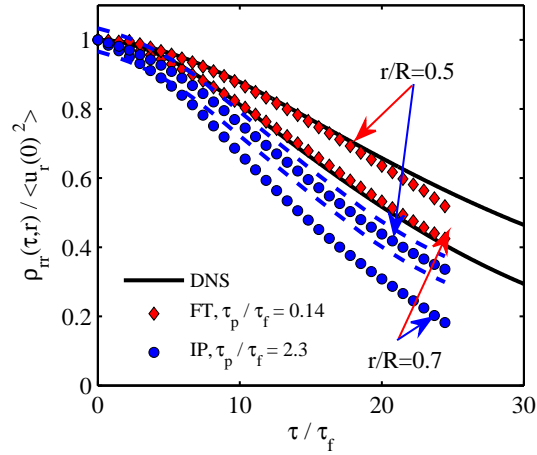
Figure 5.4 Comparison of measured autocorrelation functions for the radial component at *r/R*=0.5 and *r/R*=0.7 with DNS data. Diamonds and circles represent 3D-PTV data of flow tracers (FT) and *inertia particles* (IP), respectively. Dashed lines indicate error-bars. At *r/R*=0.5, values of $<u_{FT,r}(0)>$ and $<u_{IP,r}(0)>$ are 5.2 and 5.4 mm/s, respectively. At *r/R*=0.7, values of $<u_{FT,r}(0)>$ and $<u_{IP,r}(0)>$ are 5.7 and 5.8 mm/s, respectively.

For *inertia particles* in $\tau = 24\,\tau_f$, the normalized radial autocorrelations are roughly: $\rho_{rr}/<u_r(0)^2> \approx 0.34$ at *r/R*=0.5 and 0.19 at *r/R*=0.7. For flow tracers in the same time lag, these values are 0.52 at *r/R*=0.5 and 0.43 at *r/R*=0.7. For the tangential correlations of *inertia particles* in $\tau = 24\,\tau_f$, values of $\rho_{\theta\theta}/<u_\theta(0)^2>$ are roughly: 0.37 at *r/R*=0.5 and 0.31 at *r/R*=0.7. For flow tracers in the same time lag, these values are 0.66 at *r/R*=0.5 and 0.50 at *r/R*=0.7.
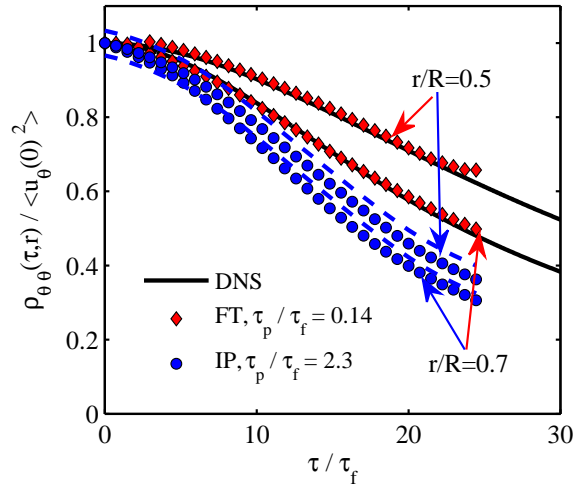
Figure 5.5 Comparison of measured autocorrelation functions for the tangential component at *r/R*=0.5 and *r/R*=0.7 with DNS data. Diamonds and circles represent 3D-PTV data of flow tracers (FT) and *inertia particles* (IP), respectively. Dashed lines indicate error-bars. At *r/R*=0.5, values of $<u_{FT,\theta}(0)>$ and $<u_{IP,\theta}(0)>$ are 5.8 and 5.7 mm/s, respectively. At *r/R*=0.7, values of $<u_{FT,\theta}(0)>$ and $<u_{IP,\theta}(0)>$ are 6.8 and 6.9 mm/s, respectively.

At radial positions closer to the pipe center (*r/R*=0.5), a slower decay of autocorrelation values is observed for both classes of particles. The presence of the wall causes the velocity correlations of particles to decay faster nearby the wall than in the pipe core. In the time interval $\tau = 24 \, \tau_f$, the ratios of autocorrelations of *inertia particles* at *r/R*=0.5 to the ones at *r/R*=0.7, $[\rho_{kk}/<u_k(0)^2>]_{r/R=0.5}/[\rho_{kk}/<u_k(0)^2>]_{r/R=0.7}$, for axial, radial and tangential components are 7, 79 and 20 %, respectively. For flow tracers, these values are: 14, 20 and 32 %. For both particles, the axial autocorrelations decay more slowly than tangential and radial ones.

3D-PTV and DNS results of the only non-zero cross-correlation functions, ρ_{rz} and ρ_{zr}, are shown for *r/R*=0.7 in Fig. 5.6. The statistical error in the 3D-PTV results is indicated by the dashed lines with size equal to $\pm 2\sigma_m$; see Eq. (5.7). Cross-correlations involving the tangential component are equal to zero, since this component is uncoupled to the other two components. This has also been found for *inertia particles*.
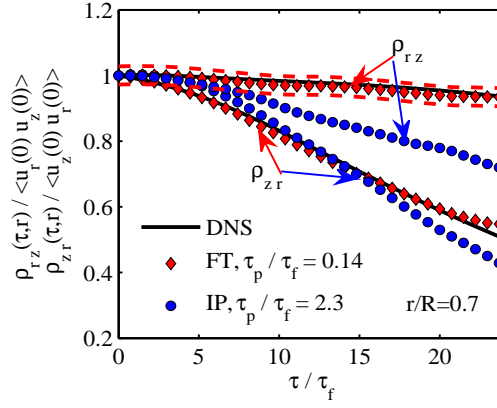
Figure 5.6 Comparison of measured cross-correlation functions, ρ_{rz} and ρ_{zr}, at r/R=0.7 with DNS data. Diamonds and circles represent flow tracers (FT) and *inertia particles* (IP), respectively. Dashed lines indicate error-bars. At r/R=0.7, values of $<u_{\mathrm{FT},r}(0)u_{\mathrm{FT},z}(0)>^{1/2}$ and $<u_{\mathrm{IP},r}(0)u_{\mathrm{IP},z}(0)>^{1/2}$ are 4.8 and 4.5 mm/s, respectively. The starting point of cross-correlations is equal: $\rho_{rz}(0) = \rho_{zr}(0)$.

Cross-correlations ρ_{zr} decay considerably faster than cross-correlations ρ_{rz}. For *inertia particles* in $\tau = 24\ \tau_f$, $\rho_{zr}/<u_z(0)u_r(0)>$ is 0.41 and $\rho_{rz}/<u_r(0)u_z(0)>$ is 0.76. Particles which move towards the wall usually retain their original axial velocity for a while and will most likely be found at larger values of r/R with a relatively large value of u_z. The opposite conclusion is drawn for particles moving towards the core of the pipe. As a consequence, the average product of u_z and u_r is positive. An inertia particle moving in radial direction tends to retain its original total axial velocity for a while, $u_z(t_0 + \tau) \approx u_z(t_0)$, resulting in an average increase of the absolute value of the velocity fluctuation. The average product $\langle u_r(t_0)u_z(t_0 + \tau)\rangle$ is larger than $\langle u_r(t_0)u_z(t_0)\rangle$. The same cannot be said about $\langle u_z(t_0)u_r(t_0+\tau)\rangle$, since $\langle u_r\rangle$=0 everywhere.

### 5.3.2 Velocity structure function and Kolmogorov constant

The second order Lagrangian velocity structure function, $D_{kk}(\tau)$, is defined by Eq. (5.8):

$$D_{kk}(\tau) = <[u_k(\tau) - u_k(0)\ ]^2> \tag{5.8}$$

Values of $D_{\theta\theta}$ at r/R=0.7 are presented in Fig. 5.7. The solid line represents DNS data at Re_b = 10300. Diamonds and circles represent flow tracers (FT) and *inertia particles* (IP),

162

respectively, in particle-laden pipe flow at the same Re_b. Dashed lines indicate error-bars, as before.
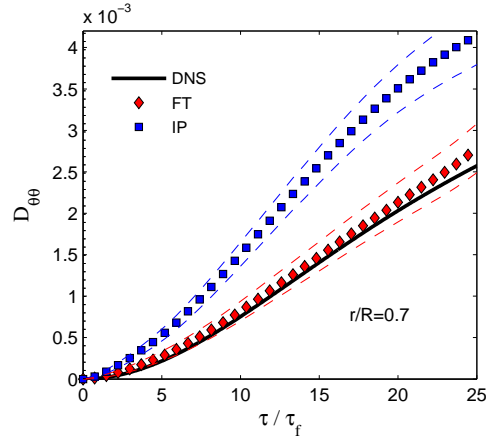
Figure 5.7 Comparison of measured structure functions for the tangential component at *r/R*=0.7 with DNS data. Diamonds and squares represent flow tracers (FT) and *inertia particles* (IP), respectively. Dashed lines indicate error-bars.

The slope of velocity structure functions is bigger for *inertia particles* than for flow tracers; see velocity tangential components in Fig. 5.7. At *r/R*=0.7, values of $D_{\theta\theta}^{1/2}$ in the range τ/τ_f =4 to τ/τ_f =24 increase from 0.02 to 0.06 m/s for *inertia particles* and from 0.015 to 0.05 m/s for flow tracers. Similar trends in the results of Fig. 5.7 are found at other radial positions and for radial and axial structure functions.

Lagrangian velocity structure functions as well as Lagrangian velocity correlations of tracers, whose results are among those shown in the last subsection, are important quantities in Lagrangian stochastic models able to predict turbulent dispersion. The quantities, $\rho_{km}(\tau,r)$ and $D_{kk}(\tau)$, determine the Kolmogorov constant C_0 and the damping coefficients in the Langevin model for fluid particle velocity.[6,8,10] Kolmogorov theory of local isotropy gives a scaling rule connecting the fluid structure functions with the universal Kolmogorov constant, C_0; see Pope.[18] The scaling rule is given by Eq. (5.9):

$$D_{kk}(\tau) = C_0 <\varepsilon> \tau \tag{5.9}$$

where ε is the dissipation rate given by $\varepsilon = 2\nu S_{km}^2$. ν is the kinematic viscosity and S_{km} the rate-of-strain tensor. The last one is given by: $S_{km} = (1/2)(\partial U_k/\partial x_m + \partial U_m/\partial x_k)$, with U the instantaneous fluid velocity and x the space coordinate. Eq. (5.9) is valid in the inertial sub-

163

range for time τ in the interval: $\tau_k \ll \tau \ll \tau_c$. The Kolmogorov time-scale, τ_k, is representative of dissipative scales, while the Lagrangian correlation time, τ_c, is representative of large energy-containing scales. In turbulent flows, τ_k is related to τ_c by the Reynolds number: $\tau_k = \tau_c \, Re^{-1/2}$. Since turbulent pipe flows are inhomogeneous in radial direction, τ_k and τ_c are function of the radial coordinate. In section 5.2.2, an average estimation for τ_k was computed, roughly 28 ms. For $Re_b = 10300$, that would result in the following average estimation of τ_c: 2.8 s.

Due to the hypothesis of local isotropy, turbulence statistics are invariant to rotations and reflections of the coordinate system. The local isotropy assumption implies that the structure functions in the three principal directions are equal and therefore C_0 is a constant. At the level of second order statistics, the local isotropy assumption for very large Reynolds numbers has been very successful, see Mydlarski and Warhaft.[19] However, the present Reynolds number is far from this limit. This makes it necessary to introduce a direction-dependent $C_0^{\,k}$, where k represents r, z, θ. This was proposed by Pope[20] in a linear stochastic model for homogeneous shear flow. Later, Walpot et al.[8] followed the same proposal for the definition of C_0 for an inhomogeneous pipe flow. According to Kolmogorov similarity, one should observe a plateau of C_0 in the inertial subrange. However, for the limited Reynolds numbers studied here, the inertial subrange has finite width. For finite Reynolds numbers, the plateaus of C_0 may be short or exist only as bumps, see Lien and D'asaro.[21] Therefore, the value of C_0 will be determined from the maximum in the function of $D_{kk}(\tau)/<\varepsilon>\tau$.

Lagrangian structure functions for the radial velocity component scaled with $<\varepsilon>\tau$ are presented at $r/R=0.7$ in Fig. 8. The solid line represents DNS data[10]. Diamonds and circles represent flow tracers (FT) and *inertia particles* (IP), respectively, in particle-laden pipe flow at $Re_b = 10300$. Dashed lines indicate error-bars, as before.
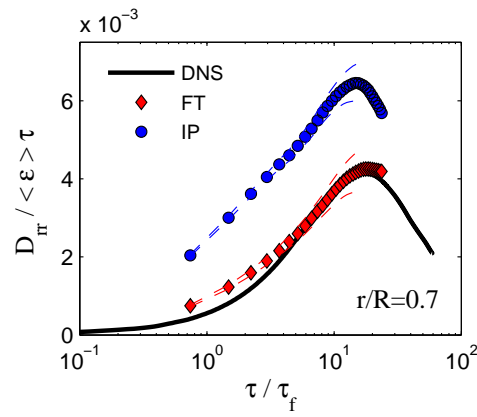
Figure 5.8 Comparison of measured structure functions for the radial component scaled with $<\varepsilon>\tau$ at r/R=0.7 with DNS data of Veenman.[10] Diamonds and squares represent flow tracers (FT) and *inertia particles* (IP), respectively. Dashed lines indicate error-bars.

Trajectories of tracers have been registered long enough to achieve the time interval where the maximum occurs; see Fig. 5.8. The value of C_0^k is the value of $D_{rr}/<\varepsilon>\tau$ at the maximum. Similar results are found at other radial position and for tangential structure functions. For axial structure functions, the Lagrangian correlation times are bigger and the time interval where the maxima occur cannot be achieved due to the limited axial length of the measurement volume. For this case, the axial structure functions are fitted with a linear function in a time interval that is assumed to be in the inertial range (roughly from $\tau/\tau_f \approx 4$ to the longest measured time lag, $\tau/\tau_f \approx 24$). This approach was also done by Walpot *et al*.[8] Results for the direction-dependent C_0^k thus obtained are provided in Fig. 5.9. For tracers, values of C_0^k are roughly 3 in the pipe core ($r/R < 0.8$) and decrease with decreasing distance to the wall. The decrease of C_0^k with decreasing distance to the wall is for tracers also found by Choi *et al*.[22] for turbulent channel flow. This result is in good agreement to single-phase experimental results of Walpot *et al*.[8] and to the numerical computations of Veenman.[10] Application of Lagrangian stochastic models to fluid particles immersed in a particle-laden flow with a mean volumetric concentration of *inertia particles* equal to 1.4×10^{-5} and with $St = 2.3$ seems feasible.

In Fig. 5.8, a maximum is also found for the velocity structure functions of *inertia particles* when they are scaled with $<\varepsilon>\tau$. The same trend is observed at other radial positions and for other structure functions. Following the same procedure as for flow

tracers, the modified direction-dependent C_0^k have been determined for *inertia particles*, see Fig. 5.9.
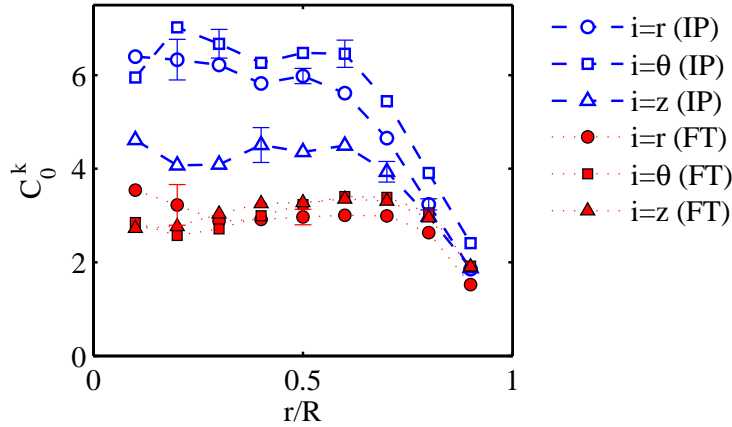
Figure 5.9 Ratios of Eulerian acceleration variance of *inertia particles* (IP) to flow tracers (FT). Subscripts *kk* stand for normal components in cylindrical coordinates: *zz*, *rr* and *θθ*. Error-bars are computed by the standard error in 95% confidence intervals.

Values of C_0^r and C_0^θ are about 6 for *inertia particles* at *r/R* < 0.6, while values of C_0^z are about 4. Values of the direction-dependent Kolmogorov constant, C_0^k, decrease with decreasing distance to the wall for *r/R* > 0.6; see open symbols in Fig. 5.9.

The determination of Lagrangian correlations and structure functions, $\rho_{km}(\tau,r)$ and $D_{kk}(\tau)$, is necessary to develop Lagrangian stochastic models.[6,8,10] The development of a model to predict turbulent dispersion of heavy particles is a challenging topic. The existence of a maximum when the structure functions of *inertia particles* is scaled with $\langle\varepsilon\rangle\tau$ allows the determination of a modified direction-dependent Kolmogorov constant, as done above. By means of C_0^k and Lagrangian velocity correlations, computations of a modified damping tensor as needed for a Langevin model are also possible, if such a model is applicable at all. Zaichik and Alipchenkov[23], for example, proposed a statistical model for the dispersion of heavy particles immersed in a turbulent fluid flow.

In order to facilitate the development of quantitative stochastic models for particles with significant inertia, Lagrangian velocity correlations and structure functions have been presented. We now proceed with the description of acceleration results.

5.3.3 Eulerian acceleration variance

The evolution of the acceleration variance of inertial particles in turbulent flows has been subject of research in recent years; see Volk *et al.*[24], for example. Most of the experimental results (if not all) were reported in flows where the turbulence is close to homogeneous, isotropic or with zero mean velocity, i.e. Qureshi *et al.*[25] or Brown *et al.*[26] For pipe flow, which is more important for practical and industrial applications, there is a lack of experimental results.

In the present study, the mass density of the *inertia particles* almost matches the fluid mass density, $\rho_p/\rho_f \approx 1.05$. For neutrally buoyant particles with $d_p > \eta$ (the Kolmogorov length-scale), Calzavarini *et al.*[27] showed that the acceleration variance decreases for increasing particle size. Moreover, when the acceleration variance of a neutrally buoyant particle is scaled with the one of a flow tracer, $\langle a_{IP}^2 \rangle / \langle a_{FT}^2 \rangle$, the decrease is expected to be in the form:

$$\langle a_{IP}^2 \rangle / \langle a_{FT}^2 \rangle \approx (d_p/\eta)^{-2/3} \tag{5.10}$$

In order to investigate the acceleration of almost neutrally buoyant particles in pipes, ratios of Eulerian acceleration variance of *inertia particles* (IP) to flow tracers (FT), $\beta_{IP,km}(0,r)/\beta_{FT,km}(0,r)$, are presented in Fig. 5.10. Results are shown for all acceleration components in cylindrical coordinates: zz, rr and $\theta\theta$.
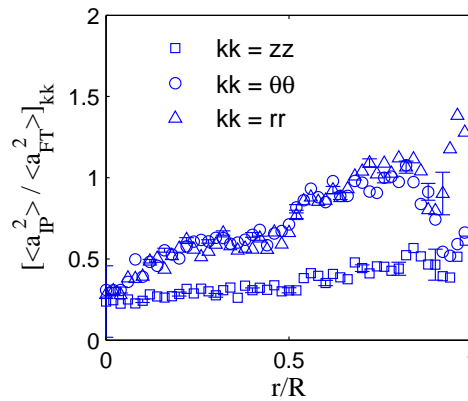
Figure 5.10 Ratios of Eulerian acceleration variance of *inertia particles* (IP) to flow tracers (FT). Subscripts *kk* stand for normal components in cylindrical coordinates: *zz*, *rr* and *θθ*. Error-bars are computed by the standard error in 95% confidence intervals.

The ratios of acceleration variance, $[\langle a_{IP}^2 \rangle / \langle a_{FT}^2 \rangle]_{kk}$, increase with decreasing distance to the pipe walls for all normal acceleration components. Tangential and radial ratios are roughly equal to 0.3 at the pipe centerline and get values of order 1 in the vicinity of the pipe wall. Streamwise ratios are 0.25 at the pipe centerline and increase to nearly 0.5 at $r/R \approx 0.98$.

Flow geometries such as Von Kármán flows and wind-tunnel turbulent flows showed a reduction in the acceleration variance with increasing particle size.[24] According to Voth *et al.*[28], pressure forces which are the main cause of the motion of particles, are averaged over an increasingly large area with increasing particle size. Thus, one expects the acceleration variance to reduce with increasing particle size. This decrease is consistent with the power law $\langle a_{IP}^2 \rangle / \langle a_{FT}^2 \rangle \approx (d_p/\eta)^{-2/3}$. In turbulent pipe flows, viscous scales are smaller near the wall than in the pipe core. The Kolmogorov length-scales for a fully developed single-phase pipe flow at $Re_b = 10300$ have been computed by the DNS code developed by Veenman.[10] The ratio d_p/η increases from roughly 1.3 at pipe centerline to 3.5 at the wall surroundings. Plotting the acceleration variance ratio according to the power law -2/3 with the present particle diameter of 0.8 mm and with η as given by the DNS results yields an unexpected behavior, see pentagrams in Fig. 5.11. Notice that the results in Fig. 5.10 increase with decreasing distance to the wall, while the pentagrams in Fig. 5.11 present opposite trend. A discussion about the unpredicted results for the Eulerian acceleration ratios is given in section 5.4.
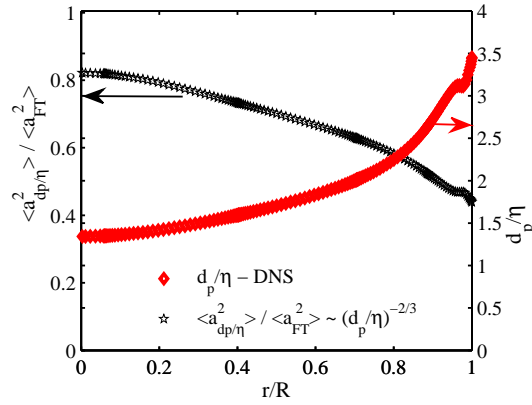
Figure 5.11 At the left side, ratios of Eulerian acceleration variance of *inertia particles* (IP) to flow tracers (FT) as given by the power law $(d_p/\eta)^{-2/3}$; see Volk *et al.*[24] At the right side, ratio of particle diameter to the Kolmogorov length-scale, η, as obtained by the DNS code of Veenman.[10]

5.3.4   Acceleration autocorrelations

Normalized autocorrelation functions for the axial acceleration component at *r/R*=0.5 are shown in Fig. 5.12. Squares and triangles represent 3D-PTV data of flow tracers (FT) and *inertia particles* (IP), respectively. Error-bars have about the same size as symbols.
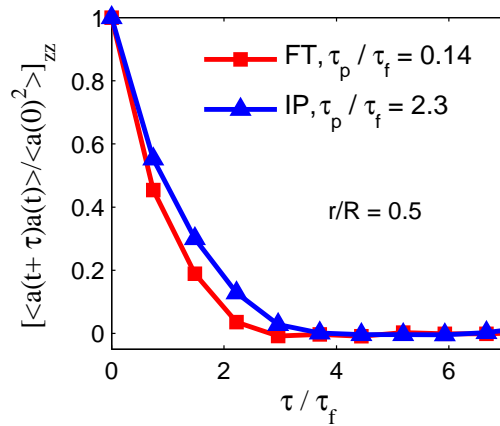
Figure 5.12 Normalized autocorrelation functions for the axial acceleration component at *r/R*=0.5. Squares and triangles represent 3D-PTV data of flow tracers (FT) and *inertia particles* (IP), respectively.

The decay of fluctuating acceleration correlations happens in shorter time intervals than the decay of velocity correlations. While the first ones de-correlate in periods of time a few times bigger than the smallest fluid time-scales, characterized by τ_k, the second ones de-correlate in intervals associated with the biggest flow structures or energy-containing eddies, τ_c. In section 5.3.2, estimations of τ_k and τ_c were given: about 28ms and 2.8s, respectively. The de-correlation of Lagrangian acceleration statistics for both categories of particles takes place in $\tau/\tau_f \approx 3$ to 4 (about 0.084 to 0.112 s). Therefore, it was possible to track particles until $\beta_{km}(\tau,r) \approx 0$. This result is similar for axial acceleration correlations at other radial positions as well as azimuthal and radial acceleration autocorrelations. If all normal accelerations are taken into account for all radial positions, the de-correlation period ratio of *inertia particles* to flow tracers is about 1.25. The increase in the de-correlation period with increasing particle inertia is in accordance with findings in Von Kármán and wind-tunnel turbulent flow experiments; see Volk *et al.*[24] In the next section, the differences in the acceleration correlation decay of both classes of particles are discussed.

5.4   Discussion

The decay of Lagrangian velocity auto and cross-correlations of *inertia particles* takes place in shorter times than the velocity decay of flow tracers (section III-A). This feature of the decay of velocity correlations was attributed to the effect of crossing trajectories by Wells and Stock.[29] According to them, a heavy particle, influenced by an external potential force field such as gravity, falls from one eddy to another at a rate faster than the average eddy-decay rate. In contrast, a light particle (or a fluid point) will generally remain within an eddy until the eddy decays. As a result, the heavy particle tends to lose velocity correlation more rapidly than a light particle.

Many in depth analytical and numerical studies revealed that an indication of the degree of interaction between particles and turbulent flow structures is given by the ratio of a characteristic root-mean-square (RMS) fluid velocity to the particle terminal velocity, u_{rms}/U_{TV}; see Sene *et al.*[30] and Spelt and Biesheuvel[31], for example. Here, the RMS fluid velocities are a function of the radial coordinate and are given by the starting point of velocity correlations, $u_{rms}=<\rho_{km}(0,r)^2>^{0.5}$. For $u_{rms}/U_{TV} << 1$ little interaction with vortices is

expected, whereas for $u_{rms}/U_{TV} \gg 1$ the turbulent motion of particles with low inertia is governed by intense interaction with flow eddies. In the last situation, particles shall behave as fluid particles. In the present particle-laden flow, the ratio u_{rms}/U_{TV} is of order 1 for *inertia particles* and of order 10 for the flow tracers. These values indicate that the applied flow tracers are expected to behave as fluid particles, while the *inertia particles* are expected to interact partially with the turbulent flow structures. As a consequence, velocity correlations of *inertia particles* decay faster than the velocity correlations of tracers. However, the fast decay in the velocity correlations of heavy particles in turbulent flows only seems reasonable if the particle is able to partially interact with the flow eddies ($u_{rms}/U_{TV} \approx 1$). Particles with high inertia do not interact with turbulent structures ($u_{rms}/U_{TV} \rightarrow 0$) and are expected to keep their velocity correlated for longer periods. Particles with high inertia cross turbulent eddies with hardly any interaction.

In opposite trend to the velocity correlations, the decay of Lagrangian acceleration correlations is slower for *inertia particles* than for flow tracers (section 5.3.4). Here, the particle inertia acts in maintaining the previously attained acceleration in response to the evolving flow conditions. The increase in the de-correlation period of the fluctuating acceleration with increasing particle inertia is in accordance with findings in Von Kármán and wind-tunnel turbulent flow experiments.[25] While the inertia of a flow tracer is small and its acceleration is quickly modified in order to follow the biggest turbulent flow structures, the inertia of a heavy particle is significant, keeping "memory" of previous pressure and velocity distributions over the particles surface. As a result, the acceleration correlations of *inertia particles* decay more slowly than the acceleration correlations of flow tracers. Thus, *inertia particles* are not able to completely follow large energy-containing eddies.

It was shown that the particle Eulerian acceleration variance increases towards the wall where viscous scales are smaller (section III-C). The ratio of the acceleration variance of *inertia particles* and the fluid ones does not obey the power law -2/3 as observed in other flow geometries such as Von Kármán and wind-tunnel turbulent flows. In homogeneous turbulent flows without shear, turbulent fluctuations of the pressure gradient in the vicinity of the particle are the main responsible force for the particle motion. For these flows, the acceleration variance of neutrally buoyant particles is properly accounted for by the second moment of pressure increments at the particle scale, see Brown *et al.*[26] When the acceleration variance of a neutrally buoyant particle is scaled with the one of a flow tracer,

171

$\langle a_{IP}^2 \rangle / \langle a_{FT}^2 \rangle$, the decrease is consistent with the power law -2/3 in the form: $\langle a_{IP}^2 \rangle / \langle a_{FT}^2 \rangle \approx (d_p/\eta)^{-2/3}$, see Calzavarini et al.[27]

In inhomogeneous shear flows as in pipes, the particle motion analysis is more complicated. In the presence of shear and for particles with relevant size, general forms of lift need to be accounted for in the particle motion. For pipe flows at Re_b=10300, the gradient of average axial velocity in the radial direction, $\partial U_z/\partial r$, is of order 60 s^{-1} at the pipe walls, see Oliveira et al.[9,16] In the wall region, ratios of acceleration variance of order 1 are found for tangential and radial components. Moreover, the turbulent flow field in pipes is inhomogeneous. Once particles move in the radial direction, they shift to areas with distinct pressure and velocity distribution characteristics. Particles with relevant inertia maintain information about the evolving flow conditions from different areas (acceleration correlations decay slower). Not surprisingly, the scaling law (-2/3) behavior fails to represent the acceleration variance of *inertia particles* for the present turbulent pipe flow.

5.5   Conclusions

3D-PTV has been applied to particle-laden pipe flow at Re_b=10300 with mean volumetric concentration of *inertia particles* equal to 1.4×10^{-5}. Fluid statistics of flow tracers have been found to be similar to the ones of a single-phase fully developed pipe flow. Velocity and acceleration Lagrangian statistics have been determined for *inertia particles* with Stokes number (*St*) equal to 2.3, based on the particle relaxation time and viscous scales. To the best of our knowledge, no measurements of Lagrangian statistics of inertial particles in a pipe flow have been reported before.

The minimum amount of data in a discrete time separation needed for the description of Lagrangian velocity correlations has been determined for Re_b =10300. Appropriate results are found if the number of correlation samples exceeds 1.5×10^4.

The decay of Lagrangian velocity correlations is faster for *inertia particles* (*St* = 2.3) than for flow tracers due to the crossing trajectories effect. On the other hand, the decay of Lagrangian acceleration correlations is about 25 % slower for *inertia particles*. Here, the particle inertia acts in maintaining the prior acceleration while the flow conditions evolve. Velocity correlations for both classes of particles decay in periods of time associated with the biggest flow structures or energy-containing eddies. For acceleration correlations, the de-correlation takes place in periods of time a few times bigger than the Kolmogorov time.

In inhomogeneous turbulent pipe flow, the acceleration variance of *inertia particles* normalized by the fluid acceleration variance does not obey the power law $(d_p/\eta)^{-2/3}$, as observed for neutrally buoyant particles in other flow geometries such as Von Kármán and wind-tunnel turbulent flows. In the presence of shear and for particles with relevant size, general forms of lift need to be accounted for in the particle motion.

All necessary ingredients of a Langevin model for *inertia particles* have been quantified for turbulent upward concurrent flow of a fluid with $\rho_f \approx 1000$ kg/m^3 and particles with $\rho_p \approx 1050$ kg/m^3, diameter of 0.8 mm, Stokes number of 2.3 and with volumetric concentration of 1.4×10^{-5}. The maximum observed in the velocity structure function of *inertia particles* when scaled with $\langle\varepsilon\rangle\tau$ allows the determination of a modified direction-dependent Kolmogorov constant, C_0^k. With the measured Lagrangian velocity correlations for *inertia particles*, a modified damping tensor can be also determined. Full examination of such a Langevin model is beyond the scope of the present experimental study.

References

[1]   C. Poelma, J. Westerweel and G. Ooms: "Turbulence statistics from optical whole-field measurements in particle-laden turbulence". Experiments in Fluids 40(3): p/347-363, (2006).

[2]   A. I. Kartusinsky, E. E. Michaelides, M. T. Hussainov and Y. Rudi: "Effects of the variation of mass loading and particle density in gas–solid particle flow in pipes". Powder Technology, 193, 176-181, (2009).

[3]   S. B. Pope: "Lagrangian PDF methods for turbulent flows". Annu. Rev. Fluid Mech. 26, 23 (1994).

[4]   P. K. Yeung: "Lagrangian investigations of turbulence". Annu. Rev. Fluid Mech. 34, 115 (2002).

[5]   L. Biferale, E. Bodenschatz, M. Cencini, A. S. Lanotte, N. T. Ouellette, F. Toschi, and H. Xu: "Lagrangian structure functions in turbulence: A quantitative comparison between experiment and direct numerical simulation". Physics of Fluids 20, 065103 (2008).

[6]   J. J. H. Brouwers: "On diffusion theory in turbulence". Journal of Engineering Mathematics, 44: 277 – 295, 2002.

[7]   Y. Suzuki and N. Kasagi: "Turbulent air-flow measurement with the aid of 3-D particle tracking velocimetry in a curved square bend". Flow, turbulence and combustion 63, 415-442, 2000.

[8]   R. J. E. Walpot, C. W. M. van der Geld, and J. G. M. Kuerten: "Determination of the coefficients of Langevin models for inhomogeneous turbulent flows by three-dimensional particle tracking velocimetry and direct numerical simulation", Physics of Fluids 19, 045102 (2007).

[9]   J. L. G. Oliveira, C. W. M. van der Geld and J. G. M. Kuerten: "Lagrangian and Eulerian statistics of pipe flows measured with 3D-PTV at moderate and high Reynolds numbers", submitted to Flow, Turbulence and Combustion.

[10]   M. P. B. Veenman, "Statistical analysis of turbulent pipe flow: A numerical approach," Ph.D. thesis, Technische Universiteit Eindhoven (2004).

[11]   R. W. Miller: 1996, Flow Measurement Engineering Handbook. McGraw-Hill, 3rd edition.

[12]   H. -E. Albrecht, M. Borys, N. Damaschke, and C. Tropea: Laser Doppler and phase Doppler measurement techniques. Springer-Verlag 2003.

[13]   C.W.M. van der Geld: "On the motion of a spherical bubble deforming near a plane wall", Journal of Engineering Mathematics, 2002, Volume 42, Number 2, Pages 91-118.

[14]   J. O. Hinze: 1975, Turbulence. McGraw-Hill.

[15]   L. Schiller and Z. Naumann: "A drag coefficient correlation". Z. Ver. Deutsch. Ing., 77 -318, (1935).

[16]   J. L. G. Oliveira, C. W. M. van der Geld and J. G. M. Kuerten: "The role of Inertia and Turbulence on Concentration Profile and Mean Relative Velocity in Particle-laden Pipe flow", (chapter 3).

[17]   R. J. E. Walpot, J. G. M. Kuerten, and C. W. M. van der Geld, "Experimental determination of Lagrangian velocity statistics in turbulent pipe flow". Flow, Turbulence and Combustion 76(2), 163-175, 2006.

[18]   S. B. Pope, "Turbulent Flows ", Cambridge University Press, Cambridge, 2000.

[19]   L. Mydlarski and Z. Warhaftz: "Three-point statistics and the anisotropy of a turbulent passive scalar", Physics of Fluids vol. 10, number 11, 1998.

[20]   S. B. Pope, "Stochastic Lagrangian models of velocity in homogeneous turbulent shear flow," Phys. Fluids 14, 1696, 2002.

[21]   R.-C. Lien and E. A. D'asaro: "The Kolmogorov constant for the Lagrangian velocity spectrum and structure function", Physics of Fluids vol. 14, number 12, 2002.

174

[22]   J. I. Choi, Y. Kyongmin, and L. Changhoon: "Lagrangian statistics in turbulent channel flow", Phys. Fluids 16, 779, 2004.

[23]   L.I. Zaichik and V.M. Alipchenkov: "Statistical models for predicting particle dispersion and preferential concentration in turbulent flows", International Journal of Heat and Fluid Flow 26, 416–430, 2005.

[24]   R. Volk, E. Calzavarini, E. Lévêque, J.-F. Pinton: "Dynamics of inertial particles in a turbulent von Kármán flow", J. Fluid. Mech. 668, 223-235 (2011).

[25]   N. M. Qureshi, M. Bourgoin, C. Baudet, A. Cartellier and Y. Gagne: "Turbulent transport of material particles: An experimental study of finite size effects", Phys. Rev. Lett. 99 (18), 2007.

[26]   R. Brown, Z. Warhaft and G. Voth: "Acceleration statistics of neutrally buoyant spherical particles in intense turbulence", Phys. Rev. Lett., 194501, 2009.

[27]   E. Calzavarini, R. Volk, M. Bourgoin, E. Leveque, J.-F. Pinton and F. Toschi: "Acceleration statistics of finite-sized particles in turbulent flow: the role of Faxén forces", J. Fluid Mech. 630, pp. 179 - 189 (2009).

[28]   G. A. Voth, A. La Porta, A. M. Crawford, J. Alexandre and E. Bodenschatz: "Measurement of particle accelerations in fully developed turbulence", J. Fluid. Mech. 469, 121-160 (2002).

[29]   M. R. Wells and D. E. Stock: "The effects of crossing trajectories on the dispersion of particles in a turbulent flow", J. Fluid. Mech. 136, 31-62, 1983.

[30]   K. J. Sene, J. C. R. Hunt and N. H. Thomas: "The role of coherent structures in bubble transport by turbulent shear flows". J. Fluid Mech. 259, 219–240, (1994).

[31]   P. D. M. Spelt and A. Biesheuvel: "On the motion of gas bubbles in homogeneous isotropic turbulence", J. Fluid. Mech., 336, 221-244, (1997).

6

Conclusions

This work aimed at experimental clarification of the essential physics of turbulent particle-laden pipe flows with a characteristic ratio of turbulent carrier-phase RMS velocity and terminal velocity of inertia particles, u_{rms}/U_{TV}, of order one. An experimental setup has been arranged in such way that the liquid and particle three-dimensional velocities in upward and downward vertical flows could be measured. With bulk flow Reynolds number equal to 10300, particle-laden flows with volumetric loads of inertia particles ranging from 0.5×10^{-6} to 1.7×10^{-4} have been tested. Two categories of inertia particles with Stokes number, based on the relaxation time for particles in stationary flow and on viscous scales, equal to 2.3 and 3.3 have been measured. By means of 3D-PTV, both Eulerian and Lagrangian velocity characterizations have been determined for both flow tracers and inertia particles.

An overview of main results and conclusions is presented in section 6.1. Recommendations for future work are given in section 6.2.

6.1   Summary of main results and conclusions

A 3D-PTV experimental setup has been validated by comparing Eulerian and Lagrangian results of a single-phase pipe flow in fully developed conditions at $Re_b = 10300$ with literature results (chapter 2). New experimental methods have been explored and presented, paving the way for measurement of Lagrangian particle statistics, be it tracers or be it inertial particles, at bulk Reynolds numbers 20,000 and higher.

Two analysis methods of Lagrangian trajectory statistics as proposed by Walpot *et al.*[1] have been revisited (chapter 2). One of the methods has been successfully applied to the trajectory analysis of flow tracers and inertia particles in particle-laden flows (chapter 5). Velocities derived by straightforward interpolations of consecutive 3D positions of a particle trajectory have been found to yield accurate pipe flow statistics at $Re_b = 10300$, if a maximum triangulation error of the order of 40 µm is allowed in the particle detection algorithm. There is no need to correct the spatial position of particles with smoothing filters, as has been done by Walpot *et al.*[1] The application of a Savitz-Golay low-pass smoothing filter to correct the spatial position of particles with a third order polynomial and a filter span of 17 points is found to be unnecessary with the measurement accuracies specified above. Naturally, such low-pass filtering is undesirable because of the *a priori* unknown cut-off frequency.

To analyze the impact of flow turbulence level on particle behavior, different stages of flow development have been tested. Transient states of pipe flows at $Re_b = 10300$ have been characterized by the characteristics of the turbulence. By quantifying the cross-section averaged diagonal components of the Reynolds stress tensor, linear fits distinguish flow conditions from the fully developed state in a convenient way. Turbulent pipe flows close to fully developed conditions exhibit linear inhomogeneous behavior in the pipe core. At $Re_b = 10300$, ratios of the diagonal components of the Reynolds stress tensor increase linearly from $r/R = 0$ to $r/R \approx 0.8$. When the terminal velocity of particles and a representative RMS turbulent flow velocity are of same order, i.e. $|u_{rms}/U_{TV}| \approx O(1)$, the time-averaged mean relative velocity decreases with increasing level of flow turbulence. A correlation between axial relative velocity and flow turbulence level has been proposed. With the observed trends being opposed to those in turbulent bubbly flows, it is conjectured that particles heavier than fluid and with $u_{rms}/U_{TV} \approx O(1)$ possess longer residence times in

the upward side of eddies. This explains the observed reduction of the mean relative velocity.

Flow orientation with respect to gravity has a strong effect on the concentration profile of particles if $|u_{rms}/U_{TV}| \approx O(1)$, with wall peaking in downflow and core peaking in upflow. It is hypothesized that a fluctuating component of the lift force on particles is responsible for these trends. If $|u_{rms}/U_{TV}| \rightarrow 0$, particles cross turbulent eddies with hardly any interaction because of their high inertia. The relative velocity approaches the terminal velocity and in the presence of enough shear, a mean lift force will be dominant in the determination of wall-normal concentration profiles, see results of Suzuki et al.[2], for example. In this situation, the magnitude of a fluctuating lift component is not relevant. If $|u_{rms}/U_{TV}| \gg 1$, the terminal velocity of particles with low inertia is not significant and the relative velocity is also small. Particles act as tracers. In this situation, the turbulent motion of particles is governed by the interaction with flow eddies and lift force does not play a role. Mean concentration profiles of the low-inertia particles will not be far from a homogeneous distribution.

When the volumetric concentration of particles for a given radial position exceeds about 3×10^{-4}, particle and fluid flow statistics experience significant changes, i.e. in the concentration profiles of particles. In this situation, the average inter-particle distance is smaller than the expected wake downstream of a single particle in an inhomogeneous flow. Two-way coupling seems to come into play. Reference values of the wake length behind a particle are taken from literature.[2]

Turbulence augmentation is observed with increasing mean concentration of particles with $St = 2.3$ or 3.3, $|u_{rms}/U_{TV}| \approx O(1)$, particle Reynolds number, Re_p, less than 12 and mass density ratio of particles to fluid, ρ_p/ρ_f, roughly 1.05. Criteria based only on Re_p, ratio of turbulence and particle length and time scales, and volume load do not suffice to predict the turbulent modulation found. Apparently, one or more parameters of influence are missing. It is conjectured that the ratio $|u_{rms}/U_{TV}|$ is also relevant to predict turbulence modulation.

The effect of particle feedback on the fluid is presented with δ-forcing. It is shown that the applied mean concentrations, 0.5×10^{-6} to 1.7×10^{-4}, are too low to affect the frictional pressure drop. For example, particle feedback on the fluid yields roughly 5.7×10^{-6} N/kg for upflow with $St = 2.3$ and mean volumetric concentration of 1.4×10^{-5}, while the frictional pressure drop yields about 7.5×10^{-4} N/kg for a fully-developed pipe flow at $Re_b = 10300$. Only mean concentrations over 10^{-3} will affect the axial pressure drop for similar conditions

(same category of particles and velocimetry results). In the pipe core region ($0 < r/R < 0.8$), drag forces are dominant on the coupling term for the streamwise direction. In the wall region ($0.8 < r/R < 1$), drag forces reduce with decreasing distance to the wall. There, the gravity term, which only affects the particle feedback via an added mass term, is the dominant contribution for the present flows.

6.1.1 Considerations about the transport of inertia particles

The distribution of particles in a cross-section may be crucial in determining collision frequency, breakage efficiency, reaction rates, deposition and entrainment. As shown above, several parameters can be relevant in the concentration profile of the dispersed phase, such as flow orientation with respect to gravity, the ratio $|u_{rms}/U_{TV}|$, the presence of shear etc. Break-up of particles is related to turbulent stresses and turbulent dissipation. In inhomogeneous turbulent pipe flow, turbulent dissipation is more pronounced at the pipe walls. Apart from the small viscous region near the wall, turbulent dissipation is of the same order of magnitude as turbulence production.[3] The latter has been measured in the present work together with the direction-dependent Kolmogorov constant, C_0^k. With these measurements, a correlation for critical Weber as a function of radius has been determined. Different break-up criteria can be evaluated for a given radial position at $Re_b = 10300$. Turbulence production has also been measured in transient states of particle-laden pipe flows at $Re_b = 10300$. In the measured development stages, turbulence production is larger than in fully developed flow. Apparently, turbulence production is enhanced for particle-laden flows with $|u_{rms}/U_{TV}| \approx O(1)$ and inertia particles with $St = 2.3$ or 3.3, and even more so if the volumetric concentration is higher or if the level of turbulence is higher.

6.1.2 Lagrangian statistics of particle-laden pipe flow

Flow tracer and inertia particle velocity and acceleration Lagrangian statistics were analyzed in a particle-laden pipe flow at $Re_b=10300$ with mean volumetric concentration of inertia particles equal to 1.4×10^{-5} and $St = 2.3$. To our knowledge, no simultaneous measurements of Lagrangian statistics of flow tracers and inertial particles in a pipe flow have been reported before. Flow tracer statistics have been found to be similar as in single-phase fully developed pipe flow.

179

The Lagrangian analysis method was successfully applied to the trajectories of inertia particles as well as flow tracers. A radial band width, Δr, of 0.5 mm in a pipe diameter of 0.1 m and a camera frequency of 50 Hz sufficed to obtain negligible bias at Re_b=10300. The minimum amount of data in a discrete time interval needed for the description of Lagrangian velocity correlations (be it tracers or inertia particles) has been determined. Appropriate results are found if the number of correlation samples exceeds 1.5×10^4.

The decay of Lagrangian velocity correlations is faster for inertia particles ($St = 2.3$) than for flow tracers ($St = 0.1$) due to the crossing trajectories effect. In opposite trend to velocity correlations, Lagrangian acceleration correlations of inertia particles decay more slowly than for flow tracers: about 25 % more slowly if all normal accelerations are taken into account and all radial positions. While the inertia of a flow tracer is small and its acceleration is quickly modified in order to follow all turbulent flow structures, the inertia of a heavy particle is significant, keeping "memory" of previous pressure and velocity distributions over the particle surface. As a result, the acceleration correlations of inertia particles decay more slowly than the acceleration correlations of flow tracers. Thus, inertia particles are not able to completely follow large energy-containing eddies. Velocity correlations for both classes of particles decay in periods of time associated with the biggest flow structures or energy-containing eddies, τ_c. For acceleration correlations, the decay takes place in periods of time a few times bigger than the Kolmogorov time, τ_k. Average estimations of τ_k and τ_c at $Re_b = 10300$ were given: about 28ms and 2.8s, respectively.

The Eulerian acceleration variance of inertia particles normalized by the fluid one does not obey the power law $(d_p/\eta)^{-2/3}$, as observed for neutrally buoyant particles in other flow geometries such as Von Kármán and wind-tunnel turbulent flows.[4] In the presence of shear and for particles with relevant size, general forms of lift need to be accounted for in the particle motion. Moreover, the turbulent flow field in pipes is inhomogeneous. Once particles move in the radial direction, they shift to areas with distinct pressure and velocity distribution characteristics. Particles with relevant inertia maintain information about the evolving flow conditions from different areas (acceleration correlations decay more slowly). Not surprisingly, the scaling law (-2/3) behavior fails to represent the Eulerian acceleration variance of inertia particles for the selected turbulent pipe flow.

All necessary ingredients of a Langevin model for inertia particles have been quantified for turbulent upward concurrent flow of a fluid with $\rho_f \approx 1000$ kg/m^3 and particles with $\rho_p \approx$

1050 kg/m^3, diameter of 0.8 mm, Stokes number of 2.3 and with volumetric concentration of 1.4×10^{-5}. The maximum observed in the velocity structure function of inertia particles when scaled with the product of mean dissipation rate and correlation time span, $<\varepsilon>\tau$, allows the determination of a modified direction-dependent Kolmogorov constant, C_0^k. With the measured Lagrangian velocity correlations for inertia particles, a modified damping tensor can be also determined. Full examination of such a Langevin model is beyond the scope of the present experimental study.

6.2 Recommendations

Experimental analysis of particle-laden flows in situations where the particle feedback on the fluid can affect the frictional pressure drop would complement the contents of the present study. This can be achieved in different ways, such as increasing the mean volumetric concentration of applied inertia particles ($St = 2.3$ or 3.3) to larger than 10^{-3} or changing the particle properties. In this situation, particle and fluid statistics may differ from the ones obtained in this work. Other interesting phenomena can be relevant in the analysis, i.e. particle-particle and particle-wall collisions. If higher mean volumetric concentrations are applied, the stronger effect of the set of wakes behind particles will also be relevant in flow and particle statistics.

The evaluation of Lagrangian approaches to modeling the dispersion of inertial particles suspended in turbulent flows is also a challenge. In the present work, the necessary ingredients of a Langevin model for inertia particles with $St = 2.3$ have been quantified. However, a more extensive study is required to further develop and validate such a model.

References

[1]   R. J. E. Walpot, J. G. M. Kuerten, and C. W. M. van der Geld, "Experimental determination of Lagrangian velocity statistics in turbulent pipe flow". Flow, Turbulence and Combustion 76(2), 163-175, 2006.

[2]   Suzuki, Y., Ikenoya, M. and Kasagi, N., "Simultaneous measurements of fluid and dispersed phases in a particle-laden turbulent channel flow with the aid of 3-D PTV", Experiments in Fluids, 185-193 (2000).

[3]   M. P. B. Veenman, "Statistical analysis of turbulent pipe flow: A numerical approach" Ph.D. thesis, Technische Universiteit Eindhoven (2004).

[4]   R. Volk, E. Calzavarini, E. Lévêque, J.-F. Pinton: "Dynamics of inertial particles in a turbulent von Kármán flow", J. Fluid. Mech. 668, 223-235 (2011).

Acknowledgements

After 4 years my PhD has finally come to an end. During this period, relatives, colleagues and friends have given important contribution to its completion. First of all, I'd like to express my gratitude to prof. Brouwers and Dr. Cees van der Geld for giving me an opportunity to work in the Process Technology group. Cees has closely and patiently guided me along this time: thank you very much. I also express my gratitude to prof. Hans Kuerten, who also gave numerous contributions to this work. Thanks to Dr. van Esch and Dr. Eric van Kemenade for interesting inputs during our Monday meetings. I would also like to acknowledge my colleagues Geert-Jan van Hoek, Marianne Meves, Henry, Marc Willekens, Paul Bloemen and Jan Hasker for all the assistance and help. Special thanks to Geert-jan for helping me during these 4 years in the completion of the experimental work.

I would like to express my appreciation to all colleagues and friends from Process Technology: Mart (and Monique), Gagan (and Sonia), Nicole (and Bas), Coen Baltis (and Nela), Guy (and Daniella), Arend, Pecenko, Marcel Lemmens, Rob, Hattie, Wictor, Daniel and Emanuelle. Special thanks to Coen, Alexandre, Adriano Ronzoni and Paôlo Candidoto who also contributed to my project in several opportunities: thanks a lot.

My appreciation is also extended to all friends who could make life in Eindhoven much funnier. Friends from Brazil, Marcos, Gierri (and Michele), Victor, Vinicius, Mauricio, Paulo, Alexandre and Nicolas (almost Brazilian), thanks for the barbecue and "truco" sessions. Thanks also to my Dutch friend Ruud Verschearen, bedankt. Friends from Chemistry group, Camille, Vladimir, Gosia, Ivelina, Maurizio, Isabelle, Bory (and Florence), thanks all for the company and the nice time at the borrel. Special thanks to my friends and for some time housemates Nicolas and Marcos for all the friendship from the very beginning to the last day of my stay in Holland.

I would like to show appreciation to my father-, mother- , brothers- and sisters- in law, Valdemar, Vírginia, Renata, Daniela, Marcos and André for all the support. I dedicate this work to my mother Inez, father Luiz and brothers Sérgio, Diogo e César. During this time, my mother followed my progress daily and she is important part of this work even at a long distance. To my wife Mirella, I cannot express with words all the effort and companion she did and gave me during this time. I would not succeed without her support and love.

Curriculum Vitae

Jorge Luiz Goes Oliveira was born on the 30th of November 1981 in Aracaju, Brazil. After finishing the secondary school in 1999, he studied Mechanical Engineering at the Federal University of Santa Catarina, Brazil. In 2004 he received his bachelor diploma in Engineering. During his education he did an internship at Whirlpool, where he worked on product development for the refrigeration segment. From 2005 to 2006 he joined Celesc S.A., where he worked on the management of the electrical grid of Santa Catarina state and on the acquisition of services and industrial equipment through public bid. From 2006 to 2007 he coursed the Master in Science in fluid mechanics at the Federal University of Santa Catarina, with final work focused on the prediction of mass flow rates of two-phase mixtures.

In 2008 he started a PhD project in the Process Technology group at the Eindhoven University of Technology (the Netherlands), under the supervision of prof. dr. ir. Brouwers and dr. van der Geld. The most important results of this work are presented in this dissertation.

List of Publications

❖ **Oliveira, J. L. G.**, Geld, C. W. M. v. d., Kuerten, J. G. M., "Lagrangian and Eulerian statistics of pipe flows measured with 3D-PTV at moderate and high Reynolds numbers". Submitted to Flow Turbulence and Combustion, 2012.

❖ **Oliveira, J. L. G.**, Passos, J. C., Verschaeren, R. L. P. and Geld, C. W. M. v. d., "Mass flow rate measurements in gas-liquid flows by means of a venturi or orifice plate coupled to a void fraction sensor". Experimental Thermal and Fluid Science, 2008.

❖ **Oliveira, J. L. G.** "Flow rates measurement in gas-liquid flows by means of a venturi or orifice plate coupled to a non-intrusive conductance type void fraction meter", (in Portuguese). Master Thesis. Florianópolis/Brazil, Federal University of Santa Catarina, October, 2007.

❖ Dalmaz, A., Passos, J. C, Caruso, G. L., **Oliveira, J. L. G.** and Beyer, H. G. Wind Forecast for electricity production at Santa Catarina/Brazil. In: IV Mechanical Engineering Brazilian Congress, 2006.